Modification of Boron-Doped Diamond Electrodes for Application in Electrochemistry

YUE MA

Supervised by Professor John S Foord

A thesis submitted in conformity with the requirements for the degree of Doctor of Philosophy in Physical and Theoretical Chemistry

University of Oxford

Department of Chemistry

Wolfson College

2022

Declaration

All research works reported in this thesis has not previously been accepted in substance for any degree and is not being concurrently submitted in candidature for any degree. This thesis is conducted by the author unless stated otherwise. All materials from other sources has been properly and fully acknowledged.

Yue Ma

Dedicated to my mother and grandparents.

Acknowledgments

Throughout my whole D. Phil process in the past three years, I would like to give my thanks and respect to my supervisor, Professor John Foord, whose expertise was invaluable in formulating and guiding me through the questions I encountered in research and methodology. His constant kindness and patience encouraged me always to be strong and cheerful when I am anxious and worried. Conducting research and organizing this thesis has become extremely challenging during the pandemic, but John provided me enormous help and support to complete.

I would particularly like to acknowledge my former colleagues Dr. Emina Hadzifejzovic and Dr. Martin Rosillo-Lopez for getting me started with electrochemical experiments which I had no experience with, helping me with operating microscopic instruments, and doing XPS analysis. I would also like to give special thanks to Prof. Christoph Salzmann from University College London for providing the synthesising equipment and reagents of cx-GNF that are used for this work. I also want to show my gratitude to other group members – Ella Bentin, Thomas Lau, Xiaosheng Cai, Yifan Wang, Chenbo Wang, and Katherine Farrow for lighting up CRL basement and building a friendly environment of discussion.

I would like to thank my dearest friends in Oxford – Ally Bo, Ella Bentin, Sushanta Mahanta, Yige Gao, Zheying Xu, and Yujia Qing; and my dearest friends in China, Japan,

and California – Corina Cao, Gina Wen, Kaori Maruyama, and Martin Moskovits, for your genuine friendship and support during the grey days. I will never forget the precious memories we shared together and may all our dreams be fulfilled. Also, I would like to especially thank my boyfriend and husband-to-be Tony Tong Qu.

Finally, I would like to give my sincerest thanks to my mother, who is a professor at Zhengzhou University and doctor of RICU. She worked frontline fighting against COVID-19. She has always been a role model for me, and I always try my best to be a daughter that makes her proud. Finally, I would like to express my heartfelt gratitude to my grandparents who were always supportive of everything I do, as being far away has not been easy. Now I have returned from my years abroad, I look forward to enjoying our time together. I would like to dedicate this thesis to them.

Abstract

Nanoparticles have gained extensive research interests since they were successfully synthesized in the last century. Their unique physical and chemical properties that are distinct from the bulk forms are versatile and have been widely applied in various fields. Electrochemistry is a common technique that yields both high accuracy and efficiency in chemical analysis (electroanalysis).

This thesis investigates nanoparticles, both carbon-containing and metal, both pure metal and alloys, as electrode modifiers for boron-doped diamond electrodes (BDDEs) in electrocatalysis and electroanalysis. Specifically, we focused on how the surface elemental components and morphologies can affect the performance of BDDEs in electrocatalysis and electroanalysis. The experiments were carried out using a range of electrochemical voltammetry methods to understand the kinetics of different reaction systems, accompanied with physical instrumental analysis, including electron microscopy, UV-Visible spectroscopy, and X-ray photoelectron spectroscopy to analyse the composition and structure of nanoparticle modifiers.

The use of nanoparticle modified BDDEs in catalysing the hydrogen evolution reaction (HER), which is one of the most critical reactions in fuel chemistry to produce clean and sustainable hydrogen gas as a renewable energy source was explored and used as the most important example reaction throughout this whole thesis to judge the quality of an electrode modifier as a heterogeneous catalyst. I explored the electrodeposition of three

morphologies (polyhedral, dendritic, and spherical) of Ag nanoparticles and two morphologies (dendritic and spherical) of AgAu nanoalloys using various electrochemical conditions spanning deposition potential, deposition method, and deposition time. The reaction kinetics were analysed, and the best candidates were selected based on Tafel analysis and the current densities in voltametric measurements. Notably, spherical Ag and spherical AgAu modified BDDEs showed the best performance in the HER electrocatalysis, which are potentially less expensive yet efficient alternatives for Pt/Pd containing catalysts.

Colloidal Ag and Au nanoparticles and AgAu nanoalloys were also synthesised using the in-situ chemical reduction method. To avoid natural aggregation, carboxylated graphene nanoflakes (cx-GNF) were used as stabilisers. cx-GNF was able to prevent the aggregation of nanoparticles through a non-covalent interaction between the metal nanoparticles and the graphenic surface. Compared with electrodeposited, unstabilised colloidal, and sodium citrate (a widely used stabiliser for nanoparticle synthesis) stabilized colloidal nano-species, cx-GNF stabilized colloidal nanoparticles showed outstanding structural stability of over 14 days and enhanced performance in electrocatalysis of the HER.

The high surface-to-volume ratio of metal nanoparticles makes them naturally suitable for aiding electrochemical sensing. The sensing performance of AuNPs of different synthesis methods including electrodeposition, unstabilised in-situ reduction, and cx-

GNF stabilized in-situ reduction were examined and compared. The effect of pH was also investigated for selected systems since the solvation of slightly acidic cx-GNF in alkaline solutions will cause the loss of metal nanoparticles. The optimal pH values were selected for each individual system based on the current signals. AuGNF showed the highest detection signal for various sensing systems, and we were able to detect As (III) ions with a LOD of 0.1 nM, 4-nonylphenol with a LOD of 0.3 μM, glucose with a LOD of 1 mM, and hydroquinone with a LOD of 0.5 nM. Notably, simultaneous detection of hydroquinone and catechol was achieved successfully with LOD of catechol 50 times lower than hydroquinone.

The effect of surface composition, morphology, and stabilizers of nanoparticle modifiers were further investigated in more complex tri-metal alloy systems. PdAuCu tri-metal nanoalloys were synthesized using electrochemical deposition of AuCu nanoalloy, followed by galvanic replacement reaction between Pd and Cu, and in-situ chemical reduction with cx-GNF stabilisation. The electrocatalysis of various fuel cell reactions, including the HER, oxygen reduction reaction (ORR), and ethanol oxidation reaction (EOR) were studied. As a result, the galvanic replacement reaction of electrodeposited AuCu was able to fully covert Cu to Pd, and gives a similar performance in every reaction compared with colloidal tri-metal PdAuCu stabilized by cx-GNF, but with minimized usage of expensive Pd.

Contents

List of Abbreviations

AOP	.....	Advanced oxidation process
B.E.	.....	Binding energy
BDDE	.....	Boron-doped diamond electrode
BSE	.....	Back-scattered electrons
CAT	.....	Catechol
CE	.....	Counter electrode
CILE	.....	Carbon ionic liquid electrode
CM	.....	Carbon materials
CNT	.....	Carbon nanotube
CNR	.....	Carbon nanoribbon
CPs	.....	Carbon particles
Col.	.....	Colloidal
CV	.....	Cyclic voltammagram
CVD	.....	Chemical vapour deposition
cx-GNF	.....	Carboxylated graphene nanoflakes
DEFC	.....	Direct methanol fuel cell
DET	.....	Dissociative electron transfer
DFT	.....	Density functional theory
DI	.....	Deionized
DPV	.....	Differential pulse voltammetry
ED	.....	Electrodeposition
EDTA	.....	Ethylenediaminetetraacetic acid
EDX	.....	Energy-dispersive X-ray spectroscopy
EOR	.....	Ethanol oxidation reaction
FEGSEM	.....	Field emission gun scanning electron microscopy
GCE	.....	Glassy carbon electrode
GNF	.....	Graphene nanoflakes
GO	.....	Graphene Oxide
GP	.....	Graphene
GRR	.....	Galvanic replacement reaction
HER	.....	Hydrogen evolution reaction
HTHP	.....	High temperature and high pressure
HQ	.....	Hydroquinone
IMFP	.....	Inelastic mean free path
K.E.	.....	Kinetic energy
LOD	.....	Limit of detection
LSV	.....	Linear sweep voltammetry
M-M	.....	Metal-metal

MPCVD	.....	Microwave plasma chemical vapor deposition
NA	.....	Nanoalloy
Naf	.....	Nafion
NPs	.....	Nanoparticles
ORR	.....	Oxygen reduction reaction
PTFE	.....	Polytetrafluoroethylene
PVP	.....	Poly(N-vinylpyrrolidone)
RE	.....	Reference electrode
RGO	.....	Reduced graphene oxide
RSF	.....	Relative atomic sensitivity factor
SC	.....	Sodium citrate
SERS	.....	Surface enhanced Raman spectroscopy
SEM	.....	Scanning electron microscopy
SWV	.....	Square wave voltammetry
TEM	.....	Transmission electron Microscopy
UV-Vis	.....	UV-Visible
WE	.....	Working Electrode
UHV	.....	Ultra-high vacuum
XPS	.....	X-ray photoelectron spectroscopy

List of Figures

List of Tables

Chapter 1 Introduction

1.1. Carbon Materials

All life on earth is based on carbon, owing to its flexibility in binding different atoms simultaneously. Such a unique characteristic makes carbon an ideal candidate for forming long molecule chains to build up the basic materials of life: protein and DNA. Researchers have sparked a deep and enduring interest in carbon materials in recent years (CMs).. CMs manifest the virtues of high surface areas, adaptable shapes, and natural abundance. Versatile in almost all fields of applications, CMs are used in aeroplane landing gears[1], wastewater treatment[2], and agricultural pharmaceutical removal[3], and even drug delivery for cancer treatment[4].

1.1.1. Graphite and Graphitic CMs

The same building blocks, carbon atoms, are used to create CMs in various allotropes. CMs can be broadly divided into three types based on the hybridization type: extended sp^2 CMs, which include graphitic CM and amorphous carbon; sp^3 CMs, which form the the (nano) diamond structure; Nanoscale sp2 carbons such as carbon naotubes, fullerenes and graphene. [5-7]

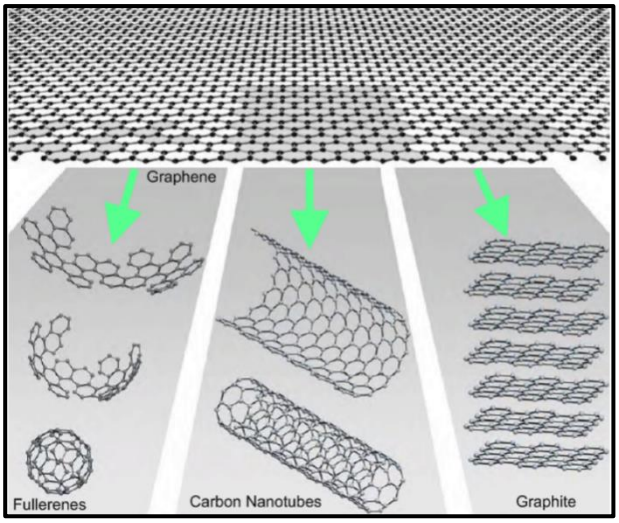

Figure 1.1 2D GP as the building block for other graphitic forms, adapted from[9]

Graphite and graphitic CMs are probably the most fundamental classes of CMs. 2D graphene (GP) was previously believed to be unstable, until Andre Geim and Konstantin Novoselov discovered the surprisingly good elasticity, stability, and conductivity of single-layered GP.[8] 2D GP is the building block for other graphitic forms and can be re-structured into 0D fullerence, carbon nanotubes (CNT), and multi-layered graphite (Figure 1.1[9]). Although initially discovered and applied as a writing material, graphite and graphitic CMs manifest extraordinary properties and can be applied in various fields. For example, graphite is regarded as an ideal refractory material to hold molten metals in industries thanks to its outstanding heat-resisting properties.[10] Graphite is also used as a moderator to regulate the reaction rate in a nuclear reactor.[11] The self-lubricating and dry-lubricating properties of graphite are ascribed to its weak interlamellar coupling between individual GP sheets.[12] Therefore, graphite is commonly used as a gear lubricant in mining machinery, as well as lock lubricants in daily life.[10] The impregnation of metals with graphite can also create self-lubricating alloys that are capable of withstanding extreme temperatures.[13]

1.1.2. Graphene: Structures and Electronic Properties

Since its discovery, GP has become recognised as an extraordinary electronic material due to its electronic properties such as ballistic transport, chemical inertness, hydrophobicity at the nanoscale, and stability in conductivity at high temperatures.[8,14] These unique features make the intrinsic GP a semi-metal or zero-gap semiconductor.[15] Within the planes of GP, the atoms are held tight by covalent bonds through sp^2 hybridization, and pi electrons are delocalized throughout. Meanwhile, unpaired electrons are found at the edges of GP. Another electron from media or other molecules can be introduced for interaction, resulting in disturbance in the pi-pi interaction. The local electronic density, physical, and chemical properties can be therefore modified.[16]

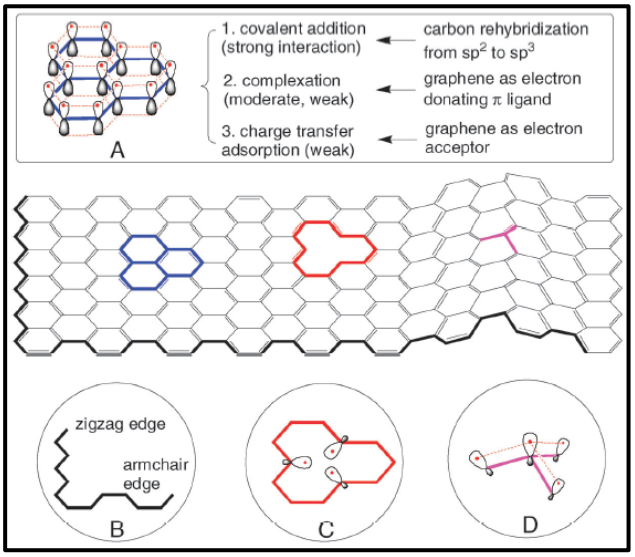

Figure1.2 Structural variance within the GP, adapted from[16]

In spite of its seemingly simplistic structure, GP is much more complicated in the real world. The common structures within GP include defects, zigzag and armchair edges, and local curvature (Figure 1.2). Along with the interactions at the planar sheets, these features jointly determine the chemical reactivity of GP. The re-hybridization from sp^2 to sp^3 at the basal plane results in a strong covalent interaction for the closely packed C atoms, causing their geometries to shift from planar to tetrahedral. Such a strain bolsters extra reactivity. The edge atoms, on the other hand, have no strain and more freedom to adopt sp^3 hybridisation, thus becoming more reactive.[16] The differences in local structures result in significantly different properties for GP's secondary structures. For example, carbon nanoribbon (CNR) with zigzag edges shows metallic electronic properties, and CNR with armchair edges exhibits either metallic or semiconductor-like properties.[17] Similarly, CNTs have different types, depending on the chirality of the starting GP unit (Figure 1.3). This feature can be used in designing and synthesising CNT via epitaxial growth, given that different types of experiment would show various preferences toward CNT with a specific degree of chirality.[18]

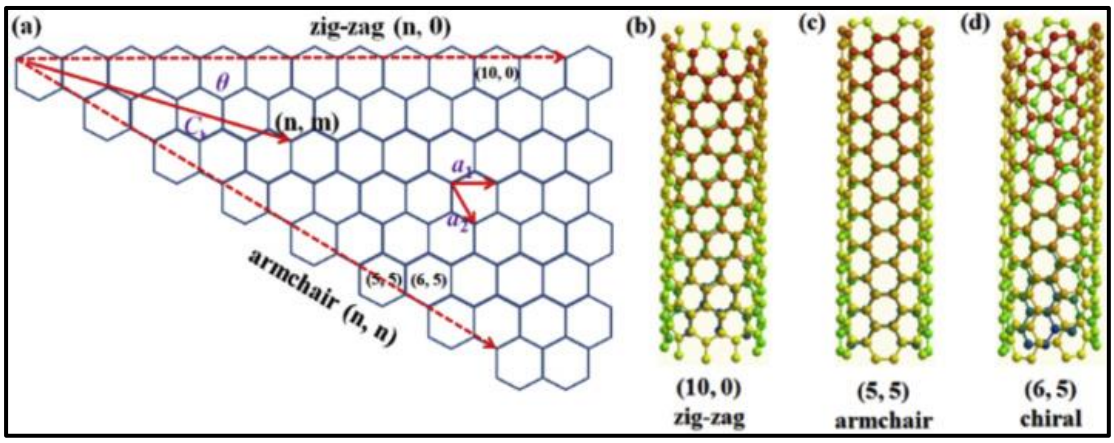

Figure 1.3 Different types of CNT depending on the chirality of the starting GP unit, adapted from[18].

Fullerene, on the other hand, manifests much higher reactivity than GP. The active sites on fullerene are readily modified by different types of molecules, including enzymes for medical applications[19], and metal alloys for supercapacitors.[20]

There has long been an interest in the electrochemical properties of films of the various nanocarbons that exist, as discussed above. It is crucial to understand the roots of electrochemical reactivity for these carbons, such as GP and its derivatives, to facilitate its further application in the field of electrochemistry. Graphene and its derivatives, such as graphene oxide (GO) and reduced graphene oxide (RGO) have broad applications such as conducting electrodes[21] and supercapacitors[22], heavy metal ion detection[23], and have been used to accelerate stem cell differentiation, drug delivery, and disease intervention[24].

1.2. Synthetic Diamond Materials

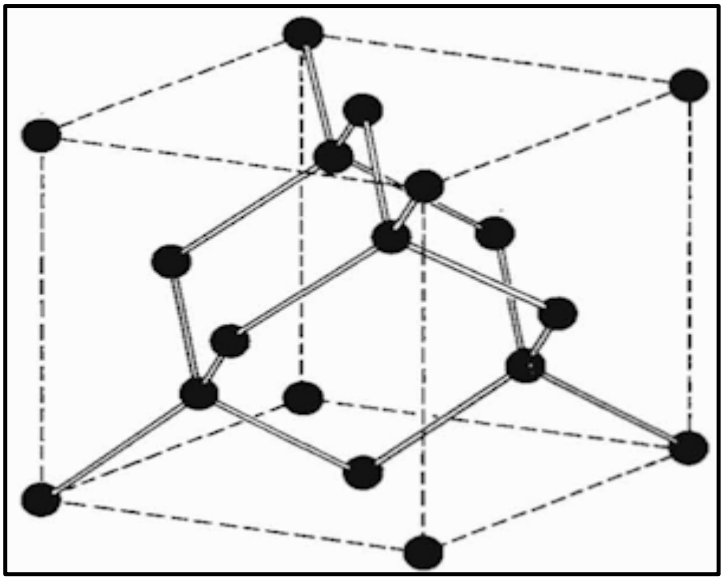

Figure 1.4 Crystal structure of diamond, adapted from [25].

Natural diamonds were discovered for the first time in the rivers Penner, Krishna and Godavari over 4000 years ago. To this day, diamonds are still a precious gemstone that symbolises affection and eternity. The diamond lattice is a cubic sp^3 structure consisting

of elemental carbon. The strong covalent bondings between the atoms makes it extremely strong mechanically and show the highest hardness (Figure 1.4).

Nowadays, artificial diamonds with high purity are commonly used in lab studies. It is known that diamonds can undergo graphitization in an oxygen-free medium at low pressure and a temperature below 1700 ^{o}C [25]. Hence, the early synthesis of crystal diamonds requires high temperature and high pressure (HTHP method). The diamond-graphite equilibrium, followed by the formation of diamond in its thermodynamic stability region, was calculated by Leipunskii for the first time. In comparison with graphite, diamond is not a thermodynamically favourable transformation of carbon under atmospheric pressure. Therefore, a HTHP condition is required to apply the transitional metal/alloy solvent as a structural controller.[26-28]

Microwave plasma chemical vapour deposition (MPCVD) is a common technique for the synthesis of large diamonds with high quality. While the HTHP method is used to usually produce diamond crystals sized in the mm range for mechanical tools, MPCVD produces thin film diamond sized from nm to cm.[29] MPCVD diamond is used in a variety of applications, including abrasives, machinery coating, electronic and optical devices. [30-31] During the process of MPCVD, methane serves as the source of carbon via the promotion of CH_3 radicals, and hydrogen also has a crucial role. The use of hydrogen gas is crucial to prevent any graphitisation once the structure of a diamond has been formed. The hydrogen gas stabilises the sp^3 dangling carbon bonds, the majority of which are hydrogen-terminated. It possibly also helps remove sp^2 carbon by etching. It also abstracts H from the surface to create vacant sites for methyl adsorption.

1.2.1. Synthetic Diamond Electrode

Figure 1.5 Energy diagram of the band gap of intrinsic diamond in selected states (left, adopted from [43]); a free-standing BDD electrode (right, adapted from [44]).

Intrinsic diamond is an insulator with a bandgap of 5.45 eV and is formed in high quality diamond MPCVD with methane and hydrogen gas.[35] The doping of boron makes the diamond material a p-semiconductor; elements such as nitrogen and phosphorus can also be employed, resulting in n-type doping.[36-39] Boron acts as an electron acceptor during the doping. It has a low charge carrier energy, which is only 0.37 eV above the valence band of diamond (Figure 1.5 left [43]). Boron-doped diamond is the most used electrode material for electrochemistry since it is simple to produce, and the boron can be introduced stably at high concentration of 10^{20} –10^{21} cm^{-3}, resulting in a (semi-) metallic material. The boron-doped diamond electrode (BDDE) is synthesised commonly by using diborane or tri-methyl-borane during the MPCVD process (Figure 1.5 right[44]).[42]

1.2.2. Electrochemical Applications

Intensive research into the electrochemical applications of diamond electrodes has been

carried out since Pleskov et al. reported its semiconductor-like behaviour in aqueous electrolytes.[45] Remarkably, BDDE shows high over-potentials and a clean, wide solvent window of around 2.5 V limited by the hydrogen evolution reaction (HER) and oxygen reduction reaction (ORR). This is vital for electrochemical analysis because the oxidation of some compounds that occurs at high positive potentials may overlap with the oxygen evolution current that often gives less reproducible analysis.[46-47] The water splitting reaction is one main reaction to produce hydrogen via electrolysis. The potential at which water splitting occurs is highly dependent of the properties of the electrode material. The sp^3 surface of BDD can be described as "catalytically inert", owing to the lack of binding sites to mediate electron transfer between the surface and a water molecule. Such an intriguing property simultaneously increases the potential window and removes the need to degas solutions, as the level of dissolved oxygen is relatively insignificant. A wider potential window indicates a wider range of electroactive analytes and a greater signal-to-noise ratio in a larger range of potentials. [48-50]

In addition to the typical reactions mentioned above, BDD is also used for energy storage and is incorporated in double-layered super-capacitors.[63] The high over-potential for oxygen production made the swift anodic production of OH· possible. OH· radical is a very strong oxidising reagent that plays a critical role in organic molecule detection and decomposition in aqueous media. Such a procedure is called the advanced oxidation process (AOP).[51] The AOP is useful for water treatments, especially in terms of the detection of common organic impurities, such as hydroquinone, phenols, EDTA, and carboxylic acids.[51, 54-56] Moreover, it is also commonly used in the detection of inorganic

molecules like nitrites, nitrates, sulfides, arsenic, and cyanides.[52-53, 57-58] With the development of biomedical science, diamond electrodes are implemented in biomedical sensors to detect small molecules, such as glucose and dopamine, and large molecules, such as DNA.[59-62]

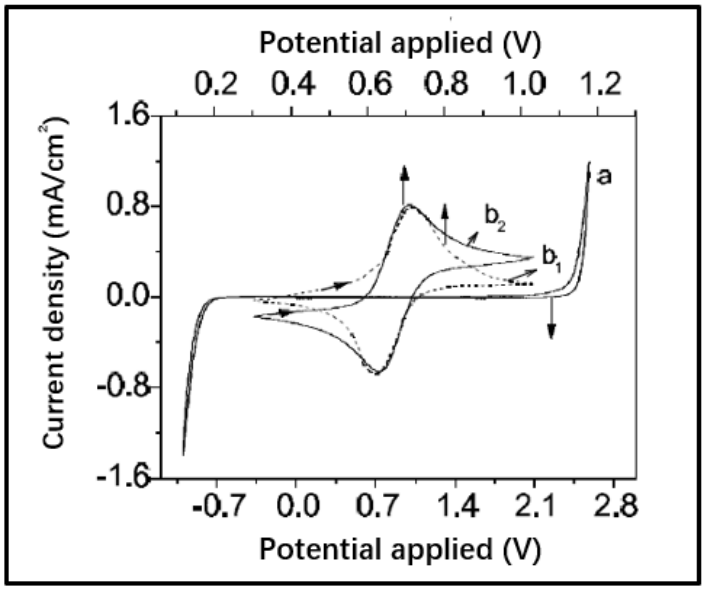

Figure 1.6 The wider potential window BDD electrode, represented by voltametric response in 0.5 M H_2SO_4 (a); and 1st scan voltammograms in 1 mM $K_4Fe(CN)_6$ with 0.5 M H_2SO_4 for the BDD electrode (b_1) and the Pt electrodes (b_2), with scan rate =100 mV/s. Adapted from [48]

1.2.3. Surface Termination of Diamond Electrodes

The common terminations of diamond surfaces include hydrogen termination and oxygen termination, which change the surface electronic characteristics of diamond electrodes and influence the electrochemical properties with regard to surface bond polarity, electrostatic interactions between electrolyte and electrode surface, and electron transfer kinetics.[64]

As-grown diamond is hydrogen terminated due to the adsorption of extra hydrogen gas

during the CVD process and has a surface conductivity of the order of 10^{-4} Ω to 10^{-4} Ω at room temperature.[29] At the surface of BDDE, hydrogen termination produces a dipole ($C^{\delta-} - H^{\delta+}$). HBDDE is prepared to receive electrons as a p-type carrier from an adsorbate because it has the positive dipole of H at the surface.[64-66] The lowest unoccupied electronic level of the adsorbates must be below the valence bond minimum of BDDE in order for direct electron transfer to occur. An HBDDE has a negative electron affinity of -1.3 eV, compared with that of a bare BDDE (0.3 eV). However, due to the large band gap of the diamond (5.5 eV), the lower limit for the electron affinity of the adsorbate (χ_{ad}=5.5 eV-1.3 eV=4.2 eV) is still impossible for electron transfer from the conduction band minimum of an H-BDDE to the atmospheric species, given the electron affinities of halogen atoms are normally below 3.7 eV.

The conductivity of H-terminated diamond is therefore explained by a surface transfer doping process. A thin water layer accumulates on the electrode surface when it is exposed to air, producing a positively charged accumulation sub-layer of H_3O^+. The difference between the chemical potential of the electrons in the wetting layer and the diamond's Fermi level causes electrons to be transported from the diamond to the water layer, reducing H_3O^+ to H_2 and H_2O. This makes it possible for an electron to pass from the diamond's valence band minimum to the positively charged wetting layer, which gives rise to the surface conductivity of HBDDE.[64-67]

Although being stable for several months in ambient conditions, slow oxidation would happen on the H-terminated surface to O-terminated surface after being exposed in air for a long term [68-69]. The exposure to hydrogen plasma at high temperature or electrochemical

treatment will restore the hydrogen termination. On the other hand, instant conversion to oxygen termination can be achieved by electrochemical treatment or the treatment of strong oxidising agents, such as nitric acid. [69]

The O-terminated diamond surface has low surface conductivity, and high charge transfer resistance but can withstand further slow oxidation in the air. Opposite to HBDDE, OBDDE results in a dipole ($C^{\delta+} - O^{\delta-}$) and has a negative surface charge. This resulted in a change in electrostatic interactions between the surface and adsorbates, resulting in lowered energy levels of the valence and conduction bands of diamond and positive electron affinity is the emission barrier of electrons from the conduction band minimum of OBDDE. [64,70-71] However, for heavily boron-doped diamond electrodes, the differences in conductivity between HBDD and OBDD are not so disparate.[72-73] In this thesis, OBDDEs are introduced and discussed all the time, depending on the surface modification for electrochemical analysis.

1.2.4. Surface Decoration of BDDE

In light of the specific usages in electrochemistry, BDDE surfaces can be decorated with different types of molecules or materials, big or small. Metal nanoparticles, metal nanoalloys, large biochemical molecules, polymers, and carbon particles are the common modifiers immobilised onto the surface of BDDE in various ways.[74] Covalent bonding of molecules to the diamond surface is a common modification. The surface of BDDE (usually OBDDE) contains different types of functional groups, with which the modifier can bond to form a strong covalent bond. Such type of modification is usually molecule-

type-specific. The other types of modifications include physical coatings of a conductive matrix. [75-77]

The modified BDDEs are expected to be structurally and chemically stable, with short-term reproducibility and long-term activity. They have dynamic and specific current responses and low background noise with potential ranges of interest. They are compatible with different types of solvent at a certain range of pH values. The amount of modification and fabrication on an individual electrode is relatively easy to control.[77]

1.2.5. Metal Nanoparticle Modification

Metal nanoparticles are small pure metal particles sized less than or equal to 100 nm, which show distinct and unique characteristic in comparison with the bulk form.[78] Metal nanoparticles usually exhibit very strong surface plasmonic resonance, which could be attributable to the oscillation of the valence electrons moving with respect to their cores. When the size of the particles is smaller, the electron density at the surface is much higher, hence giving off a stronger surface plasmonic resonance. This feature can be used in several spectroscopic sensing techniques, such as SERS.[79-80] In electrochemical studies, metal nanoparticles are essentially useful by virtue of their high surface-to-volume ratio, which provides active sites for binding and reaction.[78] In aqueous-phased reactions, the advantage of convergent diffusion is observed on the surface of metal nanoparticles. In contrast, planar diffusion is observed for bulk macro-electrodes (Figure 1.7). Therefore, we conclude that metal NP modified electrodes are more sensitive and catalytically

reactive. [81-83]

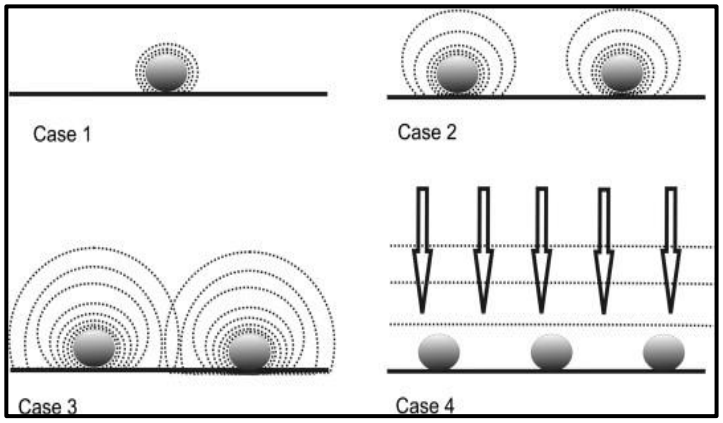

Figure 1.7 Different cases of diffusion that happen in a nanoparticle array. Case 1: At an isolated particle, the diffusion layer is rather small compared to the radius of that nanoparticle. Therefore, the diffusional pattern is almost planar; Case 2: The diffusional pattern is convergent diffusion at two adjacent but diffusional-independent nanoparticles; Case 3: Partially overlapped diffusion pattern at two adjacent nanoparticles; Case 4: When treating the arrays as a whole, heavily overlapping diffusion layers lead to linear diffusion again. Adapted from [83]

The methods to modify BDDEs with metal NPs include electrodeposition from metal salt, physical adsorption, and ion implantation.[78] Potentiostatic electrodeposition is the most commonly used method for metal NP modification. Although it is quick and simple to operate, its drawbacks, including large particle sizes and aggregations, along with poor adhesion to the electrode surfaces should be noted. Drop-coating of formed colloidal nanoparticles can have a very small particle size, yet the uneven distribution and the lack of parameters make it hard to control the deposition. Different parameters can be controlled in each type of process to ensure the morphologies and performance of the modified electrodes.[84]

It is important to choose the right metal NP as modifier. Certain influencing factors, such as the solubility of metal NP in the pH of the buffer/electrolyte used and sensitivity towards certain reactions, should be considered. For example, sulfuric acid is normally

used in the acidic media of the HER reaction as an electrolyte, so CuNPs do not constitute a wise choice in this specific case. Moreover, the antibacterial features of AgNPs render AgNPs modified BDDE inapplicable in biomedical fields.[85-86] Small inorganic, organic, and gas molecules, as well as energy generation, are detected using Pt and PdNP modified BDDE[87-91]. Mercury drop electrodes are used for heavy metal detection. However, recent studies found that BiNP-modified BDDE can achieve extra sensitivity in the detection of Cd and Pb.[78,92] More specific applications of metal NP-modified BDDEs are discussed in the following chapters throughout the review.

1.2.6. Metal Nanoalloy Modification

Metal nanoalloys are homogeneous metal clusters composed of two or more metal elements, and can be synthesised by applying various methods, such as cluster beams, colloidal solutions, immobilisation on the surface, and inside pores. NA can be subdivided into three types according to various hetero-metal mixing: (1) NA with distinct segregation between elements and limited bonding; (2) a complete mixture of two metals, either random or organized; and (3) core-shell NA with single or multiple core-shell structures. The specific structures of NAs can be viewed and understood by using

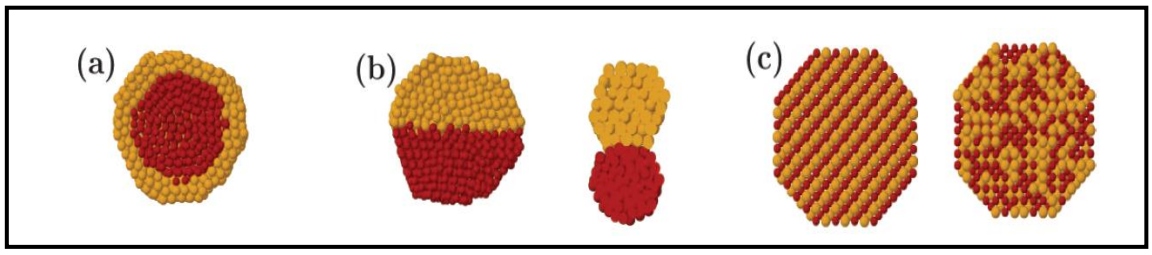

Figure 1.8 Different mixing patterns of bimetallic nanoalloys shown by cross sections of clusters: core−shell (a), subcluster segregated (b), mixed (c), three shell (d), adopted from [9].

various techniques, such as SEM, TEM, EDX, XPS, and CV. Their properties with respect to size, compositions, atomic ordering, and structures can be changed remarkably.[93]

Often, due to the synergistic effect, NAs may exhibit enhanced electrochemical properties compared to the individual composites. The selection of catalysts for the system of interest is all about finding the optimal geometry and electronic structure. By alloying, the geometry can be fine-tuned by forming numerous defects at the kinks and steps, which therefore provides more activation sites; the electronic structure can be fine-tuned by the rearrangement of valence electrons in the new potential field that is formed by different elements. At a more microscopic level, the synergistic effect is often a combination of two alloy effects: ensemble and ligand effects. For different alloy compositions and reaction systems, one effect can govern the catalytic process over another.[94-95]

The ensemble effect refers to the alternation of geometric orientations and arrangement patterns that are required to enhance a particular catalytic process. For example, in PdAuNA, the ensemble effect is mainly the dilution of continuous Pd (the more catalytically active component) clusters by Au (the less catalytically active component), and ultimately increases the exposure of highly active surface sites, *e.g.*, more isolated Pd pairs.[96]

The ligand effect means the modification of the electronic structure of the individual constituent atoms in the surfaces. And in the example of PdAuNA, the charge transfer from an Au atom (with higher electronegativity) to Pd will cause the shift of the d band centre, which is a good measure of reactivity, away from the original Fermi level. This

shift weakens the interaction between adsorbates and the surface and speeds up the desorption process.[95-96]

1.2.7. Carbon Particle Modification

The inspection of the 3D structure of BDDE reveals that it has a somewhat larger surface area for reaction than planar 2D carbon electrodes, such as a glassy carbon electrode (GCE). Further modification using porous carbon particles (CPs) could provide extra conductivity and active sites. Since some metals are toxic to the human body, CPs are considered the ideal modifier for bio-chemical-related electrochemical analysis.[101-102]

CNT is a common modifier because it is chemically and structurally stable. CNT-BDDE has a flexible porous structure and shows enhanced electrochemical performance over bare BDDEs.[105-106] Compared to some metal nanoparticles, metal oxide nanoparticles exhibit limited and controllable toxicities depending on their modification, surrounding environment, structure, and length.[103-104] CNT-modified BDDEs are used in the detection of biomolecules, including bisphenol, acetaminophen, dopamine, and epinephrine.[107-108]

Additional modifications/surfactants can be added to CNT and other CP modifiers, such as metal nanoparticles, polymers, and biochemical large molecules, all of which exhibit outstanding activities in specific reactions [109-112]. The mechanisms and performance of the chosen CP will be discussed in detail in the corresponding chapter(s).

1.3. Aims and Scope

The following aspects of BDDE surface modification and performance in fuel cell

chemistry and molecule sensing have been investigated:

1. Local and overall morphologies of modifiers;
2. Electrochemical behaviour and parameters of modified BDDE;
3. The overall performance of modified BDDE in fuel cell reaction, and molecule sensing.

The current thesis demonstrates how the structures and distributions of the modifiers either promote or inhibit the overall activity of the electrode. Controllable synthesis methods are proposed. The types of chosen modifier are metal NP, metal NA, CPs or a combination of all three. The differences in electrochemical activities between specific modifier types and structures are compared.

Chapter 2 introduces the theoretical principles of electrochemistry, specifically the systems and techniques employed. Moreover, the working principles of UV-Visible Spectroscopy, X-Ray Photoelectron Spectroscopy, and Scanning Electron Microscopy will be briefly discussed.

Chapter 3 explores the electrodeposition of AgNPs along with their morphology and surface composition. Application in electrocatalysis will be illustrated based on the example of the HER. The purpose of this chapter is to uncover a plausible correlation between the electrodeposition method and the morphology of AgNPs, both local and overall. The morphology directly influences the surface composition of Ag-BDDEs, which is determined via XPS. Finally, the different catalytic performances in HER with respect to structures are investigated by using LSV and are compared by performing Tafel analysis. The ideal candidate is selected and, therefore, the optimal condition of Ag

electrodeposition on BDDE can be determined.

Chapter 4 studies the similar problems for AgAu nanoalloy. The modifications of BDDE using AgAu are investigated with respect to morphology and surface composition. Similarly, the HER is a test reaction. In this part, the optimal Ag-BDDE is used as a base/core for making AgAuNA. The relationship between deposition methods and surface structures is devised. The surface compositions are investigated by using XPS, and CV of sequential depositions of Au. AgNP, AuNP, AgAuNA (with different structures) are compared with respect to their catalytic reactivities to determine the best candidate.

Chapter 5 investigates the synthesis of colloidal Ag, AuNPs, and AgAuNAs, and their stabilisation by using carboxylate graphene nanoflakes (cx-GNF) to compare the catalytic performance of unstabilised colloidal nanospecies, cx-GNF stabilised nanospecies, andcolloidal nanospecies stabilised by sodium citrate (SC), a common stabiliser used for nanoparticle wet chemistry synthesis. Secondary stabilisations are also performed to improve dispersion and solvation of cx-GNF stabilised nanospecies: Ni (II) modification to immobilise cx-GNFs' carboxylic ends by forming precipitation, and cx-GNF-Nafion (GNFNaf) polymer protective topcoat.

Chapter 6 studies the sensing capabilities of cx-GNF stabilised AuNPs (AuGNF) to show that AuGNF exhibits higher sensitivity in the detection of many kinds of molecules than unstabilised AuNPs, as well as electrodeposited AuNPs (with similar amount of loading). The detections of As (III), 4-nonylphenol, glucose, and hydroquinone are performed via CV, SWV, and DPV. The electrochemical parameters of AuGNF-BDDE are calculated

and compared to other fabricated electrodes listed in the literatures. Simultaneous detection of hydroquinone and the interfering molecule, catechol, is also being studied. *Chapter 7* investigates the catalytic abilities of Pd-containing nanospecies synthesised via electrodeposition and wet chemistry methods. A galvanic replacement reaction is introduced to form PdAuNA. cx-GNF is again used as an excellent stabilizer for colloidal Pd-containing nanospecies, and a PdAuCu trimetal nanoalloy is synthesied. A comprehensive surface analysis was carried out by using XPS and SEM to establish the connection between surface composition and structure. ORR (Oxygen Reduction Reaction), EOR (Ethanol Oxidation Reaction), and HER are used to examine the performance of Pd-containing nanoalloys.

References

(1) Chowdhury, P.; Sehitoglu, H.; Rateick, R. Damage Tolerance Of Carbon-Carbon Composites In Aerospace Application. *Carbon* 2018, *126*, 382-393.

(2) Moreno-Castilla, C. Adsorption Of Organic Molecules From Aqueous Solutions On Carbon Materials. *Carbon* 2004, *42*, 83-94.

(3) Baccar, R.; Sarrà, M.; Bouzid, J.; Feki, M.; Blánquez, P. Removal Of Pharmaceutical Compounds By Activated Carbon Prepared From Agricultural By-Product. *Chemical Engineering Journal* 2012, 211-212, 310-317.

(4) Liu, Z.; Robinson, J.; Tabakman, S.; Yang, K.; Dai, H. Carbon Materials For Drug Delivery & Cancer Therapy. *Materials Today* 2011, *14*, 316-323.

(5) Pierson, H. *Handbook Of Carbon, Graphite, Diamond, And Fullerenes*; Noyes Publications: Park Ridge, N.J, 2001; pp. 40-41.

(6) Pierson, H. *Handbook Of Carbon, Graphite, Diamond, And Fullerenes*; Noyes Publications: Park Ridge, N.J, 2001; pp. 355-365.

(7) Pierson, H. *Handbook Of Carbon, Graphite, Diamond, And Fullerenes*; Noyes Publications: Park Ridge, N.J, 2001; p. 359.

(8) Novoselov, K. Electric Field Effect In Atomically Thin Carbon Films. *Science* 2004, *306*, 666-669.

(9) Geim, A.; Novoselov, K. The Rise Of Graphene. *Nature Materials* 2007, *6*, 183-191.

(10) Jara, A.; Betemariam, A.; Woldetinsae, G.; Kim, J. Purification, Application And Current Market Trend Of Natural Graphite: A Review. *International Journal of Mining Science and Technology* 2019, *29*, 671-689.

(11) Zhou, X.; Tang, Y.; Lu, Z.; Zhang, J.; Liu, B. Nuclear Graphite For High Temperature Gas-Cooled Reactors. *New Carbon Materials* 2017, *32*, 193-204.

(12) Yoshimoto, S.; Amano, J.; Miura, K. Synthesis Of A Fullerene/Expanded Graphite Composite And Its Lubricating Properties. *Journal of Materials Science* 2010, *45*, 1955-1962.

(13) Kestursatya, M.; Kim, J.; Rohatgi, P. Wear Performance Of Copper–Graphite Composite And A Leaded Copper Alloy. *Materials Science and Engineering: A* 2003, *339*, 150-158.

(14) Choi, W.; Lahiri, I.; Seelaboyina, R.; Kang, Y. Synthesis Of Graphene And Its Applications: A Review. *Critical Reviews in Solid State and Materials Sciences* 2010, *35*, 52-71.

(15) Kuzmenko, A.; van Heumen, E.; Carbone, F.; van der Marel, D. Universal Optical Conductance Of Graphite. *Physical Review Letters* 2008, *100*.

(16) Yan, L.; Zheng, Y.; Zhao, F.; Li, S.; Gao, X.; Xu, B.; Weiss, P.; Zhao, Y. Chemistry And Physics Of A Single Atomic Layer: Strategies And Challenges For Functionalization Of Graphene And Graphene-Based Materials. *Chem. Soc. Rev.* 2012, *41*, 97-114.

(17) Wilder, J.; Venema, L.; Rinzler, A.; Smalley, R.; Dekker, C. Electronic Structure Of Atomically Resolved Carbon Nanotubes. *Nature* 1998, *391*, 59-62.

(18) Zhang, F.; Hou, P.; Liu, C.; Cheng, H. Epitaxial Growth Of Single-Wall Carbon Nanotubes. *Carbon* 2016, *102*, 181-197.

(19) Bakry R, Vallant RM, Najam-ul-Haq M, Rainer M, Szabo Z, Huck CW, Bonn GK. Medicinal applications of fullerenes. *Int J Nanomedicine.* 2007;2(4):639-49.

(20) Winkelmann, C.; Roch, N.; Wernsdorfer, W.; Bouchiat, V.; Balestro, F. Superconductivity In A Single-C60 Transistor. *Nature Physics* 2009, *5*, 876-879.

(21) Cai, W.; Zhu, Y.; Li, X.; Piner, R.; Ruoff, R. Large Area Few-Layer Graphene/Graphite Films As Transparent Thin Conducting Electrodes. *Applied Physics Letters* 2009, *95*, 123115.

(22) Liu, C.; Yu, Z.; Neff, D.; Zhamu, A.; Jang, B. Graphene-Based Supercapacitor With An Ultrahigh Energy Density. *Nano Letters* 2010, *10*, 4863-4868.

(23) Chung, C.; Kim, Y.; Shin, D.; Ryoo, S.; Hong, B.; Min, D. Biomedical Applications Of Graphene And Graphene Oxide. *Accounts of Chemical Research* 2013, *46*, 2211-2224.

(24) Wei, Y.; Gao, C.; Meng, F.; Li, H.; Wang, L.; Liu, J.; Huang, X. Sno2/Reduced Graphene Oxide Nanocomposite For The Simultaneous Electrochemical Detection Of Cadmium(II), Lead(II), Copper(II), And Mercury(II): An Interesting Favorable Mutual Interference. *The Journal of Physical Chemistry C* 2011, *116*, 1034-1041.

(25) Khmelnitsky, R.; Gippius, A. Transformation Of Diamond To Graphite Under Heat Treatment At Low Pressure. *Phase Transitions* 2013, *87*, 175-192.

(26) Lysakovskyi, V.; Novikov, N.; Ivakhnenko, S.; Zanevskyy, O.; Kovalenko, T. Growth Of Structurally Perfect Diamond Single Crystals At High Pressures And Temperatures. Review. *Journal of Superhard Materials* 2018, *40*, 315-324.

(27) Ulrich, H., *Chemische Thermodinamik,* Dresden, Leipzig: Steinkopff, 1930.

(28) Novikov, N.V., *Sintez sverkhtverdykh materialov. V 3 tomakh* (Synthesis of Superhard Materials. In 3 Volumes), Kiev: Naukova Dumka, 1986, Volume 1.

(29) Yan, C.; Vohra, Y.; Mao, H.; Hemley, R. Very High Growth Rate Chemical Vapor Deposition Of Single-Crystal Diamond. *Proceedings of the National Academy of Sciences* 2002, *99*, 12523-12525.

(30) Altukhov, A.; Afanas'ev, M.; Kvaskov, V.; Lyubchenko, V.; Mityagin, A.; Murav'ev,

E.; Pomortsev, L.; Potapov, V.; Spitsyn, B. Application Of Diamond In High Technology. *Inorganic Materials* 2004, *40*, S50-S70.

(31) Balmer, R.; Brandon, J.; Clewes, S.; Dhillon, H.; Dodson, J.; Friel, I.; Inglis, P.; Madgwick, T.; Markham, M.; Mollart, T. et al. Chemical Vapour Deposition Synthetic Diamond: Materials, Technology And Applications. *Journal of Physics: Condensed Matter* 2009, *21*, 364221.

(32) Ristein, J. Diamond Surfaces: Familiar And Amazing. *Applied Physics A* 2005, *82*, 377-384.

(33) Larsson, K.; Ristein, J. Diamond Surface Conductivity Under Atmospheric Conditions: Theoretical Approach. *The Journal of Physical Chemistry B* 2005, *109*, 10304-10311.

(34) Zoski, C. *Handbook Of Electrochemistry*; Elsevier: Amsterdam, 2007.

(35) Geis, M.; Twichell, J.; Efremow, N.; Krohn, K.; Lyszczarz, T. Comparison Of Electric Field Emission From Nitrogen-Doped, Type Ib Diamond, And Boron-Doped Diamond. *Applied Physics Letters* 1996, *68*, 2294-2296.

(36) Compton, R.; Foord, J.; Marken, F. Electroanalysis At Diamond-Like And Doped-Diamond Electrodes. *Electroanalysis* 2003, *15*, 1349-1363.

(37) Ristein, J.; Riedel, M.; Stammler, M.; Mantel, B.; Ley, L. Surface Conductivity Of Nitrogen-Doped Diamond. *Diamond and Related Materials* 2002, *11*, 359-364.

(38) Wang, Y.; Yin, Z. Structural And Electrical Properties Of Sulfur-Doped Diamond Thin Films. *Plasma Science and Technology* 2014, *16*, 255-259.

(39) Nesladek, M. Conventional N-Type Doping In Diamond: State Of The Art And Recent Progress. *Semiconductor Science and Technology* 2005, *20*, R19-R27.

(40) Eaton, S.; Anderson, A.; Angus, J.; Evstefeeva, Y.; Pleskov, Y. Co-Doping Of Diamond With Boron And Sulfur. *Electrochemical and Solid-State Letters* 2002, *5*, G65.

(41) Vaddiraju, S.; Eaton-Magana, S.; Chaney, J.; Sunkara, M. UPS Of Boron-Sulfur Co-Doped, N-Type Diamond. *Electrochemical and Solid-State Letters* 2004, *7*, G331.

(42) Okano, K.; Naruki, H.; Akiba, Y.; Kurosu, T.; Iida, M.; Hirose, Y.; Nakamura, T. Characterization Of Boron-Doped Diamond Film. *Japanese Journal of Applied Physics* 1989, *28*, 1066-1071.

(43) Kraft, A.. Doped Diamond: A Compact Review on a New, Versatile Electrode Material. *Int. J. Electrochem. Sci.*, 2007, *2*, 355 - 385

(44) Practical Electrochemical Sensors Using Boron Doped Diamond (BDD) Diamond Electrodes https://www.fierceelectronics.com/components/practical-electrochemical-sensors-using-boron-doped-diamond-bdd-diamond-electrodes

(accessed Aug 2, 2021).

(45) Pleskov, Y.; Sakharova, A.; Krotova, M.; Bouilov, L.; Spitsyn, B. Cheminform Abstract: Photoelectrochemical Properties Of Semiconductor Diamond. *ChemInform* 1987, *18*.

(46) Martin, H.; Argoitia, A.; Landau, U.; Anderson, A.; Angus, J. Hydrogen And Oxygen Evolution On Boron-Doped Diamond Electrodes. *Journal of The Electrochemical Society* 1996, *143*, L133-L136.

(47) Rao, T.; Fujishima, A. Recent Advances In Electrochemistry Of Diamond. *Diamond and Related Materials* 2000, *9*, 384-389.

(48) Suffredini, H.; Machado, S.; Avaca, L. The Water Decomposition Reactions On Boron-Doped Diamond Electrodes. *Journal of the Brazilian Chemical Society* 2004, *15*, 16-21.

(49) Halima, A.; Rana, U.; MacFarlane, D. Boron-Doped Diamond (BDD) Coatings Protect Underlying Silicon in Aqueous Acidic Media–Application to the Hydrogen Evolution Reaction (accessed Aug 2, 2021).

(50) Khan, M.; Hayat, A.; Baburao Mane, S.; Li, T.; Shaishta, N.; Alei, D.; Zhao, T.; Ullah, A.; Zada, A.; Rehman, A. et al. Functionalized Nano Diamond Composites For Photocatalytic Hydrogen Evolution And Effective Pollutant Degradation. *International Journal of Hydrogen Energy* 2020, *45*, 29070-29081.

(51) Andreozzi, R. Advanced Oxidation Processes (AOP) For Water Purification And Recovery. *Catalysis Today* 1999, *53*, 51-59.

(52) Welch, C.; Hyde, M.; Banks, C.; Compton, R. The Detection Of Nitrate Using In-Situ Copper Nanoparticle Deposition At A Boron Doped Diamond Electrode. *Analytical Sciences* 2005, *21*, 1421-1430.

(53) Ward-Jones, S.; Banks, C.; Simm, A.; Jiang, L.; Compton, R. An In Situ Copper Plated Boron-Doped Diamond Microelectrode Array For The Sensitive Electrochemical Detection Of Nitrate. *Electroanalysis* 2005, *17*, 1806-1815.

(54) Zhao, G.; Tang, Y.; Liu, M.; Lei, Y.; Xiao, X. Direct And Simultaneous Determination Of Phenol, Hydroquinone And Nitrophenol At Boron-Doped Diamond Film Electrode. *Chinese Journal of Chemistry* 2007, *25*, 1445-1450.

(55) Denisova, A.; Pleskov, Y. Electrooxidation Of Ethylenediaminetetraacetic Acid At A Polycrystalline Boron-Doped Diamond Anode. *Russian Journal of Electrochemistry* 2008, *44*, 1083-1085.

(56) Chailapakul, O. The Electrooxidation Of Organic Acids At Boron-Doped Diamond Electrodes. *Electrochemistry Communications* 2000, *2*, 422-426.

(57) Fuku, X.; Iftikar, F.; Hess, E.; Iwuoha, E.; Baker, P. Cytochrome C Biosensor For Determination Of Trace Levels Of Cyanide And Arsenic Compounds. *Analytica*

Chimica Acta 2012, *730*, 49-59.

(58) Ivandini, T.; Sato, R.; Makide, Y.; Fujishima, A.; Einaga, Y. Electrochemical Detection Of Arsenic(III) Using Iridium-Implanted Boron-Doped Diamond Electrodes. *Analytical Chemistry* 2006, *78*, 6291-6298.

(59) Weng, J.; Zhang, J.; Li, H.; Sun, L.; Lin, C.; Zhang, Q. Label-Free DNA Sensor By Boron-Doped Diamond Electrode Using An Ac Impedimetric Approach. *Analytical Chemistry* 2008, *80*, 7075-7083.

(60) Xie, S.; Shafer, G.; Wilson, C.; Martin, H. In Vitro Adenosine Detection With A Diamond-Based Sensor. *Diamond and Related Materials* 2006, *15*, 225-228.

(61) Suzuki, A.; Ivandini, T.; Yoshimi, K.; Fujishima, A.; Oyama, G.; Nakazato, T.; Hattori, N.; Kitazawa, S.; Einaga, Y. Fabrication, Characterization, And Application Of Boron-Doped Diamond Microelectrodes For In Vivo Dopamine Detection. *Analytical Chemistry* 2007, *79*, 8608-8615.

(62) Nantaphol, S.; Watanabe, T.; Nomura, N.; Siangproh, W.; Chailapakul, O.; Einaga, Y. Bimetallic Pt–Au Nanocatalysts Electrochemically Deposited On Boron-Doped Diamond Electrodes For Nonenzymatic Glucose Detection. *Biosensors and Bioelectronics* 2017, *98*, 76-82.

(63) Almeida, E.; Trava-Airoldi, V.; Ferreira, N.; Rosolen, J. Electrochemical Insertion Of Lithium Into A Doped Diamond Film Grown On Carbon Felt Substrates. *Diamond and Related Materials* 2005, *14*, 1673-1677.

(64) Macpherson, J. A Practical Guide To Using Boron Doped Diamond In Electrochemical Research. *Physical Chemistry Chemical Physics* 2015, *17*, 2935-2949.

(65) Bandis, C.; Pate, B. Photoelectric Emission From Negative-Electron-Affinity Diamond (111) Surfaces: Exciton Breakup Versus Conduction-Band Emission. *Physical Review B* 1995, *52*, 12056-12071.

(66) Maier, F., Riedel, M., Mantel, B., Ristein, J., Ley, L., Origin of Surface Conductivity in Diamond. *Physical Review Letters* 2000, *85*, 3472-3475.

(67) Maier, F.; Ristein, J.; Ley, L. Electron Affinity Of Plasma-Hydrogenated And Chemically Oxidized Diamond (100) Surfaces. *Physical Review B* 2001, *64*.

(68) Ristein, J. The Physics Of Hydrogen-Terminated Diamond Surfaces. *AIP Conference Proceedings* 2005, *772*, 377.

(69) Szunerits, S.; Boukherroub, R. Different Strategies For Functionalization Of Diamond Surfaces. *Journal of Solid State Electrochemistry* 2007, *12*, 1205-1218.

(70) Shi, D., Liu, L., Zhai, Z., Chen, B., Lu, Z., Zhang, C., Yuan, Z., Zhou, M., Yang, B., Huang, N., Jiang, X., 2021. Effect of oxygen terminated surface of boron-doped diamond thin-film electrode on seawater salinity sensing. *Journal of Materials*

Science and Technology 2021, *86,* 1-10.

(71) Yagi, I., Notsu, H., Kondo, T., Tryk, D., Fujishima, A., 1999. Electrochemical selectivity for redox systems at oxygen-terminated diamond electrodes. *Journal of Electroanalytical Chemistry* 1999, *473*, 173-178.

(72) Hayashi, K.; Yamanaka, S.; Watanabe, H.; Sekiguchi, T.; Okushi, H.; Kajimura, K. Investigation Of The Effect Of Hydrogen On Electrical And Optical Properties In Chemical Vapor Deposited On Homoepitaxial Diamond Films. *Journal of Applied Physics* 1997, *81*, 744-753.

(73) Yagi, I.; Notsu, H.; Kondo, T.; Tryk, D.; Fujishima, A. Electrochemical Selectivity For Redox Systems At Oxygen-Terminated Diamond Electrodes. *Journal of Electroanalytical Chemistry* 1999, *473*, 173-178.

(74) Kondo, T.; Ito, H.; Kusakabe, K.; Ohkawa, K.; Einaga, Y.; Fujishima, A.; Kawai, T. Plasma Etching Treatment For Surface Modification Of Boron-Doped Diamond Electrodes. *Electrochimica Acta* 2007, *52*, 3841-3848.

(75) Salazar-Banda, G.; Suffredini, H.; Calegaro, M.; Tanimoto, S.; Avaca, L. Sol–Gel-Modified Boron-Doped Diamond Surfaces For Methanol And Ethanol Electro-Oxidation In Acid Medium. *Journal of Power Sources* 2006, *162*, 9-20.

(76) Svítková, J.; Ignat, T.; Švorc, Ľ.; Labuda, J.; Barek, J. Chemical Modification Of Boron-Doped Diamond Electrodes For Applications To Biosensors And Biosensing. *Critical Reviews in Analytical Chemistry* 2015, *46*, 248-256.

(77) Baldwin, R.; Thomsen, K. Chemically Modified Electrodes In Liquid Chromatography Detection: A Review. *Talanta* 1991, *38*, 1-16.

(78) Toghill, K.; Compton, R. Metal Nanoparticle Modified Boron Doped Diamond Electrodes For Use In Electroanalysis. *Electroanalysis* 2010, *22*, 1947-1956.

(79) Kanipe, K.; Chidester, P.; Stucky, G.; Moskovits, M. Large Format Surface-Enhanced Raman Spectroscopy Substrate Optimized For Enhancement And Uniformity. *ACS Nano* 2016, *10*, 7566-7571.

(80) Laurence, T.; Braun, G.; Talley, C.; Schwartzberg, A.; Moskovits, M.; Reich, N.; Huser, T. Rapid, Solution-Based Characterization Of Optimized SERS Nanoparticle Substrates. *Journal of the American Chemical Society* 2008, *131*, 162-169.

(81) Streeter, I.; Compton, R. Diffusion-Limited Currents To Nanoparticles Of Various Shapes Supported On An Electrode; Spheres, Hemispheres, And Distorted Spheres And Hemispheres. *The Journal of Physical Chemistry C* 2007, *111*, 18049-18054.

(82) Molina, A.; Laborda, E.; González, J.; Compton, R. Effects Of Convergent Diffusion And Charge Transfer Kinetics On The Diffusion Layer Thickness Of Spherical Micro- And Nanoelectrodes. *Physical Chemistry Chemical Physics* 2013, *15*, 7106.

(83) Zhou, Y.; Campbell, F.; Belding, S.; Compton, R. Nanoparticle Modified Electrodes:

Surface Coverage Effects In Voltammetry Showing The Transition From Convergent To Linear Diffusion. The Reduction Of Aqueous Chromium (III) At Silver Nanoparticle Modified Electrodes. *Chemical Physics Letters* 2010, *497*, 200-204.

(84) Nelson, G.; Foord, J. Nanoparticle-Based Diamond Electrodes. *Topics in Applied Physics* 2014, 165-204.

(85) Pal, S.; Tak, Y.; Song, J. Does The Antibacterial Activity Of Silver Nanoparticles Depend On The Shape Of The Nanoparticle? A Study Of The Gram-Negative Bacterium Escherichia Coli. *Applied and Environmental Microbiology* 2007, *73*, 1712-1720.

(86) Wei, L.; Lu, J.; Xu, H.; Patel, A.; Chen, Z.; Chen, G. Silver Nanoparticles: Synthesis, Properties, And Therapeutic Applications. *Drug Discovery Today* 2015, *20*, 595-601.

(87) Hrapovic, S.; Liu, Y.; Luong, J. Reusable Platinum Nanoparticle Modified Boron Doped Diamond Microelectrodes For Oxidative Determination Of Arsenite. *Analytical Chemistry* 2007, *79*, 500-507.

(88) Brülle, T.; Denisenko, A.; Sternschulte, H.; Stimming, U. Catalytic Activity Of Platinum Nanoparticles On Highly Boron-Doped And 100-Oriented Epitaxial Diamond Towards HER And HOR. *Physical Chemistry Chemical Physics* 2011, *13*, 12883.

(89) Hutton, L.; Newton, M.; Unwin, P.; Macpherson, J. Amperometric Oxygen Sensor Based On A Platinum Nanoparticle-Modified Polycrystalline Boron Doped Diamond Disk Electrode. *Analytical Chemistry* 2008, *81*, 1023-1032.

(90) Batchelor-McAuley, C.; Banks, C.; Simm, A.; Jones, T.; Compton, R. The Electroanalytical Detection Of Hydrazine: A Comparison Of The Use Of Palladium Nanoparticles Supported On Boron-Doped Diamond And Palladium Plated BDD Microdisc Array. *The Analyst* 2006, *131*, 106-110.

(91) Szunerits, S.; Boukherroub, R. Investigation Of The Electrocatalytic Activity Of Boron-Doped Diamond Electrodes Modified With Palladium Or Gold Nanoparticles For Oxygen Reduction Reaction In Basic Medium. *Comptes Rendus Chimie* 2008, *11*, 1004-1009.

(92) Toghill, K.; Wildgoose, G.; Moshar, A.; Mulcahy, C.; Compton, R. The Fabrication And Characterization Of A Bismuth Nanoparticle Modified Boron Doped Diamond Electrode And Its Application To The Simultaneous Determination Of Cadmium(II) And Lead(II). *Electroanalysis* 2008, *20*, 1731-1737.

(93) Shan, S.; Luo, J.; Yang, L.; Zhong, C. Nanoalloy Catalysts: Structural And Catalytic Properties. *Catal. Sci. Technol.* 2014, *4*, 3570-3588.

(94) Mokkath, J.; Schwingenschlögl, U. Catalytically Favorable Surface Patterns In Pt–Au Nanoclusters. *RSC Advances* 2013, *3*, 15350.

(95) Liu, P.; Nørskov, J. Ligand and ensemble effects in adsorption on alloy surfaces. *Phys. Chem. Chem. Phys.*, 2001,*3*, 3814-3818.

(96) Gao, F.; Goodman, D. Pd–Au Bimetallic Catalysts: Understanding Alloy Effects From Planar Models And (Supported) Nanoparticles. *Chemical Society Reviews* 2012, *41*, 8009.

(97) Salazar-Banda, G.; Suffredini, H.; Avaca, L.; Machado, S. Methanol And Ethanol Electro-Oxidation On Pt–SnO_2 And Pt–Ta_2O_5 Sol–Gel-Modified Boron-Doped Diamond Surfaces. *Materials Chemistry and Physics* 2009, *117*, 434-442.

(98) Siné, G.; Fóti, G.; Comninellis, C. Boron-Doped Diamond (BDD)-Supported Pt/Sn Nanoparticles Synthesized In Microemulsion Systems As Electrocatalysts Of Ethanol Oxidation. *Journal of Electroanalytical Chemistry* 2006, *595*, 115-124.

(99) Zhou, Y.; Jing, T.; Hao, Q.; Zhou, Y.; Mei, S. A sensitive and environmentally friendly method for determination of chemical oxygen demand using NiCu alloy electrode (accessed Sep 6, 2021).

(100) Lu, X.; Hu, J.; Foord, J.; Wang, Q. Electrochemical Deposition Of Pt–Ru On Diamond Electrodes For The Electrooxidation Of Methanol. *Journal of Electroanalytical Chemistry* 2011, *654*, 38-43.

(101) Lubick, N. Nanosilver Toxicity: Ions, Nanoparticles—Or Both?. *Environmental Science & Technology* 2008, *42*, 8617-8617.

(102) Bahadar H, Maqbool F, Niaz K, Abdollahi M. Toxicity of Nanoparticles and an Overview of Current Experimental Models. *Iran Biomed J.* 2016, *20(1)*, 1-11.

(103) Liu, Y.; Zhao, Y.; Sun, B.; Chen, C. Understanding The Toxicity Of Carbon Nanotubes. *Accounts of Chemical Research* 2012, *46*, 702-713.

(104) Zhao, X.; Liu, R. Recent Progress And Perspectives On The Toxicity Of Carbon Nanotubes At Organism, Organ, Cell, And Biomacromolecule Levels. *Environment International* 2012, *40*, 244-255.

(105) Hébert, C., Mazellier, J., Scorsone, E., Mermoux, M., Bergonzo, P. Boosting the electrochemical properties of diamond electrodes using carbon nanotube scaffolds. *Carbon*, 2014, *71*, 27-33.

(106) Zanin, H.; May, P.; Fermin, D.; Plana, D.; Vieira, S.; Milne, W.; Corat, E. Porous Boron-Doped Diamond/Carbon Nanotube Electrodes. *ACS Applied Materials & Interfaces* 2014, *6*, 990-995.

(107) Lourencao, B.; Silva, T.; Zanin, H.; May, P.; Corat, E.; Fatibello-Filho, O. Promising Electrochemical Performance Of High-Surface-Area Boron-Doped Diamond/Carbon Nanotube Electroanalytical Sensors. *Journal of Solid State Electrochemistry* 2016, *20*, 2403-2409.

(108) Zehani, N., Fortgang, P., Saddek Lachgar, M., Baraket, A., Arab, M.,

Dzyadevych, S., Kherrat, R., Jaffrezic-Renault, N. Highly sensitive electrochemical biosensor for bisphenol A detection based on a diazonium-functionalized boron-doped diamond electrode modified with a multi-walled carbon nanotube-tyrosinase hybrid film. *Biosensors & bioelectronics* 2015,*74*, 830-5.

(109) Firkowska, I.; Boden, A.; Vogt, A.; Reich, S. Effect Of Carbon Nanotube Surface Modification On Thermal Properties Of Copper–CNT Composites. *Journal of Materials Chemistry* 2011, *21*, 17541.

(110) Park, O.; Jeevananda, T.; Kim, N.; Kim, S.; Lee, J. Effects Of Surface Modification On The Dispersion And Electrical Conductivity Of Carbon Nanotube/Polyaniline Composites. *Scripta Materialia* 2009, *60*, 551-554

(111) Xu, Y.; Jiang, Y.; Cai, H.; He, P.; Fang, Y. Electrochemical Impedance Detection Of DNA Hybridization Based On The Formation Of M-DNA On Polypyrrole/Carbon Nanotube Modified Electrode. *Analytica Chimica Acta* 2004, *516*, 19-27.

(112) Pandurangappa, M.; Kempegowda, G. Chemically Modified Carbon Nanotubes: Derivatization And Their Applications. *Carbon Nanotubes Applications on Electron Devices* 2011.

Chapter 2 Experimental Techniques

This chapter aims to provide an overview of the techniques and instrumentation used for this thesis, including the underlying theories relating to the methods used.

First, electrochemistry will be explained, beginning from the basic theories behind a simple electrochemical cell at equilibrium, to dynamic electrochemical redox reactions, followed by specific analytical techniques used in electrochemistry. The implementation of them in real-world experiments will also be emphasized. Working principles and features of secondary techniques also used in this thesis, specifically x-ray photoelectron spectroscopy (XPS), scanning electron microscopy (SEM), and UV-Visible spectroscopy (UV-Vis Spec), are also presented in this chapter.

2.1. Electrochemistry - Overview

Electrochemistry is a branch of chemistry that involves chemical redox reactions that occur at the interface of an electronic conductor (electrode, usually metals or semiconductors) and an ionic conductor (electrolyte, commonly in an aqueous solution phase). Charge transfer between the electrode and electrolyte results in reduction and oxidation of species in solution, and electrochemistry is applied to analyse the properties of such redox reactions. The characteristics of such processes are related to the analytes' nature, the electrolytes used, and the electrodes' nature, as well as the electrical potential drop across the interface. Such processes underlie important areas of science and technology such as the production of bulk chemicals, battery energy storage and fuel cell technologies for the conversion of chemical to electrical energy.[1] Electrochemical based

chemical sensing is also of importance [2],offering advantages including (1) high selectivity; (2) high sensitivity and low limit of detection; (3) and real-time results feedback; (4) application as miniaturised sensors, which is hard for other types of chemical detection and measurement instrumentation. [3-4]

2.1.1. Electrochemical cells

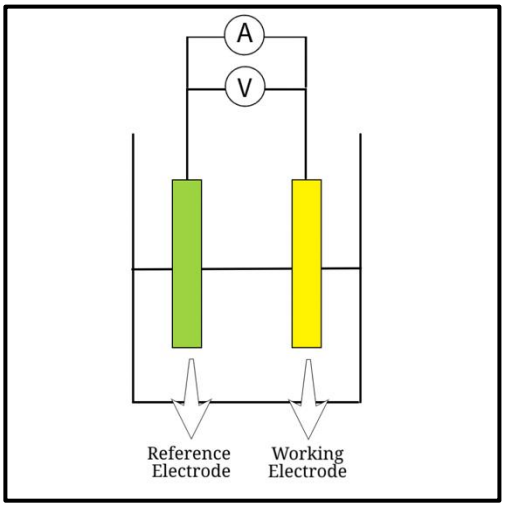

Figure 2.1 A schematic illustration of a simple 2-electrode electrochemical cell, adapted from [5].

Electrochemistry studies typically involve heterogeneous electron transfer between an aqueous-phase electrolyte and a solid electrode. The transfer is driven by the potential difference between the electrode and the electrolyte.[5] However, it is not possible to measure that potential difference at a single immersed electrode. Therefore, a second electrode is introduced into the system as shown in Figure 2.1, and the potential difference between the two electrodes can then be measured straight-forwardly. If the same electrode/electrolyte composition is used for one of the electrodes, then that electrode component of the cell can be designated a reference, enabling the potential drop developed by other electrode systems to be compared. The two electrodes, together with

the electrolyte, illustrated in Figure 2.1 make up the simplest functioning electrochemical cell, and a readable measurement can be performed following the equation below:

$$\Delta\phi = (\phi_{\mathrm{WE}} - \phi_{\mathrm{aq}}) - (\phi_{\mathrm{ref}} - \phi_{\mathrm{aq}}) \qquad (1)$$

where $\Delta\phi$ is the readable difference potential, $\phi_{\mathrm{WE}} - \phi_{\mathrm{aq}}$ is the potential difference between the electrode of interest, called the working electrode (WE), and the electrolyte (aq), and $\phi_{\mathrm{ref}} - \phi_{\mathrm{aq}}$ is the potential difference between the reference electrode and the solution. It is impossible to determine the absolute value of the single electrode quantity $\phi_{\mathrm{WE}} - \phi_{\mathrm{aq}}$. However, if $\phi_{\mathrm{ref}} - \phi_{\mathrm{aq}}$is a fixed quantity, then any changes in the $\phi_{\mathrm{WE}} - \phi_{\mathrm{aq}}$ appear directly as changes in the measured potential. In this way, a reference electrode allows us to study the test electrode or electrolyte of interest. The reference used in this thesis was typically a silver wire coated with porous silver chloride, which is kept in a solution of constant chloride concentration to maintain a constant composition. [5]

2.1.2. Electrochemical Equilibrium

Electrochemical processes can be in equilibrium at the electrode-electrolyte interface if no current flows through the cell, such as when the two electrodes are connected by a high impedance voltmeter, or under kinetic control if a current is allowed to flow around the relevant electrical circuit, such as a battery under discharge. The charge transfer processes can be simplified by consideration of the reaction equation below, with A as the oxidized species, B as the reduced species, both in the liquid electrolyte phase:

$$\mathrm{A} + n\mathrm{e}^{-} \leftrightharpoons \mathrm{B}$$

In this reaction, A receives n electrons and is transformed into B. One very common example is the redox pair $K_4Fe(CN)_6$ and $K_3Fe(CN)_6$. The electrochemical equilibrium is represented by the equation below:

$$Fe(CN)_6^{3-}\,(aq) + e^- \rightleftharpoons Fe(CN)_6^{4-}(aq)$$

This reaction happens spontaneously when a metal electrode is immersed in the solution. Two anions are dissolved in the solution and the equilibrium is established when a potential difference at the electrolyte/electrode interface is established such that the rate at which "$Fe(CN)_6^{4-}$gives the electrons to the metal electrode" is the same as the rate of "electrons released by the metal electrode are donated to $Fe(CN)_6^{3-}$ ". At this point, the system has no current flow, and any change in redox pair concentrations, as well as any potential drop at the electrode-solution interface, are negligible.[6]

The potential drop is quantified by a general Nernst equation:

$$\phi_{\mathrm{WE}} - \phi_{\mathrm{aq}} = \left(\frac{\Delta\mu}{nF}\right) + \left(\frac{RT}{nF}\right) \qquad (2)$$

where $\phi_{\mathrm{WE}} - \phi_{\mathrm{aq}}$ is the electrical potential between the working electrode and the aqueous electrolyte, $\Delta\mu$ is the difference between the standard chemical potentials of A and B, F is Faraday's constant, n is the number of electrons transferred, R is the universal gas constant 8.314JK^{-1}mol^{-1}, T is the temperature, α_{A} and α_{B} are the activities of A and B, which in the low concentration roughly equals the concentration of A and B. In a real experiment, where RE is used, and the term $(\frac{\Delta\mu}{nF})$ is defined as the standard electrode potential (E_0) for the reaction, depending on the type of RE, when *n*=1, (2)is simplified to:

$$E_{\mathrm{eq}} = E_0 + \left(\frac{RT}{F}\right)\ln\left(\frac{\alpha_{\mathrm{A}}}{\alpha_{\mathrm{B}}}\right) \qquad (3)$$

where E_{eq} is the readable potential drop across the electrode-electrolyte interface at equilibrium.[6]

2.2. Dynamic Electrochemistry

When an external circuit is connected to the cell to induce current flow, the equilibrium at the interface is broken and kinetic processes influence the behaviour observed. The current flow mainly depends on three factors: the magnitude of the applied potential which influences the potential drop at the electrode surface, electrode kinetics relating to electron transfer, and mass transport, the transfer of A (reactant) (step 1) and B (product) from the bulk solution to the electrode (step 1). A simplified schematic is shown in Figure 2.2.[5]

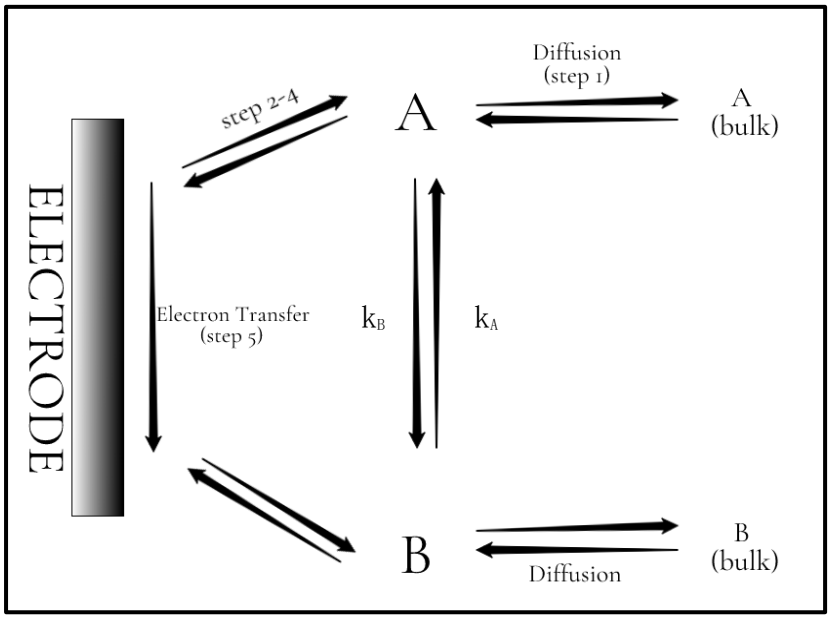

Figure 2.2 Electron transfer at an electrode. Step 1: diffusion; step 2: rearrangement of the ionic atmosphere; step 3: reorientation of solvent dipoles; step 4: alternations in central ion-ligand distances; step 4: electron transfer. Adapted from [5].

2.2.1. Electrode Kinetics

At low over-potentials (meaning the potential difference between theoretical equilibrium

potential and the actual potential added during the experiment), electrode kinetics often represent the rate limiting processes which must be considered while the diffusion model mainly explains the electrode behaviour at higher over-potential far away from the equilibrium.

2.2.1.1. Butler-Volmer model

The Butler-Volmer model is a fundamental model to describe electrode kinetics. In this model, an over-potential η from the equilibrium potential is applied to the electrode and the current flowing is calculated as a function of this overpotential. The applied potential modifies the free energy barrier that exists in the reaction coordinate promoting one electrochemical process (oxidation or reduction) and slowing the reverse step. Thus, the Gibbs free energy of activation for the forward and reverse steps are given by[7]

$$\Delta G_{\mathrm{B}}^{\ddagger} = \Delta G_{\mathrm{B}_0}^{\ddagger} \Delta + \alpha F \eta \qquad (4)$$

and

$$\Delta G_{\mathrm{A}}^{\ddagger} = \Delta G_{\mathrm{A}_0}^{\ddagger} - (1-\alpha) F \eta \qquad (5)$$

Where α is the transfer coefficient which shows how "sensitive" the transitional state is to the drop of potential between the electrode and solution. Usually, that value is found to be around 0.5. $\Delta G_{\mathrm{B}_0}^{\ddagger}$ and $\Delta G_{\mathrm{A}_0}^{\ddagger}$ are $\Delta G^{\ddagger}$for B and A at equilibrium, respectively. Transition state theory then illustrates relationships between overpotential and rate constant, plugging in (4), (5) into Arrhenius equations, give:

$$k_{\mathrm{B}} = k_{\mathrm{B}}^{\ddagger} \exp\left(\frac{-\alpha F \eta}{RT}\right) \qquad (6)$$

and

$$k_{\mathrm{A}} = k_{\mathrm{A}}^{\ddagger} \exp\left(\frac{(1-\alpha)F\eta}{RT}\right) \qquad (7)$$

where k_{A} and k_{B} are rate constants

of A and B at a particular overpotential, and $k_{\mathrm{A}}^{\ddagger}$ and $k_{\mathrm{B}}^{\ddagger}$ are corresponding rate constants for A and B at equilibrium where the overpotential is zero.

Hence the complete current-potential characteristic for Butler-Volmer model can be obtained by plugging (6) and (7) for rate constant of forward and backword reactions, respectively:

$$i = i_0 \left\{ \frac{[\mathrm{B}]_0}{[\mathrm{B}]_{\mathrm{bulk}}} \exp\left(\frac{(1-\alpha)nF\eta}{RT}\right) - \frac{[\mathrm{A}]_0}{[\mathrm{A}]_{\mathrm{bulk}}} \exp\left(\frac{-\alpha nF\eta}{RT}\right) \right\} \qquad (8)$$

where i is the current density at electrode in A/m^2, i_0 is the standard exchange current density in A/m^2, α is the charge transfer coefficient, F is the Faraday constant, η is the activation potential defined as $\eta = E - E_0$ where E_0 is the equilibrium potential in V, R is the universal gas constant, n is the number of electrons transferred, $[A]_{\mathrm{bulk}}$ and $[B]_{\mathrm{bulk}}$ are bulk concentrations of the species to be reduced and oxidized, respectively, $[A]_0$ and $[B]_0$ are the concentrations of A and B at the electrode surface.

Depending on the magnitude of i_0, there are two limiting cases. When i_0 is large, a small over-potential is enough to drive a large current, making the whole reaction a reversible process, meaning the charge transfers are fast and transitions from A to B and B to A are occurring at the same time at same rate without significant thermodynamic barriers. On the other hand, if the value of i_0 is small, it will need high over-potential to drive the whole reaction, and thus the process is irreversible, meaning the electron transfer are very slow and have a high barrier to overcome.[6]

Notably, when i_0 is small (the reaction is irreversible) and a large over potential is applied, the overpotential η forms a linear relationship with $\ln i$:

$$\eta = \frac{\ln i_o}{\alpha f} - \frac{\ln i}{\alpha f} \qquad (9)$$

where $f = \frac{F}{RT}$. The relationship described in (9) is called Tafel relationship, and the slope of it is called Tafel slope.

Tafel analysis is an experimentally concluded method to determine the kinetics of the hydrogen evolution reaction. Tafel slope has a unit of mV/dec and implied how much over potential needed to increase in order to increase the reaction rate by a factor of 10. Once the Tafel slope is calculated, the number of electrons transferred during and before the rate determining step can be determined, referring to the 3-step the HER mechanism, we will know which step is the rate determining step.

2.2.1.2. Marcus Theory of Transitional States

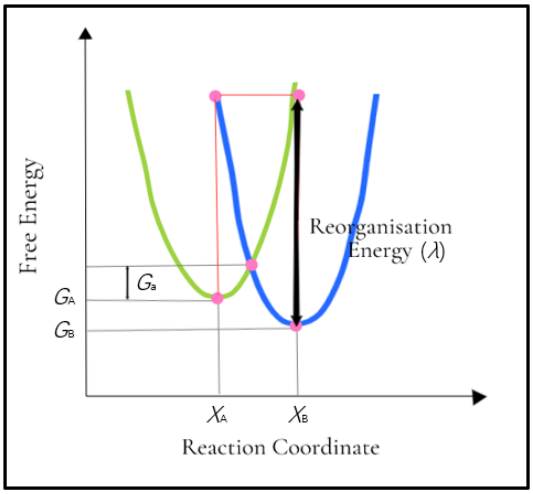

Figure 2.3 A simple energy scheme of the Marcus Theory: the oxidised species A at configuration X_A has free energy G_A; the reduced species B at configuration X_B has free energy G_B. The activation energy barrier is G_a. The reorganisation energy is noted in the graph. Adapted from [9].

In macroscopic electrode kinetics, the Butler-Volmer model is very useful to provide

approximately a qualitative relationship between the applied overpotential and the current flowing. However, it does not provide a chemical explanation as to why some processes are irreversible or irreversible. To explain this, and for more accurate predictions about the rates of electron transfer reactions between the reagent (A, the oxidised species), and product (B, the reduced species), Marcus theory of transitional states has been frequently used.

Marcus Theory states that electron transfer occurs faster than nuclear motions (vibrations). Therefore, for an electron transfer reaction, the reorganisation of the molecule from A to B is the crucial parameter that needs to be considered.[5] The reorganisation energy (λ) means the energy to distort A and B, making them geometrically similar enough for electron transfer, and can be calculated:

$$\lambda = \frac{1}{2} h\nu \, (x_{\mathrm{A}} - x_{\mathrm{B}})^2 \qquad (10)$$

Since it represents the change in energy moving along either of the parabolas between states on reaction coordinates x_{A} and x_{B}, the value of λ is always positive.[6] When the geometries of A and B are similar, the reorganisation energy is small; on the other hand, the reorganisation energy is large for large changes in equilibrium geometry. The easiness of electron transfer depends on the magnitude of this reorganisation energy, and it is true for electrochemical cell reactions as well: fast electrode process can be observed for A and B with similar geometry. [10]

2.2.2. Mass Transport

Mass transport is the movement of bulk chemical species from one position in the solution

to another and becomes a limiting factor at higher overpotentials where electrode kinetics are fast. Types of mass transport in electrochemical cells are diffusion, migration, and convection, or the controlled movement of the solution (hydrodynamics) over the electrode surface.

Migration is a process where charged species move to or from the electrode surface driven by a potential difference at different points in the electrolyte, yielding an electrical field producing the migrating flux. Migration is minimised by highly using a background highly conductive electrolyte, usually at a concentration much larger e.g., $\times 100$ than that of the electroactive species. Convection is dictated by the temperature gradient in the solution and can be minimized by controlling the temperature.[8]

In total, mass transfer to an electrode is governed by the Nernst-Planck equation, for one-dimensional mass transfer along the *x*-axis:

$$j_i(x) = \frac{q_i F}{RT} D_i c_i \frac{\partial \phi_i(x)}{x} + c_i v(x) - D_i \frac{\partial c_i(x)}{\partial x} \qquad (11)$$

where the term $j_i(x)$ (mol s^{-1} cm^{-2}) is the flux of electroactive species i, at distance x from the electrode surface, D_i is the diffusion coefficient (cm^2/s), c_i is the concentration of *i* at position *x* (mol cm-3), $\phi_i(x)$ is the potential at position i, and $v(x)$ is the velocity of a volume element in solution moves along direction x. The terms at the right-hand side represent migration, convection, and diffusion, respectively.[12]

2.2.2.1. Diffusion

If conditions in the electrochemical cell are chosen to eliminate convection and migration, then mass transport in the cell occurs through diffusion. Diffusion in electrochemistry is

the movement of the electroactive species down the concentration gradient to or from the electrode surface produced by electrochemical change at the electrode. The relationship between the diffusion speed (flux) and concentration gradient, as a function of position and time, is defined by Fick's laws of diffusion. Suppose the flux of substance *i* at given location *x* and time *t* is written as $J_i(x,t)$, the net mass transfer rate of *i*, expressed as an amount per unit time per unit area (mol s^{-1} cm^{-2}), then the $J_i(x,t)$ represents the number of moles of *i* that pass a given location per second per unit area perpendicular to the *x*-axis.

Fick's 1st law of diffusion says that flux is proportional to the concentration gradient:

$$J_i(x,t) = -D_i\left(\frac{\partial C_i(x,t)}{\partial x}\right) \qquad (12)$$

Fick's 2nd law is derived from the first law, it pertains to the change of concentration of i with time:

$$\frac{\partial C_i(x,t)}{\partial t} = Di\left(\frac{\partial^2 C_i(x,t)}{\partial x^2}\right) \qquad (13)$$

It can be modified and apply to electrodes with any geometry

$$\frac{\partial C_i}{\partial t} = D_i \nabla^2 C_i \qquad (14),$$

where ∇^2 is the Laplacian operator.[8]

When an external potential is added, the difference between the applied potential and the potential at the equilibrium state, the over-potential (η) results in chemical change according to

$$I_{\text{red}} = AFk_{\text{red}}[i] \qquad (15)$$

Where A is the electrode area, F is Faraday constant, k_{red} is the rate constant for the

electron transfer reaction, and $[i]$ is the concentration of i at the electrode surface. A similar expression can be written for k_{ox}. A concentration gradient is thus created by the consumption/generation of electroactive species i, at the electrode surface. When the kinetics at the surface is fast, i.e., *k* is big, the current will be diffusion-controlled.

2.2.2.2. Chronoamperometric Method and Nernst Diffusion Layer

If the potential at the working electrode is stepped, the resulting current from this applied potential can be monitored as a function of time, giving rise to the technique of chronoamperometry. The current declines according to the diffusion of analyte from bulk solution towards the electrode surface at sufficiently high overpotentials, providing a good example of the role of diffusion in controlling the observed electrochemical currents. Therefore, chronoamperometry is a useful technique to consider the current-time dependence, which can be calculated from(13) . The change in current follows the Cottrell equation:

$$I = nFAj = \frac{nFAD^{1/2}C_0}{(\pi t)^{1/2}} \qquad (16)$$

where I is the current, n is the number of electrons transferred, F is Faraday's constant, A is the area of working electrode, j is the diffusional flux, D is the diffusion coefficient, C_0 is the bulk concentration of analyte. From the equation it's easy to see that the current gradually decreases with the square root of time, and when time is very long, the current will decline to 0.[5]

Equation (16) has useful applications for the determination of *n, D or A* if the two other variables are known. In practice it has limitations when used with macroelectrodes. At

short reaction times, an additional ‘charging current’ is observed due to the double layer charging. At long times, the current measured tends to a constant value, since mixing of the solution due to processes such as convection (see above) tend to occur[13] and effects of non-planar diffusion can set in when the diffusion layer thickness becomes appreciable compared to the lateral dimension of the electrode. [6]

2.3. Experimental Implementation

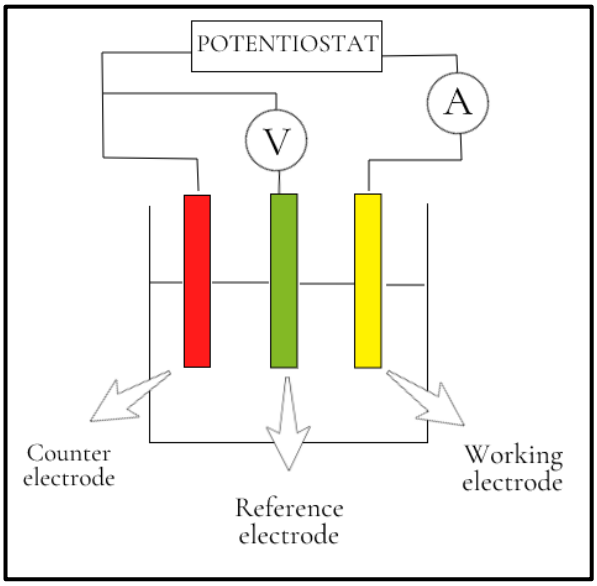

Figure 2.4 A schematic illustration of a simple 3-electrode electrochemical cell, adapted from [2].

In the case of a two-electrode system, the reference electrode is an ideal nonpolarizable electrode, meaning a faradaic current can freely pass and its potential will not vary from its equilibrium value upon application of current. However, in real applications such as battery and sensor studies, electrochemical reactions happen and current can flow through the reference electrode, causing a change in potential and deviation from the ideal scenario. To ensure current does not flow through the reference electrode and ensure its stability and accuracy, a third electrode, known as the counter electrode (CE) is

introduced. The polarity of the counter electrode is opposite to that on the working electrode, and the potential added on the counter electrode is adjusted so that the current flows just between the WE and CE. The CE is commonly simply a coil of platinum wire, with a large enough surface area to provide adequate current flow at accessible potential to match that of the WE under investigation.

2.4. Techniques in Electrochemical Analysis

2.4.1. Cyclic Voltammetry

Cyclic voltammetry (CV) is the most common method used to monitor a dynamic electrochemical process of a particular redox pair at a specific electrode. In CV, the current flowing through the working electrode is recorded as a function of the applied potential between the WE and the reference electrode. A plot of current versus potential is constructed, known as a voltammogram. [6]

The name cyclic voltammetry arises from the fact that the applied potential is varied in a cyclic manner, normally a linear sweep as shown in figure 2.5 below. Only a chosen region of potential, in which electron transfer for the analyte of interest is kinetically and thermodynamically favourable, is swept, and the redox processes which occur in the region are measured as a current response arising from electron transfer and associated reactions. The scheme is shown in figure 2.5 below. [6]

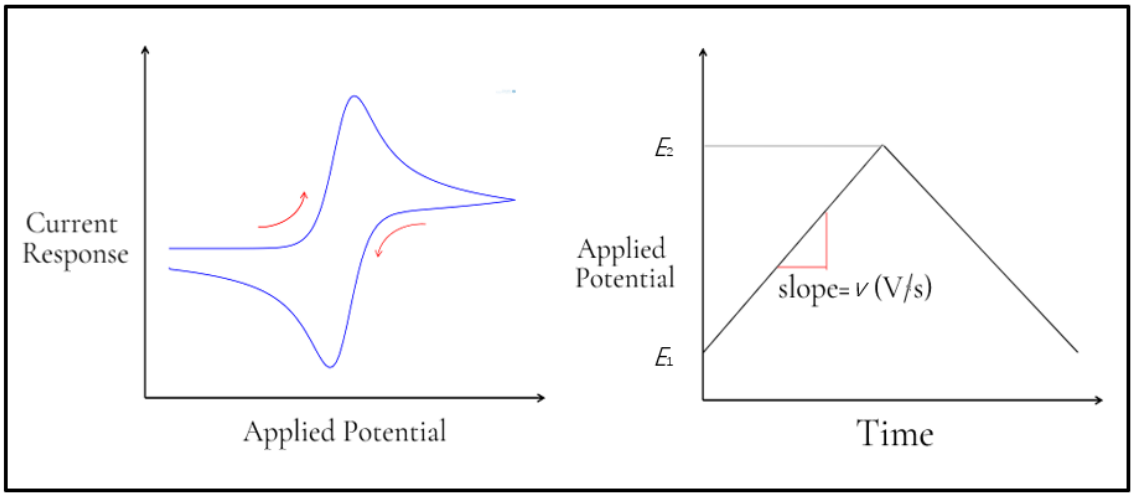

Figure 2.5 A classic CV scan (left); and a schematic illustration of CV waveform (right). The slope *v* is the scan rate. Adapted from [6].

CV probes both the oxidation and reduction regimes. The scan begins at a selected potential E_1 that is very negative compared to the electroactive potential region, where the electroactive species is neither reduced nor oxidised. As the potential is moving towards the positive direction, oxidation occurs, and the oxidation current will be recorded. Because of the diffusion limitations, the electroactive species will be gradually used up, and the concentration will drop, resulting in a fading of the responding current according to the Cottrell equation. After the potential reaches E_2, where the species is fully oxidised and the current drops back to zero, the direction of the potential scan is reversed. The backward potential usually sweeps back to the original value. [11]

CV provides useful information on the kinetics of electron transfer and the features of a CV can be characterised in terms of electrochemical reversibility. We can classify the reactions into reversible, quasi-reversible, and irreversible, depending on the rates of electron transfer. Typical CVs are shown in figure 2.6 below.[15]

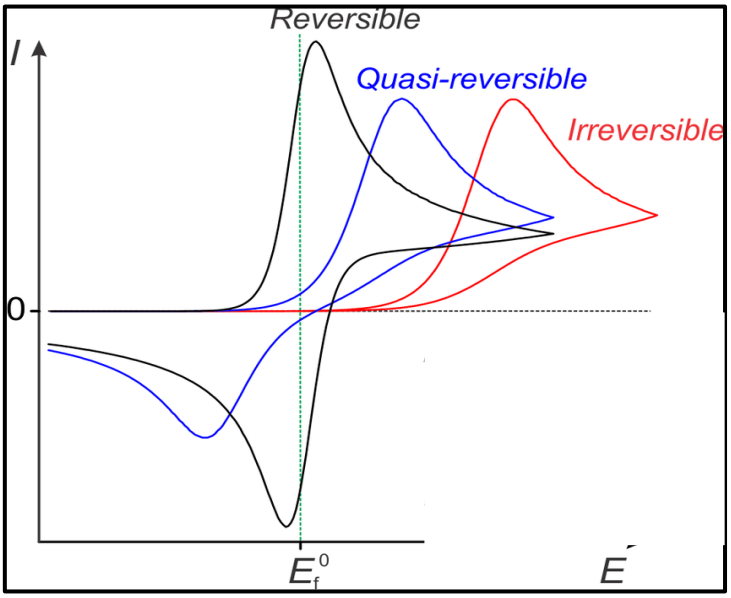

Figure 2.6 CV shapes of reversible, quasi-reversible, and irreversible electron transfers. Adapted from [15].

2.4.1.1. Reversible Electrochemical Process

A reversible wave appears when the electron transfer is fast. In this case, the system is also called a Nernstian system. The waveshape is usefully characterised by the difference between the peak potential E_p and $E_{1/2}$, which is the half-peak potential. For a reversible system:[6]

$$E_p - E_{\frac{1}{2}} = 2.218\frac{RT}{F} \qquad (17)$$

the peak current i_p, is given by the Randles-Sevčik equation:

$$i_p = (2.65 \times 10^5) n^{3/2} A D^{1/2} C v^{1/2} \qquad (18)$$

where n is the number of electrons transferred, A is the electrode surface area, D is the

diffusion coefficient, C is the concentration in bulk solution, and v is the scan rate. This equation applies to a system that is controlled solely by diffusion between the bulk solution and the electrode surface, and the value of the peak current is linearly related to the square root of the scan rate. For such reversible kinetics, the peak separation at 298 K is given by

$$E_{\mathrm{c}} - E_{\mathrm{a}} \cong \frac{57\mathrm{mV}}{n} \qquad (19)$$

where E_{c} is the reduction peak potential, E_{a} is the oxidation potential, and n is the number of electrons transferred. At room temperature (298 K), the reversible limit peak to peak separation value is approximately 57 mV. This peak-to-peak separation value is independent of the scan rate in reversible processes. Conversely, in quasi-reversible and irreversible processes, when the electron transfer kinetics are slow, the peak separations observed will increase and depend on the scan rate.[6]

2.4.1.2. Irreversible and Quasi-reversible Electrochemical Process

For irreversible electrochemical processes, the electron transfer rate is slow, and high potentials are needed to drive the electron transfer and record any current change on the potentiostat. The waveshape of an irreversible electrochemical process can also be characterised through calculating the half-peak potential[6]:

$$E_{\mathrm{p}} - E_{\frac{1}{2}} = 1.857\frac{RT}{\alpha F} = \frac{47.7}{\alpha}mV \quad (\text{at } 298\mathrm{K}) \qquad (20)$$

Notably, all processes are, in principle, electrochemically irreversible when the measurement is done at a sufficiently fast scan rate. When the voltammogram is swept

from E_1 to E_2, the thickness of the diffusion layer around the electrode will increase gradually. The longer it takes to scan, the thicker the diffusion layer. When the scan rate is fast, the diffusion layer is thin.

The thickness of the diffusion layer plays a crucial role in controlling the mass transport to the electrode. As predicted by equation (12), greater fluxes for a fixed concentration drop will occur in the case of a thin diffusion layer. Since the irreversible vs. reversible distinction reflects the competition between electrode kinetics and mass transport, increasing the scan rate will make the mass transport win over the electrode kinetics and essentially increase the irreversibility.[11]

Quasi-reversible electrochemical processes are given to electron transfers that fall between the previous two categories.

2.4.2. Chronoamperometry

In chronoamperometry, a pulsed potential is applied to the working electrode, and the current response is measured as a function of time. The change in the current reflects the variations in the diffusion layers of the analyte at the electrode surface. When an appropriate potential is applied to the system, the local concentration of analyte suddenly drops to zero at the electrode surface, and a concentration gradient is generated, so that the analyte is able to transfer through diffusion layers from the bulk solution section to the electrode surface.[13] A single-potential-step Chronoamperometry process is illustrated

by figure 2.7 below:

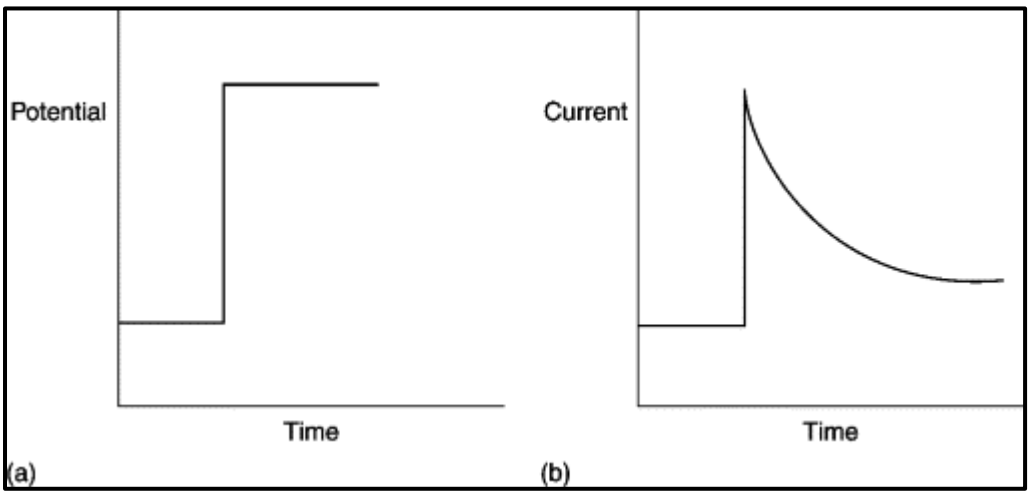

Figure 2.7 Potential waveform of Chronoamperometry (a), and current vs. time plot (b). Adapted from [13].

Chronoamperometry initially begins with an open circuit, or at a potential where the target analyte is not electrochemically active. Then the potential is stepped to a point beyond that required for the redox reaction for this species, i.e., E_0. The shape of the chronoamperometry plot reflects the changes in concentration versus the distance to the electrode. The current response as a function of time can be obtained from equation (16), and electroactive species in the solution can be characterised in terms of the diffusion constant and electrons transferred in particular redox steps.

Double-step chronoamperometry is also used in many electrochemical analyses. After the potential E_s is reached and kept for a time period t, the potential either returns to the initial value E_i, or switches to another value. The potential wave form is shown in figure 2.7. Double-step chronoamperometry provides a more comprehensive overview of the system, including rate constants[16]

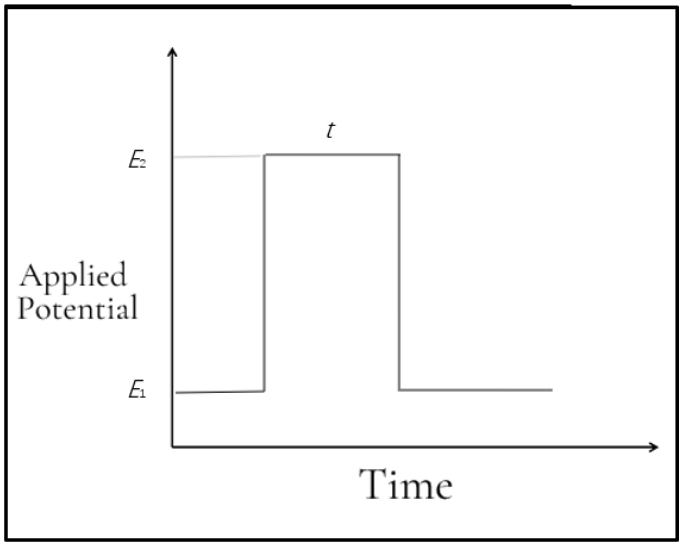

Figure 2.8 Potential waveform of double-step chronoamperometry. After *t*, the potential is usually switched back to E_1, and kept for another time interval *t*. Figure adapted from [13].

2.4.3. Square Wave Voltammetry and Differential Pulsed Voltammetry

Different from CV, which is a linear potential sweep method, square wave voltammetry (SWV) and differential pulsed voltammetry (DPV) are potential step voltammetric techniques. The total current response I in all electrochemical analysis is the sum of contributions from a faradaic reaction and capacitive interaction:

$$I = I_c + I_f = vC_d + I_f \qquad (21)$$

where I_c is the capacitive component, proportional to the scan rate v, and C_d is the capacitance of the electrode, I_f is the faradaic current. In those potential step methods, enhanced responses to the faradaic current component relative to the capacitative current can be detected, which makes them preserve extra sensitivity.[5]

As discussed before, the faradaic response is a function of $t^{1/2}$ and gradually fades away as electroactive species at the surface of the electrode are consumed. The capacitive

interaction, due to the double-layer charging (the movement of ions to and from the electrode), is a much faster process, and thus the capacitive current dies away much faster than the faradaic current. SWV and DPV can be parameterised so that the current recorded is the faradaic current after the capacitive current fades away. [5]

In SWV, a square wave waveform, which is superimposed on a potential staircase, is applied to the the working electrode. A square wave is characterised by a pulse height, or amplitude ΔE_{p}; the staircase heightΔE_{s}; the pulse timet_p; square wave frequency f, which is half of the pulse time, and the cycle period. At the start of each cycle, the staircase shifts by ΔE_{s}, so the scan rate is:

$$\frac{\Delta E_{\mathrm{s}}}{2t_{\mathrm{p}}} = f\Delta E_{\mathrm{s}} \qquad (22)$$

The currents at the end of the forward and reverse pulses (marked as forward sample and reverse sample in the figure) are both monitored as a function of staircase potential. The difference between them, the net currentΔI, is larger than either of its two component parts I_1, and I_2 in the region and is centred at the half-wave potential. Afterwards, ΔI is plotted as a function of the staircase potential:

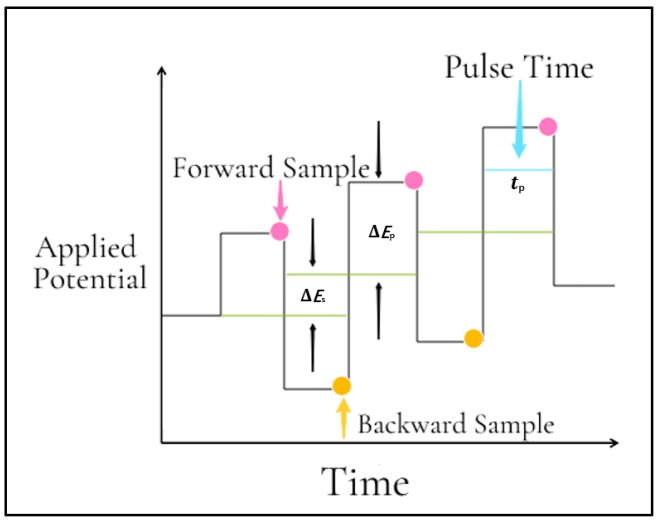

Figure 2.9 Potential waveform of SWV. Adapted from [5].

$$\triangle I = I_1 - I_2 \qquad (23)$$

Through this subtraction, SWV effectively cancelled out the capacitive contributions to the overall current measured. Over the small potential range between forward and reverse pulses, the interfacial capacitance is approximately constant. [5]

DPV is another widely used potential step method. Similar to SWV, the potential waveform is pulsed and superimposed on a staircase. However, the currents just before the pulse is applied and just before the end of each pulse are measured, and the difference is plotted against the staircase potential. DPV also greatly reduces the contribution of the capacitive process by taking the difference between current responses, since the capacitive currents are roughly the same from the beginning towards the end of the pulse.[5]

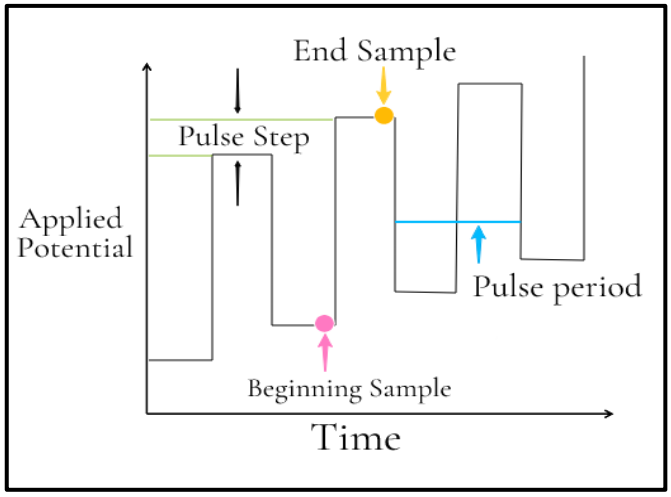

Figure 2.10 Potential Waveform of DPV. Adapted from [5].

SWV has detection limits of ~ 10^{-8} M, whereas DPV can achieve optimal detection limits of ~10^{-7} M, both suitable for sensitive, trace detection. In addition, they can also provide information about the identification of oxidation states and recognition of complexation effects, which are very useful when interfering chemicals present in the solution.[11]

In this thesis, DPV and SWV are both used. DPV was attempted first, due to its simplicity

and faster processing time. On the other hand, SWV requires more complicated data processing. However, SWV was introduced when the limit of detection needed to be pushed lower. The high sensitivity of SWV is due to the lack of background current, which is a major interference in the detection of lower concentrations.

2.5. Experimental

2.5.1. Materials and Instruments for Electrochemistry

All chemicals were purchased from Sigma Aldrich. The polycrystalline diamond electrodes (BDDE) was purchased from Element Six Ltd (SKU 145-500-0030, 10.0x10.0mm, 0.60mm thick) and had a boron doping concentration of ~ 5×10^{20} cm^{-3}, with bulk resistivity 2 to 1.8×10-3 Ohm×m, ± 0.25×10-3 Ohm×m, operating current density of >20,000 Am^{-2}, and a solvent window >3.0 V in 0.1 M KNO3 versus SCE. The surface of BDDEs were not polished, and the free-standing electrodes had very rough

grain relief, Ra ~50 μm.

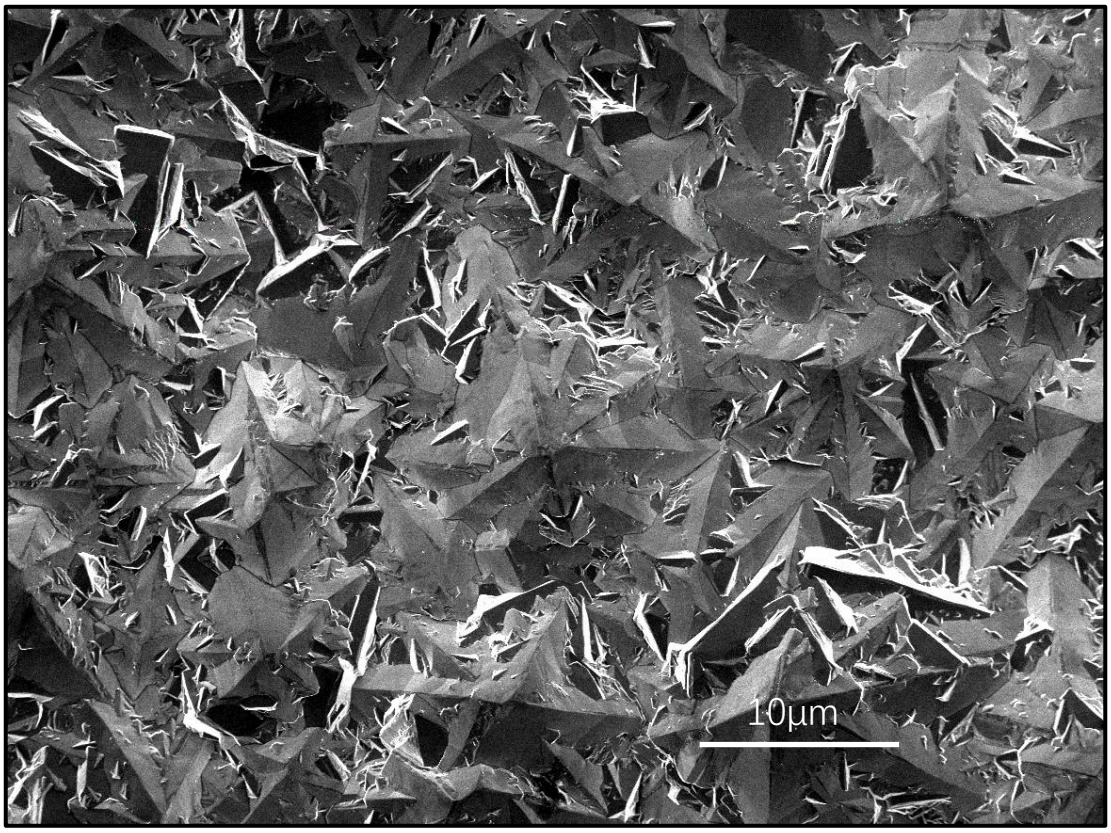

Figure 2.11 SEM of a typical pristine BDDE diamond used for this thesis.

All solutions are prepared using deionized water with resistivity around 18.2 MΩ at room temperature (25 °C). Ag/AgCl (1 M KCl) reference electrode and Pt coil counter electrode were purchased from Sigma Aldrich, and the BDDE working electrode was fixed in a custom-made polytetrafluoroethylene (PTFE) holder. Electrochemistry experiments were performed and controlled by an Autolab potentiostat and software NOVA 2.1.4. The analysis of data was prpcessed by OriginsPro, unless specified.Cleaning of BDDEs

Thanks to the superior physical hardness and chemical stability of BDDEs, there are three safe ways to clean BDDEs between experiments:

2.5.1.1. Electrochemical Cleaning

Dilute nitric acid (0.1 M) was used for electrochemical cleaning. Firstly, a positive potential of 2.5 V is applied to the BDDE and impurities on the electrode surfaceoxidised, leaving the surface oxygen-terminated, which is more favourable for deposition of metal nanoparticles (will also be proven through XPS in Chapter 3). CV was swept between 0 V and 2.3 V at a scan rate of 50 mV/s for 10+ cycles, until a flat solvent window (Figure 2.12) was observed. After cleaning cycles, a separate CV in with same setting will be produced for checking, if a CV with flat solvent window (Figure 2.12) can be reproduced, we conclude this electrode to be "clean" and ready for use.

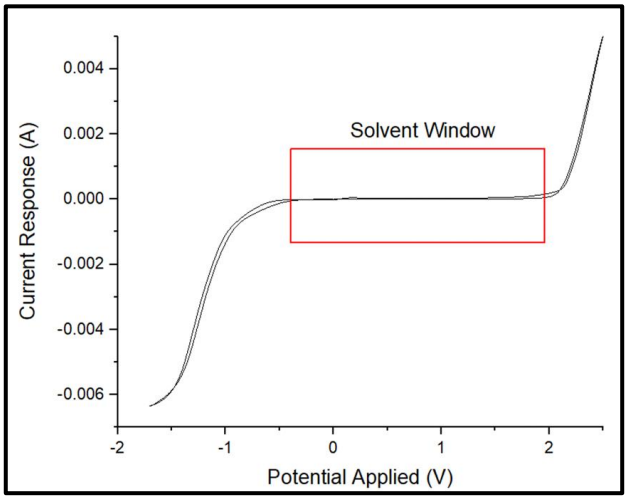

Figure 2.12 CV of a BDDE diamond after nitric acid cleaning and a clean solvent window observed.

2.5.1.2. Concentrated Acid Cleaning

BDDEs decorated by metal nanoparticles can also be cleaned by soaking into concentrated acid. Aqua Regia (3:1 v:v mixture of ~12 M HCl and ~15 M HNO_3) was used for removing Au-containing nanospecies and other precious metals, whereas Ag containing nanospecies were removed by concentrated nitric acid (~15 M). The solubilities of metals in concentrated acids were checked to make sure the electrodes

could be cleaned effectively. BDDEs were left overnight in the concentrated acid, followed by ultrasonic cleaning in DI water.

2.5.1.3. Mechanical Polishing

When polymers like Nafion were used for electrode modification, electrochemical cleaning and concentrated acid cleaning were not as effective as mechanical polishing. In this thesis, commercially available chemomet polishing pads (Buehler, ∅203 mm) and alumina (Al_2O_3) powder (Buehler micropolish, a mixture of 1.0 and 0.3 microns) were used. The alumina is mixed with water on the polishing pad to make a paste. The BDDEs were then rubbed on the polishing pad with some alumina paste while ensuring that the face of the BDDEs were flat and polishing was performed by the KENT 3 automatic lapping and polishing unit. After polishing for 3 minutes, the electrodes were ultrasonicated 3 times using acetone, acetone: DI water (1:1), and DI water, individually, and each cycle lasted for 3 minutes.

2.6. X-Ray Photoelectron Spectroscopy

2.6.1. Theoretical Principle

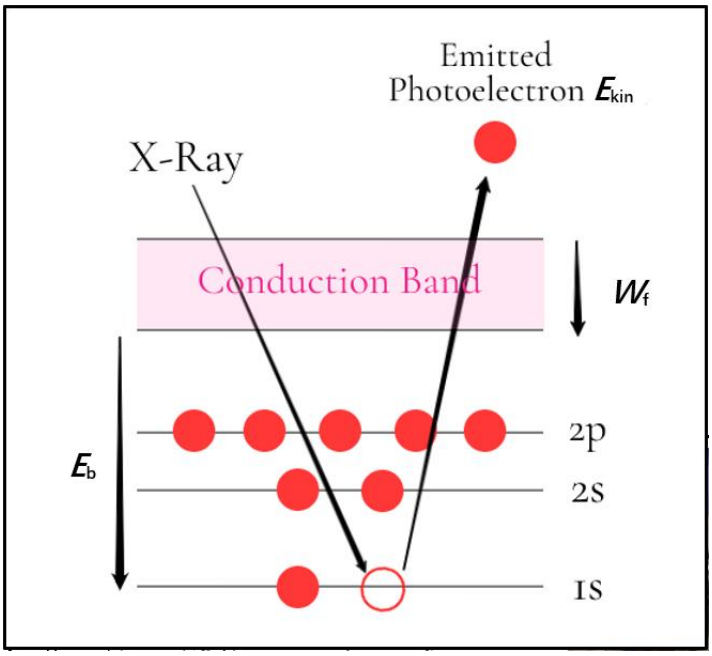

Figure 2.13 Basic theory behind XPS. X-ray with energy *hv* initiates the s on sample, releasing a photoelectron with energy E_{kin}. Figure adapted from [18].

X-Ray Photoelectron Spectroscopy (XPS), also known as Electron Spectroscopy for Chemical Analysis (ESCA) was first developed in the mid-1960s in Sweden by Kai Siegbahn, who was awarded the Noble Prize in physics for that. Nowadays, it is commonly used as one of the major methods for chemical surface analysis.

XPS works by determining the kinetic energy spectrum of photoelectrons emitted from the specimen's surface whilst irradiating the sample with X-rays with a constant energy, *hv*, in vacuum conditions with a pressure less than 10^{-7} Pa, denoted as ultra-high vacuum (UHV). The photons emitted from the X-ray source can penetrate the specimen surface for up to 1 μM and create photoelectrons in this region. However, not all these photoelectrons can be detected in XPS. Most of the photoelectrons lose their kinetic

energies in inelastic scattering and cannot escape the surface or simply contribute to a spectral background. Consequently, only the electrons from the top several atomic layers (~ 5 nm) are analysed, so XPS is a very surface sensitive method. The XPS spectrum is obtained by plotting the number of electrons at a given kinetic energy versus their kinetic energy or the corresponding binding energy as determined from the following the equation below. [17]

$$E_{\mathrm{b}} = h\nu - E_{\mathrm{kin}} - W_{\mathrm{f}} \qquad (24)$$

where W_{f} is the work function.

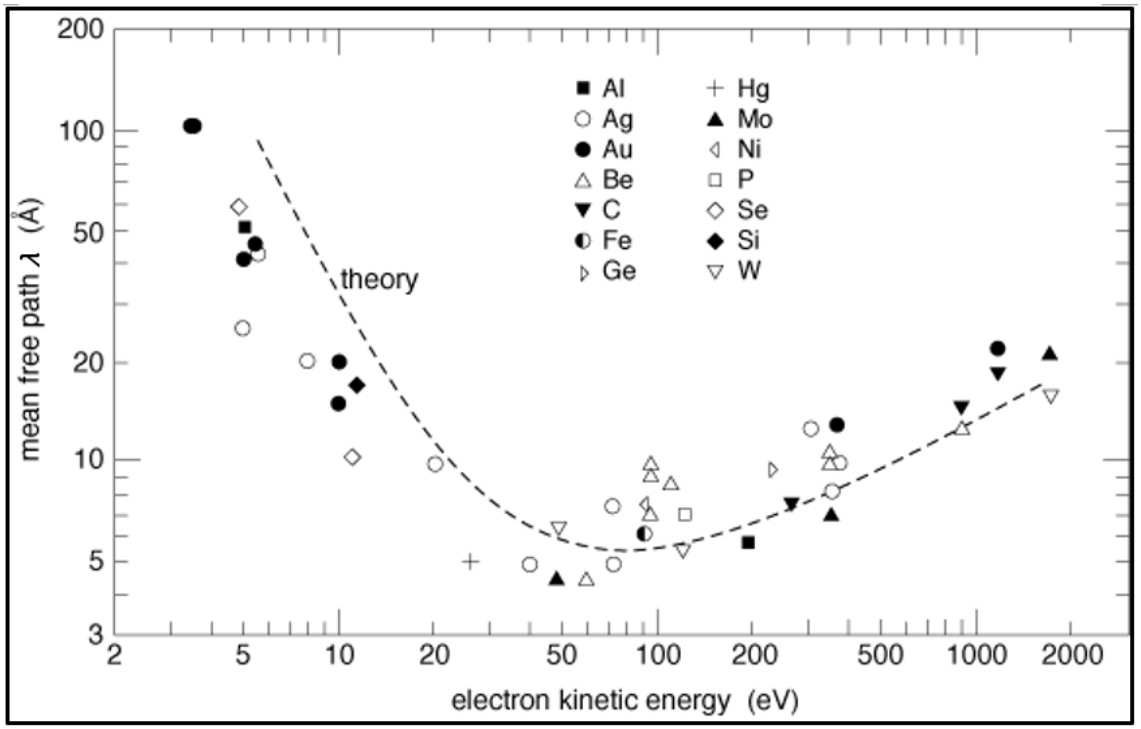

Figure 2.14 The relationship and variation between mean free path and kinetic energy of emitted electron (universal curve).[19-20]

The depth scale, or surface sensitivity, of XPS is controlled by the electron inelastic mean free path (IMFP). Inelastic mean free path (IMFP) is dependent on kinetic energy and shows how far an electron can travel through a solid before losing energy. When the kinetic energy of photoelectrons is higher, they can travel farther before scattering

happens, so the depth scale of XPS increases, as the sampling depth is defined as 3 times of IMFP. By changing the X-ray photon energy, the kinetic energy of core level photoelectrons can be controlled. In this way, IMFP, scale depth, and sensitivity can also be altered.[21-23]

After X-ray excitation of the atom and a core level photoelectron is emitted, non-fluorescent relaxation results in the appearance of Auger peaks in the spectrum as a result of the relaxation process shown in Figure 2.14. For example, KLL transition means there is an initial vacancy in the K shell and two vacancies in the L shell in the final state. In XPS spectra, we can mostly see the KLL, LMM, MNN, and NOO series of Auger lines.[22]

Figure 2.15 Schematic illustration of a KLL transition in an Auger process.[19]

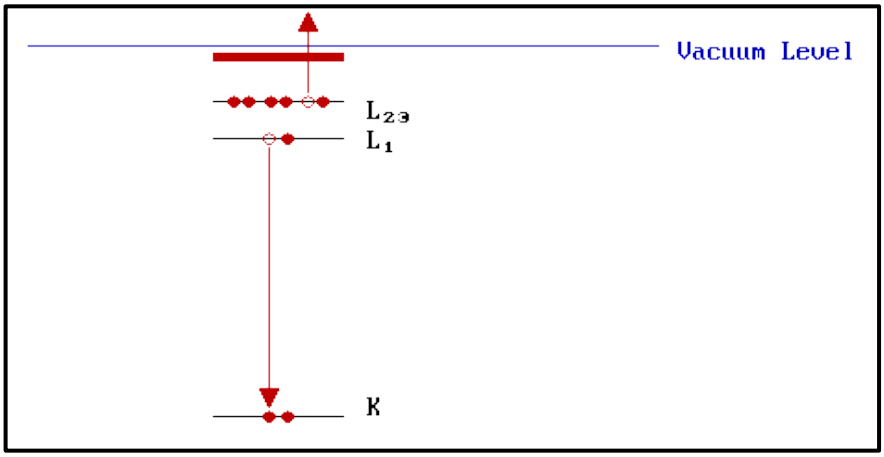

Small variations in binding energy, also known as chemical shifts, reflect the chemical state of the material as well. The binding energy peak position of a specific element depends on the oxidation state and local chemical environment of that element. Atoms of higher positive oxidation states tend to have higher binding energies due to extra columbic interaction between the ion core and the core electrons in the atom.

Chemical shifts provide information on oxidation states and functional groups that immediately bond to the atom. For example, when a C atom is bonded to another atom,

if the electronegativity of that atom is higher than C, the electron density around the C atom itself will decrease and therefore the binding energy will increase, resulting in a positive shift of binding energy peak. Otherwise, a negative shift of the binding energy peak will be observed.[15]

The Auger parameter, originally defied by Wagner, can also be used for analysis of chemical states. The Auger parameter is not influenced by surface charging and is extremely useful when an electron core level of two states is indistinguishable just by looking at kinetic or binding energy. The value of the Auger parameter (α) can be calculated using the difference in kinetic energy between a core peak and Auger peak:

$$\alpha = E_{\mathrm{k}}(C_1C_2C_3) - E_{\mathrm{k}}(C) \qquad (25)$$

where $E_{\mathrm{k}}(C_1C_2C_3)$ is the kinetic energy corresponding to the Auger peak, and $E_{\mathrm{k}}(C)$ is the kinetic energy of the core photoelectron peak.[24]

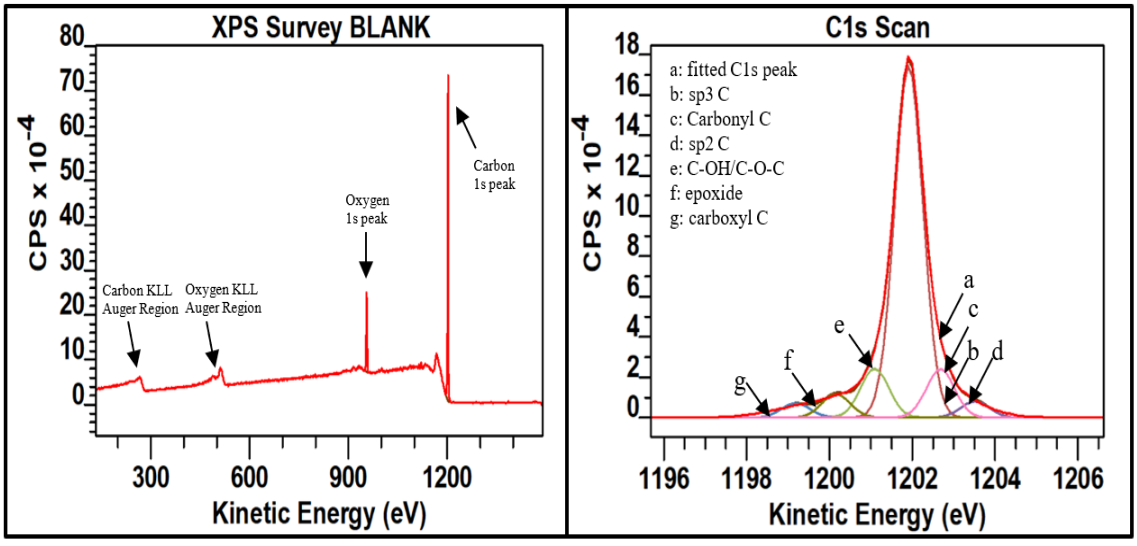

Figure 2.16 A survey XPS (left) and chemical shifts representing different chemical states in C1s scan (right) of a clean BDDE.

XPS is not only for qualitative analysis, i.e., element identification, the intensity of the photoelectron peak of XPS also provides quantitative information about surface

composition. The intensity of a photoelectron peak is determined by the equation below:

$$I = j\rho\sigma K\lambda \qquad (26)$$

where *j* is the flux of the photon, ρ is the concentration of atoms, σ is the photonionisation cross-section for photoelectron emission, *K* is the instrumental parameter and λ is the electron attenuation length. The area under the peak after background subtraction is denoted as $I_{i,}$ and the relative atomic sensitivity factor (RSF) is denoted as $S_{i.}$ The relative atomic sensitive factor (RSF) is characteristic for each element and is determined by the photo-ionisation cross section and inelastic mean free path. It means how likely it is that a photoelectron from a particular orbital and element is produced and detected. Together with these two parameters, N_i, which is the number of atoms per cm^3 (i.e. the surface percentage of one element), can be determined. [19-20]

$$N_i = \frac{I_i/S_i}{\sum_i I_i/S_i} \qquad (27)$$

here $I_{i,}$ is the peak area of the element after background subtraction, S_i is the RSF, and $\sum_i I_i/S_i$ means sum over all elements.

2.6.2. Instrumental and Experimental

The instrumentation of XPS is based on UHV system to avoid gas contamination of the sample specimen surface and collisions between emitted photoelectrons and gas residuals. It has the following components: an X-ray source, an electron energy analyser, and an electron detection system, as shown in figure 2.17. Since the exciting energy provided by the X-ray source is very high, core level spectra of all elements (except for H and He, which has no core level) can be obtained and the binding energy can be determined for peak assignments. Mg Kα (1253.6 eV) and Al Kα (1486.6 eV) X-rays are commonly used as excitation sources.[17]

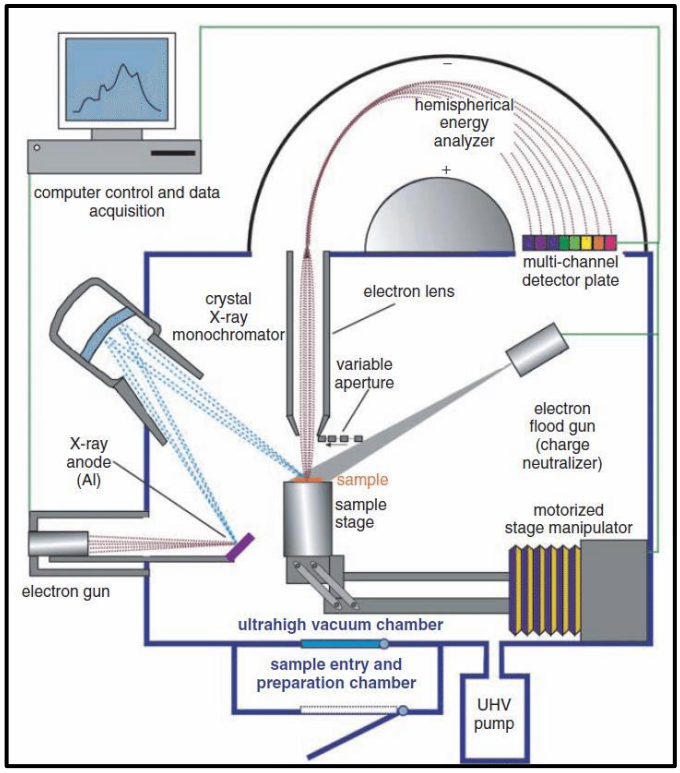

Figure 2.17 Schematic view of the XPS instrumentation. [39]

All XPS analysis in this thesis was done by a Thermoscientific K-alpha instrument using Al Kα radiation. The analysis of collected data and graphs were proceeded by CasaXPS (version 2.3) software.

2.7. Scanning Electron Microscopy

2.7.1. Theoretical Principle

Microscopy is a subject that uses instrumentation – a microscope - to study objects of a scale outside the resolution range of the naked human eye. Optical light microscopes are the most widely used type. Although very simple to assemble and use, an optical microscope has limitation in its resolution. It uses visible light and a series of glass optical lenses. Since it uses visible light, whose wavelength is 300-800 nm, the magnification is limited to around 1000× determined by the wavelength.[22]

In 1920s, Busch investigated the trajectories of charged particles in axially symmetric electric and magnetic fields and showed such fields could be used as particle lenses. On the other hand, de Broglie introduced the concept of corpuscule waves, associated frequency, or wavelength to charged particles. These two are fundamental concepts of electron microscopy. Using de Broglie equation (where λ is the de Broglie wavelength, h is Planck's constant, p is the momentum, m is the mass and v is the speed), wavelengths of charged moving electrons can be determined, which is almost five orders of magnitude smaller than the wavelength of visible light used in optical microscopy. In 1932, Knoll and Ruska attempted to estimate the resolution limit of the electron microscope, using the formula for optical lens resolution limits. They substituted the wavelength by electrons wavelength at an accelerating voltage of 75 kV and were able to get a theoretical limit of 0.22 nm. This magnitude was later reached by transmission electron microscope (TEM).

$$\lambda = \frac{h}{p} = \frac{h}{mv} \qquad (28)$$

In SEM, however, several factors constrain the resolution. Electron optics are used to constrain the beam width of electrons emitted from an electron source - a small tungsten tip most simply- in order to form the smallest possible probe beam controlled by the voltage of the electron source, and tightness of the electron beam focus as it strikes on the sample. At higher magnifications, the resolution is approximately the width of this probe. When there are lens aberrations, the ability of focusing the beam decreases, resulting in a blurred image. The second limiting factor is the conservation of brightness throughout the microscope column. If the size of the electron probe is decreased, the current will decrease at the same time, and when current is low, there are limited numbers of electrons in the probe, making the signal poor and the noise ratio very high. As a result, the resolution of SEM typically can go down to the 10 nm range. [26-27]

To achieve a higher resolution, a field emission gun SEM (FEGSEM) can be used. A field emission gun can help to produce an electron beam that is more narrow, condensed, and coherent with up to three orders of magnitude greater current density of brightness than an ordinary SEM. As a result, the resolution can be greatly increased, and the signal-to-noise ratio can be improved.[28-30]

The schematic diagram of SEM's working principle is shown below. A primary electron beam is generated by an electron source and accelerated by an anode. After that, the direction is controlled by electromagnetic lenses, which are coils of wires inside metal poles.

After striking the sample, the electron beam rasters across the surface. Then, secondary electrons, originate from the atoms of the sample's surface, as a result of inelastic interactions between the electron beam and the sample. To produce an image of the surface, a positively charged detector at an angle is placed to catch as many secondary electrons scattered as possible. The signals detected are amplified and modulated to produce a map of the surface morphologies. [31]

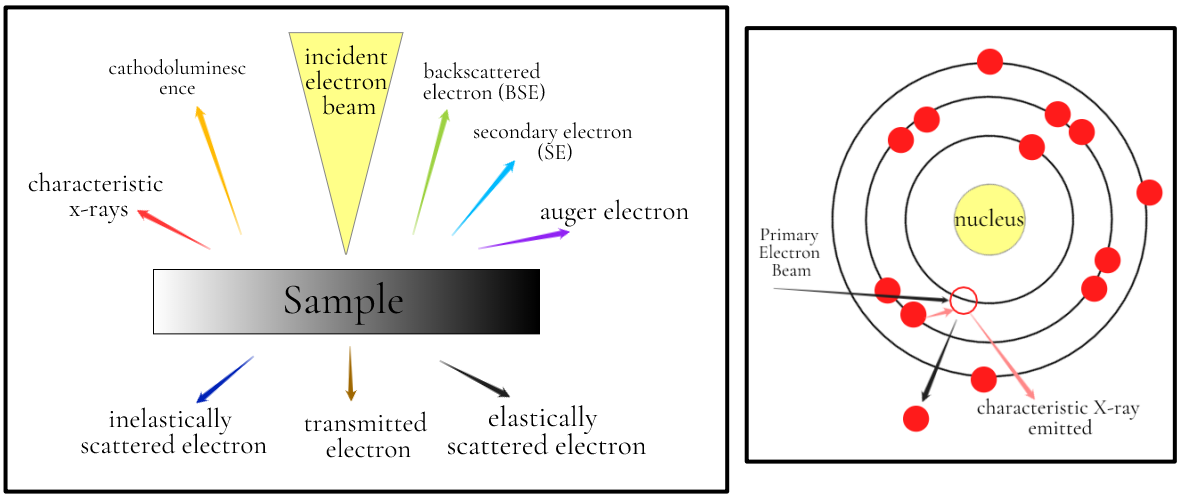

Figure 2.18 Types of electrons emitted from sample after electron beam irradiation (left); and how characteristic x-rays are emitted after the primary electron escapes(right). Figure adapted from [31].

SEM produces signals mostly based on the scattering of secondary electrons, however, back scattered electrons are also produced once the electron beam strikes the specimen. Back scattered electrons (BSE), unlike secondary electrons, appear very close to the region of the primary electrons. BSE images can be used to distinguish phase or compositional variations from site to site among the specimen, since the BSE coefficient increases with the atomic number. [30]

Other than secondary and BSEs, cathodo-luminescence gives information on the electronic structure and chemical composition of materials, and transmitted electrons can

depict the inner structure and crystallography, which is detected and characterised in transmitted electron microscopy (TEM). X-rays are also produced when the electron beam transfers energy to the atoms on the sample, and electron core holes are produced. During relaxation, characteristic X-rays, which have the exact energy difference between the two electronic shells, are emitted. This energy depends on the atomic number and can be used to distinguish the atomic composition. This type of analysis is called energy-dispersive x-ray analysis (EDX). [32]

2.7.2. Instrumental and Experimental

In this thesis, the SEMs used were a Hitachi S-4300 SEM and JEOL JSM-6010LV SEM. The high-resolution images were taken using the JEOL-6500F SEM. The TEM machine used for chapter 5 was a JEOL-3000F TEM. The data were analysed by GMS3 software.

2.8. Ultraviolet-visible Spectroscopy

2.8.1. Theoretical Principle

Ultraviolet-visible Spectroscopy (Spectrophotometry), or UV-Vis Spec, is a common method in analytical chemistry. The light sources it uses are the in the range of visible light, near-UV and near IR, and measurements can be done in either absorption or reflection mode. The light source is separated into its component wavelength by diffraction grating or a prism. The grating is rotated to make a measurement, to allow only a specific wavelength of light source to go through and interact with the sample. By

this manner, the complete spectrum can be recorded. [34]

After the light strikes on the sample, it interacts with it and promotes electronic excitations. A Jablonski diagram represents the energy levels within a molecule where valence electrons can be excited. Shown in the figure below, every column represents specific spin multiplicity for a particular species, or electronic energy states (S, T). Within each of them, multiple vibrational energy states are found (v). We can use this diagram to explain where the energy goes, and this process can be viewed as a multi-step kinetic pathway. The first step is absorbance (Abs.), in which electrons in the ground state (S_0) absorb energy and jump to higher energy states. Any excited singlet states have higher energy than S_1 will then undergo fast decay, called internal conversion (IC). Relaxations between the different vibrational states in the same electronic level are called vibrational relaxation (VR). Afterwards electrons from higher energy states relax to lower energy states, and emit photons, this process is called fluorescence (Fl.), and it is often observed between the first exited electron state and the ground state. The process of electron changing spin from excited singlet states to excited triplet states is called intersystem crossing (ISC), followed by a slow radiative transition which is spin-forbidden called phosphorescence (Phos.). [35]

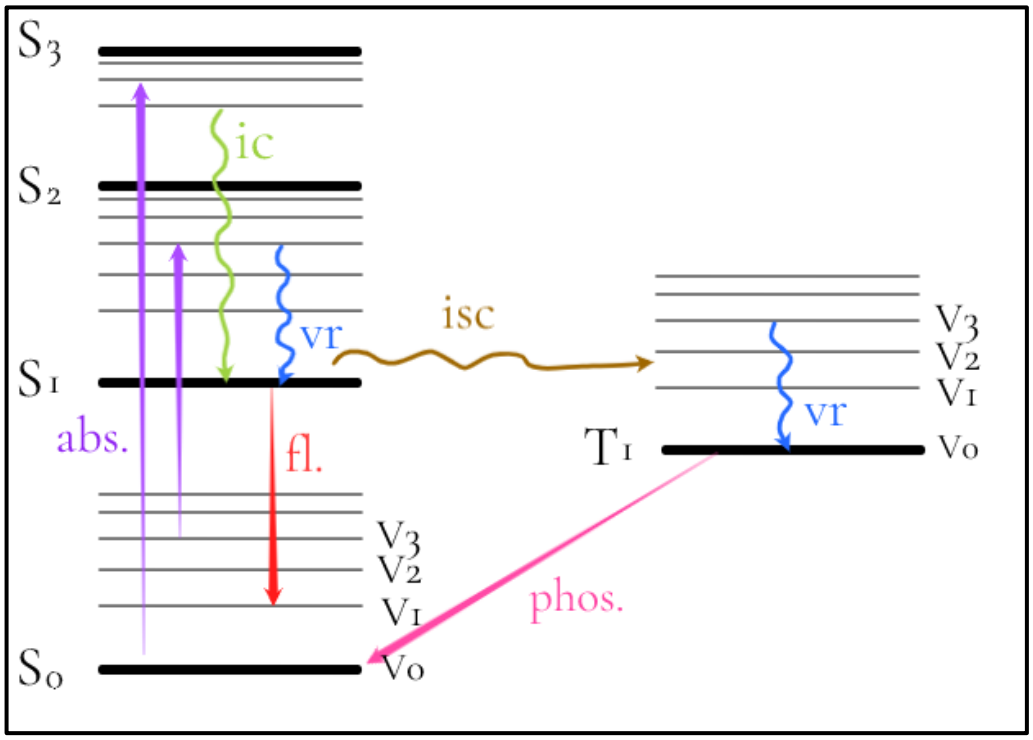

Figure 2.19 Jablonski diagram, showing different types of electron and energy transfer, whenlight is absorbed. Figure adapted from [35].

In this thesis, we refer to experiments done in the absorption mode, which measures the first step, the electronic promotion of electrons or the energy absorption for the electron from the ground state to the excited state, in contrast to fluorescence spectroscopy, which measures the emission process. The most fundamental working principle behind UV-Vis Spec is the Beer-Lambert Law. [36]

$$A = \log_{10}\frac{I_0}{I} = \varepsilon c l \qquad (29)$$

In this equation, A is the measured absorbance, l is the path length the light source travelled through the sample (the inner width of the cuvette), c is the concentration of the analyte, and ε is the extinction coefficient constant. The absorption measured by UV-Vis Spec can be analysed both qualitatively and quantitatively: the signal height of absorbance is proportional to the concentration of the analyte, and since l and ε are given constants, the concentration of the analyte can be solved simply.[36-37]

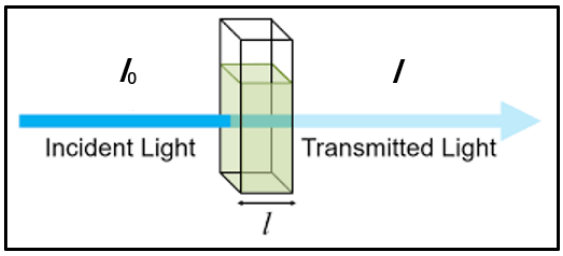

Figure 2.20 Monochromatic light with intensity I_0 transmitted through a solution (cuvette length l). The transmitted light has intensity I.[31]

2.8.2. Instrumental and Experimental

In this thesis, we mainly used UV-Vis Spec to evaluate the size of metal nanoparticles, and degree of aggregation. When nanoparticles are well-dispersed in the solution without aggregation, a narrow peak in UV-Vis Spec will be observed, as a result of plasmonic resonance. Plasmonic resonance is a consequence of the oscillations of the valence electrons, when the nanoparticles are small and well dispersed, the electron density at the surface is high, and plasmonic resonance is very strong, resulting in absorption of light with a particular wavelength. When the particles begin to aggregate, and the plasmonic resonance is weaker, a red-shift of this characteristic peak can be observed, and eventually fade away when heavy aggregation occurs.[37-38] The signals obtained by the samples are normalised and then used for analysis in this work, unless indicated. The UV-Visible instrument used in this thesis is a Cary-3500 double beam UV-Vis spectroscopy from Agilent Technologies. The light source used is an Xenon flash lamp (250 Hz), with maximum scanning speed 150000nm/min, spectral bandwidth 0.1-5.0nm, and a scan range of wavelength 190-1100nm.

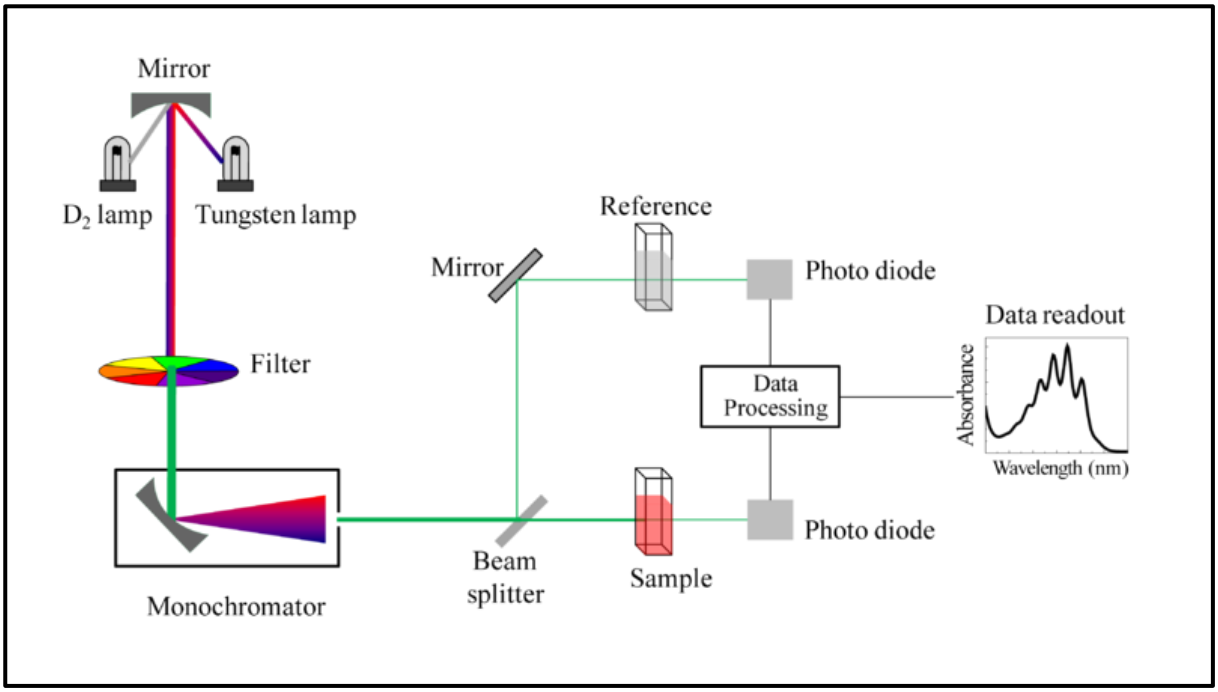

Figure 2.21 Schematic illustration of UV-Visible working mechanism.[33-34]

References

(1) Brkovic, S.; Marceta Kaninski, M.; Lausevic, P.; Saponjic, A.; Radulovic, A.; Rakic, A.; Pasti, I.; Nikolic, V. Non-Stoichiometric Tungsten-Carbide-Oxide-Supported Pt–Ru Anode Catalysts For PEM Fuel Cells – From Basic Electrochemistry To Fuel Cell Performance. *International Journal of Hydrogen Energy* 2020, 45, 13929-13938.

(2) Maduraiveeran, G.; Sasidharan, M.; Ganesan, V. Electrochemical Sensor And Biosensor Platforms Based On Advanced Nanomaterials For Biological And Biomedical Applications. *Biosensors and Bioelectronics* 2018, 103, 113-129.

(3) Choudhury, S. Molecular Tools For The Detection Of Waterborne Pathogens. *Waterborne Pathogens* 2020, 219-235.

(4) M.A.Brett, C.; Brett, A. M. O. Electroanalysis; *Oxford University Press: Oxford,* 1998.

(5) R. G. Compton and G. H. W. Sanders, Electrode Potentials. Oxford Chemistry Primers, *Oxford: Oxford University Press,* 1996.

(6) R. G. Compton and C. E. Banks, Understanding Voltammetry. *London: Imperial College Press,* 2nd ed., 2011.

(7) Guidelli, R. et al. Defining the transfer coefficient in electrochemistry: An assessment (IUPAC Technical Report). *Pure Appl. Chem.* 86, 245–258 (2014).

(8) A. C. Fisher Electrode Dynamics.Oxford Chemistry Primers, *Oxford: Oxford University Press* 1996.

(9) Marcus, R.A., Electron transfer reactions in chemistry, theory and experiment *Rev. Modern Physics*1993 *65,* 599-610.

(10) Silverstein, T. Marcus Theory: Thermodynamics CAN Control The Kinetics Of Electron Transfer Reactions. *Journal of Chemical Education* 2012, 89, 1159-1167

(11) J. Albery, Electrode kinetics, *Clarendon Press, Oxford,* 1975.

(12) Kodým, R.; Šnita, D.; Bouzek, K. Mathematical Modeling Of Electromembrane Processes. *Current Trends and Future Developments on (Bio-) Membranes* 2019, *12* 285-326.

(13) Prudenziati, M.; Hormadaly, J. Printed Films; *Woodhead Publishing: Cambridge, UK,* 2012.

(14) Heinze, J. Cyclic Voltammetry—"Electrochemical Spectroscopy". New Analytical Methods(25). *Angewandte Chemie International Edition in English* 1984, 23, 831-847.

(15) Lee, J.; Hussain, G.; Banks, C.; Silvester, D. Screen-Printed Graphite Electrodes As Low-Cost Devices For Oxygen Gas Detection In Room-Temperature Ionic Liquids. *Sensors* 2017, 17, 2734.

(16) Ensafi, A. Electrochemical Biosensors, *Elsevier* 2019, *1-2*11-43.

(17) Hercules, D. Electron Spectroscopy For Chemical Analysis. *Journal of Electron Spectroscopy and Related Phenomena* 1974, *5,* 811-826.

(18) Krebs, F. Polymer Photovoltaics; *SPIE: Bellingham, Wash,* 2008; pp. 189-196.

(19) Egerton, R. F. Electron energy-loss spectroscopy in the electron microscope *Springer,* 1996, *233*, 293-397.

(20) Briggs, D.; Ceasar, G. Editorial. Surface and Interface Analysis *Wiley*, 1979, *1*, 2.

(21) Yaghoubi, H.; Lafalce, E.; Jun, D.; Jiang, X.; Beatty, J.; Takshi, A. Large Photocurrent Response And External Quantum Efficiency In Biophotoelectrochemical Cells Incorporating Reaction Center Plus Light Harvesting Complexes. *Biomacromolecules* 2015, 16, 1112-1118.

(22) Buschow, K. Encyclopedia Of Materials; *Elsevier: New York,* 2001; pp. 393-398.

(23) Clark, P.; Radtke, H.; Pengpad, A.; Williamson, A.; Spencer, B.; Hardman, S.; Leontiadou, M.; Neo, D.; Fairclough, S.; Watt, A. et al. The Passivating Effect Of Cadmium In Pbs/Cds Colloidal Quantum Dots Probed By Nm-Scale Depth Profiling. *Nanoscale* 2017, 9, 6056-6067.

(24) Auger parameter – HarwellXPS Guru https://www.harwellxps.guru/knowledge-base/auger-parameter/ (accessed Jul 25, 2021).

(25) Bradbury, S. An Introduction To The Optical Microscope; *Oxford University Press: New York*, 1984.

(26) Bogner, A.; Jouneau, P.; Thollet, G.; Basset, D.; Gauthier, C. A History Of Scanning Electron Microscopy Developments: Towards "Wet-STEM" Imaging. *Micron* 2007, 38, 390-401.

(27) Catto, C.; Smith, K. Resolution Limits In The Surface Scanning Electron Microscope. *Journal of Microscopy* 1973, 98, 417-435.

(28) Wells, O. Scanning Electron Microscopy. *Encyclopedia of Materials: Science and Technology* 2001, 8265-8269.

(29) Williams, D. Electron Microscopy: Transmission. *Encyclopedia of Materials: Science and Technology* 2001, 2577-2584.

(30) Allen, T.; Goldberg, M. Scanning Electron Microscopy In Cell Biology. *Encyclopedia of Cell Biology* 2016, 14-21.

(31) R.W.Cahn; P.Haasen; E.J.Kramer Materials Science and Technology: a comprehensive treatment; *VCH*, 1992; Vol. 2A.

(32) Nanakoudis, A. EDX Analysis with a Scanning Electron Microscope (SEM): How Does it Work? https://blog.phenom-world.com/edx-analysis-sem (accessed Apr 29,

2020).

(33) Scrivener, K. Backscattered Electron Imaging Of Cementitious Microstructures: Understanding And Quantification. *Cement and Concrete Composites* 2004, 26, 935-945.

(34) Skoog, D. A. Principles of instrumental analysis, *Thomson Brooks/Cole,* 2007

(35) Zimmermann, J.; Zeug, A.; Röder, B. A Generalization Of The Jablonski Diagram To Account For Polarization And Anisotropy Effects In Time-Resolved Experiments. *Phys. Chem. Chem. Phys.* 2003, 5, 2964-2969.

(36) Beer, A. Determination of the absorption of red light in colored liquids. *Annalen der Physik* 1852, *86,* 78-88.

(37) Sivasankar, B. Engineering Chemistry; *Tata McGraw-Hill Publishing Company Limited: New Delhi,* 2008.

(38) Haiss, W.; Thanh, N.; Aveyard, J.; Fernig, D. Determination Of Size And Concentration Of Gold Nanoparticles From UV−Vis Spectra. *Analytical Chemistry* 2007, 79, 4215-4221.

(39) J. C. Vickerman and I. S. Gilmore edithors, Surface Analysis – The Principal Techniques, 2nd Edition, Manchester Interdisciplinary Biocentre, University of Manchester, UK Ian S. Gilmore National Physical Laboratory, Teddington, UK.

Chapter 3: Electrochemical Synthesis of Ag Nanoparticles and their Morphology-Dependent Performance in Catalysing Hydrogen Evolution Reactions

3.1 Introduction

Studies on nanoparticles have become of interest because of their distinct physical and chemical properties that are very different from those of macromolecules and extended solids[1-2]. The applications are wide-ranging and include fields such as surface-enhanced Raman scattering (SERS), bioremediation and wastewater treatments, antimicrobial applications, biosensing and drug delivery [3-8]. One of the original and most important applications of nanoparticles is in the field of heterogeneous catalysis. Here, the advantages offered include high surface area, which ensures efficient utilisation of the material in question, and electronic and structural atomic properties modified from those of the bulk material, which provide enhancements in catalytic performance. [9-11]

Pt is probably the most important nanomaterial in this area on account of the unprecedented levels of performance in conventional heterogenous catalytic applications in areas such as hydrocarbon reforming[12-14]. More recently, the electrocatalytic applications of Pt nanoparticles have attracted attention in fields such as fuel cells and water splitting on account of the high levels of activity offered in redox processes such as the oxygen reduction reaction (ORR) and hydrogen evolution reaction (HER) [15-18]. However, a well-recognised problem with the use of Pt is its high economic cost, which has led to considerable research efforts to investigate the performance of cheaper

materials. One approach has been to explore Pt alloys, including Pt-Ni[19], Pt-Au[20], and Pt-Cu[21]. Alternatively, materials completely free of Pt have been examined. For example, the hydrogen evolution reaction has attracted great interest for the splitting of water to hydrogen for use as an energy carrier, leading to the development of materials such as nanostructured MoS_2[22] and Ni_2P[23] to replace Pt in this application. However, whilst these materials may offer high levels of performance, the chemical conditions for their synthesis are unsuitable for a wide range of deployment in practical applications.

Ag is approximately 40 times cheaper than Pt, and Ag nanoparticle catalysts have long been used in heterogeneous catalysis, for example the epoxidation of ethene. More recently, Ag nanoparticles have been commonly used in the biomedical field due to their antibacterial and anticancer activities[24-25] and electrochemical applications in areas such as supercapacitors, metal ion detection, and biochemical sensing have also emerged.[26-31] Studies of the ORR using Ag nanoparticles showed that Ag is also quite capable of electrocatalysis and is potentially a less expensive yet efficient alternative for Pt [32-33]. Traditional top-down methods of synthesis of Ag nanoparticles have been used, such as mechanical milling and laser ablation, alongside chemical reduction methods; for example, $AgNO_3$ can be used as the source of Ag, in conjunction with reductants such as hydrazine or $NaBH_4$. However, many of these latter preparation methods use chemicals that are extremely hazardous to the environment. Electrochemistry is an alternative method to reduce chemicals on the electrode surface in an environmentally benign and sustainable approach. The method is rapid and requires relatively simple instrumentation. A feature of Ag nanoparticles is the wide range of structures and morphologies which

these species can display. Different morphologies have been reported in the literature, including nanocubes[34], nanowires[35], and nanospheres[36], though there have been few detailed studies on how conditions can be systematically varied to control the morphology and chemical reactivity. In the present work, we therefore present systematic studies of the electrochemical deposition of Ag nanoparticles to understand how reaction conditions can be changed to alter the structures of the nanoparticles obtained. The hydrogen evolution reaction is employed as an exemplar of how the particle structure influences the observed electrocatalytic particles, following previous reports concerning the activity of Ag nanoparticles in this area. In particular, we report how three differing particle morphologies can be obtained by switching the electrochemical deposition conditions and identify which of these structures provides optimal activity with regard to the HER. The experiments are carried out on diamond electrodes as a dimensionally stable carbon-based electrode material for support of the deposited nanoparticles.

3.2 Aim of This Chapter

We fabricated Ag nanoparticle modified-BDDEs with three types of nanostructures (polyhedral-pAgNP; dendritic-dAgNP; and spherical-sAgNP) under controlled electrochemical deposition. Different parameters, including deposition potential, deposition time, and steps of deposition, were varied in order to study their effects on the Ag's nanostructure. The distinct morphologies were confirmed using SEM, and the surface composition was studied via XPS. The catalysis of the HER was performed using linear sweep voltammetry in acidic conditions. The best Ag-BDDE was selected according to its large current responses at designated voltages, and the correlation

between its performance in the HER and structures was drawn.

3.3. Results and Discussion

3.3.1 Electrodeposition of Ag nanoparticles

Initial experiments were performed to prepare Ag nanoparticle decorated BDDE's using different deposition protocols to investigate the range of structures which can be formed. The electrodeposition of Ag nanoparticles on BDDE was performed using a standard, three-electrode setup described in chapter 2, using an Ag/AgCl reference electrode (1M KCl) and a Pt counter electrode, and all potentials quoted are referred to the Ag/AgCl electrode (1M KCl). The BDDE was cleaned before each modification using HNO_3 (0.1 M) at an anodic potential of 2.5 V for 50 s, which made the electrodes O-terminated and therefore likely to be more favourable for metal deposition (proven using XPS in the following section). The source of silver used was $AgNO_3$ (20 mM solution in DI water) and the electrolyte was sodium acetate/acetic acid buffer (pH=4.6).

In one series of experiments, electrodeposition was carried out with the potential being held at -0.1 V for 50 s. As observed below by SEM, the particles formed had a polyhedral appearance, and samples formed in this approach are denoted pAg-BDDE, referring to this polyhedral form.

By using a more negative electrode potential of -0.5 V and increasing the deposition time to 100 s, the form of the Ag deposits switched to a dendritic form denoted as dAg-BDDE.

A more spherical amorphous form of deposit was prepared under a two-step electrodeposition scheme, by first applying -0.2 V for 2 s, and then increasing the

potential immediately to 0 V for 30 s, offering different parameters for nucleation and growth. Electrodes prepared with this approach are denoted sAg-BDDE.

An alternative approach to electrodeposition is coating using preformed colloidal nanoparticles. In order to compare this method to electrodeposition, colloidal AgNPs were therefore synthesized via in-situ reduction using $NaBH_4$ as described previously[37]. $NaBH_4$ was weighed and added with stirring into iced 30 mL DI water to make 2 mM solution. Then 2 mL 1 mM $AgNO_3$ was slowly added to the $NaBH_4$ solution. The formation of a yellow colloidal AgNP solution was observed. Drop coating of this solution using a volumetric pipette onto the diamond electrode was then carried out using quantities calculated to produce surface concentrations of Ag nanoparticles roughly the same as those for electrodeposition as calculated by coulometry.

SEM images of the differing electrodeposits are shown in Figure 3.1

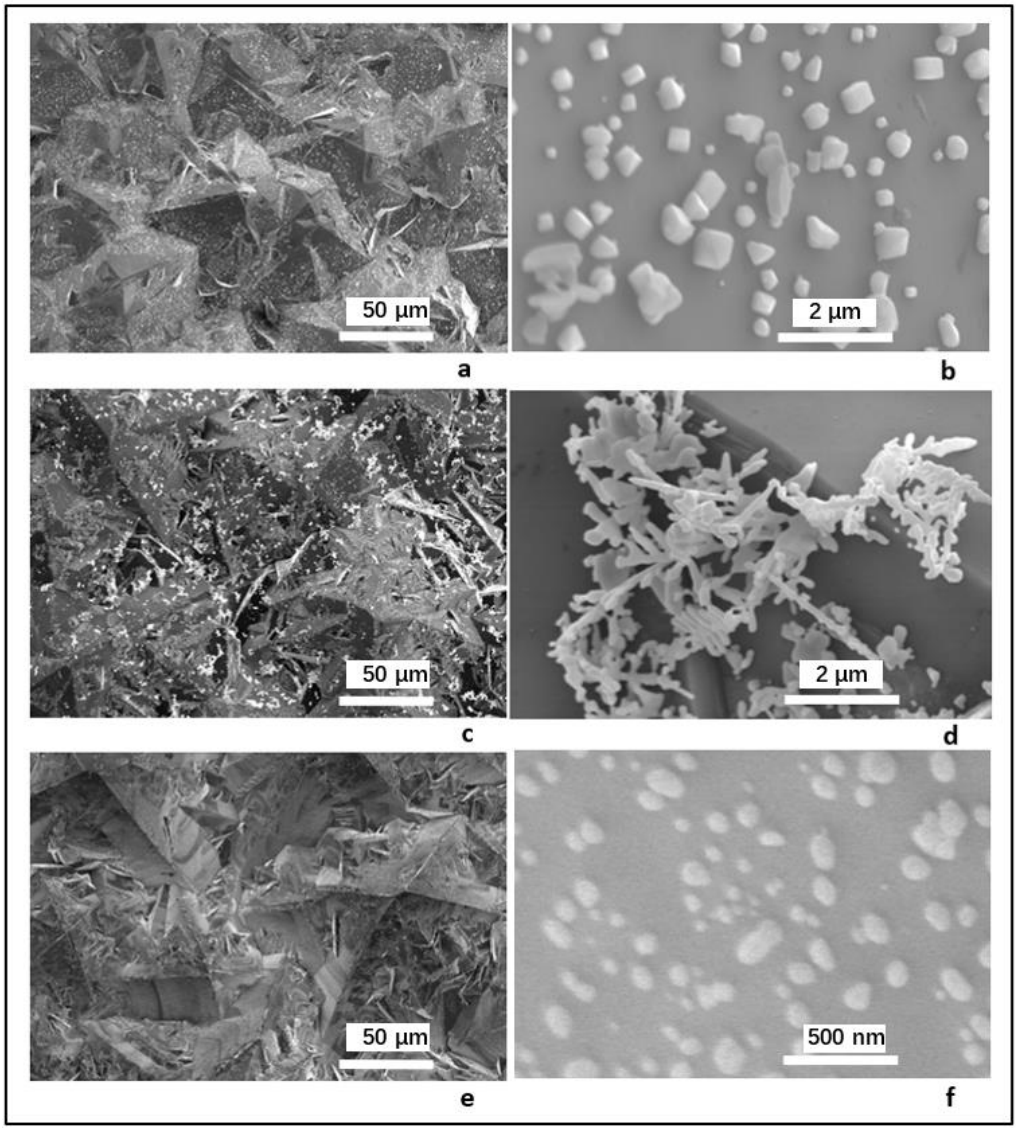

Figure 3.1: SEM images of Ag-BDDEs. Polyhedral (a and b), dendritic (c and d), and spherical (e and f) silver nanoparticles. Low resolution images with ×500 magnification (a, c, and e) are shown to observe overall coverage, and high resolution images with ×15k (b and d) and ×60k (f) magnifications are shown to illustrate morphologies and enable measurement of particle size.

It is clear from the images recorded that the form of the Ag deposited depends critically on the deposition conditions employed. Variations in morphology with deposition conditions are shown in more detail in Figure 3.2. With regard to potential, at low negative potentials, pAgNPs are formed, and a potential of -0.1 V gives reasonably exclusively pAgNPs. When the potential was more negative, the shape of AgNPs changes

gradually with mixtures of pAg and dAg, indicating low energy barriers between the two morphologies. Uniform dAgNPs were not formed until -0.5 V. The branches of the dAgNPs are enhanced when deposition time was elongated. It is obvious to see that, dendritic silver can only be formed when a very strong electrochemical driving force is used.

The effect of deposition potential on AgNP nanostructure was studied in detail by Fukui *et al.* on GC electrodes where similar trends to that seen here were observed within a range from -0.25 V to -1.6 V with a gradual shape change from polyspherical to dendrites occurring. [38] Similarly, Sivasubramanian et al. verified a change from porous polygons to dendrites when the potential changed from -0.1 V to -0.5 V, carried out from a solution of 0.1 M KNO_3 and 10 mM $AgNO_3$.[39] The observations therefore appear quite general.

When negative potentials are applied to the electrode, cations in solution move through the electrode double layer at the electrode:electrolyte interface and undergo reduction at surface sites on the modified electrode surface. For an instantaneous nucleation mechanism, which seems to be observed here, this results in the formation of nuclei on the electrode surface at the start of the deposition experiment, which undergo enlargement as the experiment is continued. Close to the equilibrium of NP formation, the distribution of nucleation sites is comparatively uniform on the surface and the strength of the electrostatic interactions (dictated by the applied potential) is not enough to overcome the intrinsic randomness in diffusion. Thus, the particles grow more or less uniformly in all dimensions resulting in the formation of compact nanoparticles on the electrode. It is interesting to note that the particles grown at a constant small negative potential have a

polyhedral appearance suggestive of a crystalline structure whereas those nucleated at more negative potential look amorphous, even when the potential is then switched more positive for growth. This most likely stems from the structure of the nuclei formed at the differing potentials since the growth phase in the stepped potential approach is more likely to favour crystalline deposits. When the potential is increased much more negatively, nucleation and growth happen fast with little uniformity and is governed by kinetics, with dendrites forming as a result of preferred directions of crystal growth. Increasing the duration time of growth in this dendritic growth simply increases the size of the initially formed dendrites rather than increasing the number and spatial uniformity of the dendritic formations. Hence the features of growth observed in these experiments can be rationalised.[39-40]

A noted feature of the growth of pAg is illustrated in Figure 3.3 which shows that the size heterogeneity of the deposited particles increases with growth time. This appears to result from an increase in the number of nuclei on the diamond surface suggesting that the nucleation mechanism is not perfectly instantaneous. However, it has been pointed out previously by Liu *et al.* [41] that a growth coupling from the overlap of the growth diffusion layers of individual nanoparticles takes place increasing the size polydispersity. To minimize this coupling effect in 1-step deposition, the deposition time must be very short to obtain size uniformity in constant (as opposed to stepped) potential deposition.

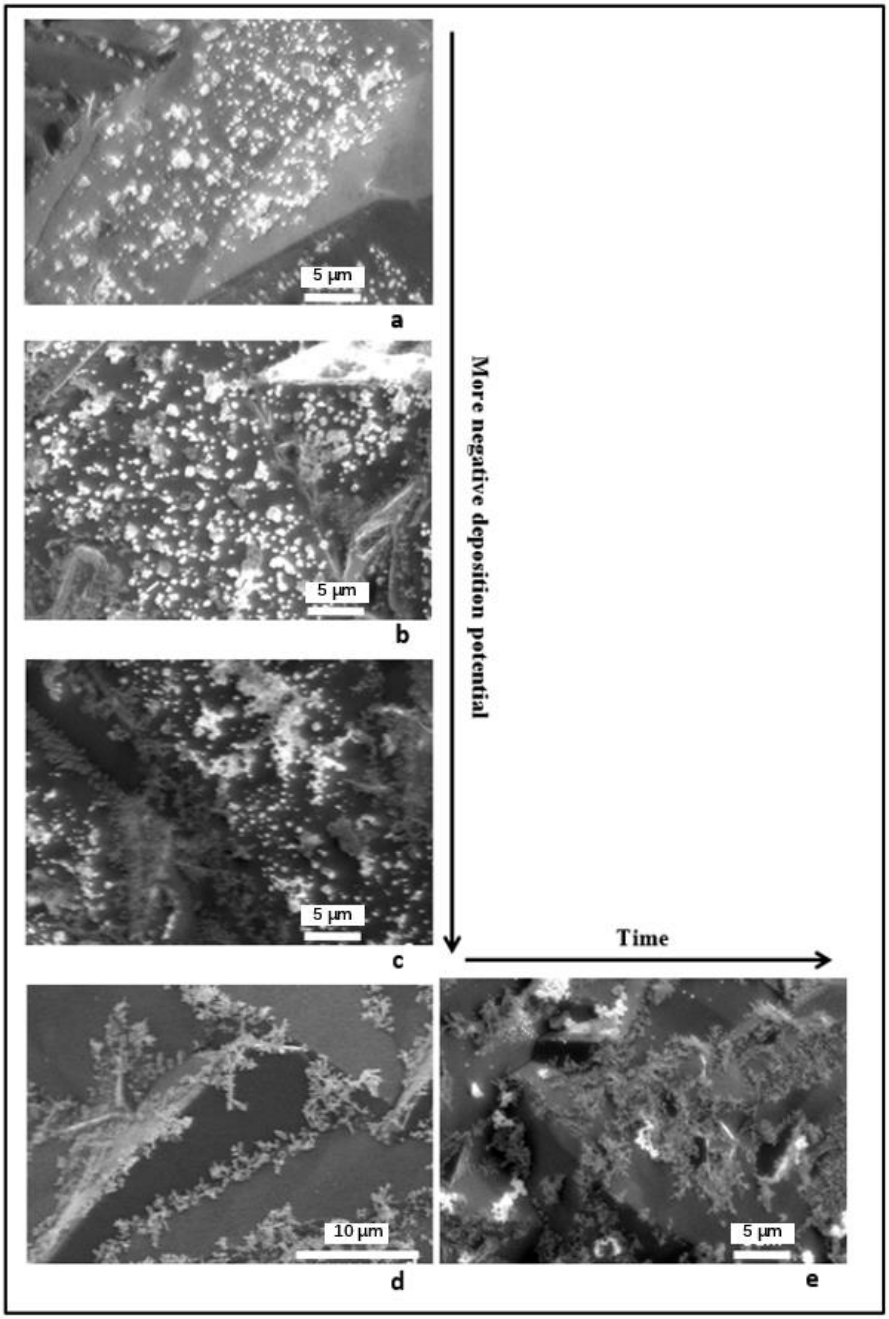

Figure 3.2 Effect of 1-step electrodeposition potential on Ag nanostructures. a: -0.1 V 50 s; b: -0.2 V 50 s; c: -0.4 V 50 s; d:-0.5 V 50 s; e: -0.5 V 100 s.

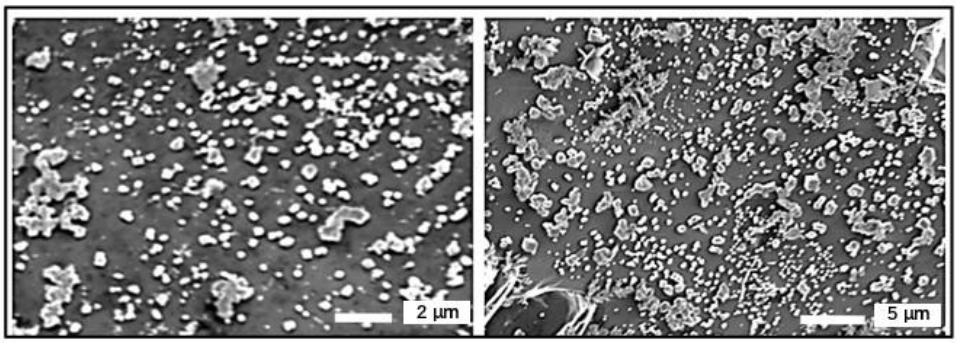

Figure 3.3 pAgNPs deposited at -0.1 V for longer time (left: 100 s, right: 150 s).

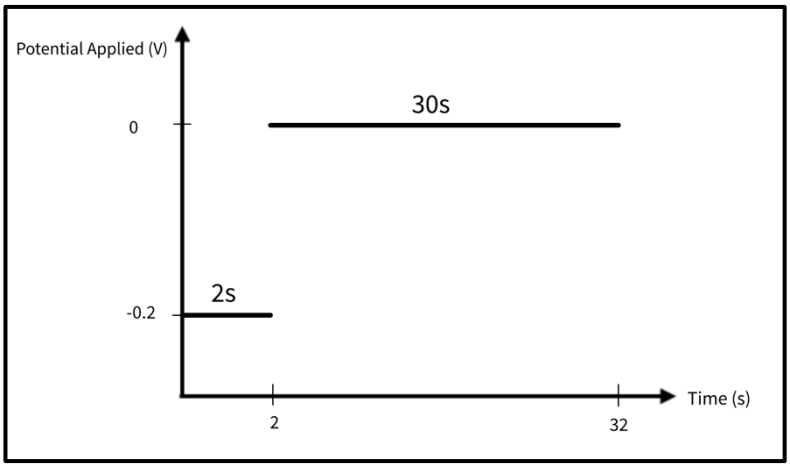

Figure 3.4 Plot of potential applied vs. time for two-step electrodeposition.

The nucleation of two-step electrodeposition only occurs within the first pulse and the second pulse is purely for particle growth. By setting these two steps apart, it is a useful tool to control the size, density and mono-dispersity by modelling the pulse parameters (i.e., the nucleation potential (E_1), nucleation time (t_1), the growth potential (E_2) and growth time (t_2)). In this case, E_1 generates nanoparticles of different sizes, and after the potential is switched to E_2, a "cutting effect" is seen which filters out the unstable nuclei with extremely small sizes. Compared to Liu *et al.*'s conditions, which can only obtain particles within a narrow range of sizes at short growth times, the two-step procedure can be more flexible by controlling each step and parameter separately. With two-step electrodeposition, nanoparticles with various size ranges and average radii can be obtained. [42]

To verify this proposed mechanism, we controlled E_1, t_1, and E_2 and only changed t_2 from 15 s, 30 s to 120 s. If the nucleation only occurred in the first step, the absolute number density of silver nanoparticles observed for these three cases should be comparable, with only size differences being seen. The expected phenomenon is observed, and the relevant

SEM pictures are shown in Figure 3.5. The absolute numbers of nucleation spots were comparable. However, the sizes of nanoparticles were different increasing with growth time t_2. This is consistent with the proposed mechanism which specified the first step to be the only nucleation step.

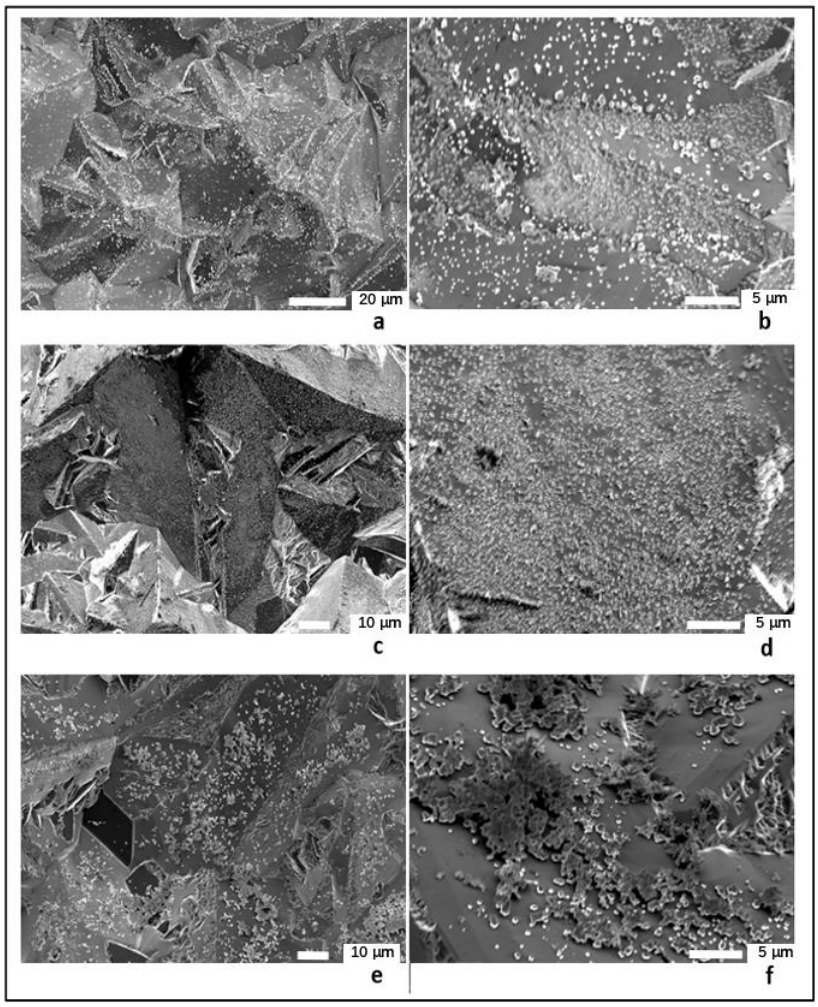

Figure 3.5 sAgNPs deposited via 2-step scheme. E_1=-0.2 V, t_1=2 s, E_2=0 V, t_2=15 s (a,b); 30 s (c,d); and 120 s (e,f).

t_2=30s was finally used as the optimal deposition condition for sAgNPs, since it gave highly covered BDDE surfaces with good uniformity, with only small size variations among individual nanoparticles.

The sizes and coverages of electrodeposited AgNPs on BDDEs were compared with drop-coated colloidal Ag-BDDE. The conditions described above resulted in the formation of

AgNPs with a sharp plasmonic peak in UV-Vis spectoscopy as shown in Figure 3.6 left. Since the size of colloidal nanoparticles are relevant to the peak position, we were able to estimate the approximate size of AgNPs from the figure inserted in Figure 3.6 left[55], and the nanoparticles with average diameter ~10 nm were synthesized in this study. SEM after drop coating the colloid using a volumetric pipette onto the diamond surface at a surface loading of 0.58ug/cm^2, roughly comparable to that of the electrochemically deposited material, is shown in Figure 3.6B. The surface coverage of Ag seems quite low in this micrograph and furthermore large aggregates of Ag are observable.

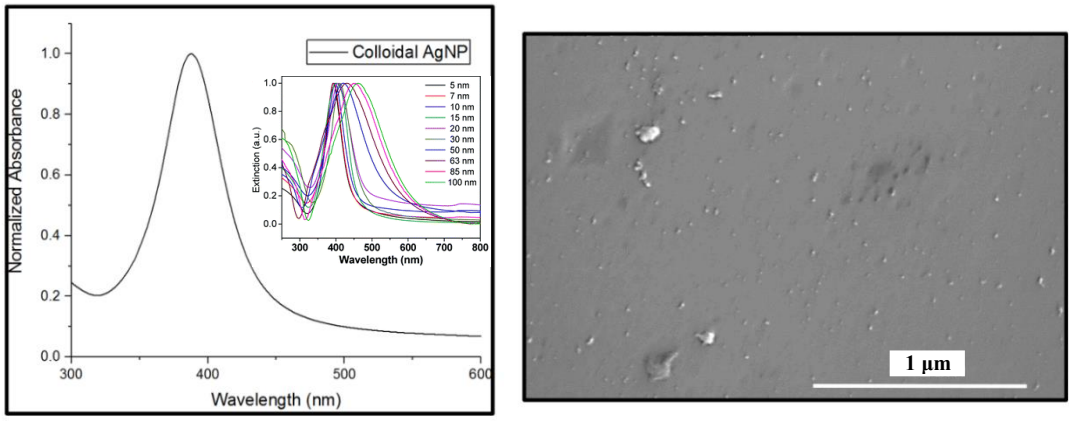

Figure 3.6 UV-Vis Spectrum (peak at 387nm) (left, insert: UV-Vis spectra of colloidal AgNPs with different sizes, synthesized through the same method reported in this chapter, adapted from [55]), and SEM image of colloidal AgNPs (right).

3.3.2 Surface Analysis

XPS was performed to probe possible surface compositional changes arising from the different approaches to depositing Ag on the diamond electrode surface. Overall elemental compositions are presented in Table 3.1, and the chemical compositions

associated with deposited Ag are shown in Table 3.2. Spectral positions were calibrated with respect to the C 1s peak and Ag peaks were fitted with literature parameters.[51]

Table 3.1 Overall elemental composition of Ag-BDDEs with different morphologies and compared with results got from drop coating colloidal AgNPs.

	% of Carbon	% of Oxygen	O:C ratio	% of Ag	% of others
Clean	88.9	10.4	0.1	0.1	Cl: 0.2;Si: 0.4
pAg	81.9	9.3	0.1	7.2	Cl: 1.7
dAg	77.7	13.6	0.2	6.5	Si: 2.1
sAg	81.0	10.1	0.1	8.9	/
Col. Ag	70.3	22.4	0.3	1.2	N:0.9; Na:5.2

+: Numbers in %.

Table 3.2 Compositional analysis of Ag peaks and comparison with drop-coated Ag-BDDE.

	Ag(0)%	Ag(I) %	Ag (III) %	Ag (III) sat. %	Pure Ag(0)%* %	A.P+
pAgNP	66.4	16.8	7.6	9.2	4.8	719.7
dAgNP	87.5	6.3	2.8	3.5	5.4	720.0
sAgNP	96.6	1.7	0.8	0.9	8.5	720.0
Col. Ag	96.9	1.6	0.7	0.9	1.2	720.1

*: Pure Ag (0) % is calculated by Ag (0) % times %of Ag in Table 1.
+: means auger parameter, as defined in the previous chapter.

In Table 3.1, the nominally clean diamond electrode shows an O concentration of about

10% typically expected of a diamond electrode completely terminated in O, given that the XPS sampling in diamond is of the order of 10 C monolayers. A small amount of Ag is seen since the electrode had previously been used for Ag deposition, suggesting the cleaning process employed subsequently was not 100% efficient. As expected from the SEM data the Ag coverage is roughly comparable for the electrochemically deposited electrodes. In contrast the colloidal Ag electrodes have an almost order of magnitude lower coverage despite the fact that the nominal loading was the same as for electrochemical deposition. There is likely to be two explanations for this difference. Firstly, SEM data showed strong nanoparticle aggregation. Secondly it appears likley that Ag has been lost from the surface prior to analysis, since the colloidal nanoparticles were drop-coated onto the electrode and the electrodeposited ones were synthesised onto the electrode with a negative overpotential, suggesting a weaker interaction between colloidal nanoparticles and BDDE. However, significant percentage of impurities have been found in many samples, probably oriented from the reusing of old electrodes.

Interestingly several different oxidation states of Ag can be discerned from the XPS spectra shown in Figure 3.7 for the differing electrodes. The Auger parameters of the differing surfaces was also calculated to aid spectral interpretation. It was clear that pure silver was obtained predominantly for the electrodes dAgNP, sAgNP and col Ag. In contrast pAg-BDDE has least pure Ag, with 1/3 of oxide impurities, as illustrated by the presence of satellite peaks associated with Ag (I) and Ag (III) oxidation peaks. The measured spectrum for pAg-BDDE was fitted according to AgO literature spectrum[43], and the other three spectra were fitted according to pure silver with mixture of oxide

impurities.[43-44] The relative compositions of Ag (0) , Ag (I) and Ag (III) oxidation states thereby calculated are shown in Table II. Ag (I) and Ag(III) are known to arise from AgO, and although the ratio of Ag (I) and Ag (III) was expected to be 1:1 (and there is no Ag (II)), the oxidation with air will transfer some Ag (III) to Ag (I), thus changing this ratio.[45] The composition of covalent Ag peaks can be directly referred to their different deposition methods. With a less negative deposition potential as for pAg, Ag ions in the solution are not fully reduced to metal Ag (0); some of them formed AgO.

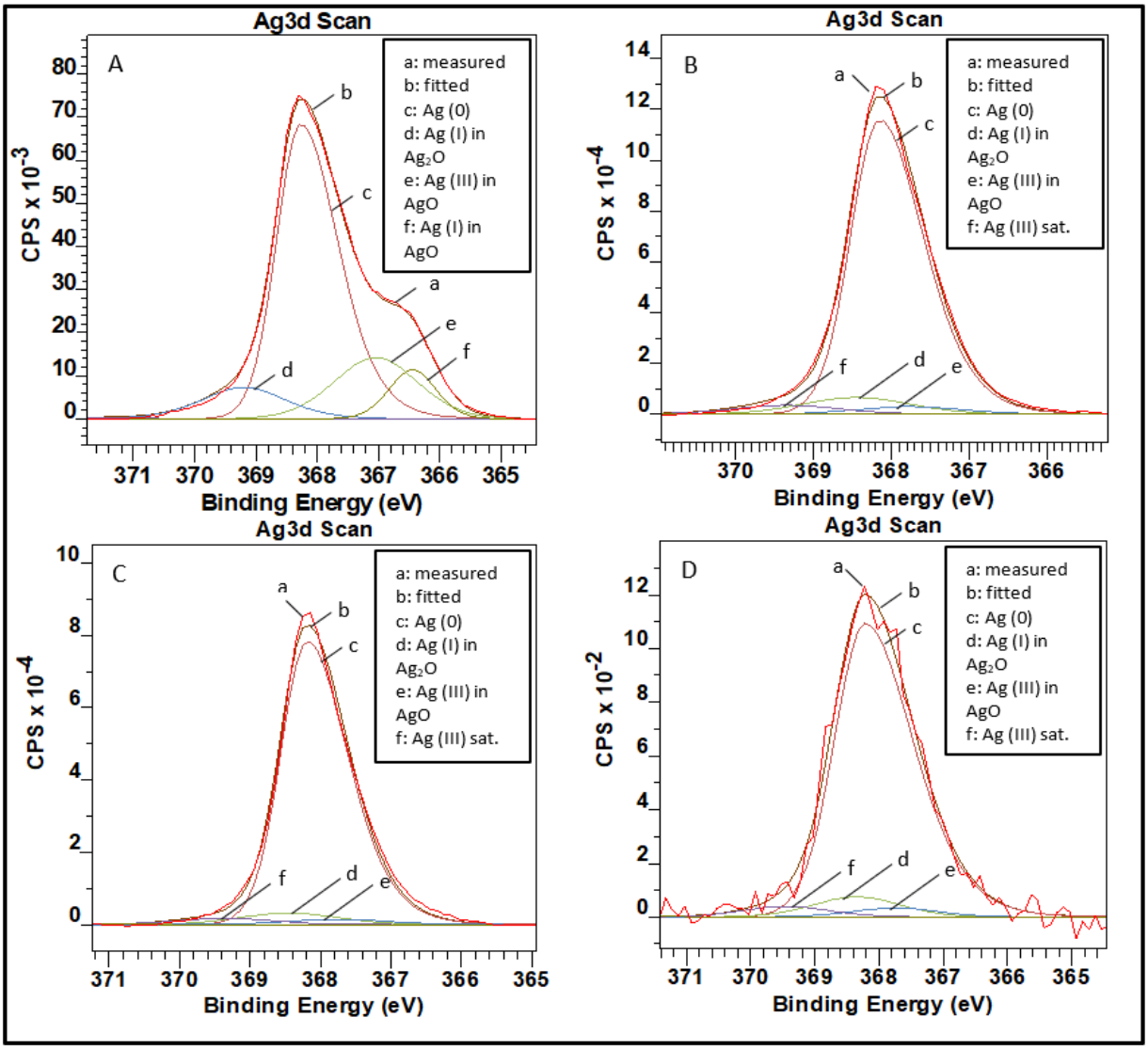

Figure 3.7 Peak fittings for XPS Ag $3d^{5/2}$ regions of pAg-BDDE (A); dAg-BDDE (B); sAg-BDDE(C); and col. Ag-BDDE (D).

Purer Ag can be formed at a more negative deposition potential, as observed for dAg, sAg has the highest percentage of pure silver, which can be attributed to the two-step mechanism. At -0.2 V, nucleation happened, seeds of Ag (0) and some AgO formed. However, when the potential was switched to 0 V, some naturally unstable particles were filtered out. The stability is dependant upon the connectivity between the particles themselves and the electrode surface. Therefore, the outliers with extreme sizes and AgO, which is not a stable species on an oxygen-terminated surface, were filtered out. Although the second step was preceded at a less negative potential, no more nucleation happened, and the purity of Ag nanoparticles was able to be maintained.

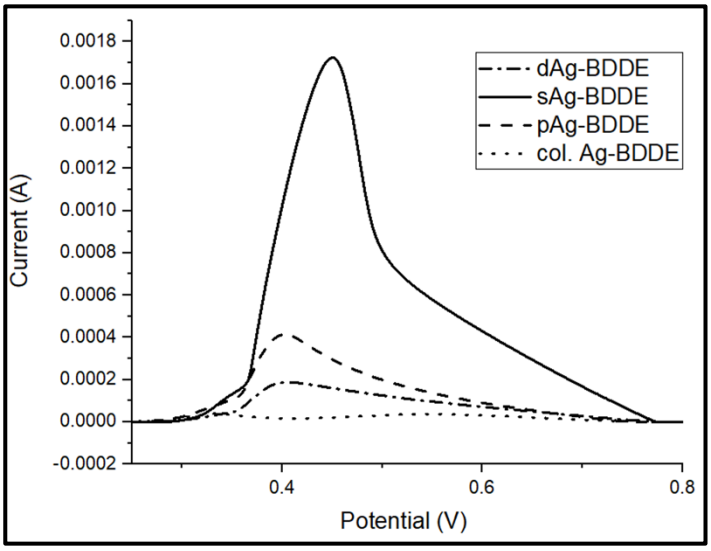

Figure 3.8 Active silver on different BDDEs examined via stripping voltammetry, signals normalised.

Stripping voltammetry was also used to determine the amount of Ag on the surface as shown in Figure 3.8. The lowest amount of active silver (the amount of silver that is able to stripp off and potentially availble for reaction single at oxidation in this potential range) is obtained from the drop-coating of colloidal Ag nanoparticles, which is consistent with the low amount observed from XPS as discussed above. Although the amount of silver

obtained from XPS was similar for the electrodeposited Ag nanoparticles, the stripping voltammetry showed a different phenomenon: sAg and pAg had higher active Ag than that of dAg (Figure 3.8). To be specific, the amount of active Ag on sAg-BDDE was 6.5-foldthat of dAg-BDDE. SEM was done before and after stripping to investigate the amount of Ag covered (Figure 3.9). It was obvious that the sAg and pAg surface had almost no Ag coverage post stripping, on the other hand, a large amount of aggregated dAg still remained. This explained the disagreement between XPS and stripping voltammetry.

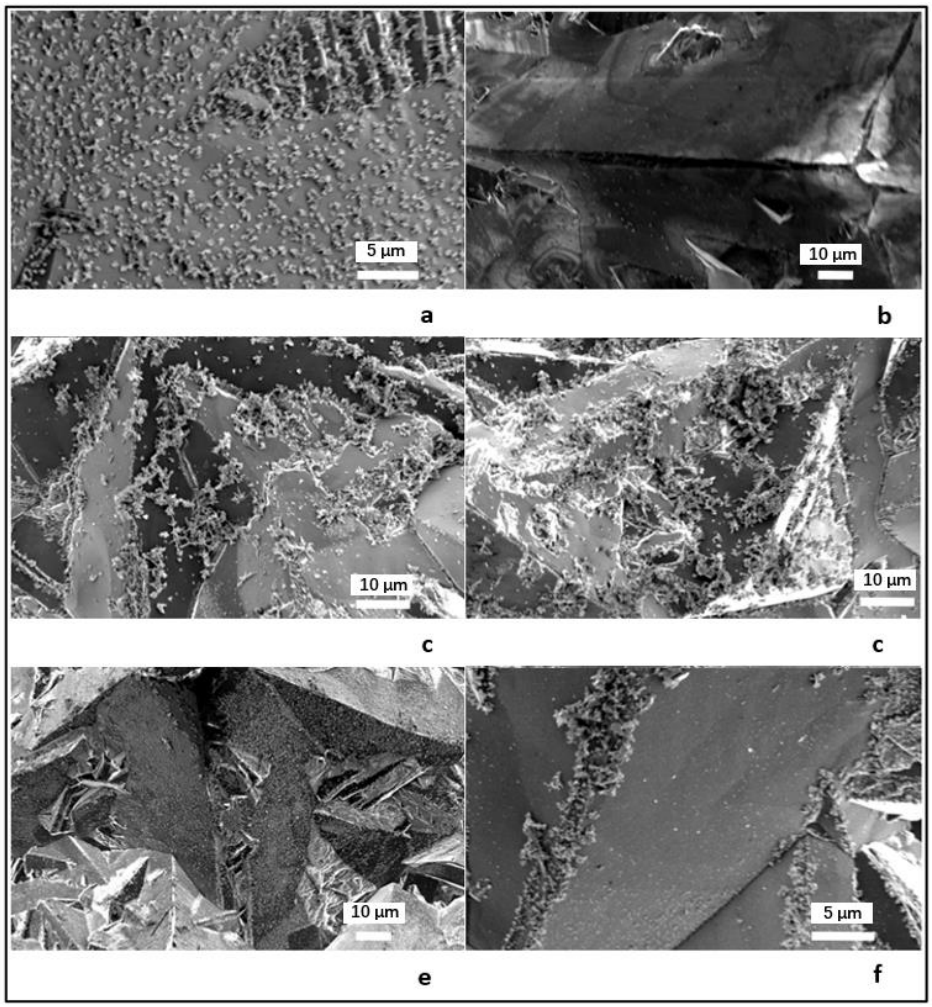

Figure 3.9 SEM images of AgBDDEs obtained pre (a, c, e) and post (b, d, f) stripping voltammetry. pAg: a, b; dAg: c, d; and sAg: e, f.

3.3.3 Catalysis of the HER

The activity of the silver treated electrodes with regard to the hydrogen evolution reaction was determined in 0.5 M sulfuric acid to compare the electrocatalytic activity of the differing forms of Ag. Experiments were performed by scanning the potential at a scan rate of 20 mV/s from an initial potential of 0 V vs SCE and measuring the current density as a function of the applied potential. The plots were independent of the scan rate in the regime employed.

Tafel analysis in which the potential is plotted against the log of the current densityis is a valuable method to demonstrate the specific mechanism in the HER reactions, which is characterized often by two paths depending on pH: (a) hydronium ion reduction,

$$2H_3O^+ + 2e^- \rightarrow H_2 + 2H_2O$$

and (b) water reduction,

$$2H_2O + 2e^- \rightarrow H_2 + 2OH^-$$

For the HER in acidic conditions, the hydronium ion reduction can take place under different pathways. The so-called Volmer step

$$H_3O^+ + e^- + M \rightarrow M - H + 2H_2O$$

takes place after which two further steps are possible

$$H_3O^+ + M - H + e^- \rightarrow H_2 + 2H_2O + M \text{ (Heyrovsky step)}$$

$$2M - H \rightarrow H_2 + 2M \text{ (Tafel step)}$$

The overall reaction schemes are denoted as Volmer-Heyrovsky and Volmer-Tafel routes. Tafel analysis for Ag-BDDEs with different morphologies is summarized in Table 3.3, including their onset potential, Tafel Slopes (averaged through 3 trails), and current

responses at designated potentials (-1.0 V for J_1 and -0.8 V for J_2, and averaged through 3 trails). The current responses with respect to different potentials applied and Tafel plots are presented in Figure 3.10 and 11, respectively.

Table 3.3 Tafel analysis for different morphologies and compared with col. Ag

	% of surface Ag(0)	**Tafel Slope (mV/dec)**	**J_1 (mA/cm2)**	**J_2 (mA/cm2)**
Blank	/	268±5	4±0.5	1±0.5
pAgNP	4.8	114±15	15±1	7±0.8
dAgNP	5.4	127±25	7±2	2±0.5
sAgNP	8.5	112±10	17±0.5	11±0.5
Col.Ag	1.2	194±20	11±2	4±1

In Tafel analysis, the most important parameter to look at is the Tafel slope (explained in chapter 2), which illustrates not only the sensitivity of current response to certain applied potentials but also give us insight into the specific routes that the reaction happened under. When the Tafel slope is larger than 120 mV/dec, it means that the Volmer step is the rate-determining step, which is the case for dAg-BDDE. On the other hand, when the Tafel slope is between 40 mV/dec to 120 mV/dec, the Heyrovsky step is the rate-determining step for the whole reaction, which are the cases for both pAg and sAg BDDEs. The differences in mechanisms must relate to AgNP morphological differences. In the case of dAg, the large surface energy on the branched surfaces made it hard to adsorb H (ads)

and form M-H bonds compared with pAgNPs and sAgNPs, causing the Volmer step to be the rate determining step.[46]

An ideal catalyst for the HER, or catalyst for other chemical fuel reactions, should have virtues including nanostructure that can maximize the number of exposed active sites and can facilitate the transport of reactants and products.[47] Therefore, when we use the same material to fabricate catalysts, the shape and size of the material itself are very important, and should be designed in a way that favours the reaction under investigation. Mass transport effects are also important. A macro electrode will only perform planar diffusion, however the electrodes coated with nanoparticles can benefit from convergent diffusion, which is far more effective than the planar one. However, when the coverage of nanoparticles is too high, the diffusional planes will couple together, thus the whole electrode will behave again like a macro electrode that is not covered with nanoparticles. In this experiment, however, the large Tafel slope and weak current response of pAgNP-BDDE might also come from the impurities in elemental silver. From the last section, we discussed that pAgNP has more than 40% of AgO. Although AgO can also be used as a catalyst, it is not as efficient as elemental Ag. [48]

dAgNP has potential to be a very good catalyst, because it has largest surface area. However, a problem was its catalytic activity was different to obtain reproducibly; for example, the Tafel slopes were found to routinely vary with the largest standard deviation. sAgNP-BDDE seemed the electrode with highest amount of silver nanoparticles plated, as well as a stable range of Tafel slope with a smaller standard deviation. The current responses at designated potentials were the highest. This could be explained by its well-

spread even coverage, as well as its small particle sizes.

Table 3.4 Statistics for stability test. Moles of Ag nanoparticles was calculated from the stripping voltammetries before and after chrono

	Before/nmol	After/nmol	%Maintained
dAgNP	4.10	2.04	49.8%
pAgNP	6.94	0.29	4.16%
sAgNP	26.7	5.62	21.0%
col. Ag	1.29	0.54	41.9%

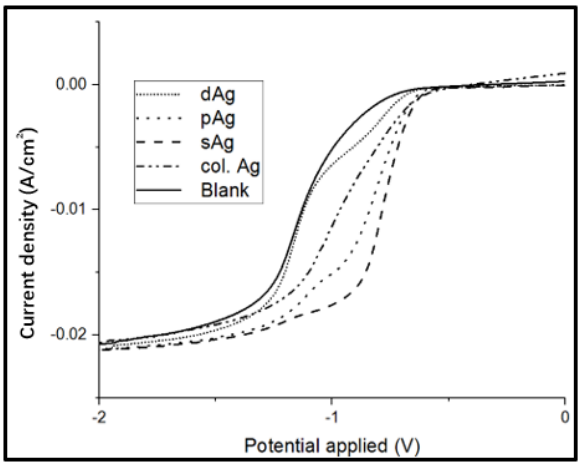

Figure 3.10 Current density responses of different AgNPs

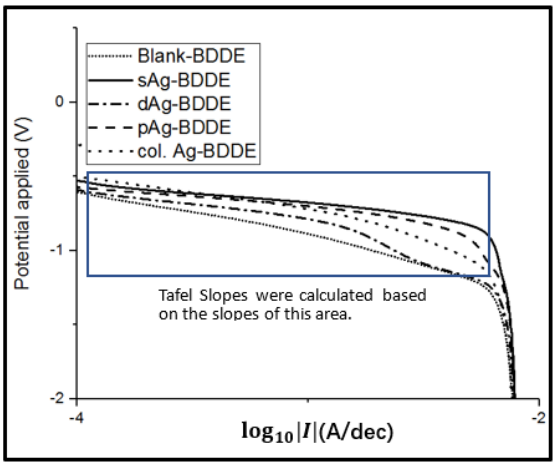

Figure 3.11 Tafel Plots of different AgNPs

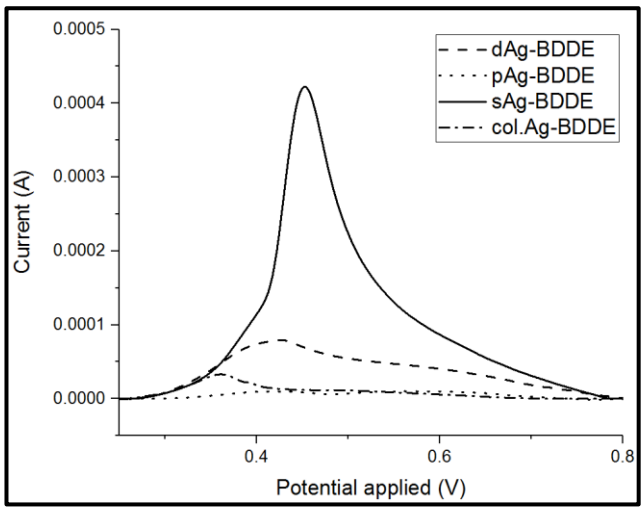

Figure 3.75 Stripping CV after stability test

The procedure of stability test was to hold the electrodes at a given potential, and the signal for each is recorded for 1h, after which the stripping CV was done for each electrode. The basic purpose was to detect how much Ag remained following 1h chrono, at a constant potential of -0.8 V in 0.5 M sulfuric acid,and compare this to the amount of silver obtained from the first previous voltammogram (Figure 3.12).

sAgNP-BDDE maintained the highest absolute amount of silver after chronoamperometry, and dAgNP-BDDE had largest percentage of silver remained, possibly because the aggregated AgNPs were not easy to remove under stripping voltammetry. This has also been observed in the case of col. Ag-BDDE, which had aggregation problems and retained a large percentage of Ag after the stability test. pAgNP-BDDE had almost no silver left after stripping; it was confirmed by SEM afterwards. This was because the composition of pAgNP-BDDE has a large proportion of AgO, which has weak interaction with the O-terminated BDDE surface and was not able to adhere under long-time chronoamperometry.

3.4 Conclusion

Ag nanoparticle modified BDDE devices have potential applications in electrocatalysis as more economic materials compared to Pt modified electrodes. In this chapter differing approaches have been employed to prepare the Ag modified electrode materials. In particular the effect of applying fixed potentials to drive deposition was compared with the results obtained when using a potential step. The results obtained were also compared with those observed by the drop coating of colloidal Ag nanoparticles on the same diamond electrode surface.

A general trend, consistent with that reported previously, with differing electrode materials and different electrolytes is seen in that the nature of the Ag deposits changes from a compact polyhedral form to a dendritic morphology as the cathodic electrochemical driving force is increased to more negative potentials. [38-39] This is ascribed to effects accompanying changes in the electrochemical double layer and a switch over from the equilibrium configurations achieved from relatively fast diffusional processes of species in the vicinity of the electrode surface, to the structures accessed by fast crystal growth at more negative potentials. Specific advantages are, however, observed by using a stepped potential electrodeposition process. By separating out the nucleation and growth steps, much more uniformly distributed nanoparticle arrays are formed on the diamond electrode and particle size can also be better controlled.

The deposits formed were subject to investigation using stripping voltammetry and XPS. Several differences were observed in the behaviour of the differing systems with regard to these experimental probes. In particular, despite the fact that the surface concentrations of Ag should have been comparatively similar with the different deposition methods, both XPS and SEM indicated that the colloidal deposits apparently had much lower Ag concentrations than the electrodeposited varieties. There are likely to be differing factors contributing to this observation, associated with a lower chemical stability for the bound colloidal forms, both against particle loss from the surface and from a tendency for particle agglomeration. A second major difference was that the amount of Ag removed by electrochemical stripping was much less for the dendritic forms of Ag compared to the compact particulates. This most likely reflects the degree of electrical communication

between the underlying electrode and the Ag deposit for the differing physical forms. Finally it was observed that differences arose in the surface chemistry of the various Ag modified electrodes – in particular the concentration of Ag (I) and Ag(III) species was much higher at the Ag modified electrode prepared at the more positive potential.

Unsurprisingly in view of these observations, differing efficiencies were observed in driving the HER reaction for the differing deposits Notably optimal results were measured for spherical Ag-NP modified BDDE with an average particle diameter of 75 nm as fabricated via a two-step electrodeposition scheme – a short nucleation step at lower potential followed by a longer growing process at a higher potential. Compared to the other two morphologies, the spherical Ag-NP modified BDDE has a very high number of active silver nanoparticles, percentage of elemental silver at the surface, stability, as well as high current response, and low Tafel slope in catalysis of the HER.

References

(1) Schmidt, E.; Kleist, W.; Krumeich, F.; Mallat, T.; Baiker, A. Platinum Nanoparticles: The Crucial Role Of Crystal Face And Colloid Stabilizer In The Diastereoselective Hydrogenation Of Cinchonidine. *Chemistry - A European Journal* 2010, 16, 2181-2192.

(2) Yacamán, M.; Ascencio, J.; Liu, H.; Gardea-Torresdey, J. Structure Shape And Stability Of Nanometric Sized Particles. *Journal of Vacuum Science & Technology B: Microelectronics and Nanometer Structures* 2001, 19, 1091.

(3) Lee, S.; Morrill, A.; Moskovits, M. Hot Spots In Silver Nanowire Bundles For Surface-Enhanced Raman Spectroscopy. *Journal of the American Chemical Society* 2006, 128, 2200-2201.

(4) Cecchin, I.; Reddy, K.; Thomé, A.; Tessaro, E.; Schnaid, F. Nanobioremediation: Integration Of Nanoparticles And Bioremediation For Sustainable Remediation Of Chlorinated Organic Contaminants In Soils. *International Biodeterioration & Biodegradation* 2017, 119, 419-428.

(5) Tungittiplakorn, W.; Cohen, C.; Lion, L. Engineered Polymeric Nanoparticles For Bioremediation Of Hydrophobic Contaminants. *Environmental Science & Technology* 2005, 39, 1354-1358.

(6) Wang, L.; Hu, C.; Shao, L. The Antimicrobial Activity Of Nanoparticles: Present Situation And Prospects For The Future. *International Journal of Nanomedicine* 2017, Volume 12, 1227-1249.

(7) Holzinger, M.; Le Goff, A.; Cosnier, S. Nanomaterials For Biosensing Applications: A Review. *Frontiers in Chemistry* 2014, 2.

(8) Kaegi, R.; Voegelin, A.; Sinnet, B.; Zuleeg, S.; Hagendorfer, H.; Burkhardt, M.; Siegrist, H. Behavior Of Metallic Silver Nanoparticles In A Pilot Wastewater Treatment Plant. *Environmental Science & Technology* 2011, 45, 3902-3908.

(9) Schauermann, S.; Nilius, N.; Shaikhutdinov, S.; Freund, H. Nanoparticles For Heterogeneous Catalysis: New Mechanistic Insights. *Accounts of Chemical Research* 2012, 46, 1673-1681.

(10) Liu, L.; Corma, A. Metal Catalysts For Heterogeneous Catalysis: From Single Atoms To Nanoclusters And Nanoparticles. *Chemical Reviews* 2018, 118, 4981-5079.

(11) Astruc, D.; Lu, F.; Aranzaes, J. Nanoparticles As Recyclable Catalysts: The Frontier Between Homogeneous And Heterogeneous Catalysis. *Angewandte Chemie International Edition* 2005, 44, 7852-7872.

(12) Alayoglu, S.; Pushkarev, V.; Musselwhite, N.; An, K.; Beaumont, S.; Somorjai, G. Reforming Of C6 Hydrocarbons Over Model Pt Nanoparticle Catalysts. *Topics in*

Catalysis 2012, 55, 723-730.

(13) Breen, J.; Burch, R.; Coleman, H. Metal-Catalysed Steam Reforming Of Ethanol In The Production Of Hydrogen For Fuel Cell Applications. *Applied Catalysis B: Environmental* 2002, 39, 65-74.

(14) Galvita, V.; Siddiqi, G.; Sun, P.; Bell, A. Ethane Dehydrogenation On Pt/Mg(Al)O And Ptsn/Mg(Al)O Catalysts. *Journal of Catalysis* 2010, 271, 209-219.

(15) Zhou, D.; Jiang, B.; Yang, R.; Hou, X.; Zheng, C. One-Step Synthesis Of Monodispersed Pt Nanoparticles Anchored On 3D Graphene Foams And Its Application For Electrocatalytic Hydrogen Evolution. *Chinese Chemical Letters* 2020, 31, 1540-1544.

(16) Sui, X.; Zhang, L.; Li, J.; Doyle-Davis, K.; Li, R.; Wang, Z.; Sun, X. Enhancing Metal–Support Interaction By In Situ Ion-Exchanging Strategy For High Performance Pt Catalysts In Hydrogen Evolution Reaction. *Journal of Materials Chemistry A* 2020, 8, 16582-16589.

(17) Garlyyev, B.; Kratzl, K.; Rück, M.; Michalička, J.; Fichtner, J.; Macak, J.; Kratky, T.; Günther, S.; Cokoja, M.; Bandarenka, A. et al. Optimizing The Size Of Platinum Nanoparticles For Enhanced Mass Activity In The Electrochemical Oxygen Reduction Reaction. *Angewandte Chemie International Edition* 2019, 58, 9596-9600.

(18) Zhang, C.; Shen, X.; Pan, Y.; Peng, Z. A Review Of Pt-Based Electrocatalysts For Oxygen Reduction Reaction. *Frontiers in Energy* 2017, 11, 268-285.

(19) Yan, Y.; Zhang, Y.; Jiang, T.; Xiao, T.; Edwards, P.; Cao, F. Glycerol Hydrogenolysis Over A Pt–Ni Bimetallic Catalyst With Hydrogen Generated In Situ. *RSC Advances* 2017, *7*, 38251-38256.

(20) Wang, L.; Zhang, J.; Wang, G.; Zhang, W.; Wang, C.; Bian, C.; Xiao, F. Selective Hydrogenolysis Of Carbon–Oxygen Bonds With Formic Acid Over A Au–Pt Alloy Catalyst. *Chemical Communications* 2017, *53*, 2681-2684.

(21) Lee, J.; Han, S.; Kwak, D.; Kim, M.; Lee, S.; Park, J.; Choi, I.; Park, H.; Park, K. Porous Cu-Rich@Cu3pt Alloy Catalyst With A Low Pt Loading For Enhanced Electrocatalytic Reactions. *Journal of Alloys and Compounds* 2017, *691*, 26-33.

(22) Li, Y.; Wang, H.; Xie, L.; Liang, Y.; Hong, G.; Dai, H. Mos2nanoparticles Grown On Graphene: An Advanced Catalyst For The Hydrogen Evolution Reaction. *Journal of the American Chemical Society* 2011, *133*, 7296-7299.

(23) Popczun, E.; McKone, J.; Read, C.; Biacchi, A.; Wiltrout, A.; Lewis, N.; Schaak, R. Nanostructured Nickel Phosphide As An Electrocatalyst For The Hydrogen Evolution Reaction. *Journal of the American Chemical Society* 2013, *135*, 9267-9270.

(24) Pal, S.; Tak, Y.; Song, J. Does The Antibacterial Activity Of Silver Nanoparticles

Depend On The Shape Of The Nanoparticle? A Study Of The Gram-Negative Bacterium Escherichia Coli. *Applied and Environmental Microbiology* 2007, *73*, 1712-1720.

(25) Zhang, X.; Liu, Z.; Shen, W.; Gurunathan, S. Silver Nanoparticles: Synthesis, Characterization, Properties, Applications, And Therapeutic Approaches. *International Journal of Molecular Sciences* 2016, *17*, 1534.

(26) Liu, H.; Wang, D.; Song, Z.; Shang, S. Preparation Of Silver Nanoparticles On Cellulose Nanocrystals And The Application In Electrochemical Detection Of DNA Hybridization. *Cellulose* 2010, 18, 67-74.

(27) Gao, N.; Gao, F.; He, S.; Zhu, Q.; Huang, J.; Tanaka, H.; Wang, Q. Graphene Oxide Directed In-Situ Deposition Of Electroactive Silver Nanoparticles And Its Electrochemical Sensing Application For DNA Analysis. *Analytica Chimica Acta* 2017, 951, 58-67.

(28) Zhou, M.; Han, L.; Deng, D.; Zhang, Z.; He, H.; Zhang, L.; Luo, L. 4-Mercaptobenzoic Acid Modified Silver Nanoparticles-Enhanced Electrochemical Sensor For Highly Sensitive Detection Of Cu^{2+}. *Sensors and Actuators B: Chemical* 2019, 291, 164-169.

(29) Goulart, L.; Gonçalves, R.; Correa, A.; Pereira, E.; Mascaro, L. Synergic Effect Of Silver Nanoparticles And Carbon Nanotubes On The Simultaneous Voltammetric Determination Of Hydroquinone, Catechol, Bisphenol A And Phenol. *Microchimica Acta* 2017, 185.

(30) Khamlich, S.; Khamliche, T.; Dhlamini, M.; Khenfouch, M.; Mothudi, B.; Maaza, M. Rapid Microwave-Assisted Growth Of Silver Nanoparticles On 3D Graphene Networks For Supercapacitor Application. *Journal of Colloid and Interface Science* 2017, 493, 130-137.

(31) Tran, L.; Tran, H.; Thi Minh Dang, H.; Huynh, C.; Mai, T. Silver Nanoparticles Decorated Polyaniline Nanowires-Based Electrochemical DNA Sensor: Two-Step Electrochemical Synthesis. *Journal of The Electrochemical Society* 2020, 167, 087508.

(32) Neumann, C.; Laborda, E.; Tschulik, K.; Ward, K.; Compton, R. Performance Of Silver Nanoparticles In The Catalysis Of The Oxygen Reduction Reaction In Neutral Media: Efficiency Limitation Due To Hydrogen Peroxide Escape. *Nano Research* 2013, *6*, 511-524.

(33) Wang, C.; deKrafft, K.; Lin, W. Pt Nanoparticles@Photoactive Metal–Organic Frameworks: Efficient Hydrogen Evolution Via Synergistic Photoexcitation And Electron Injection. *Journal of the American Chemical Society* 2012, *134*, 7211-7214.

(34) Sun, Y.; Xia, Y. Shape-Controlled Synthesis Of Gold And Silver Nanoparticles. *ChemInform* 2003, *34*.

(35) Zhang, P.; Wyman, I.; Hu, J.; Lin, S.; Zhong, Z.; Tu, Y.; Huang, Z.; Wei, Y. Silver Nanowires: Synthesis Technologies, Growth Mechanism And Multifunctional Applications. *Materials Science and Engineering: B* 2017, *223*, 1-23.

(36) Liang, H.; Wang, W.; Huang, Y.; Zhang, S.; Wei, H.; Xu, H. Controlled Synthesis Of Uniform Silver Nanospheres. *The Journal of Physical Chemistry C* 2010, *114*,

7427-7431.

(37) Song, K.; Lee, S.; Park, T.; Lee, B. Preparation Of Colloidal Silver Nanoparticles By Chemical Reduction Method. *Korean Journal of Chemical Engineering* 2009, *26*, 153-155.

(38) Fukui, R.; Katayama, Y.; Miura, T. The Influence Of Potential On Electrodeposition Of Silver And Formation Of Silver Nanoparticles In Some Ionic Liquids. *Journal of The Electrochemical Society* 2011, *158*, D567.

(39) Sivasubramanian, R.; Sangaranarayanan, M. Electrodeposition Of Silver Nanostructures: From Polygons To Dendrites. *CrystEngComm* 2013, *15*, 2052.

(40) Sivasubramanian, R.; Sangaranarayanan, M. A Facile Formation Of Silver Dendrites On Indium Tin Oxide Surfaces Using Electrodeposition And Amperometric Sensing Of Hydrazine. *Sensors and Actuators B: Chemical* 2015, *213*, 92-101.

(41) Bottari, F.; De Wael, K. Electrodeposition Of Gold Nanoparticles On Boron Doped Diamond Electrodes For The Enhanced Reduction Of Small Organic Molecules. *Journal of Electroanalytical Chemistry* 2017, *801*, 521-526.

(42) Liu, H.; Penner, R. Size-Selective Electrodeposition Of Mesoscale Metal Particles In The Uncoupled Limit. *The Journal of Physical Chemistry B* 2000, *104*, 9131-9139.

(43) Ferraria, A.; Carapeto, A.; Botelho do Rego, A. X-Ray Photoelectron Spectroscopy: Silver Salts Revisited. *Vacuum* 2012, *86*, 1988-1991.

(44) Lützenkirchen-Hecht, D. Anodic Silver Oxide (Ago) Layers By XPS. *Surface Science Spectra* 2011, *18*, 102-109.

(45) Tudela, D. Silver(II) Oxide Or Silver(I,III) Oxide?. *Journal of Chemical Education* 2008, *85*, 863.

(46) Shinagawa, T.; Garcia-Esparza, A.; Takanabe, K. Author Correction: Insight On Tafel Slopes From A Microkinetic Analysis Of Aqueous Electrocatalysis For Energy Conversion. *Scientific Reports* 2020, *10*.

(47) Jiang, P.; Liu, Q.; Ge, C.; Cui, W.; Pu, Z.; Asiri, A.; Sun, X. Cop Nanostructures With Different Morphologies: Synthesis, Characterization And A Study Of Their Electrocatalytic Performance Toward The Hydrogen Evolution Reaction. *Journal of Materials Chemistry A* 2014, *2*, 14634.

(48) Zhao, Qiang & Dong, Jinxiang & Li, Jinping. (2011). A novel silver oxides oxygen evolving catalyst for water splitting. International Journal of Hydrogen Energy. 36. 7374-7380. 10.1016/j.ijhydene.2011.03.096.

Chapter 4 Electrodeposition of AgAu nanoalloys with Distinct Morphologies and their Catalytic Activities in Hydrogen Evolution Reaction

4.1 Introduction

AuNPs have applications including cancer treatment, X-ray imaging, drug deliveries, and toxin detection. [1-3] The role of AuNPs in heterogeneous catalysis is also crucial for a wide range of transformations, such as C-C bond addition and coupling, selective oxidation, and selective hydrogenation.[4-5]

The usage and role of AuNPs in fuel cell reactions like oxygen reduction reaction (ORR) and the HER are well-investigated.[6-7] Although Au is a poor catalyst for the HER reaction theoretically due to its weak adsorption of H atoms on the catalyst surface, it is widely used as an electrode support, especially for transition metal sulfides. Au can stabilise sulfide catalysts through strong chemical interaction with the ligands which can lower the Gibbs free energy of hydrogen adsorption, and boost conductivity.[8-10] With different sizes altered and the presence of supporting materials such as carbon and metal oxides, AuNPs themselves can be used as a catalyst for fuel cell reactions as well.[11-13]

The catalytic performance in fuel cell reactions can be boosted if Au is alloyed with other metals.[14-21] The alloying effect and how it contributes to improvements in catalytic performances have been discussed in detail in chapter 2, and will not be repeated here.

When NA materials are prepared for catalysis, noble metals, normally referred to Au, Ag,

and platinum group metals (Pt, Pd, Os, Ir, Ru and Rh) which have both high stability and high catalytic activity are preferred. Noble metal alloys have many Fermi electrons, and are very capable of catalysing coupling reactions, the HER, and selective oxidations.[22-26] However, to reduce the cost, different architectures of noble metal NAs are used to increase the active surface and minimise the components used.[27-29] Other transitional metals in the fourth period, including Cu, Fe, Co, and Ni, are also widely used in synthesis of NA materials. Their alloys have advantage in industrial catalysis because of the lower cost. They are widely used in nitro-amination reactions and hydrogenolysis reactions.[30-33] When these cheap metals are alloyed with noble metals, high catalytic reactivity and low cost can both be achieved. By altering the composition, atomic efficiency and flexibility is highly improved.[34-36]

As mentioned before, the HER reaction is usually carried out under catalysis using Pt (£21/g) and Pd (£52/g) metal. By alloying cheap Ag (£0.48/g) with a small amount of costly metal Au (£45/g),[37] the performance can benefit from the alloying effect, and the overall cost for this alloy material will be a lot less than if pure Pt and Pd metals are used. Nanostructured Pd and Pt containing alloys including PtNi, PtCu, and PtNiCu are widely used for the HER with high stability and reactivity[38-40] Similarly in this chapter, we aim to alloy cheap Ag with a small amount of Au and compare its performance to pure metals. AgAu nanoalloys can be easily synthesized via electrochemical methods or chemical reductions and play active role in heterogeneous catalysis[41-44], especially in fuel cell reactions.[45-46] Here we report the synthesis of AgAu nanoalloys (NAs) and examine their catalytic performance using the HER as an example.

4.2 Aim of This Chapter

In chapter 3, we developed ways in synthesising AgNPs with distinct morphologies: polyhedral, dendritic, and spherical nanoparticles. In this chapter, we investigated different morphologies of Ag (core) Au (shell) NAs using dendritic and spherical AgNPs as core building blocks. Polyhedral AgNPs are not used in this chapter since the purity is too low, and the shapes are not well controlled compared to the other two structures. Two different types of AgAuNAs – spherical and dendritic were synthesized. The compositional analysis of the surface was investigated using XPS, and the pattern of AuNPs alloy with Ag was confirmed using Cyclic Voltammetry. Afterward, their electrocatalytic activities were examined and compared with both pure AuNPs and AgNPs. Enhanced current responses were observed for both types of NAs. The method of synthesising the most optimal AgAuNA was selected due to the enhanced performance in catalysing the HER.

4.3 Experimental Strategies

When AgAuNAs were about to fabricated for electrocatalytic applications, a more active form of NAs was desired and not the stable form. To form a stable alloy, several properties of the two metal atoms were considered. First, the core metal should have a stronger M-M bond; second, it is more stable for the smaller atom to occupy the core; moreover, the surface energy of the core atom should be smaller for a stable structure. From the theoretical computations, the M-M bond lengths of Ag-Ag and Au-Au are comparable, with Ag-Ag bond length 2.90 Å, Au-Au bond length 2.88 Å. The size of an

Au atom (atomic radii 166 pm) is smaller than that of Ag (172 pm), and the surface energy of Au-Au (97 meV $Å^{-2}$) is larger than that of Ag-Ag (78 meV $Å^{-2}$). Hence, Au (core) Ag (shell) alloy is a more stable structure, and Ag (core) Au (shell) is the more active form that we desire.[47-48] Therefore, Ag was chosen to be plated first.

4.4 Results and Discussion

4.4.1 Synthesis and Morphological Characterisation of AgAuNAs

The previous chapter showed different electrodeposition methods for synthesising AgNPs with different morphologies. Three types of AgNPs (polyhedral, dendritic, and spherical) were synthesised, and we chose dendritic and spherical AgNPs to be the "bases" for the depositions of AuNPs. As mentioned in chapter 3, the spherical AgNPs were plated on BDDEs under a two-step electrodeposition scheme, by first applying -0.2 V for 2 s, and then increasing the potential immediately to 0 V for 30 s. On the other hand, the dentritic AgNPs were deposited with a one-step chronoamperometry holding potential at -0.5 V for 100 s. Similarly, Au nanoparticles were plated either alone or on top of AgNPs in two different ways, by either holding the potential constant at -0.1 V for 150 s, or a two-step scheme -0.7V 2s and then -0.1V 150s. Different conditions of Ag deposition and Au deposition were used to investigate the structural differences that resulted. The resulting morphologies and coverages are summarized in Table 4. 1, and SEM images are included in Figure 4.1.

When AuNPs were plated on top of AgNPs via a 2-step scheme, the structures resulted were more distinct. Notably, when the dentritic silver was plated first, and the method of plating gold was changed, the morphologies of the resulting alloy nanoparticles were not quite the same. Dentritic AgNPs +1 step AuNPs gave a complete coverage, however the morphology of the particles changed completely, and lost their dendritic features. This could be explained by proposing that when the deposition potential of Au was more positive than that of dendritic AgNPs, the big dendritic structures were destroyed and dissolved, indicating an unstable structure. In contrast, for the case of dentritic AgNPs +2 step AuNPs, the nucleation potential was also very low for the dendritic silver; therefore, it was able to maintain its morphologies. Moreover, the sizes of the nanoalloys were a lot smaller. Therefore, for future analysis, we consistently used 2-step AuNPs to form NAs with sAgNPs and dAgNPs.

From Figure 4.1. a to c, we can see that the NAs preserved a better dispersion than pure AuNPs; however, from figure b to d, the uniform dispersity of gold nanoparticles seemed to be lost. These observations suggested that it is the shape and dispersion of the silver nanoparticles plated first that controlled the resulting morphology of the AgAuNPs. This is again confirmed in the next row. Comparing Figure 4.1 a to e, and b to f, we saw that no matter how we deposited AuNPs afterwards, we obtained dendritic NAs. Therefore, we conclude that the shape of AgNPs controlled the shape of AgAuNAs.

Table 4.1 Morphological summary of different types of NPs and NAs synthesized in this study.

	1-step AuNPs	**2-step AuNPs**

No Ag	Small aggregates ~750 nm Poor and uneven coverage. **(a)**	Very small aggregates ~250 nm; Very complete and even coverage. **(b)**
sAgNPs	Small aggregates ~2 μm Uneven coverage favoured on the edge. **(c)**	Small aggregates~1 μm Better coverage, there were more on the surface, however still more favoured on the edge **(d)**
dAgNPs	Small aggregates ~575 nm. High and even coverages over the edge and the slides **(e)**	Large branches of dentritic nanoalloy, moderate coverage. **(f)**

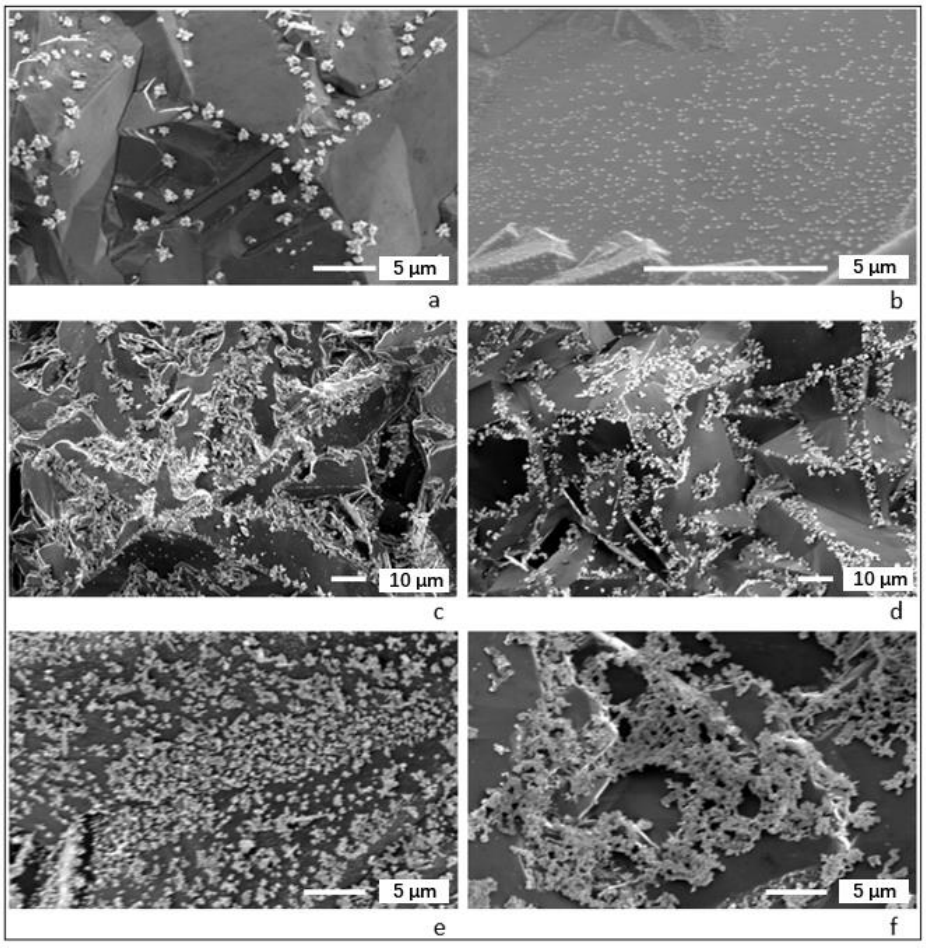

Figure 4.1 SEM images of NPs and NAs synthesised in this study, with letters a-f referring to the synthesis patterns in Table 4.1.

4.4.2 Surface Compositional Analysis using XPS:

XPS was carried out to understand the surface compositional differences in various

AgAuNAs. The overall elemental compositions are presented in Table 4. 2. Carbon peak positions were calibrated with respect to the blank sample in chapter 3.

Table 4.2 Overall elemental composition of electrodeposited nanospecies with different morphologies

	% of C	% of O	% of Ag	% of Au	% of others
Bare	**91.9**	**7.7**	**0**	**0**	N: 0.4
dAg	**84.8**	8.9	5.9	0	Cl: 0.5
sAg	**85.2**	9.1	5.7	0	0
Au	**92.4**	5.8	0.0	1.8	0
dAgAu	**81.0**	5.8	10.0	3.3	0
sAgAu	**82.9**	8.5	6.4	2.3	0

XPS identifies the elemental composition at the surface of nanospecies. An immediate observation was when AgNPs were plated first, the amount of Au discovered on the surface significantly increased, meaning electrodeposition of AuNPs is more favored and stable with AgNPs On the other hand, shifts in elements' composition were expected if a Ag (core) Au (shell) alloy formed, especially when Au covers some of the Ag the percentage of Ag is expected to decrease for both dAgAu and sAgAu. However, distinct changes in elemental composition were not observed in this case. The percentages of C and O reduced in the alloy case, since more metal was deposited on the electrodes covering the diamond surface. This could cause the fluctuations in Ag composition, however, significant changes in Ag% were not observed.

Notably, when comparing the metal components of sAgBDDE; AuBDDE and sAgAuBDDE, it is obvious that the percentage didn't change much. However, both the

percentage of surface silver and gold increased significantly in dAgAuBDDE; this might be anonlous which deposited too much metal on it. However, the absolute percentage of metal should not affect our study concerning the inner alloying method of AgAuNAs.

To figure out how Au got alloyed with Ag, the areas of Ag 3d and Auger regions for each Ag-containing nanospecies were integrated. Auger parameters measured the energy differences of a photoelectron and that of the sample's Auger electron; therefore it is independent of sample charging and work function. An Auger electron is a high energy electron that is ejected from an excited atom.[49-50] Ag 3d binding energy is approximately 300 eV and gives rise to electrons with kinetic energy of around 1000 eV. Ag Auger on the other hand has kinetic energy of 300-400 eV, meaning Ag Auger is more surface sensitive. Hence, signals in the Auger regions measure more "surface" electrons of targeted atoms, and if the ratio of the areas of Auger/3d region (A_2/A_1) for the NAs decreases more than that of the ratio for pure AgNPs, that means there is a lower surface concentration of Ag.

Table 4.3 Comparison of Areas of Ag 3d and Auger regions

	Area of Ag 3d XPS peak (A_1)	**Area of Ag MNN Auger peak (A_2)**	**Ratio of (A_2/A_1)**
dAg	171.8	935.4	0.54
sAg	177.2	993.5	0.60
dAgAu	231.5	1507.0	0.65
sAgAu	172.9	909.2	0.52

Compared with AgNPs, The ratio A_2/A_1 increased for dAgAu, and decreased for sAgAu.

This suggested that for the sAgAu case, there were less Ag exposed on the surface, which is not the case for dAgAu. This difference made us think the alloying pattern might be completely different for the two types of NAs. For the sAgAu case, a core-shell model can be considered, in which AuNPs are covering AgNPs. However, the unusual increase of A_2/A_1 value from dAg to dAgAu suggests that the dispersion of Ag is better, and therefore a closer interaction of AuNP and AgNPs are suggested.

4.4.3 Sequential Deposition of AuNPs onto Different AgNP Structures

To confirm this concept, CV was done to deposit AuNPs, and the deposition potentials of AuNPs onto different substrates were measured and compared. The deposition potential of Au was recorded on different substrates – bare BDDE, sAgNPs, and dAgNPs. Multiple cycles of CVs were done to compare the shift of deposition potentials. The potential range scanned was 0.04 V to 1.44 V, with a step -0.00244 V, and a scan rate 0.1 V/s.

The deposition potential for AuNPs on bare electrodes was recorded, and a shift in the reduction peak was expected when Au was deposited on the metal NP-coated surfaces. Generally speaking, the nucleation of AuNPs would happen a lot easier on metal surfaces, indicating the deposition peak potentials would be more positive for the alloy case. Multiple cycles were done to observe the change in deposition substrates of AuNPs, and from the shift in deposition potential, alloying patterns for different NAs were proposed.

When the number of cycles for electrodeposition of AuNPs on bare BDDE increased, the deposition potential shifted to a more positive value, that indicated AuNPs aggregates formed as more cycles were performed (Figure 4.2). The first deposition potential for both sAgNPs and dAgNPs were a lot more positive than that of AuNPs on bare electrodes, this suggested that the alloying effect made deposition of AuNPs on AgNPs a lot easier. The deposition peaks of AuNPs became more sharp and well-separated when AgNPs were plated first. This has shown also that it is obvious that the deposition of Au on Ag is more specific and preferred. However, when the number of cycles increased, the deposition potential for dAgNP shifted to a more negative value, and stayed at 0.24 V, which was the same value for bare-Au deposition after the 7^{th} cycle. On the other hand, the deposition potential of sAgAu stayed at the same value, 0.30 V after 9 cycles.

This interesting difference suggested that, in the case of dAgAu, AuNPs elongated the dendritic branches of AgNPs rather than thickening. Therefore, in the first cycle, the AuNPs deposited on AgNPs and formed an alloy interface, however when the cycle increased, the AuNPs deposited on themselves, and so they started to feel less and less background of Ag (Figure 4.3). In the case of sAgAu, the AuNPs deposited on top of sAgNPs, and a core-shell NA was formed. Since the sizes of AuNPs were small and the concentration of Au was very dilute, AuNPs continuously plated on AgNPs (Figure 4.4).

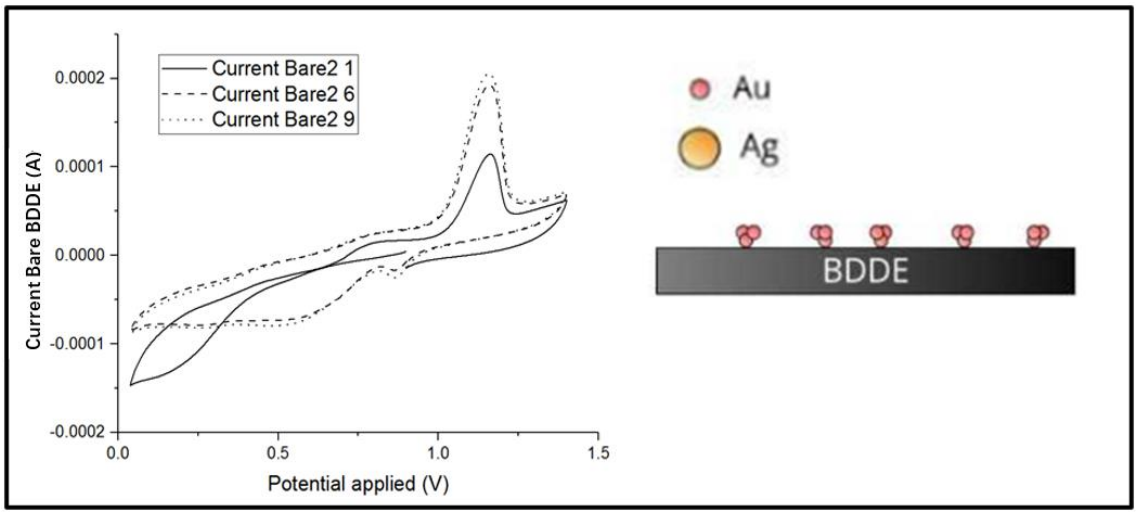

Figure 4.2 CV of AuNP deposition on bare BDDE (left), the numbers 1, 6 and 9 were the number of cycles. An ideogram on the right shows the deposition of Au on a bare BDDE.

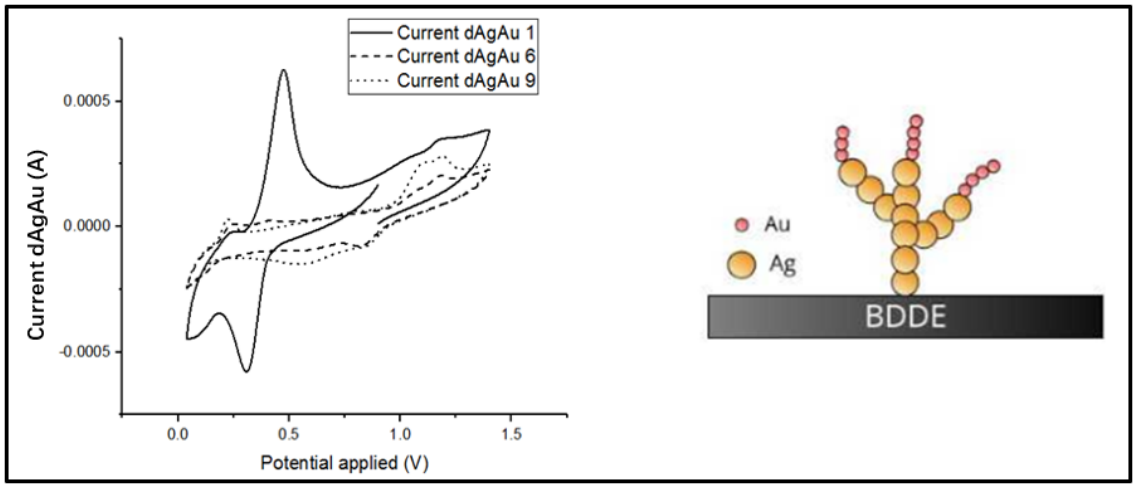

Figure 4.3 CV of AuNP deposition on dAg-BDDE (left), the numbers 1, 6 and 9 were the number of cycles. An ideogram on the right shows the deposition of Au on dAg-BDDE.

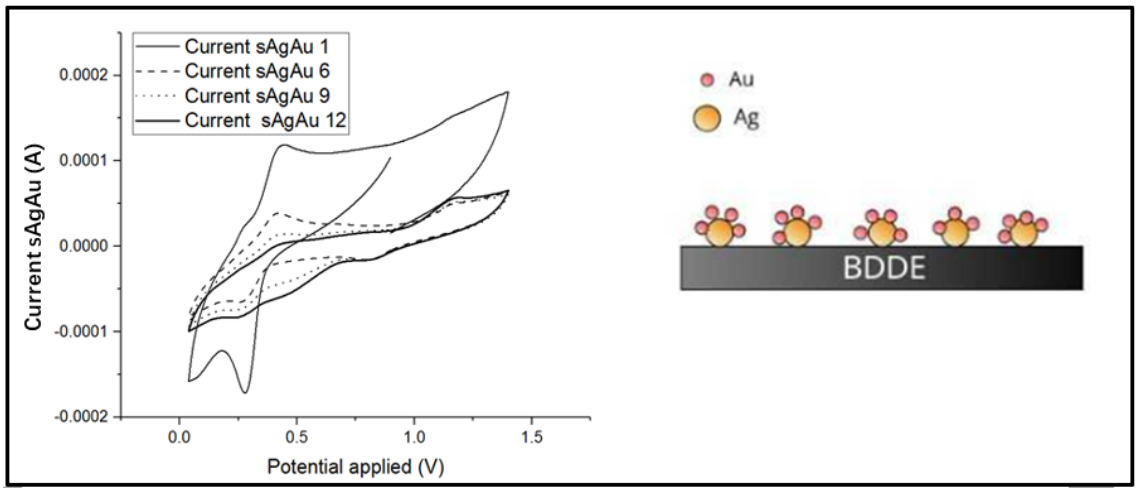

Figure 4.4 CV of AuNP deposition on sAg-BDDE (left), the numbers 1, 6, 9 and 12 were the number of cycles. An ideogram on the right shows the deposition of Au on sAg-BDDE.

4.4.4 Electrocatalytic analysis using the HER as a model

Pure AgNPs and AuNPs were synthesized through electrodeposition to compare the electrocatalysis reactivities. The AgNPs were deposited on BDDEs through the two-step scheme: -0.2 V for 2 s; 0 V for 30 s, forming spherical AgNPs, since this is the species with most optimal catalytic performance in the HER. The source of Ag used for electrodeposition was 20 mM $AgNO_3$, and the supporting electrolyte was acetate buffer pH=4.60. The AuNPs were electrodeposited via a single-step electrodeposition, by holding the potential at -0.1 V for 150 s. The source of Au used was $HAuCl_4$ 1 mM, and the supporting electrolyte for AuNP deposition used was 0.1 M H_2SO_4.

The catalytic activities of Ag-BDDEs, Au-BDDEs, and AgAu-BDDEs during the HER are monitored using Linear Sweep Voltammetry (LSV) from 0 V to -2.0 V at 20 mV/s performed in 0.5 M sulfuric acid.

Tafel analysis for all nanocomposites is summarized in Table 4. 3, including Tafel Slopes

(averaged through 3 trails), and current responses at designated potentials (-1.0 V for J_1 and -0.8 V for J_2, and averaged through 3 trails). The current responses with respect to different potentials applied and Tafel plots are presented in Figure 4.6 and 7, respectively.

Table 4.4 Tafel analysis for different structured AgAuNAs compared with bare BDDE, pure AgNPs and pure AuNPs on BDDE.

	Tafel Slope (mV/dec)	***J*$_1$ (mA/cm^2)**	***J*$_2$ (mA/cm^2)**
Bare	233±3	4±0.5	1±0.5
AuNP	119±4	17±0.8	13±1
dAgNP	127±10	12±2	7±0.5
sAgNP	112±5	14±0.5	4±0.5
dAgAuNP	125±12	19±1	15±0.5
sAgAuNP	116±4	19±0.5	15±0.5

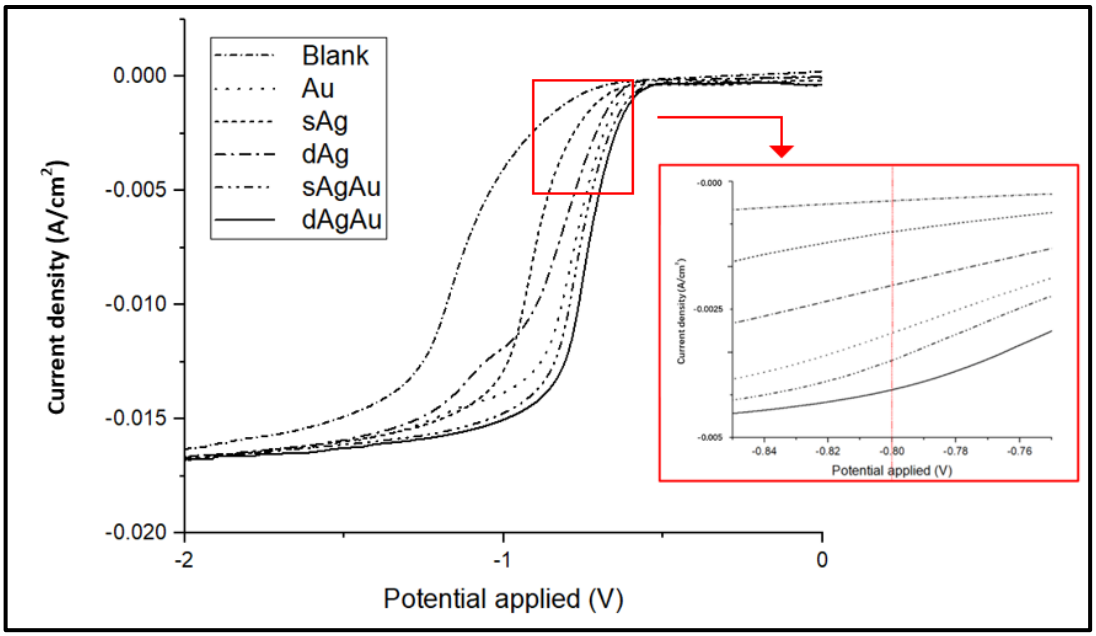

Figure 4.5 Plot of potential applied vs. current densities of nanospecies and a zoom in of current density at -0.8V.

In Tafel analysis, the most important parameter to look at is Tafel slope, which illustrates not only the sensitivity of current response to certain applied potentials but also provides insight into the specific routes that the reaction happened under. When the Tafel slope is larger than 120 mV/dec, it means that the Volmer step is the rate-determining step. On the other hand, when the Tafel slope is between 40 mV/dec to 120 mV/dec, the Heyrovsky step is the rate-determining step for the whole reaction. From the Tafel slope values in Table 4.4, it is clear that AuNPs, sAgNPs, and sAgAuNPs catalysed the HER via a Heyrovsky-Volmer step, and the adsorption of electrons was the rate-determining step for the whole reaction. On the other hand, the Volmer step is the rate-determining step for the other nanospecies. [51]

The differences in Tafel slopes and mechanisms come from their morphological differences. The spherical species have more available sites for electron adsorption, whereas for other species the rate determining step has always been the adsorption of H to the metal nanoparticles. The dendritic structures and the aggregations made that step adsorption harder, therefore it became the rate determining step.

To conclude, the Tafel slopes for all nanospecies are very close and within error. However, when we look at the current density plot, more distinct differences are observed. This is because Tafel slope, or the reaction path alone, cannot determine the efficiency of electrocatalysis. The number of reaction sites is also an important factor to consider. dAgAuNA has the largest Tafel slope yet outstanding performance in current density for all potentials because it has more reaction sites, due to its morphology. The dispersion of metal nanospecies play an important role in its catalysis. [52-53]

As for the current responses, the alloyed species have superior performances over the pure metal species since the alloying effect allowed more defects at the position that formed the alloy. Although dAgAu and sAgAu exhibited comparable magnitudes of current responses at designated potentials, the excellent performance of dAgAu might because of the excess metal, rather than the alloying effect. According to the alloying structure, the alloying surfaces were very limited, while on the other hand, sAgAu has more complete alloying effect.

4.5 Conclusion

Au nanoparticles may not be the best choice to catalyze fuel cell reactions like the HER due to the poor adsorption of hydrogen atoms on the Au surface. However, they play an important role in supporting sulfide catalysts by forming chemical bonds with sulfide ligands and improving conductivity. To use AuNPs directly as the catalyst for fuel cell catalysis, extra supporting materials like carbon or oxides are essential. Another more common way is by forming a nanoalloy (NA) with Ag nanoparticles, and by carefully tuning the composition and structural optimization, the performance can be enhanced with reasonable cost that is suitable for industrial implementation.

In this chapter various electrochemical approaches have been employed to prepare AgAuNA modified BDDEs. AgNPs with distinct spherical and dendritic morphologies were plated first followed by Au deposition to form an active alloy structure that is favoured by electrocatalysis. Then the effect of alloy morphologies was investigated by controlling and varying the deposition method of Au. When AuNPs were deposited via a two-step electrodeposition scheme, similar to the deposition procedure of spherical

AgNPs in chapter 3, two types of nanoalloys (spherical and dendritic, depending on the AgNPs structure used) were formed, with fine-tuned structure and dispersity.

The surface composition of modified BDDEs were examined via XPS, and a decrease in Ag percentage was expected for NA modified ones compare with Ag modified ones, since the Au covers the Ag. However, this was not the case, and we analyzed the NA modified BDDEs using Auger spectroscopy instead. The important value was the ratio of the integrated area of the Ag MNN Auger peak to that of the area of the Ag 3d peak. For dendritic species, this ratio increased after Au was deposited, and the opposite trend was observed for spherical species. This suggested the alloying structures of these two types of alloys were different.

We confirmed the alloying structuress of dAgAu and sAgAu using multi-cycled Cyclic Voltammetry (CV). sAg, dAg modified BDDEs and a clean BDDE were prepared, and Au was deposited via CV. The deposition potential of Au at the first cycle was a lot more positive for Ag modified BDDEs than for a bare electrode, suggesting the alloying effect made deposition of Au more favoured. However, as more cycles occured, the deposition potential of dAgAu shifted towards right and eventually became the same as that of bare-Au, whereas the deposition potential of Au kept constant for sAgAu. Therefore, we conclude dAgAu has a small alloying interface and sAgAu preserves a core-shell structure.

Afterwards, the electrocatalytic abilities of the AgAuBDDEs were examined and compared with AgBDDEs and AuBDDEs. Both spherical and dendritic nanoalloy modified BDDEs exhibited enhanced activities in catalysing HER compared with pure

metal and colloidal nanoparticles, although their alloying structures were different.

References

(1) Cheng, Y.; Samia, A.; Meyers, J.; Panagopoulos, I.; Fei, B.; Burda, C. Highly Efficient Drug Delivery With Gold Nanoparticle Vectors For In Vivo Photodynamic Therapy Of Cancer. *Journal of the American Chemical Society* 2008, 130, 10643-10647.

(2) Yang, C.; Bromma, K.; Di Ciano-Oliveira, C.; Zafarana, G.; van Prooijen, M.; Chithrani, D. Gold Nanoparticle Mediated Combined Cancer Therapy. *Cancer Nanotechnology* 2018, 9.

(3) Elahi, N.; Kamali, M.; Baghersad, M. Recent Biomedical Applications Of Gold Nanoparticles: A Review. *Talanta* 2018, 184, 537-556.

(4) Corma, A.; Garcia, H. Supported Gold Nanoparticles As Catalysts For Organic Reactions. *Chemical Society Reviews* 2008, 37, 2096.

(5) Schimpf, S.; Lucas, M.; Mohr, C.; Rodemerck, U.; Brückner, A.; Radnik, J.; Hofmeister, H.; Claus, P. Supported Gold Nanoparticles: In-Depth Catalyst Characterization And Application In Hydrogenation And Oxidation Reactions. *Catalysis Today* 2002, 72, 63-78.

(6) Chen, W.; Lu, Y.; Dong, W.; Chen, Z.; Shen, M. Plasmon Mediated Visible Light Photocurrent And Photoelectrochemical Hydrogen Generation Using Au Nanoparticles/TiO_2 Electrode. *Materials Research Bulletin* 2014, 50, 31-35.

(7) Huff, C.; Dushatinski, T.; Barzanji, A.; Abdel-Fattah, N.; Barzanji, K.; Abdel-Fattah, T. Pretreatment Of Gold Nanoparticle Multi-Walled Carbon Nanotube Composites For Catalytic Activity Toward Hydrogen Generation Reaction. *ECS Journal of Solid State Science and Technology* 2017, 6, M69-M71.

(8) Tran, T.; Nguyen, M.; Le, H.; Nguyen, D.; Truong, Q.; Tran, P. Gold Nanoparticles As An Outstanding Catalyst For The Hydrogen Evolution Reaction. *Chemical Communications* 2018, 54, 3363-3366.

(9) Merga, G.; Saucedo, N.; Cass, L.; Puthussery, J.; Meisel, D. "Naked" Gold Nanoparticles: Synthesis, Characterization, Catalytic Hydrogen Evolution, And SERS. *The Journal of Physical Chemistry C* 2010, 114, 14811-14818.

(10) B. Hinnemann, P. G. Moses, J. Bonde, K. P. Jørgensen, J. H. Nielsen, S. Horch, I. Chorkendorff and J. K. Nørskov, *J. Am. Chem. Soc.*, 2005, 127, 5308–5309

(11) Thompson, D. Using Gold Nanoparticles For Catalysis. *Nano Today* 2007, 2, 40-43.

(12) Marinoiu, A.; Raceanu, M.; Andrulevicius, M.; Tamuleviciene, A.; Tamulevicius, T.; Nica, S.; Bala, D.; Varlam, M. Low-Cost Preparation Method Of Well Dispersed Gold Nanoparticles On Reduced Graphene Oxide And Electrocatalytic Stability In PEM Fuel Cell. *Arabian Journal of Chemistry* 2020, 13, 3585-3600.

(13) Zhao, Y.; Wang, C.; Liu, Y.; MacFarlane, D.; Wallace, G. Engineering Surface Amine Modifiers Of Ultrasmall Gold Nanoparticles Supported On Reduced Graphene Oxide For Improved Electrochemical CO_2 Reduction. *Advanced Energy Materials* 2018, 8, 1801400.

(14) Xu, J.; Zhao, T.; Liang, Z. Carbon Supported Platinum–Gold Alloy Catalyst For Direct Formic Acid Fuel Cells. *Journal of Power Sources* 2008, 185, 857-861.

(15) Lee, K.; Byun, J.; Shin, H.; Kim, S. Nanoporous Gold-Palladium: A Binary Alloy With High Catalytic Activity For The Electro-Oxidation Of Ethanol. *Journal of Alloys and Compounds* 2020, 842, 155847.

(16) Caglar, A.; Cogenli, M.; Yurtcan, A.; Kivrak, H. Effective Carbon Nanotube Supported Metal (M=Au, Ag, Co, Mn, Ni, V, Zn) Core Pd Shell Bimetallic Anode Catalysts For Formic Acid Fuel Cells. *Renewable Energy* 2020, 150, 78-90.

(17) Fang, H.; Yang, J.; Wen, M.; Wu, Q. Nanoalloy Materials For Chemical Catalysis. *Advanced Materials* 2018, 30, 1705698.

(18) Stamenkovic, V.; Mun, B.; Arenz, M.; Mayrhofer, K.; Lucas, C.; Wang, G.; Ross, P.; Markovic, N. Trends In Electrocatalysis On Extended And Nanoscale Pt-Bimetallic Alloy Surfaces. *Nature Materials* 2007, 6, 241-247.

(19) Zhang, J.; Sasaki, K.; Sutter, E.; Adzic, R. Stabilization Of Platinum Oxygen-Reduction Electrocatalysts Using Gold Clusters. *ChemInform* 2007, 38.

(20) Wang, P.; Zhou, F.; Wang, Z.; Lai, C.; Han, X. Substrate-Induced Assembly Of Ptau Alloy Nanostructures At Choline Functionalized Monolayer Interface For Nitrite Sensing. *Journal of Electroanalytical Chemistry* 2015, 750, 36-42.

(21) Xiao, F.; Mo, Z.; Zhao, F.; Zeng, B. Ultrasonic-Electrodeposition Of Gold–Platinum Alloy Nanoparticles On Multi-Walled Carbon Nanotubes – Ionic Liquid Composite Film And Their Electrocatalysis Towards The Oxidation Of Nitrite. *Electrochemistry Communications* 2008, 10, 1740-1743.

(22) Holmberg, N.; Laasonen, K.; Peljo, P. Charge Distribution And Fermi Level In Bimetallic Nanoparticles. *Physical Chemistry Chemical Physics* 2016, 18, 2924-2931.

(23) Xiao, Q.; Sarina, S.; Jaatinen, E.; Jia, J.; Arnold, D.; Liu, H.; Zhu, H. Efficient Photocatalytic Suzuki Cross-Coupling Reactions On Au–Pd Alloy Nanoparticles Under Visible Light Irradiation. *Green Chemistry* 2014, 16, 4272.

(24) Xu, C.; Hao, Q.; Duan, H. Nanoporous Pdpt Alloy As A Highly Active Electrocatalyst For Formic Acid Oxidation. *Journal of Materials Chemistry A* 2014, 2, 8875.

(25) Cho, Y.; Cho, Y.; Lim, J.; Park, H.; Jung, N.; Ahn, M.; Choe, H.; Sung, Y. Performance Of Membrane Electrode Assemblies Using Pdpt Alloy As Anode Catalysts In Polymer Electrolyte Membrane Fuel Cell. *International Journal of*

Hydrogen Energy 2012, 37, 5884-5890.

(26) Liu, Y.; Liu, S.; Che, Z.; Zhao, S.; Sheng, X.; Han, M.; Bao, J. Concave Octahedral Pd@PdPt Electrocatalysts Integrating Core–Shell, Alloy And Concave Structures For High-Efficiency Oxygen Reduction And Hydrogen Evolution Reactions. *Journal of Materials Chemistry A* 2016, 4, 16690-16697.

(27) Wang, S.; Zhu, W.; Ke, J.; Lin, M.; Zhang, Y. Pd–Rh Nanocrystals With Tunable Morphologies And Compositions As Efficient Catalysts Toward Suzuki Cross-Coupling Reactions. *ACS Catalysis* 2014, 4, 2298-2306.

(28) Zaleska-Medynska, A.; Marchelek, M.; Diak, M.; Grabowska, E. Noble Metal-Based Bimetallic Nanoparticles: The Effect Of The Structure On The Optical, Catalytic And Photocatalytic Properties. *Advances in Colloid and Interface Science* 2016, 229, 80-107.

(29) Dent, A.; Evans, J.; Fiddy, S.; Jyoti, B.; Newton, M.; Tromp, M. Structure–Performance Relationships Of Rh And RhPd Alloy Supported Catalysts Using Combined EDE/DRIFTS/MS. *Faraday Discuss.* 2008, 138, 287-300.

(30) Wu, J.; Gao, G.; Li, J.; Sun, P.; Long, X.; Li, F. Efficient And Versatile Cuni Alloy Nanocatalysts For The Highly Selective Hydrogenation Of Furfural. *Applied Catalysis B: Environmental* 2017, 203, 227-236.

(31) SINFELT, J. Catalytic Hydrogenolysis And Dehydrogenation Over Copper-Nickel Alloys. *Journal of Catalysis* 1972, 24, 283-296.

(32) Gu, C.; Wu, D.; Wen, M.; Wu, Q. A Freestanding SiO_2 Ultrathin Membrane With Nicu Nanoparticles Embedded On Its Double Surfaces For Catalyzing Nitro-Amination. *Dalton Transactions* 2018, 47, 7083-7089.

(33) Cao, X.; Han, Y.; Gao, C.; Xu, Y.; Huang, X.; Willander, M.; Wang, N. Highly Catalytic Active Ptnicu Nanochains For Hydrogen Evolution Reaction. *Nano Energy* 2014, 9, 301-308.

(34) Oh, A.; Sa, Y.; Hwang, H.; Baik, H.; Kim, J.; Kim, B.; Joo, S.; Lee, K. Rational Design Of Pt–Ni–Co Ternary Alloy Nanoframe Crystals As Highly Efficient Catalysts Toward The Alkaline Hydrogen Evolution Reaction. *Nanoscale* 2016, 8, 16379-16386.

(35) Chen, D.; Sun, P.; Liu, H.; Yang, J. Bimetallic Cu–Pd Alloy Multipods And Their Highly Electrocatalytic Performance For Formic Acid Oxidation And Oxygen Reduction. *Journal of Materials Chemistry A* 2017, 5, 4421-4429.

(36) Yang, F.; Zhang, Y.; Liu, P.; Cui, Y.; Ge, X.; Jing, Q. Pd–Cu Alloy With Hierarchical Network Structure As Enhanced Electrocatalysts For Formic Acid Oxidation. *International Journal of Hydrogen Energy* 2016, 41, 6773-6780.

(37) Live Gold Prices | Gold News And Analysis | Mining News | KITCO

https://www.kitco.com/ (accessed Jul 3, 2020).

(38) Chaudhari, N.; Joo, J.; Kim, B.; Ruqia, B.; Choi, S.; Lee, K. Recent Advances In Electrocatalysts Toward The Oxygen Reduction Reaction: The Case Of PtNi Octahedra. *Nanoscale* 2018, 10, 20073-20088.

(39) Bao, M.; Amiinu, I.; Peng, T.; Li, W.; Liu, S.; Wang, Z.; Pu, Z.; He, D.; Xiong, Y.; Mu, S. Surface Evolution Of Ptcu Alloy Shell Over Pd Nanocrystals Leads To Superior Hydrogen Evolution And Oxygen Reduction Reactions. *ACS Energy Letters* 2018, 3, 940-945.

(40) Wei, Y.; Zhang, X.; Liu, Y.; Jia, C.; Yang, P. Ternary Ptnicu Self-Assembled Nanocubes For Plasmon-Enhanced Electrocatalytic Hydrogen Evolution And Methanol Oxidation Reaction In Visible Light. *Electrochimica Acta* 2020, 349, 136366.

(41) Shirman, T.; Lattimer, J.; Luneau, M.; Shirman, E.; Reece, C.; Aizenberg, M.; Madix, R.; Aizenberg, J.; Friend, C. New Architectures For Designed Catalysts: Selective Oxidation Using Agau Nanoparticles On Colloid-Templated Silica. *Chemistry – A European Journal* 2017, 24, 1833-1837.

(42) Rodrigues, T.; da Silva, A.; de Moura, A.; Geonmonond, R.; Camargo, P. Agau Nanotubes: Investigating The Effect Of Surface Morphologies And Optical Properties Over Applications In Catalysis And Photocatalysis. *Journal of the Brazilian Chemical Society* 2016.

(43) da Silva, A.; Rodrigues, T.; Slater, T.; Lewis, E.; Alves, R.; Fajardo, H.; Balzer, R.; da Silva, A.; de Freitas, I.; Oliveira, D. et al. Controlling Size, Morphology, And Surface Composition Of Agau Nanodendrites In 15 S For Improved Environmental Catalysis Under Low Metal Loadings. *ACS Applied Materials & Interfaces* 2015, 7, 25624-25632.

(44) Zhang, J.; Lou, Y.; Zhou, H.; Zhao, Y.; Wang, Z.; Shi, L.; Yuan, S. Electrodeposited Agau Nanoalloy Enhancing Photoelectric Conversion Efficiency Of Dye Sensitized Solar Cells. *Electrochimica Acta* 2019, 324, 134858.

(45) De, S.; Nandy, A.; Mondal, S.; Roy, A.; Mondal, S.; Senapati, D. Void-Enriched And Highly Strained Porous Au–Ag Nanoalloy As A Bifunctional Electro-Catalyst In Alkaline Direct Alcohol Fuel Cell. *ACS Applied Energy Materials* 2021, 4, 5367-5374.

(46) Mo, J.; Barbosa, E.; Wu, S.; Li, Y.; Sun, Y.; Xiang, W.; Li, T.; Pu, S.; Robertson, A.; Wu, T. et al. Atomic-Precision Tailoring Of Au–Ag Core–Shell Composite Nanoparticles For Direct Electrochemical-Plasmonic Hydrogen Evolution In Water Splitting. *Advanced Functional Materials* 2021, 31, 2102517.

(47) Atomic radii of the elements (data page) https://en.wikipedia.org/wiki/Atomic_radii_of_the_elements_%28data_page%29 (accessed Jul 3, 2020).

(48) Ferrando, R.; Jellinek, J.; Johnston, R. Nanoalloys: From Theory To Applications Of Alloy Clusters And Nanoparticles. *Chemical Reviews* 2008, 108, 845-910.

(49) Biesinger, M.; Lau, L.; Gerson, A.; Smart, R. The Role Of The Auger Parameter In XPS Studies Of Nickel Metal, Halides And Oxides. *Physical Chemistry Chemical Physics* 2012, 14, 2434.

(50) Chang, C. Auger Electron Spectroscopy. *Surface Science* 1971, 25, 53-79.

(51) Shinagawa, T.; Garcia-Esparza, A.; Takanabe, K. Insight On Tafel Slopes From A Microkinetic Analysis Of Aqueous Electrocatalysis For Energy Conversion. *Scientific Reports* 2015, 5.

(52) Thomas, J. Kinetics Of Electrolytic Hydrogen Evolution And The Adsorption Of Hydrogen By Metals. *Transactions of the Faraday Society* 1961, 57, 1603.

(53) de Chialvo, M.; Chialvo, A. Hydrogen Evolution Reaction: Analysis Of The Volmer-Heyrovsky-Tafel Mechanism With A Generalized Adsorption Model. *Journal of Electroanalytical Chemistry* 1994, 372, 209-223.

Chapter 5: Carboxylated Graphene Nanoflakes (GNF) as a Superior Stabilizer for Colloidal Ag, Au Nanoparticles and AgAu Nanoalloys, and Enhanced Performance in the Hydrogen Evolution Reaction in Acidic Media

5.1 Introduction

As mentioned in the previous chapters, colloidal Ag and AgAuNPs as catalysts for the HER can be synthesized via chemical reduction method with $NaBH_4$ as the reducing agent[1-2]. Compared to the other colloidal non-Pt catalysts including SeV_2, MoS_2, and WSe_2, the synthesis process is easy to control as well as less hazardous. The resulting colloidal nano-species can be used to modify BDDE surfaces via a drop-coating or spin-coating method. To achieve the best catalytic performance, the dispersion of nanoparticles is a crucial parameter to control[3], as they tend to aggregate to reduce surface energy and are lost from the electrode surfaces with the progression of time because of weak binding forces [4-5].

Different types of stabilizers varying from biomolecule ligands[6], to inorganic molecules[7], and polymers[8] are used in current studies to prevent aggregation of colloidal nanoparticles, and one of them is sodium citrate (SC) [9]. However, the final stabilising effect is highly influenced by the amount of SC added and the arrangement of metal-citrate coordination complexes.[10-11] Therefore, better alternatives to support metal nanospecies should be used.

Graphene and its derivatives like graphene oxide (GO) and reduced graphene oxide (rGO) have flexible structures, which are extremely useful for modification by metal nanoparticles through forming various graphene-based composite nanomaterials. These nanomaterials are ready to apply in research areas including drug delivery and imaging reagents.[12-13] More importantly, the architecture of graphene modification can boost electrocatalysis in terms of regulating the dispersion therefore providing more active catalyst sites.[14-16] The resulting materials are relatively stable, mediated possibly by the oxygen-containing functional groups [17 18-19].

In this area, an interesting new material is based on carboxylated graphene nanoflakes (cx-GNF) which also has potential application as an electrode support for metal nanoparticles. Similar to GO, cx-GNF has oxygen-containing groups. However, cx-GNF only has sp2 carbon on the sheets and COOH groups on the edges whereas GO has lots of functional groups like epoxide and alcohols randomly distributed. The level of oxidation of GNF is therefore much more reproducibility defined compared to GO, and of course the flake size is much smaller, 15-30 nm for GNF versus 1 μm to 50 μms for GO. cx-GNF are easily synthesised and their significantly high solubility in water means cx-GNF can be easily manipulated chemically. By dialysis, cx-GNFs can be separated on the basis of size, which allows investigation of the size effect of cx-GNF upon its stabilizing performance[20-21].

To explore how these cx-GNF stabilised nanomaterials can be used for more applications, further stabilisations were performed to prevent the solvation of metal-GNF complex in aqueous electrolytes, especially in higher pH, since the carboxylate ends will ensure cx-

GNF becomes extremely soluble in alkaline conditions. Two types of stabilisation were considered: internal and external. An internal stabilisation functionalised the carboxylate ends of cx-GNF, which have very specific affiliations towards +2 metal ions including Ni^{2+}, Pb^{2+}, and Cd^{2+}. The resulting metal salts are insoluble and since the metal nanoparticles were adsorbed on the graphene surface, away from the functionalization, this will not destroy the metal-GNF interaction.[22]

For external stabilisation, Nafion, a conducting polymer that is often used in proton exchange membranes, was chosen. [23] To better disperse Nafion molecules and achieve optimal conduction, a cx-GNF/Nafion complex was synthesized under a similar procedure to that used for GO/Nafion complexes in previous studies.[24] The cx-GNF/Nafion complex was top-coated on cx-GNF stabilised metal nanoparticles to yield a (cx-GNF)-metal nanoparticle-(cx-GNF/Nafion) sandwich structure.

5.2 Aim of This Chapter

In the previous two chapters, we have investigated the electrodeposition of nanospecies as a quick and reliable way to modify BDDE for enhanced reactivities in the HER. However, the drawback of this method, including large particle size and variable NP shapes, local aggregations and varied dispersity resulting from the nature of diamond surface and uneven boron doping of the electrode, made us seek an alternative way of synthesizing functionalized electrodes. Herein, we proposed a simple one-step in-situ reduction synthesis scheme of cx-GNF stabilised metal nanoparticles and studied the effect of cx-GNF on stabilising metal nanospecies including AgNP, AuNP, and AgAu

nanoparticles. The individual size, overall dispersions, and surface compositions of cx-GNF stabilised nanospecies were investigated through surface analysis methods and compared with unstabilised and sodium citrated stabilised species. To make sure the nanoparticles were stable for longer term usage, the progress of aggregation was inspected and recorded using the UV-Vis spectrum over long time spans. The hydrogen evolution reaction was performed as an exemplar of how different types of stabiliser will change the catalytic reactivities of nanospecies. The most catalytically active nanoparticle species were selected according to their large current responses at designated voltages, and the role of GNF and sodium citrate in both preventing aggregation and enhancing catalytic abilities were shown. Furthermore, AuGNF nanoparticles were further stabilised under Ni-edge functionalisation and GNF/Nafion external coating, and enhanced performance was observed in both cases.

5.3 Results and Discussion

5.3.1 Modification Mechanism, Characterization and Stability

cx-GNF powder was synthesised by Dr. Rosillo-Lopez at University College London. The source of graphene used was single wall carbon nanotubes. The nanotubes (purchased from Sigma Aldrich, SKU 900711, $\geqslant$98% carbon basis, with average diameter of 3-5nm, and spec. surface area 800-1000 m^2/g). were heated to boil refluxed in concentrated sulfuric acid and nitric acid for 2 hours. Afterwards, the solution was neutralised with KOH followed by filtration. Ion exchange chromatography was

performed, exchanging K^+ cations with H^+. The flake sizes of cx-GNF were controlled by dialysis, using a membrane with a pore size of 3.5 kDa.[21]

cx-GNF stabilisation of nano-species was achieved through a single-step in-situ reduction. 10 mL of 5 mM solution of $NaBH_4$ was prepared and chilled in an ice bath while a 2 mL cx-GNF (after dialysis) solutions with density 0.5 mg/mL were prepared and mixed with equivalent volume of 1 mM $AgNO_3$ solution. The resulting solution was slowly added into the NaBH4 solution dropwise upon gentle stirring. A yellow brownish colloidal solution was formed. Similar procedures were used to produce AgAu (concentration 1:1) mixed solution to form cluster nanoalloys, exchanging 2 mL 1 mM $AgNO_3$ solution for a mixture of 1 mL of 1 mM $AgNO_3$ and 1 mL of 1 mM $HAuCl_4$. Colloidal nano-species (AgNPs and AgAuNAs) without modifications were also prepared by swapping cx-GNF with the same volume of DI water, and 20× mass sodium citrate was added to half the volume of the non-stabilised nano-species for purpose of control experiments.

The formation of homogeneous colloidal nano-species was illustrated through UV-Vis spectra. A small shoulder peak at around 305 nm is assigned to n-π* transitions of C=O bonds at carboxylate functional groups in the UV-Vis spectrum of pure GNF[47]. The modified AgGNF exhibited a strong plasmonic resonance peak from silver nanoparticles as expected, however, the position of AgGNF peak shifted from 387 nm to 397 nm, which could result from charge transfer between GNFs' aromatic graphene surface and the AgNPs. According to Umadevi et. al[25], when Li and Mg metal atoms became adsorbed on the GNF surface, their charge changed from neutral to +0.8 e and +0.7 e, respectively. This indicated that there's a transfer of charge from metals (less electronegative species)

to the graphene surface, and thus induced a redshift in their spectroscopic analysis[25]. A similar trend is observed also by Soroush et. al when they modified GO with AgNPs[26]. (Figure 5.1a)

The formation of AgAuNAs was also confirmed using UV-Vis spectra. Compared with the spectrum obtained by mixing already made AgNP and AuNPs, the resulting AgAuNA spectrum showed a single peak with no sharp peak at around 400 nm (Figure 5.1b). The peak position at AuNP range shifted to the left from 525 nm to 510 nm. These indicated a homogeneous nanoalloy was successfully synthesized.[27]

Compared to the free AgAuNA, when GNF is bound to the nanoalloys, a slight blueshift is observed instead in UV-Vis Spectra. This difference could come from the different surface electron configuration and electron density distribution between pure metal nanoparticles and alloys. In Umadevi et al.'s work, there is another case, which might explain the blueshift. When metal ions, Li^{+} and Mg^{2+}, are bonded to graphene surface, the charges on them decreased from +1 to +0. 8e, and +2 to +1.7e, respectively.[25] This is opposite to the case of pure metal, with the resultant charge changes inducing a blueshift in UV-Vis. According to Ustinovshchikov's work[28], when metallic bonds are formed during an alloying process, it is possible for valence electrons to be localized around two atoms of different kinds. This induces the formation of common orbitals unequally distributed between the centres of an ionic bond. [28] So it is possible for AgAu nanoalloy to have some ionic character and that might be the root cause of this blueshift. It suggests that subtle changes in the electronic character of the nanoparticle produced by alloying

are sufficient to reverse the charge transfer between the metal nanoparticle and the GNF.

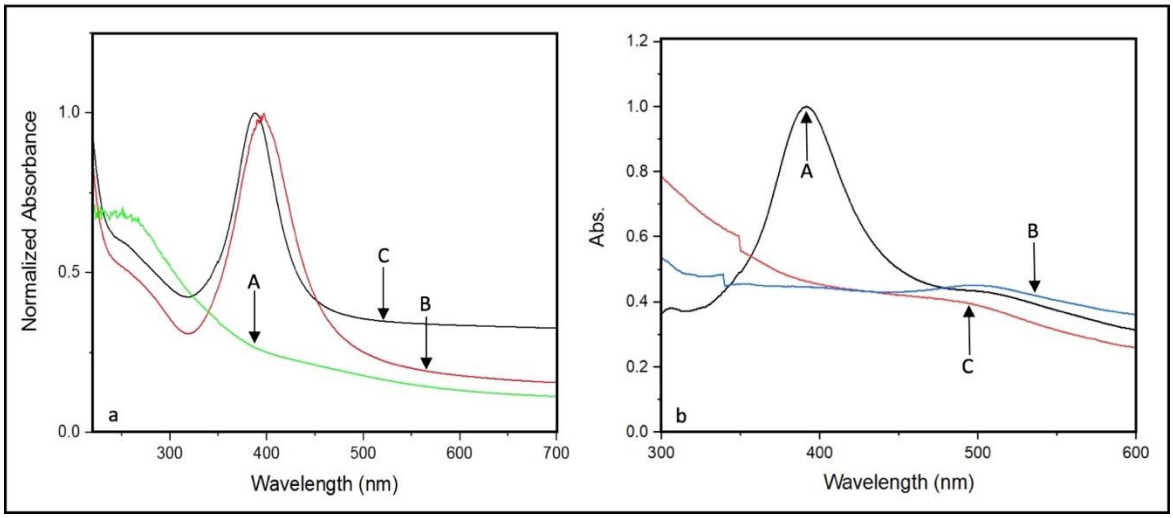

Figure 5.1 (a) UV-Vis spectra for GNF (A), AgGNF (B) and freshly prepared AgNPs, scanned from 270 to 700nm. A distinct redshift happened due to charge transfer from metal atom to GNF surface, which indicated the formation of AgGNF nanocomposite. (b) UV-Vis spectra for mixing freshly formed AgNPs and AuNPs (A), homogeneous AgAuNPs (B) and AgAuGNF (C)

These subtle changes could influence where the metal nanoparticles bond on the GNF. As explained in Figure 5.2a, because of the carboxylate groups on the GNF edges, aromatic carbon atoms on the sheets are likely to be more positive on the edges of the sheets because of the inductive effect and are therefore likely to favour bonding of metal nanoparticles where there is charge transfer to the graphene. In contrast, the opposite situation may hold at the centre of the sheets. The role of SC in colloidal nanoparticle solutions is simpler to understand. As a weak reducing agent, SC provides extra driving force to drive the reduction to completion and the partially negative tail of citrate ion can attach to the AgNPs.[10,29] With excess of SC added, multiple small citrate ions are able to insert onto AgNPs. Therefore, the aggregation of AgNPs is prevented due to the steric

effect (Figure 5.2b).

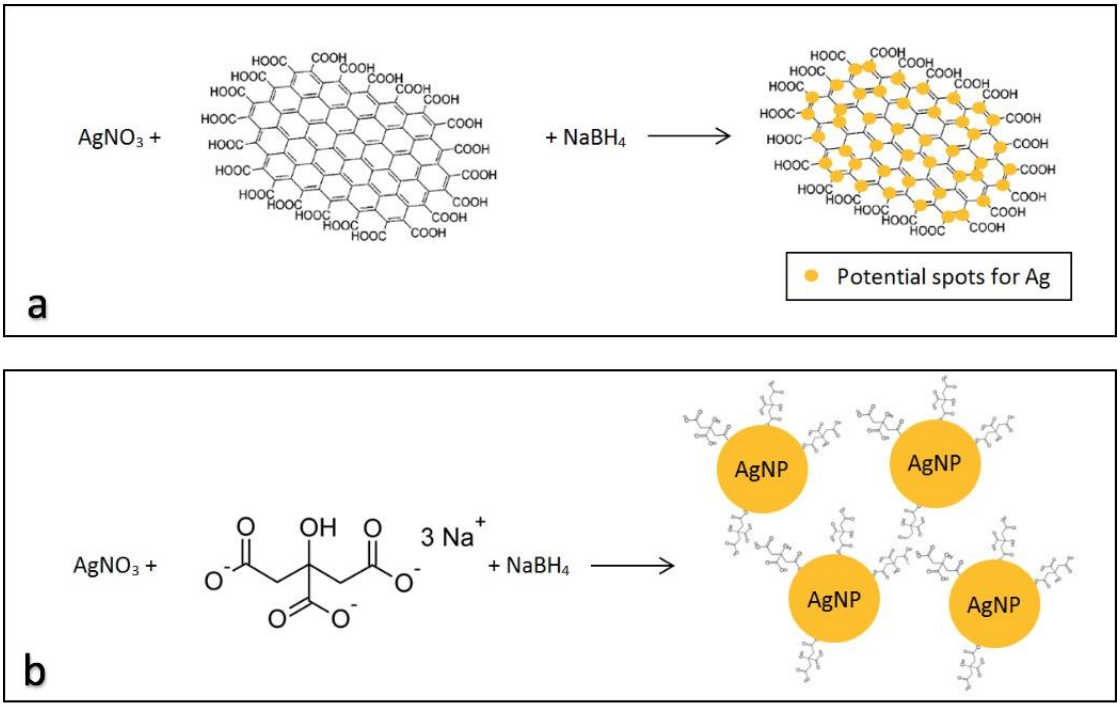

Figure 5.2 (a) In situ synthesis of Ag modified cx-GNFs, with yellow dots on cx-GNF sheets indicated for more "positive" carbon atoms, which are more favourable for the non-covalent charge transfer. (b) Scheme of Sodium Citrate as stabilizer to prevent AgNPs from aggregation. Since 20× mass of SC was added, multiple citrate ions were inserted on one AgNP, and the dispersion of AgNP was achieved due to steric effect.

Figure 5.3 illustrates a clear comparison in size and dispersity between different nanoparticles and confirmed that SC prevented the natural aggregation of AgNPs and AgAuNA effectively. The SEM images of as-made nanoparticles and SC stablilized nanoparticles were obtained after 1 day's natural aggregation for comparison. Unstabilised nanospecies aggregated heavily, with numerous big clusters larger than 100 nm appearing just 1 day after synthesis. SC stabilised nanospecies, also presented clusters larger than 100 nm were also presented, but the overall dispersity was higher and the size distribution was more even, with average size about 10 nm.

Compared with Figure 5.3E, SC stabilisation preserved the features of freshly made

colloidal nanoparticles.

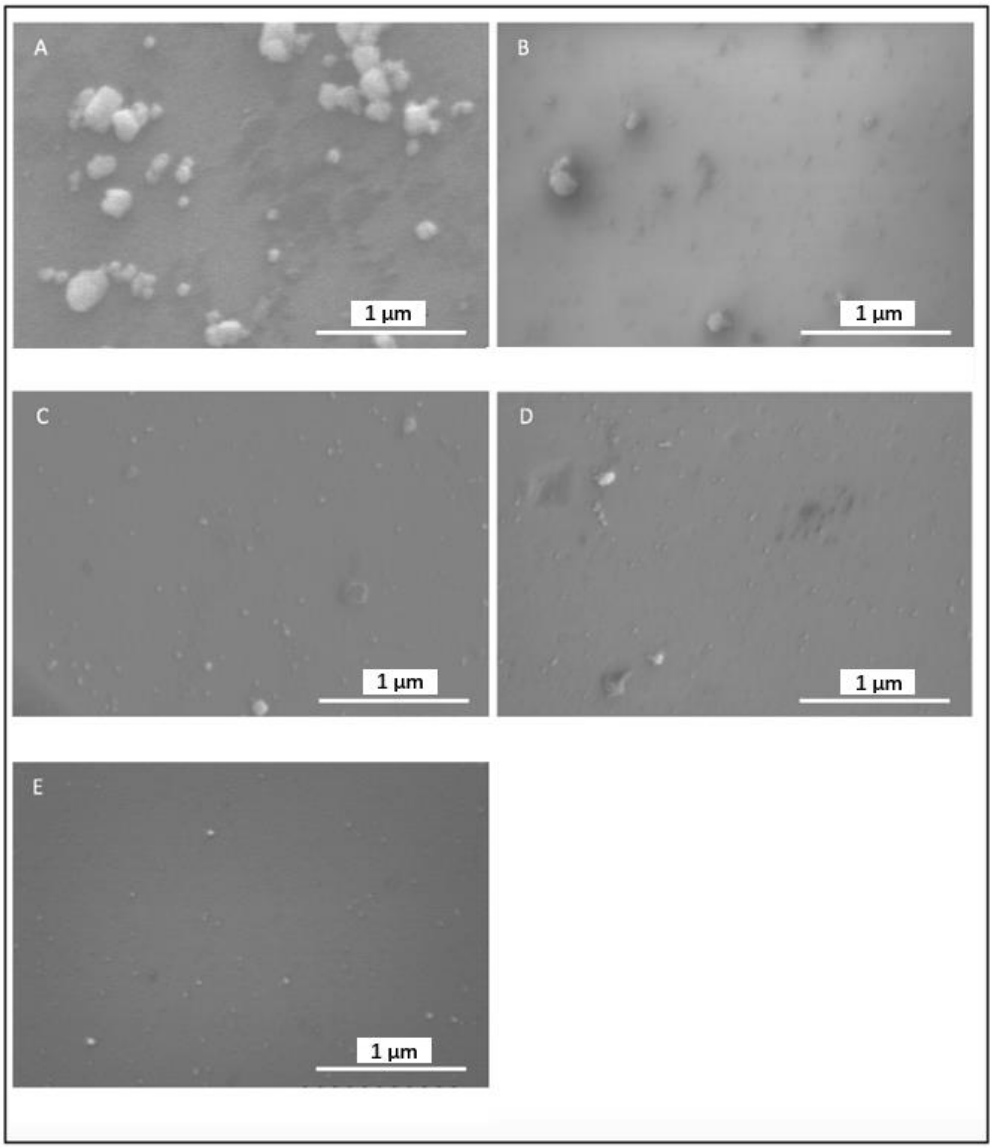

Figure 5.3 SEM images of natural aggregated AgNPs (A), AgAuNPs (B), and SC stabilized AgNPs (C), AgAuNPs (D). Images were obtained 1 day after of synthesis. E is the SEM image for freshly prepared AgNPs, the majority of the nanoparticles are too small and aggregations of ~20 nm are visible.

The individual size and overall distribution of cx-GNF modified nanoparticles was viewed by TEM since the particles appeared to be too small, and the charging problem persisted when attempted to observe them using SEM. As shown in Figure 5.4, AgGNF (4A and D), AuGNF (4B and E), and AgAuGNF (4C and F) were successfully modified on the graphene sheets of cx-GNF as expected. Although there was variation in local coverage from point to point, the overall dispersity of nanospecies was high. No aggregation or coupling was observed, and every nanoparticle has a well-defined spherical shape. The size of individual nanoparticles was very small, varing from 2.5 nm to 4 nm and was about the same across different types of metal/alloy nanospecies. It was obvious that the dispersity of cx-GNF stabilised species was a lot higher, and the average size was a lot smaller with smaller variance, compared with both unstablised and SC stabilised colloidal nanospecies. The observation showed that cx-GNF has superior performance for the dispersity of nano-species.

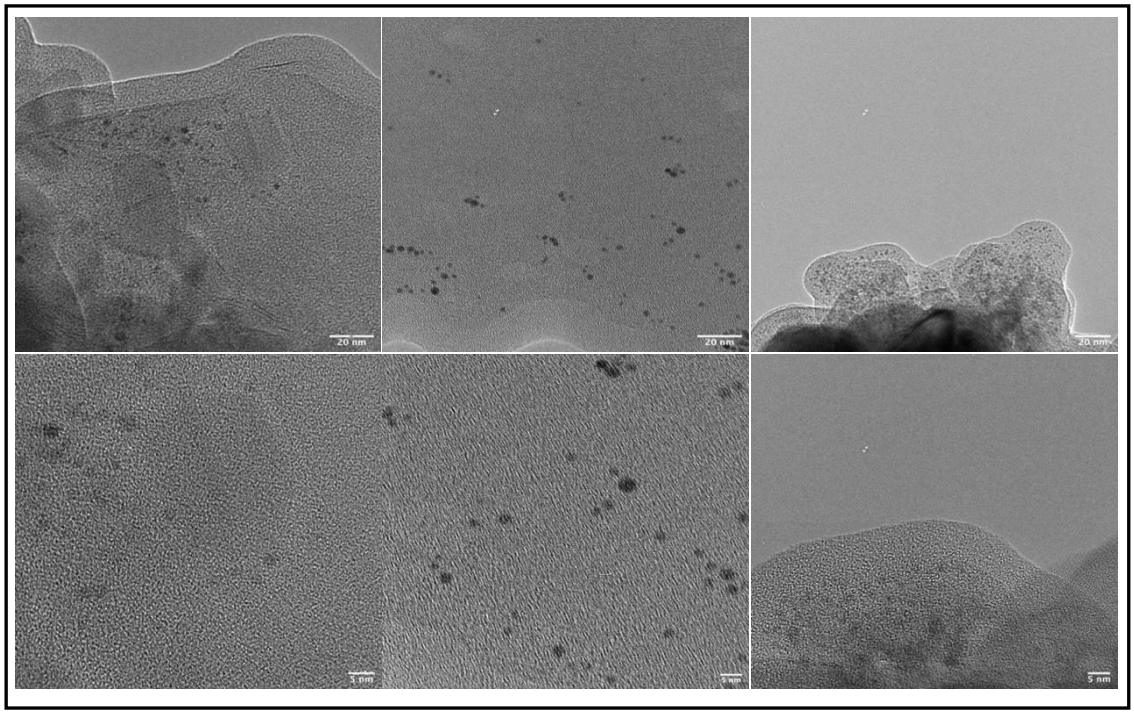

Figure 5.4 TEM images of freshly prepared cx-GNF stabilised nanospecies: AgGNF (A and D); AuGNF (B and E); and AgAuGNF (C and F).

The ability of preventing NP aggregation for a longer period of time was tracked via UV-Vis spectra over more than 14 days. The aggregation of Ag is successfully prevented if a sharp peak corresponding to plasmonic resonance of metal/alloy nanoparticles is observed and the position is fixed. AgGNF (Figure 5.5a) and AgAuGNF (Figure 5.5d) exhibited excellent stability for over 14 days. The plasmonic peak of AgGNF remained at 367 nm, while peak that corresponded to AgAu nanoalloy remained at 501 nm. However, the UV-Vis spectra of SC stabilized AgNPs showed shifted and the peaks became wider as days went by, indicating a natural aggregation had happened, which made the nanoparticles lose the plasmonic features (Figure 5.5c). This indicated that SC was an ideal candidate for preventing nanoparticle aggregation for only a shorter period of time. On the other hand, even when the SC stabilized nanoparticles were used during the days that the aggregation was not significant, it was hard to confirm the size and degree of dispersion of nanoparticles, since the shifting of UV-Vis peak was huge and unpredictable.

Afterward, the size effect of cx-GNF on preventing aggregation of nanoparticles was also investigated. cx-GNF flakes without dialysis are smaller in size and wider size distribution with an average size of 15 nm and are denoted as GNFs. They are more of a size appropriate to the metal nanoparticle itself (Figure 5.6) which could obviously influence the structure of the synthesized material. The stability of AgGNFs in a longer time span was also investigated (Figure 5.5b). AgNPs were adsorbed onto the GNF surface after modification, and a sharp plasmonic peak was observed at 401 nm, which

was preserved at the same position after 1 day's aggregation. However, as shown in Figure 5.5b, the peak got broader and faded out after 5 days. After 7 days, there was no defined peak observed, and the shape of the curve appeared more identical to that of GNFs. This suggested a separation of AgNPs and GNFs, and that AgNPs had aggregated on their own due to weakened bonding between the graphene and the Ag nanoparticle. Therefore, big flakes of cx-GNF are always desired to maximize the stability of nanoparticle modified nanocomposites.

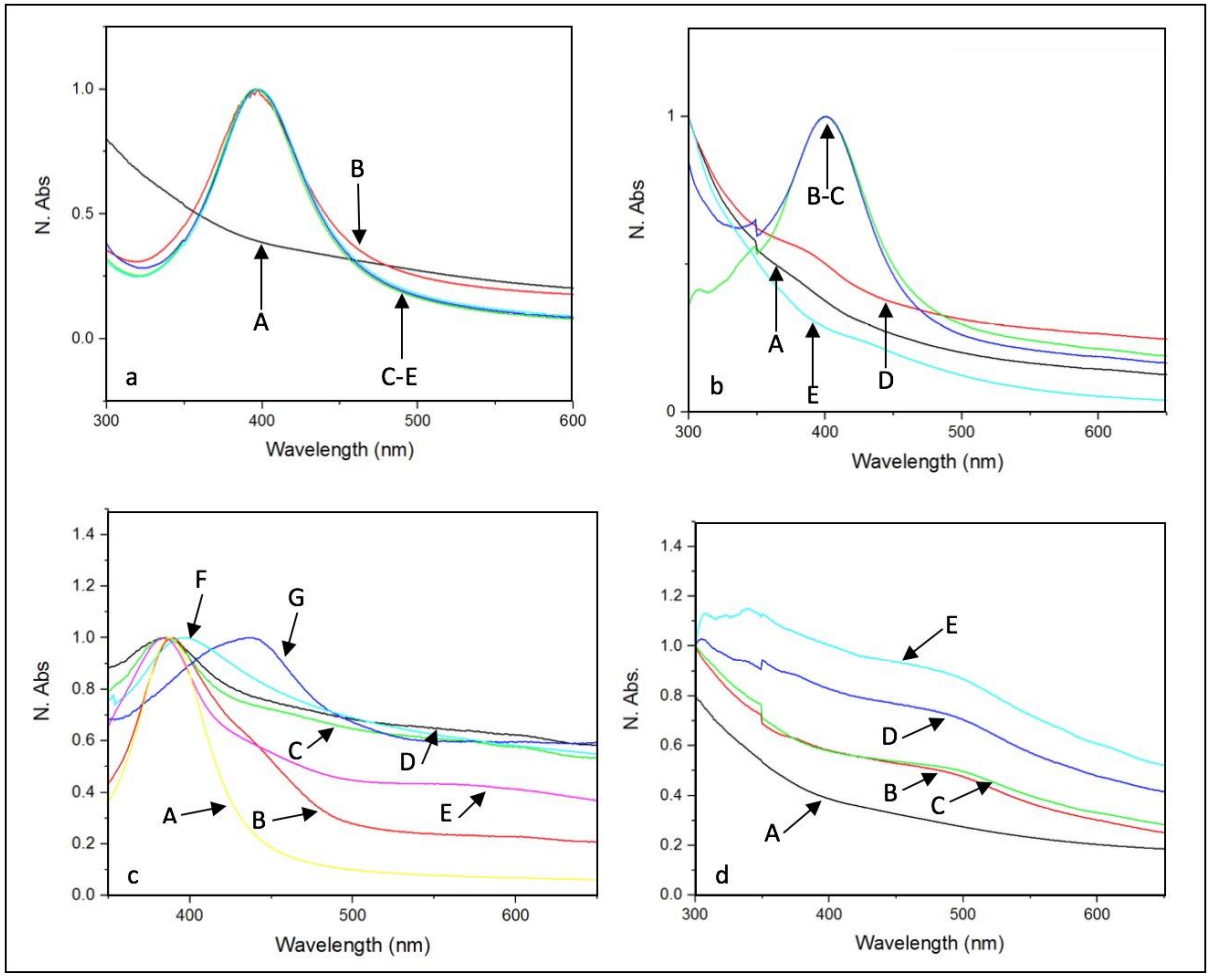

Figure 5.5 (a) UV-Vis spectra of cx-GNF stabilized AgNPs and the stability on preventing aggregation over 14 days. A: cx-GNF; B: fresh AgGNF; C-E: AgGNF naturally aged in room temperature for 1, 7 and 14 days. (b) UV-Vis spectra of AgNPs stabilised using non-dialysed small cx-GNF (denoted as cx-GNFs). A: cx-GNFs; B-C: fresh AgGNFs and AgGNFs aged for 1 day; D: AgGNFs aged for 7 days; E: AgGNFs aged for 14 days. (c) UV-Vis Spectra for SC stabilised AgNPs. A: fresh AgNPs; B: AgNPs+SC aged 1 day; C: AgNPs aged 1 day; D: AgNPs aged 7

days; E: AgNPs + SC aged 7 days; F: AgNPs aged 14 days; G: AgNPs + SC aged 14 days. (d) UV-Vis spectra of cx-GNF stabilised AgAuNAs. A: cx-GNF; B: fresh AgAuGNF; C: AgAuGNF aged 1 day; D: AgAuGNF aged 7 days; E: AgAuGNF Aged 14 days.

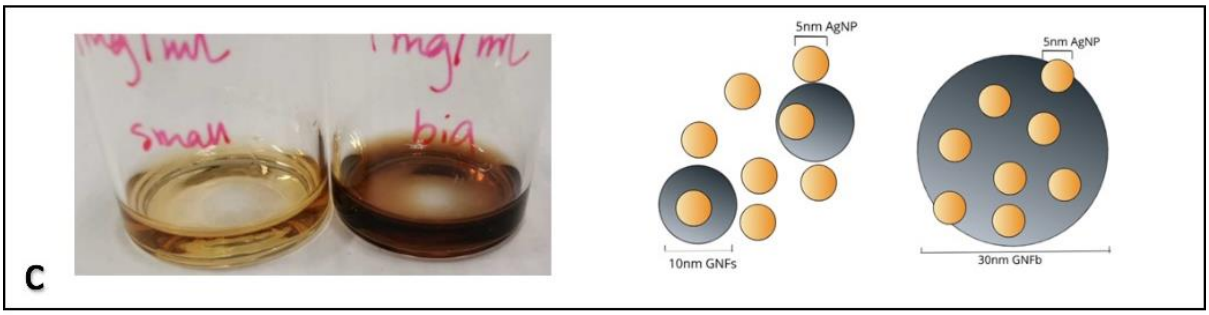

Figure 5.6 cx-GNF before and after dialysis with same density (1mg/mL), and the size-dependency of GNFs on interactions with AgNPs.

5.3.2 Surface Analysis using XPS

The colloidal nanocomposites were drop-coated on the BDDEs and XPS was performed to analyse the surface composition of colloidal AgNP, GNF, AgGNF and interaction pattern of Ag and GNF. Overall surface compositions were determined as described in chapter 2.

Table 5.1 Overall surface elemental composition of different nanocomposites drop-coated on BDDEs.

	% of C	**% of O**	**% of Ag**	**% of others**
AgNP	75.38	16.23	0.57	Na: 5.02; B: 2.79
AgNP+SC	74.40	18.80	0.71	Na: 5.31; N: 0.32 Cl: 0.46
AgGNF	54.51	31.59	3.94	Na: 7.61; N: 2.35

GNF	73.78	25.17	/	N: 1.45

Although the Ag concentration was kept the same, the detected amounts of Ag on the surface of AgGNF was 3.3-fold of that on AgNP. Since XPS is a method to identify only surface composition, aggregations of AgNP will result in smaller amounts of Ag detected than actually deposited (Figure 5.7).

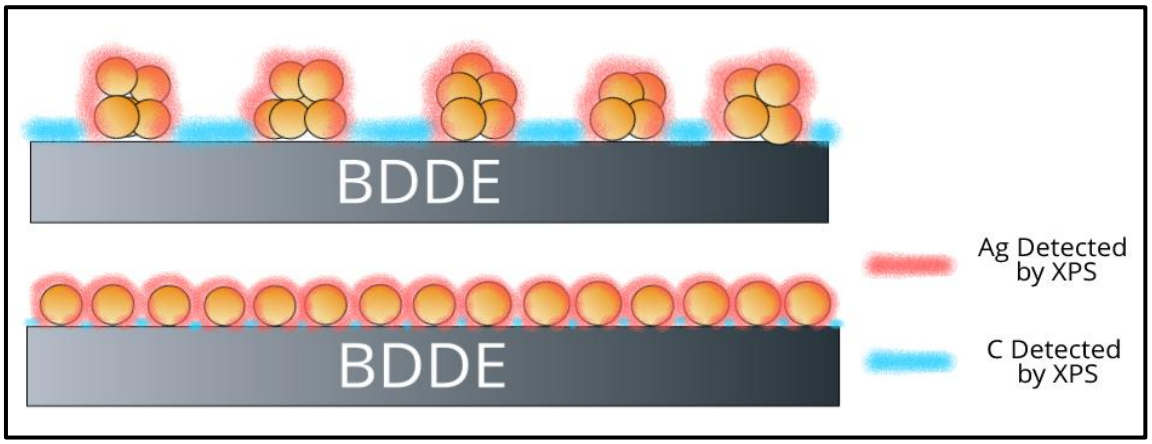

Figure 5.7 Ideogram showing how aggregation of AgNP will affect the amount of Ag detected from XPS analysis.

The carbon peaks of both AgGNF and cx-GNF consisted of 2 components: sp^2 carbon and carboxyl, which has a higher binding energy than sp^2 carbon[30-31]. On the other hand, the carbon peak of col. AgNP consisted of mainly sp^3 carbon, which is the surface of bare BDDE (Figure 5.6). Carbon 1s peaks of GNF and AgGNF also provided important information about the interactions between Ag and the cx-GNF surface. When metal is bonded to a carboxylate group, the binding energy of carboxylate carbons in XPS will be shifted to lower binding energy by 0.25 eV, which is not observed in our analysis. On the other hand, the silver has been successfully reduced to Ag (0) by adding excess amount of $NaBH_4$, which is confirmed from the Ag peak component, as more than 85% of pure Ag (0) was observed. However, when we compared Figure 5.8C and D, a newly formed peak at around 287.0 eV indicated M-π interactions between Ag and the graphenic basal

plane of cx-GNF, suggesting the interaction between Ag and cx-GNF is adsorption. The appearance of this peak can be explained by considering the electrostatic attraction between the less electronegative AgNP and the graphenic π electrons which create a local de-shielding effect. Moreover, as AgNPs are adsorbed to carbons on the basal plane, the relative peak intensities of carboxyl carbon compared to graphenic carbon has increased. [31]

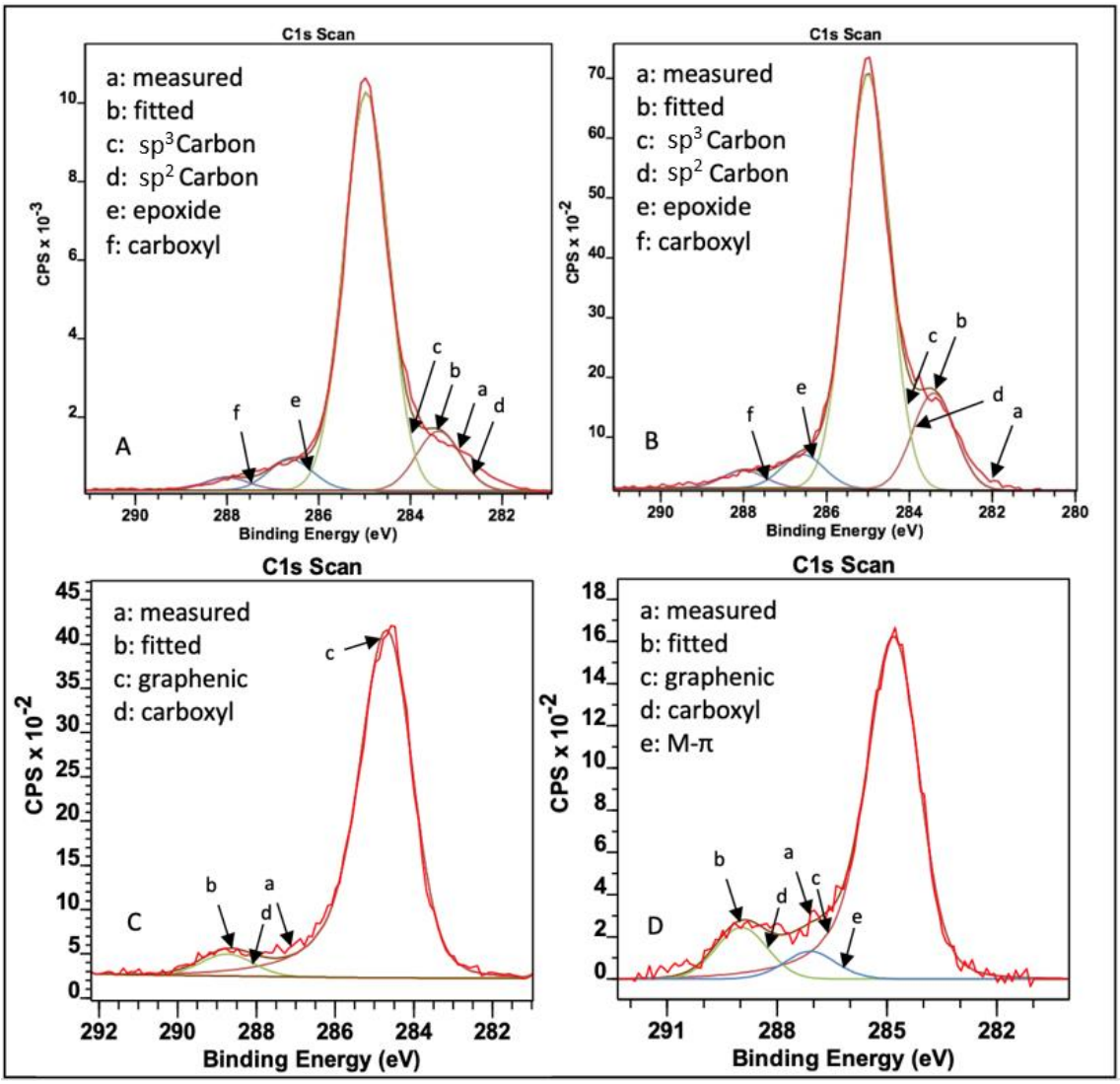

Figure 5.8 XPS Carbon Peaks of blank (A), AgNPs drop-coated (B), GNF drop-coated (C), and AgGNF drop-coated (D) BDDEs.

5.3.3 Electrocatalytic analysis using the HER as model

Similar to previous chapters, the catalytic activities of modified BDDEs during the HER were monitored using Linear Sweep Voltammetry LSV from 0 V to -2.0 V at 20 mV/s performed in 0.5 M sulfuric acid. Data for all nanocomposites are summarized in Table 5.2, including Tafel Slopes (averaged through 3 trails), and current responses at designated potentials. The current responses with respect to different potentials (-1.0 V for J_1 and -0.8 V for J_2 and averaged through 3 trails) applied and Tafel plots are presented in Figure 5.12 and 13, respectively.

Table 5.2 Summary of Tafel slope and current densities at different applied potentials of colloidal nano-species

	Tafel Slope (mV/dec)	**J_1 (mA/cm^2)**	**J_2 (mA/cm^2)**
AgNP	233±5	16±0.8	6±1
AgNP+SC	263±3	12±0.5	3±0.8
AgGNF	140±5	25±0.3	18±0.5
AgAuNP	154±8	20±1	6±0.5
AgAuNP+SC	182±6	18±0.3	4±0.3
AgAuGNF	138±5	30±0.5	24±0.3

Although all the the HERs catalysed by nanospecies in this study suggest Tafel-Volmer mechanisnms from the Tafel slope, the magnitude of Tafel slopes differed by a lot. The differences in Tafel slopes seems to reflect the aggregation of nanospecies. Compared with GNF stabilized species, the more intensive aggregation of bare Ag and AgAu

nanoparticles made the barrier for forming M-H even harder, therefore a higher Tafel slope for Volmer step is observed.[32]

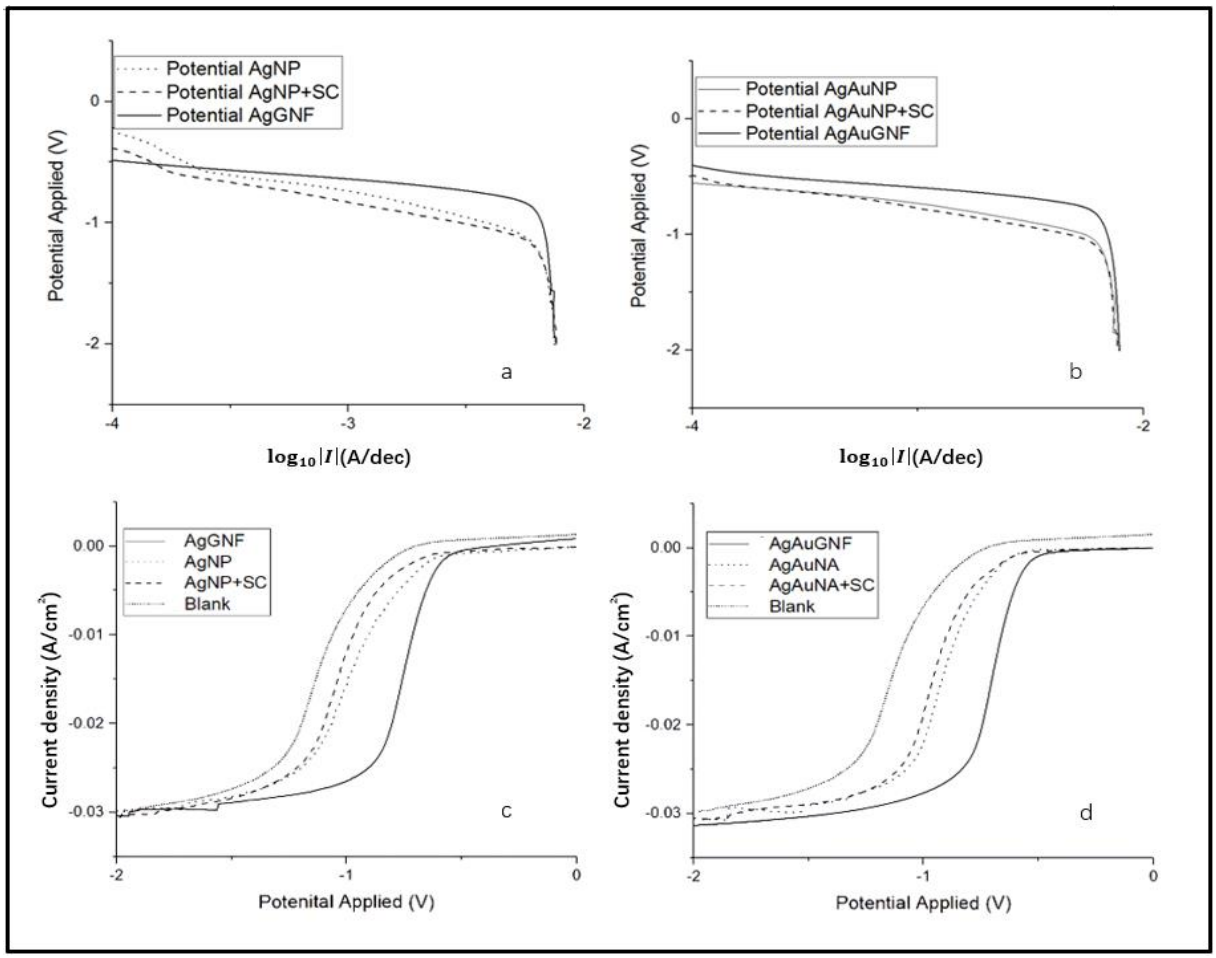

Figure 5.9 Tafel plot (a) and current density plot (c) of colloidal Ag nano-species; Tafel plot (b) and current density plot (d) of colloidal AgAu nano-species.

The current density plot showed GNF boosted the electrocatalysis of metal nanoparticles, illustrated by much higher current densities at designated potentials. As discussed before, when the nanoparticles are well-dispersed, the reactivity will be much higher due to the reduction of inter-particle diffusion plane coupling, and more available active sites resulted from the larger surface areas. However, although SC showed outstanding performance in preventing aggregations for both AgNP and AgAuNP, it hindered their

electrocatalytic activities. Due to the small size and excess amount of SC, the citrate ions formed a layer that covered up the metal nanoparticles, which further inhibited the conduction since the citrate ions themselves are not conducting. On the other hand, GNF provided extra conductivity to metal nanoparticles. Therefore, GNF modified species not only showed their merit in preserving the nanoparticle dispersity, but also making them more conductive and reactive in electrocatalysis.

5.3.4 Further Stabilisations and Catalytic Reactivities

Although metal-GNF nanocomposites showed good capacity in catalysing the HER, the high solubility of GNF, which is advantageous while drop-coating and cleaning electrodes, became a problem. The solvation of metal-GNF in electrolytes made the species not stable on the electrode, which resulted in poor signal and unpredictable results. One way to prevent the solvation was to form insoluble metal salts decorated with metal nanoparticles.

The influence of Ni (II) in the HER was examined using AuGNF-Ni as an example. After drop-coating AuGNF nanocomposites, the electrodes were immersed into 1.5 M Ni (II) solutions for 30 mins and rinsed with DI water to get rid of any excess nickel on top. The high concentration used ensured complete modification. An obvious colour change is observed, and a brown-greyish film is formed because of precipitation of Ni-GNF salt. After drying, the electrodes underwent the HER in acidic media (0.5 M sulfuric acid) following previous potentiostat setups. The treatment using Ni (II) significantly stabilised AuGNF at the surface of BDDEs, shown by enhanced current densities at designated

potentials because the more well-dispersed Au nanoparticles were able to stay on the surface of BDDEs and participate in catalysis (Figure 5.11).

Adding an external protective film of Nafion would be another way to stabilise AuGNF. Cx-GNF/Nafion (GNFNaf) nanopolymers with different weight percentage of cx-GNF: Nafion were prepared. After designated amounts of Nafion 117 solution were mixed with 0.5 mg/mL cx-GNF in 1:1 DI water: isopropanol solvent, the solutions were sonicated for 1 hour to ensure complete mixing and minimize aggregations.

In this case, AuGNF was not directly in contact with the electrolyte, but the electron transfer can happen. The hydrophilic acidic sidechains of Nafion provided excellent conductivity whereas the hydrophobic backbones stick with AuGNF to prevent the solvation. To prevent the aggregation of Nafion, which will cause insulation, GNF was again used as a stabiliser. The hydrophobic backbone of Nafion is naturally favoured to the graphene surface of GNF, and the hydrophilic heads are attached to carboxylic edges (Figure 5.10). The mixture of two composites in 1:1 DI water:isopropanol solvent with various weight compositions was sonicated for 1 hour to achieve a thorough mixing.

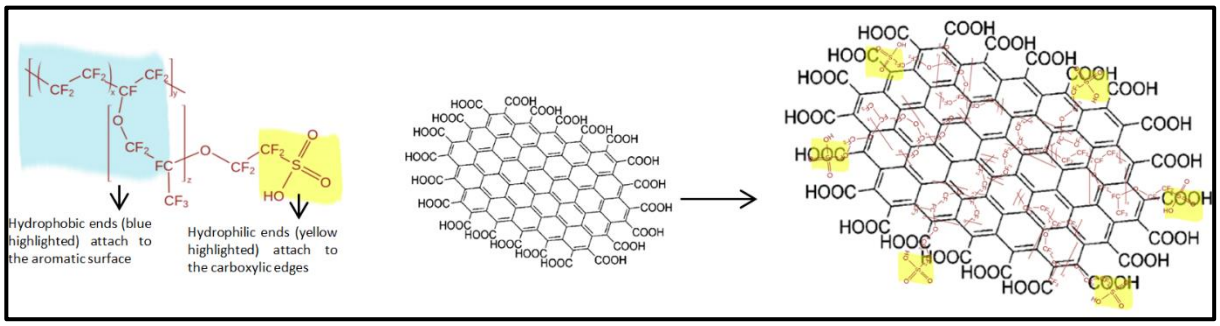

Figure 5.10 Formation of GNFNaf nanopolymer.

The effect of weight ratio of GNF: Nafion on catalysing performances in the HER was studied. GNFNaf nanocomposites with GNF: Nafion (wt ratio) 1:2, 1:4, 1:6, 1:8, 1:10, 1:15, 1:20 was synthesised and same volume of each solution was drop-coated on top of AuGNF modified BDDEs. The current density diagrams were recorded for each sample (Figure 5.11), and when GNF: Nafion was 1:8, the best catalytic reactivity was achieved. When there was less Nafion, the GNFNaf was still too soluble, and not as conducting. However, when there was too much Nafion in the polymer, the Nafion aggregated, and thus hindered the conduction again, therefore, it is crucial to find the optimal weight ratio.

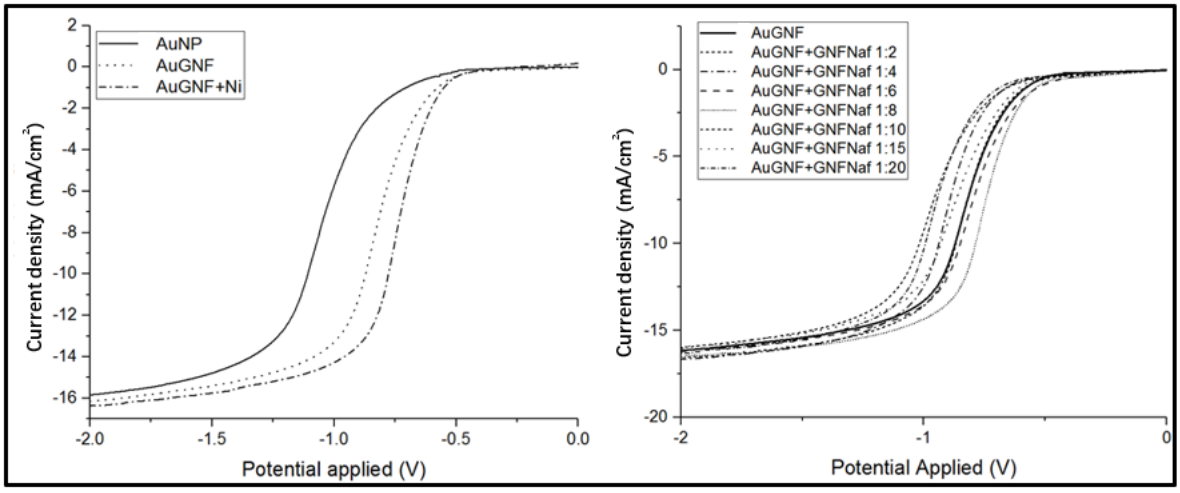

Figure 5.11 Catalytic performances of further stabilised AuGNF-BDDEs in the HER. Left: current density responses of AuNP, AuGNF, and AuGNF+Ni. Right: Current density responsies of GNFNaf stabilised AuGNFs with different GNF:Naf weight ratios.

Both methods, either by functionalising AuGNF itself, or provide an external conducting stabiliser, helped the AuGNF from possible solvation and therefore enhanced the performance of electrocatalysis. The current density responses at designated potentials were summarised in Table 5.3, each averaged over 3 samples, with error of $\pm$0.3~0.5 mA/cm^2).

Table 5.3 Summary of current density responses at designated potentials of stabilised AuGNF-BDDEs in the HER.

	J **(mA/cm^2) at -0.8 V**	***J*** **(mA/cm^2) at -1.0 V**
AuNPs	1.8	6.7
AuGNF	6.9	13.6
AuGNF-Ni	11.5	14.5
AuGNF+GNFNaf 1:2	3.0	10.3
AuGNF+GNFNaf 1:4	3.8	12.7
AuGNF+GNFNaf 1:6	7.7	13.7
AuGNF+GNFNaf 1:8	10.8	14.4
AuGNF+GNFNaf 1:10	6.9	13.5
AuGNF+GNFNaf 1:15	5.2	12.3
AuGNF+GNFNaf 1:20	2.7	10.7

5.4 Conclusion

Dispersity of colloidal nano-species is crucial in catalysis of fuel cell reactions like the HER, and to minimize the aggregation, external stabilisers are commonly used. In this chapter we propose an innovative yet simple in-situ reductive synthesis scheme of carboxylated graphene nanoflake (cx-GNF) stabilised Ag particles and AgAu nanoalloys. The resulting colloidal solutions were drop-coated onto BDD electrodes and their extraordinary stability and reactivity of cx-GNF containing nano-species were illustrated by comparing with unstabilised species and those stabilised with sodium citrate, a commonly used stabiliser for nanoparticles.

The formation of homogeneous Ag and AgAuGNF nanospecies was confirmed through UV-Vis spectra, and a subtle shift in plasmonic peaks compared with unstabilised ones indicated a non-covalent electrostatic interaction between the metal/alloy nanoparticles and the graphenic surface of cx-GNF. The microscopic structures of these nano-species were observed via SEM and TEM, showing that GNF stabilised species have smaller sizes of sub 5 nm and more even size distributions.

The continuous stabilisation effect of cx-GNF and SC were monitored through UV-Vis Spectra over two weeks. Colloidal AgGNF and AgAuGNF were extremely stable against natural aggregation by preserving a sharp and unshifted plasmonic peak. SC stabilised nanoparticles, although showing obvious stabilising effect in SEM, were not able to maintain the dispersity and the plasmonic peak faded away after several days. In this part, we also investigated how the difference in sizes of cx-GNF could influence the aggregation. cx-GNF before dialysis has a smaller average size, and when they were used as stabilisers, they could not sustain the nano-species

The surface compositions of the modifiers were investigated using XPS. A higher amount of surface Ag in AgGNF confirmed a better dispersion compared to unstabilised and SC stabilised Ag nanoparticles. More importantly, the carbon 1s peak of AgGNF indicated our proposed scheme of how metal nanoparticles are adhered to cx-GNF surface. A subtle peak indicating metal-π bonding is presented in between peaks of graphenic carbon and carboxylates carbon.

The electrocatalytic abilities of the stabilized species were afterward examined using the HER as an example to investigate the role and effect of GNF. Compared with both as-

made natural aggregated and sodium citrate stabilized nano species, GNF stabilized species exhibited larger current response at designated potentials, as well as more positive on-set potentials and low Tafel slopes in the HER catalysis whereas sodium citrate hindered surface electrochemistry of the nanospecies because they made the surface less conductive. Therefore, it is not a perfect stabiliser for colloidal nanoparticles in electrochemical reactions.

cx-GNF, as we can predict by its structure, is very soluble in aqueous phase. Although performing the HER under acidic conditions can immobilise the cx-GNF stabilise nanospecies onto electrode, meaning they will not be ionized in solution and react with electrolytes, there might still be room to prevent the loss in material at the electrode surface to the solution and make it more versatile in different conditions. Therefore, extra stabilisations were performed to prevent solvation. Ni^{2+} ions were used as an internal stabiliser by forming a non-soluble precipitate without disturbing the dispersion of metal nanoparticles. Nafion, on the other hand, is used as an external stabiliser. GNF-Nafion nanopolymers with different weight rations were synthesised and coated on previously modified BDDEs. In both cases, current densities of the HER were further promoted, and GNFNaf nanopolymer with a weight ratio of 1:8 is the most optimal external stabiliser.

References

(1) Song, K.; Lee, S.; Park, T.; Lee, B. Preparation Of Colloidal Silver Nanoparticles By Chemical Reduction Method. *Korean Journal of Chemical Engineering* 2009, 26 (1), 153-155.

(2) Chen, H.; Liu, R.; Jang, L.; Lee, J.; Hu, S. Characterization Of Core–Shell Type And Alloy Ag/Au Bimetallic Clusters By Using Extended X-Ray Absorption Fine Structure Spectroscopy. *Chemical Physics Letters* 2006, 421 (1-3), 118-123.

(3) Gao, J.; Huang, X.; Liu, H.; Zan, F.; Ren, J. Colloidal Stability Of Gold Nanoparticles Modified With Thiol Compounds: Bioconjugation And Application In Cancer Cell Imaging. *Langmuir* 2012, 28 (9), 4464-4471.

(4) Zhu, Y.; Murali, S.; Cai, W.; Li, X.; Suk, J.; Potts, J.; Ruoff, R. Graphene And Graphene Oxide: Synthesis, Properties, And Applications. *Advanced Materials* 2010, 22 (35), 3906-3924.

(5) Cai, W.; Zhu, Y.; Li, X.; Piner, R.; Ruoff, R. Large Area Few-Layer Graphene/Graphite Films As Transparent Thin Conducting Electrodes. *Applied Physics Letters* 2009, 95 (12), 123115.

(6) Zhang, S.; Gai, S.; He, F.; Ding, S.; Li, L.; Yang, P. In Situ Assembly Of Well-Dispersed Ni Nanoparticles On Silica Nanotubes And Excellent Catalytic Activity In 4-Nitrophenol Reduction. *Nanoscale* 2014, 6 (19), 11181-11188.

(7) TANG, Z.; YIN, X.; ZHANG, Y.; ZHANG, N.; XU, Y. Inhibiting Pd Nanoparticle Aggregation And Improving Catalytic Performance Using One-Dimensional CeO_2 Nanotubes As Support. *Chinese Journal of Catalysis* 2013, 34 (6), 1123-1127.

(8) Ansar, S.; Kitchens, C. Impact Of Gold Nanoparticle Stabilizing Ligands On The Colloidal Catalytic Reduction Of 4-Nitrophenol. *ACS Catalysis* 2016, 6 (8), 5553-5560.

(9) Ranoszek-Soliwoda, K.; Tomaszewska, E.; Małek, K.; Celichowski, G.; Orlowski, P.; Krzyzowska, M.; Grobelny, J. The Synthesis Of Monodisperse Silver Nanoparticles With Plant Extracts. *Colloids and Surfaces B: Biointerfaces* 2019, *177*, 19-24.

(10) Ranoszek-Soliwoda, K.; Tomaszewska, E.; Socha, E.; Krzyczmonik, P.; Ignaczak, A.; Orlowski, P.; Krzyzowska, M.; Celichowski, G.; Grobelny, J. The Role Of Tannic Acid And Sodium Citrate In The Synthesis Of Silver Nanoparticles. *Journal of Nanoparticle Research* 2017, 19 (8).

(11) Shen, X.; Wang, G.; Hong, X.; Zhu, W. Nanospheres Of Silver Nanoparticles: Agglomeration, Surface Morphology Control And Application As SERS Substrates. P*hysical Chemistry Chemical Physics* 2009, 11, 7450.

(12) Liu, J.; Cui, L.; Losic, D. Graphene And Graphene Oxide As New Nanocarriers For Drug Delivery Applications. *Acta Biomaterialia* 2013, 9, 9243-9257.

(13) Cheng, S.; Chiu, H.; Kumar, P.; Hsieh, K.; Yang, J.; Lin, Y.; Shen, Y.; Chen, G. Simultaneous Drug Delivery And Cellular Imaging Using Graphene Oxide. *Biomaterials Science* 2018, 6, 813-819.

(14) Muszynski, R.; Seger, B.; Kamat, P. Decorating Graphene Sheets With Gold Nanoparticles. *The Journal of Physical Chemistry C* 2008, 112, 5263-5266.

(15) Li, Y.; Tang, L.; Li, J. Preparation And Electrochemical Performance For Methanol Oxidation Of Pt/Graphene Nanocomposites. *Electrochemistry Communications* 2009, 11, 846-849.

(16) Shi, L.; Li, Y.; Rong, X.; Wang, Y.; Ding, S. Facile Fabrication Of A Novel 3D Graphene Framework/Bi Nanoparticle Film For Ultrasensitive Electrochemical Assays Of Heavy Metal Ions. *Analytica Chimica Acta* 2017, 968, 21-29.

(17) Chen, X.; Wu, G.; Chen, J.; Chen, X.; Xie, Z.; Wang, X. Synthesis Of "Clean" And Well-Dispersive Pd Nanoparticles With Excellent Electrocatalytic Property On Graphene Oxide. *Journal of the American Chemical Society* 2011, 133, 3693-3695.

(18) He, Y.; Chen, Q.; Yang, S.; Lu, C.; Feng, M.; Jiang, Y.; Cao, G.; Zhang, J.; Liu, C. Micro-Crack Behavior Of Carbon Fiber Reinforced Fe_3O_4/Graphene Oxide Modified Epoxy Composites For Cryogenic Application. *Composites Part A: Applied Science and Manufacturing* 2018, 108, 12-22.

(19) Shubhadarshinee, L.; Jali, B.; Barick, A.; Mohapatra, P. Preparation And Characterisation Of Silver Nanoparticles/Graphene Oxide Hybrid Nanofiller Reinforced-Polyaniline. *Plastics, Rubber and Composites* 2021, 1-13.

(20) Georgakilas, V.; Vrettos, K.; Katomeri, K.; Kouloumpis, A.; Dimos, K.; Gournis, D.; Zboril, R. Highly Dispersible Disk-Like Graphene Nanoflakes. *Nanoscale* 2015, *7* (37), 15059-15064.

(21) Salzmann, C.; Nicolosi, V.; Green, M. Edge-Carboxylated Graphene Nanoflakes From Nitric Acid Oxidised Arc-Discharge Material. *J. Mater. Chem.* 2010, *20* (2), 314-319.

(22) Rosillo-Lopez, M.; Salzmann, C. Highly Efficient Heavy-Metal Extraction From Water With Carboxylated Graphene Nanoflakes. *RSC Advances* 2018, 8, 11043-11050.

(23) Lu, P.; Yu, J.; Lei, Y.; Lu, S.; Wang, C.; Liu, D.; Guo, Q. Synthesis And Characterization Of Nickel Oxide Hollow Spheres–Reduced Graphene Oxide–Nafion Composite And Its Biosensing For Glucose. *Sensors and Actuators B: Chemical* 2015, 208, 90-98.

(24) Choi, B.; Im, J.; Kim, H.; Park, H. Flow-Injection Amperometric Glucose Biosensors

Based On Graphene/Nafion Hybrid Electrodes. *Electrochimica Acta* 2011, 56, 9721-9726.

(25) Umadevi, D.; Sastry, G. Molecular And Ionic Interaction With Graphene Nanoflakes: A Computational Investigation Of CO_2, H_2O, Li, Mg, Li^+, And Mg^{2+} Interaction With Polycyclic Aromatic Hydrocarbons. *The Journal of Physical Chemistry C* 2011, 115 (19), 9656-9667.

(26) Soroush, A.; Ma, W.; Silvino, Y.; Rahaman, M. Surface Modification Of Thin Film Composite Forward Osmosis Membrane By Silver-Decorated Graphene-Oxide Nanosheets. *Environmental Science: Nano* 2015, 2, 395-405.

(27) Chen, H.; Liu, R.; Jang, L.; Lee, J.; Hu, S. Characterization Of Core–Shell Type And Alloy Ag/Au Bimetallic Clusters By Using Extended X-Ray Absorption Fine Structure Spectroscopy. *Chemical Physics Letters* 2006, 421 (1-3), 118-123.

(28) Ustinovshchikov, Y. Ionic Bond ⇄ Covalent Bond Electron Transitions In Alloys. Russian Metallurgy (Metally) 2018, 2018, 287-293.

(29) Agnihotri, S.; Mukherji, S.; Mukherji, S. Size-Controlled Silver Nanoparticles Synthesized Over The Range 5–100 nm Using The Same Protocol And Their Antibacterial Efficacy. *RSC Adv.* 2014, *4* (8), 3974-3983. (reduce, plasmonic resonance)

(30) Bar-Tow, D. A Study Of Highly Oriented Pyrolytic Graphite As A Model For The Graphite Anode In Li-Ion Batteries. *Journal of The Electrochemical Society* 1999, 146 (3), 824.

(31) Rosillo-Lopez, M.; Lee, T.; Bella, M.; Hart, M.; Salzmann, C. Formation And Chemistry Of Carboxylic Anhydrides At The Graphene Edge. *RSC Advances* 2015, 5, 104198-104202.

(32) Shinagawa, T.; Garcia-Esparza, A.; Takanabe, K. Insight On Tafel Slopes From A Microkinetic Analysis Of Aqueous Electrocatalysis For Energy Conversion. *Scientific Reports* 2015, 5.

Chapter 6 Enhanced Electrochemical Sensing Performances of Carboxylated Graphene Nanoflake Stabilised Au Nanoparticles

6.1 Introduction

Molecular sensing is a very important field of research and has gained increasing interest over the recent decades since it is very meaningful for both understanding a complicated system and monitoring the processing of materials under certain reactions. [1-3] Enzyme-based glucose sensors, for example, have been widely commercialized nowadays.[4] With the rising concern of environmental crisis, the detection of toxic materials, such as heavy metals and organic pollutants have raised interest of many.[5-8]

Compared to traditional sensing methods (including colorimetric and luminescent sensing), electrochemical sensing has advantages including easy assembly, flexibility, rapid response, high sensitivity, and selectivity.[9] Metal nanoparticles are popular agents used for molecular sensing as their high surface to volume ratio compared to macromolecules provides much more active surfaces. [10-13] Molecular sensors implemented with nanoparticles are found in broad use in detection of gas molecules, heavy metals, biomedical toxicants, bacteria, viruses, proteins, DNA, and even macro cancer cells. [14-17] Biochemical detection, electrodes modified with metal nanoparticles make the electron transfer process faster, the over-potentials are reduced, and thus the redox process is more kinetically favored. This is very crucial when molecules with very low concentrations are being detected or detecting a target molecule in a mixture with

other interfering molecules.[18]

Colloidal Au nanoparticles are one of the most common types of nanoparticles used for electrochemical sensing. In recent studies, electrochemical sensors implemented with AuNPs showed their versatility and have been applied in various scenarios such as detections of small molecules like hydrogen peroxide and CO and CO_2 gas molecules, and metal ions like Hg (II), Cr (III) and Pb (II)[19-21]. As an excellent biotag, AuNPs are perfect for biomedical detections from smaller species like thiocyanate, quercetin, to macro-DNA and proteins[22-26]. The selectivity and sensitivity can be ensured by modifications of colloidal Au nanoparticles – functional modifications including DNA and antigen modification targeted specific biospecies[27-28], and structural modification like Au nanoarrays increase the surface area and active reaction spots on the macro electrode[29]. As discussed in the previous chapter, the dispersion of colloidal nanoparticles directly affects their performance in electrochemical experiments, therefore it is crucial to prevent colloidal AuNPs from natural aggregation in electrochemical sensing. We have shown that cx-GNF was able to provide outstanding stabilizing effect for nanospecies and AgGNF and AgAuGNF showed better dispersion than both unstablized colloidal ones and electrodeposited ones. Here we report the synthesis and applications of AuGNF, following the same procedure in chapter 5, for electrochemical detection of As (III) ions, 4-nonylphenol, glucose, and hydroquinone.

Arsenic is widely distributed in nature, including rock, soil, and air (when coals containing As were burnt).[30-31] Both organic and inorganic arsenic compounds such as arenite, arsenate, and dimethylated arsenosugars are hard to degenerate, however, the

most problematic arsenic exposure was through drinking water due to its high water solubility.[32-33] Because of that, As(III) is listed as one of the most toxic metal ions by WHO (World Health Organization). Arsenic exposure via drinking water has severe neurotoxicity and is directly increasing the rate of chronic diseases including bladder and skin cancer.[33-35] According to WHO, the recommended level of drinking is set at 10 μg/L.[35] Detection of trace As ions in aqueous solution can be done using inductive coupled plasma mass spectroscopy with a limit of detection (LOD) down to nanomolar but its high cost and limited mobility make electrochemical detection the more optimal technique. Past studies used AuNPs supported on carbon electrodes for As detection, and the performace could be enhanced using AuCNT (AuNP modified nanotubes) instead, or with other external stablisers.[36-39]However, the formation of AuCNTs and other stabilised forms of AuNPs involved a long procedure of synthesis and large number of reagents.[37-39]

As one of the most common ingredients of dish detergents, 4-nonylphenol can also be found in surface water.[40] It is believed that alkylphenols (including 4-nonylphenol) are one group of the potentially estrogenic molecules that can mimic the action of endogenous estrogen and disrupt the regular activity of estrogen-responsive genes [41] and its acute toxicity will cause irregular morphology of secondary sex characteristics and other poisonous effect in fish species.[41-42] Currently the quantitative detections of nonylphenol in labs are mostly done by HPLC, which requires long processing time and expensive instruments.[43] Other detection methods like magnetic solid-phase extraction using Mg-Al-layered double hydroxide (Mg-Al-LDH) modified nanoscale zero-valent iron (NZVI)

(Fe@MgAl-LDH) demands long and sophisticated synthesis procedures of the magnetic nano species.[44]

Nowadays, diabetes has become a worldwide problem. Specifically in UK, about 7 of 100 people are living under diabetes, and statistics in 2019 has illustrated that there is an inclination towards the younger generation with 1.1 million children are living with type I diabetes.[45] The blood sugar level is the most direct and important index to diagnose diabetes. Since 1960s, enzyme biosensors have been used for blood sugar detection.[46] Although they are very sensitive, prevalent, and specific to glucose molecules, their lack of stability has always been a big problem and scientists have not ceased to improve their performance by various means.[47-49] Nowadays, studies of non-enzyme biosensors for glucose electrochemical detections are attracting more attention and have all shown excellent performance, including Pt and Au containing alloys[50], carbon nanotubes[51], and polyaniline modified electrodes[52]. The structures of nanoparticles are experiencing a revolution to lower the cost and nanostructured metal nanoparticles such as porous gold nanotube arrays and foam gold nanocomposites show advantage in enhancing signals with limited amount of metal.[53-54]

Hydroquinone (1,4-benzenediol, HQ) and catechol (1,2-benzenediol, CAT) are widely used in areas including cosmetics, pesticides, medicines and photography agents.[56-57] However, their toxicity to human beings, aquatic and soil organisms is not negligible and can cause stress of ecological degeneration.[57-59] Therefore, the concentrations of them in environment samples should be closely monitored. The major difficulty faced by the researchers during detection is the mixing and mutual interference of HQ and CAT due

to the similarities in structure, activity, and various behaviours.[56-57] Various techniques are presented to detect trace amount of these two chemicals, including florescence, chromatography, and chemiluminescence but the disadvantages including expensive instruments, sophisticated preparation and analysis procedures again make electrochemical detection more favorable.[60-63] In the case of HQ and CAT detections, high sensitivity and selectivity are equally necessary. Different nanomaterials are implemented, including graphite mesoporous carbon, Ti_3C_2/MWCNTs nanocomposites, and porous AuNPs[64-66] but there is still plenty of room to explore for synthesis and detection with minimal operation and pre-treatment.

6.2 Aim of this Chapter

In previous chapters, we have confirmed cx-GNF is an extraordinary stabiliser for metal nanoparticles including Ag, Au and nanoalloys. The active surface area and conductivity were shown to be improved with this carbon-based stabiliser. These features, together with the economic cost, safe procedure, high sensitivity, and selectivity are also very crucial for electrochemical sensing. Therefore, it is going to be very meaningful to have a nanoparticle detection reagent that requires fewer synthesis steps yet retains the virtues of high reaction area and high conductivity. Throughout this series of experiments, our modified electrode will have a more pronounced application in wider field other than fuel cell chemistry.

To do that, we synthesized cx-GNF stabilized colloidal AuNPs (AuGNF) and drop-coated them onto BDDE. Specifically, we focused on the electrochemical detection of three

chemical species that are very crucial for the environment and human bodies: As (III) ion, 4-nonylphenol, and glucose, and various detection methods including CV, DPV and SWV were used to push down the detection limit. We also investigated the effect of pH in detection to decide the most optimal conditions, and the influence of external stabilisation of cx-GNF modified nanoparticles using Ni (II) ions. The most optimal loading of AuGNF nanoparticles on the electrode was also proposed through experiments. The detection of the target molecule with interfering species present was also achieved, confirming the high sensitivity and selectivity of cx-GNF modified BDDEs.

6.3 Results and Discussions

6.3.1 Synthesis and Characterisations of AuGNF Modified BDDE

Colloidal AuGNF nanoparticles were synthesized via the same scheme as in chapter 5, though a a single-step reduction by $NaBH_4$ in icebath. 1 mM $HAuCl_4$ was chosen to be the source of Au (III) and mixed with cx-GNF water solution (0.5 mg/mL) before being reduced. The volume ratio of metal solution: cx-GNF solution was 1:1, and the concentration of $NaBH_4$ was 5 mM. Afterwards, Metal + GNF solution was added dropwise into chilled $NaBH_4$ solution and wrapped with aluminum foil for storage. The original Au^{3+} solution appeared bright yellow, and when mixed with dark brown cx-GNF water solution, it turned into a yellow-ish brown. The resulting colloidal AuGNF solution appeared reddish-brown and was characterized by UV-Vis spectra to confirm its

homogeneity and stability (Figure 6.1). Colloidal AuNPs were also synthesized,

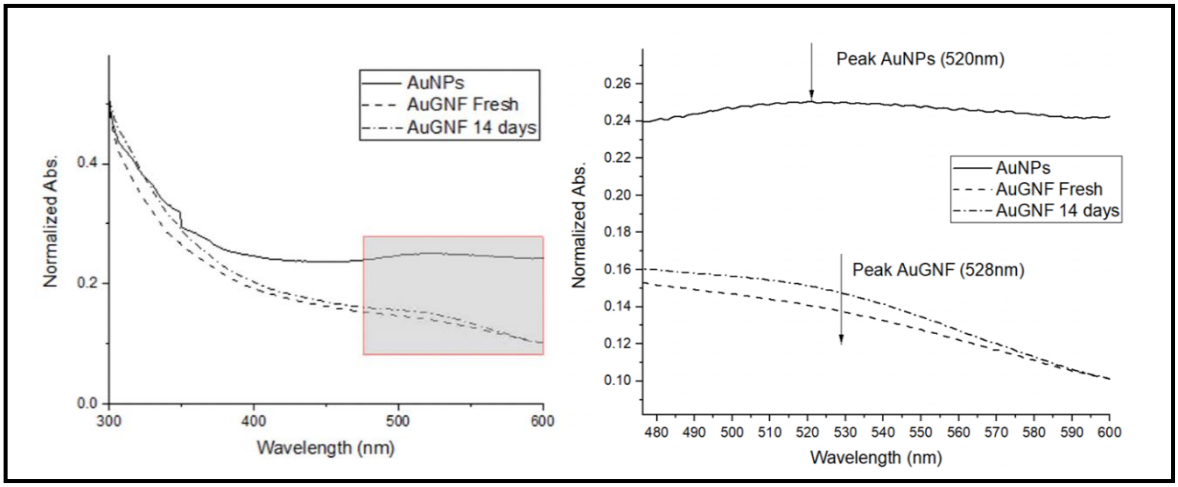

exchanging cx-GNF water solution with same volume of DI water.

Figure 6.1 UV-Vis spectra of colloidal species: AuNPs, AuGNF (fresh), and AuGNF (after 14 days); and a zoom graph of the peak area (right).

The freshly made AuNPs has a plasmonic peak at around 520 nm, indicating their was about 5-10 nm. [67]. The cx-GNF stabilisation preserved this clear plasmonic peak and no other peak was observed, meaning homogeneous AuGNF was successfully synthesized. Notably, there's a redshift of this plasmonic peak from 520 nm to 528 nm, originating from the interaction between metal nanoparticles and the graphene surface. The formation of this phenomenon was explained more thoroughly in chapter 5 therefore will not be repeated here. [68] The freshly made AuGNF was kept in a capped glass vial wrapped with aluminium foil and left at room temperature for 14 days. The UV-Vis spectrum of AuGNF after 14 days was also obtained. The aged AuGNF did not lose its plasmonic peak, and the position of the plasmonic peak did not shifted within 14 days, which confirmed the stability of cx-GNF modified AuNPs. On the other hand, visible aggregations appeared

for the unstabilised colloidal AuNPs after only 1 day.

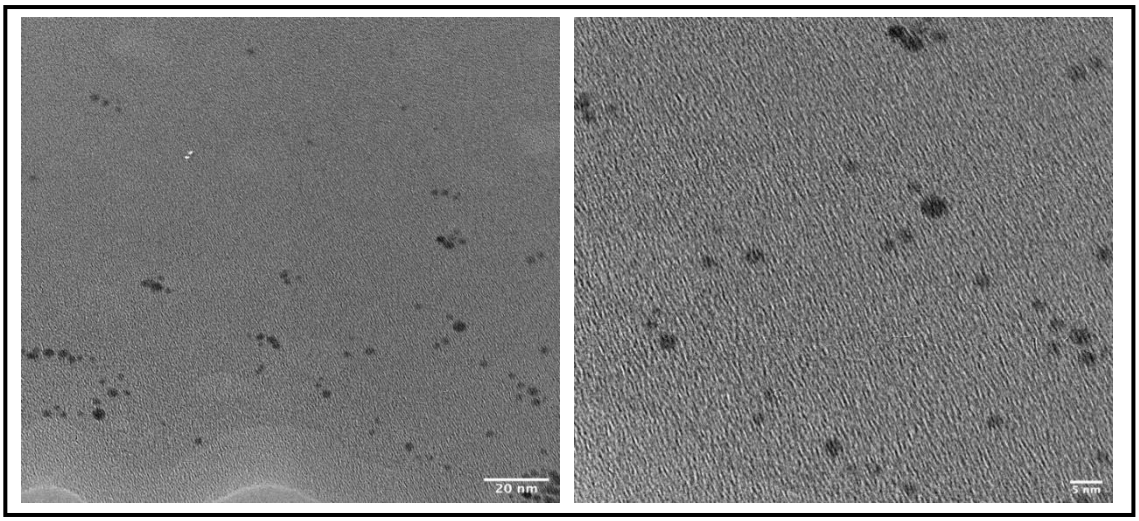

Figure 6.2 TEM images of fresh AuGNF.

After the confirmation of successful synthesis and stability, the size of freshly made AuGNF was observed through TEM (Figure 6.2). A small amount of colloidal solution was dropped onto a TEM grid using a drop pipette and dried for 10 minutes before transferred into the TEM. From the TEM image at a larger scale, the AuGNF are well dispersed on the cx-GNF surface, and no aggregation was observed, and the spreading was even at different positions.

On the other hand, from the higher magnification image, we could confirm the size of the nanoparticles. The variance of size between individual nanoparticles was not huge. Most of the nanoparticles were below 5 nm, and the average size was about 4.1 nm. This is coherent with the sizes of AgGNF and AgAuGNF nanoparticles we synthesized in chapter 5, and again confirmed this simple 1-step reduction scheme with cx-GNF modification was able to produce fine nanospecies with high mono-dispersity that are suitable for many electrochemical applications.

The surface composition of AuGNF was examined using XPS and compared with that of

colloidal AuNPs and electrodeposited AuNPs. 20μL of AuGNF and unstabilized AuNPs, both containing 2.8 nmol Au were drop-coated using a volumetric pipette onto BDDE and dried before XPS analysis. The electrodeposited AuNPs (ED AuNPs) were synthesized using the same technique mentioned in chapter 4, and 3 nmol of Au was deposited, which was comparable to the colloidal ones.

Table 6.1 Summary of XPS data on survey spectra

Sample	**Au%**	**C%**	**O%**	**Others%**
ED AuNPs	1.8	92.3	5.8	/
AuNPs	1.3	60.0	25.8	N: 0.7 Na: 6.8 B: 5.4
AuGNF	2.7	48.1	31.8	Na: 8.8 B: 8.6

From the survey spectrum of these three samples, we can once again confirm the stabilising effect of cx-GNF in AuGNF synthesis, since the surface amount of Au is higher than other two samples, meaning the nanoparticles are more dispersed with minimal aggregation. On the other hand, the percentage of oxygen in AuGNF went up compared with the other two samples. This originated from the carboxyl groups at the edge of cx-GNFs. The Na and B compositions in colloidal samples are from the reducing agent $NaBH_4$.

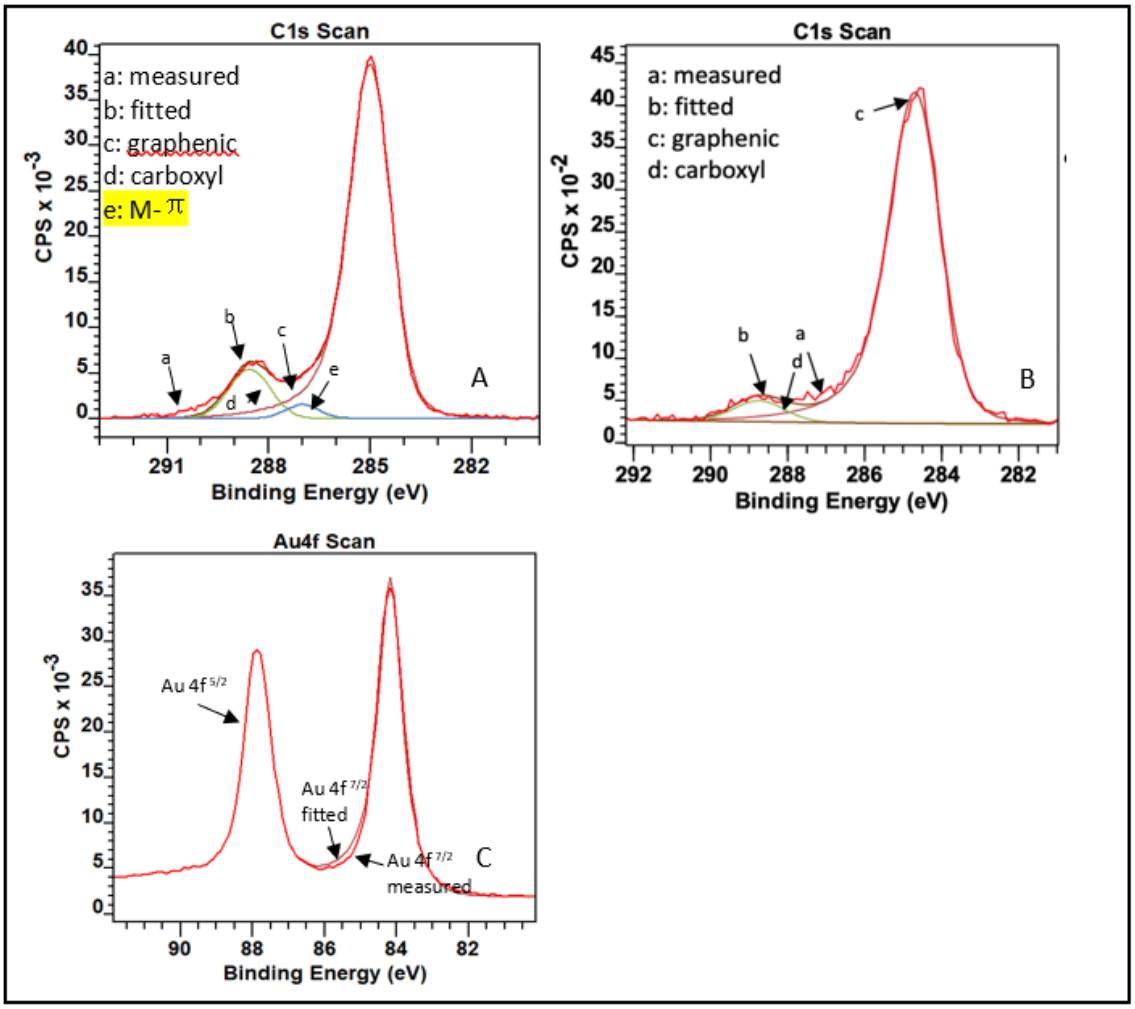

Figure 6.3 XPS Carbon Peaks of AuGNF(A) and GNF drop-coated (B) BDDEs; and XPS Au 4f Peaks of AuGNF (C).

From Figure 6.3, we observed that the C1s scan of AuGNF has a higher carboxyl peak than pure GNF, and a small metal-pi bond between graphenic carbon and carboxyl carbon peaks. This is consistent with our findings from chapter 5 and the theoretical origin will not be repeated here. The Au 4f showed preserved two clean peaks, representing Au 4f 5/2 and 7/2 from left to right. A fitting of the Au 4f $^{7/2}$ peak was done, using literature data for elemental Au. The splitting between these two peaks was 3.69 eV, which is very close to the literature value.[69] Therefore, we can confirm Au was fully reduced through the synthesis and elemental Au was decorated successfully on the graphenic surface of

cx-GNF.

6.3.2 Electrochemical Detection of As (III)

Sodium arsenite ($NaAsO_2$) purchased from Sigma Aldrich (analytical pure) was chosen to be the source of As (III) in this chapter due to its high solubility in various aqueous solvents. As (III) stock solution was prepared by dissolving $NaAsO_2$ in 0.1 M HCl.

6.3.2.1 Effect of cx-GNF stabilization, Loading, and Synthesis Methods

In this section, we investigated how various factors, including the stabilizing effect of cx-GNF, loading and method of synthesis can facilitate or block the detection. 20 μL of colloidal AuGNF and AuNPs were drop-coated onto BDDEs using a volumetric pipette. 5 mM As (III) solution was prepared, and cyclic voltammetry from -0.5 V to 0.5 V was recorded under a scan rate of 100 mV/s with 1 M HCl as the supporting electrolyte.

Both AuGNF and AuNPs were able to detect the As (III) solution, with a peak at around 0.17 V, however, the intensity of the peak was much higher for AuGNF decorated BDDE, indicating the AuGNF modified BDDE was more favorable for the reaction (Figure 6.5a). On the other hand, the loading of AuGNF could also affect the effectiveness of detection and the magnitude of peak current. The concentration of AuGNF solution synthesized was 0.14 mM, and we loaded different amount of colloidal AuGNF using pipette onto same area of BDDE electrodes. To compare the performance of detection across different synthesis methods, detection of As (III) using electrodeposited AuNPs was also evaluated. The concentration of As (III) solution used was 0.1 mM, and the peak current responses

in table were averaged over 3 samples, with error of ~5μA. (Table 6.2, Figure 6.4b).

Table 6.2 Effect of AuGNF loading and synthesis method on As(III) detection.

Loading	Amount of Au (nmol)	Peak Current Response (μA)
5μL	0.7	20
10μL	1.4	61
20μL	2.8	106
30μL	4.2	97
40μL	5.7	17
Electrodeposition	3.0	25

From this experiment, we observed that at the same As (III) concentration and electrode area, 20 μL loading of AuGNF could obtain the highest current response and therefore is the most optimal choice. The reason behind that was, consistent with other studies, that when the amount of loading was small, there was not enough active Au surface for the detection to happen, but when the loading was too high, the nanoparticles tended to gather and forms layers , making the exposed active surfaces less.[70] The electrodeposited AuNPs, although having similar absolute amount of Au on the surface, has a very low current response due to aggregation effects which was discussed in chapter 3 and 5. Notably, the current response of 20 μL loading and 30 μL loading did not differ by much, but in this chapter, we used 20uL for all experiments to be more economic.

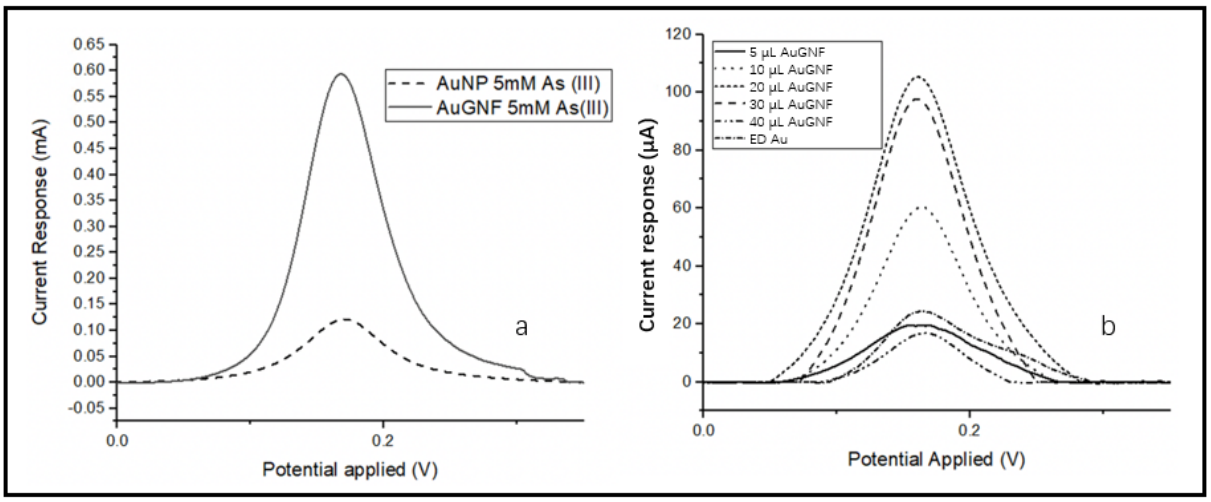

Figure 6.4 Effect of cx-GNF stabilization (a), loading and synthesis method (b) in As (III) detection of 0.1 mM As (III).

6.3.2.2 Limit of Detection

We attempted to obtain the limit of detection firstly using CV, with the settings mentioned in the previous section (Figure 6.5).

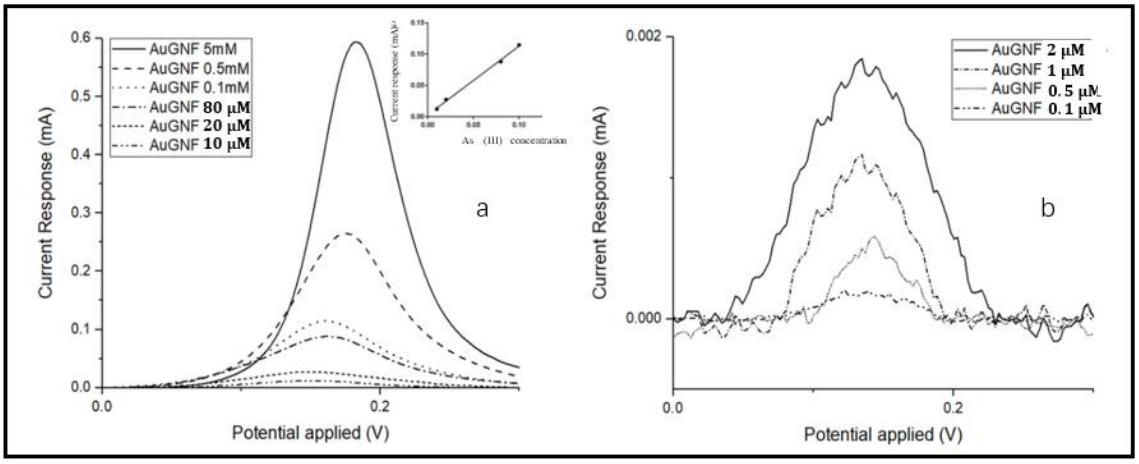

Figure 6.5 Detection of As (III) at various concentrations using CV: at higher concentrations (a, inset: plot of peak height against arsenic concentration); and lower concentrations (b).

The detection of As (III) using CV was successful at higher concentrations above 10 μM and followed a nice linear relationship, with an average error of ±~0.01mA (Figure 6.5a a). However, when the concentration of As (III) was pushed below 10 μM, the noise level was large and the LOD of As (III) using CV was about 0.2 μM, where the signal was comparable to the noise (Figure 6.5b).

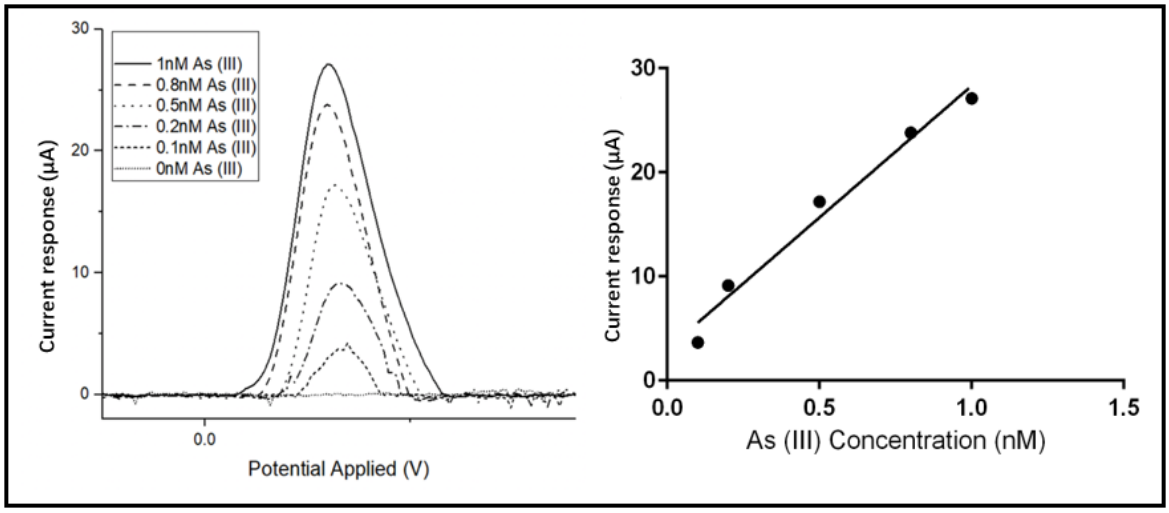

Figure 6.6 Detection of As (III) at various concentrations using SWV: at higher concentrations (left); and plot of peak height against arsenic concentration (right).

At this point, SWV as a more sensitive method will be used for detection at lower concentrations. SWV parameter used for this section was: pre-deposition at −0.5 V for 120 s, f = 50 Hz, E_{sw} = 20 mV, ΔEs = 2 mV. In a previous work by Dai et. al, the main obstacle for decreasing the LOD using SWV was the noises from baseline.[71] However, we didn't observe the same situation, since the background line was comparably clean, and the peaks were distinguishable.

As a result, we were able to detect As (III) at concentrations in range of sub-nanomolar, with LOD (based on 3σ) less than 0.1 nM, sensitivity about 25.3 μA/nM and a fairly good linear relationship between concentration and signal intensity with an average error

of ± 2.75 μA, each data spot averaged over 3 samples (Figure 6.6). Similar LOD was recorded by Xiao *et. al*, using a glassy carbon electrode (GCE) modified with AuNP decorated carbon nanotubes, but the sensitivity they recorded was higher than ours. One possible reason could be the amount of gold and they deposited on the GCE was more than 2 times our loading, and the electrode area was 5 times smaller than ours, meaning there was much more gold per area, which enhanced the sensitivity.. [72]

6.3.3 Electrochemical Detection of 4-Nonylphenol

4-nonylphenol (4-NP) poweder was purchased from Sigma Aldrich, analytical pure. The 5 mM stock solution of 4-NP was prepared by disolving 4-nonylphenol crystals with ethanol, since its solubility in DI water was very low.

6.3.3.1 Effect of cx-GNF stabilization, Ni^{2+} modification, and pH

Several factors were investigated during the detection of 4-nonylphenol, including the stabilization using cx-GNF, external stabilization using Ni^{2+}, and pH.

First, similar to the detection of As (III), we examined the stabilizing effect of cx-GNF for AuNPs in 4-NP detections using CV. 20 μL of colloidal AuNPs and AuGNFs were drop-coated onto BDDEs using volumetric pipette and the CV scanned from 0 V to 1 V and recorded under a scan rate of 100 mV/s with 0.1 M PBS (pH=7) as the supporting electrolyte (Figure 6.8a) and 12.5 μM 4-NP as the analyte. A similar result was again expected, the cx-GNF stabilized nanoparticle showed highest current density at about 0.54 V. This again proved cx-GNF was able to better disperse the AuNPs and prevent from aggregation, therefore increase the active surface that were available for 4-NP

sensing.

On the other hand, since cx-GNF was less soluble in acidic media, and in this neutral pH, extra stabilization of AuGNF was performed to make sure the solvation of cx-GNF did not lower the current density. In chapter 5, we have formulated a procedure to internally stabilize AuGNF by forming an insoluble salt with Ni^{2+} ions by immersing AuGNF modified BDDEs in $Ni(NO_3)_2$ solution for 15 minutes, rinsing the excess $Ni(NO_3)_2$ by DI water, and drying at room temperature. From the current density, we have seen that AuGNF nanospecies stabilized with Ni (AuGNF-Ni) exhibited higher current response since they successfully prevented the solvation of cx-GNF and loss of AuGNF at electrode surface.

Afterward, the pH effect on the detection of 4-NP using AuGNF was also investigated. 0.1 M PBS buffer with pH from 5 to 9 were used. Figure 6.7b showed how current response (averaged over 3 samples, with an error of $\pm$~3.8 μA) (black solid line, left axis) and peak potential (red dashed line, right axis) varied with respect to pH (averaged over 3 samples, with an error of $\sim \pm 0.023$ V).

At pH=5, no signal was presented, meaning the acidic condition was not favorable for the detection to happen. By nature, phenols are naturally slightly acidic, and with external potential applied, they underwent electro-oxidation to form phenoxy radicals, followed by the formation of quinone An oxidation peak observed reflected this transformation. This reaction is generically less favored in pH<7 due to the instability of quinone in acidic media. [73]

Notably, the peak potentials (E_p) at pH=6, 7, 8, and 9 follow a descending trend. When

an external potential is applied, the reaction is electrochemically irreversible, and the peak potential E_p will show a pH dependence given by:

$$E_{\mathrm{p}} = const + \frac{RT}{(n' + \alpha)F} \ln \frac{[\mathrm{H}^+]^m}{K + [\mathrm{H}^+]^m} \qquad (30)$$

where n' is the number of electrons transferred before the rate-determining electron transfer step, α is the transfer coefficient, F is the Faraday's constant, R is the gas constant, m is the number of protons involved, and K is the equilibrium constant, here equals to the acid dissociation constant K_a. When the concentration of hydrogen is much less than K_a, the peak potential is highly dependent on pH variation, otherwise the peak potential stays constant. 4-NP, as a weak acid, has a pK_a about 10, therefore, at any pH less than 10, the peak potential shifts to more negative value as pH increases.[74]

The peak current, however, was highest when pH=7, which was consistent with previous work by Su et.al, where pH=7.4 was used for 4-NP detection. [75] This showed the adsorption of 4-NP was more favoured in neutral pH and more 4-NP was captured by AuGNF, because the 4-NP is nonionic and hydrophobic. According to Zhou et al., the ionization level of 4-NP increased with the pH, and the intermediate ion was negatively charged. In alkaline media, the adsorbent surface charged negatively too, and the adsorption of 4-NP will not be favoured at higher pH.[76-77]

Similar result was also obtained by Javadi et al. and Zhou et al, confirming the adsorption of 4-NP at neutral pH was the most favorable and thus beneficial for our detection. [78-79] Therefore, the resulted current response was quite low at higher pH, and peaked at pH=7. In this section, all later experiments were done in 0.1M PBS neutral buffer, using AuGNF-Ni modified BDDEs.

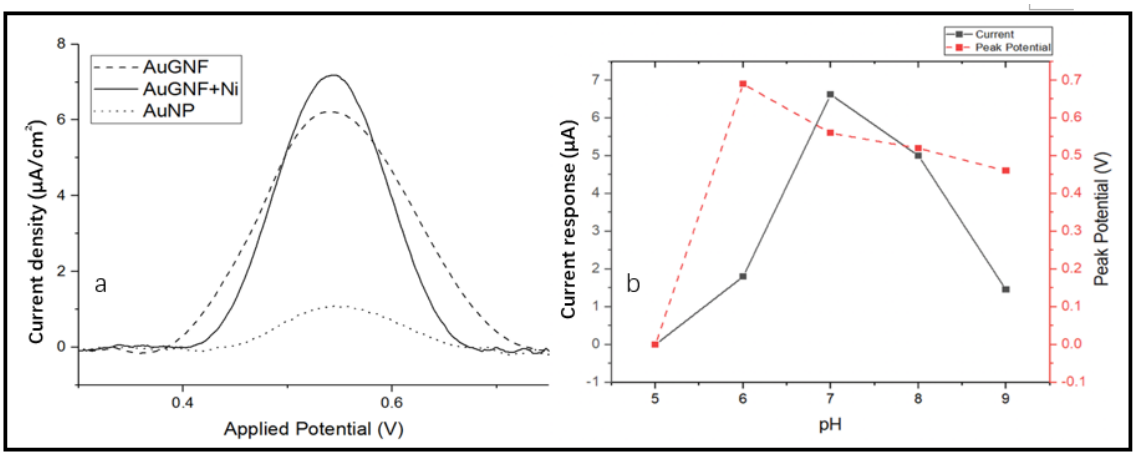

Figure 6.7 Detection of 12.5 μM 4-NP with AuNP, AuGNF, and AuGNF-Ni modified BDDEs (a); effect of pH on current response and peak potential of 4-NP detection using AuGNF modified BDDEs (b).

6.3.3.2 Limit of Detection

Electrochemical detection of 4-NP was successful between 0.3μM-12.5μM using CV and the relationship between current response and 4-NP was close to linear with a sensitivity of 0.55 μA/uM (averaged over 3 samples, with an error of $\pm$~0.16μA). Generally, the peak potential moved further to the right as the analyte is more dilute. (Figure 6.8)

Similar detection was done by Su *et al.*, using a glassy carbon electrode modified by electrodepositing gold nanoparticles decorated graphene nano platelets. Moreover, sol-gel and β-cyclodextrin were used as external stabilizers. Their linear LOD was 0.1 μM (based on 3σ), with a sensitivity of 7.4 μA/uM. Compared to their work, our electrode employed a much simpler modification method, with much smaller amount of Au on the electrode surface but achieved a similar LOD of about 0.3 μM (based on 3σ). On the other hand, the sensitivity is much higher in their work since the sol-gel and β-cyclodextrin they used can efficiently enhance the electrochemical response and conductivity in solutions due to the synergistic effect.[75]

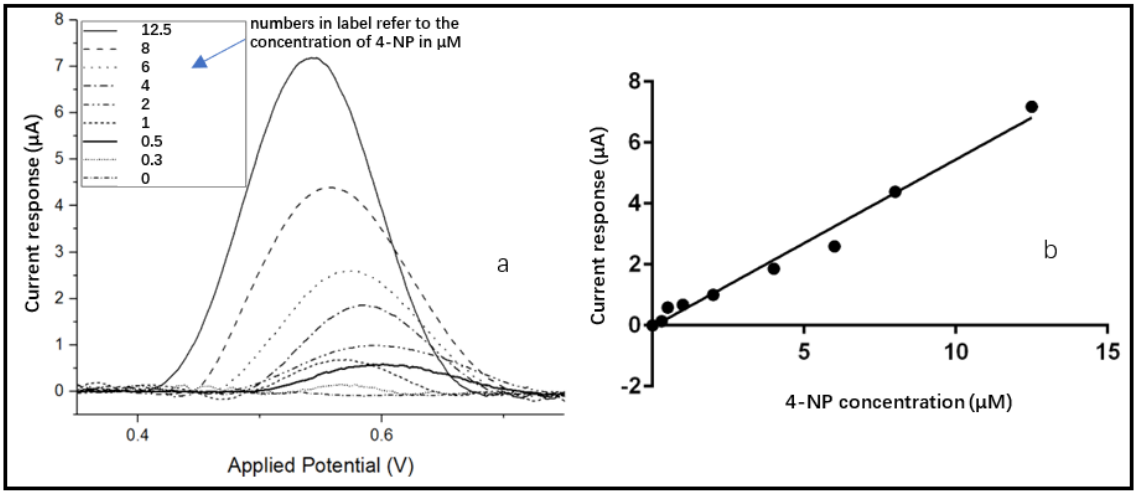

Figure 6.8 Detection of 4-NP at various concentrations using CV(a); and plot of current response against 4-NP concentration (b).

6.3.4 Electrochemical Detection of Glucose

d-Glucose (glucose) was purchased from Sigma Aldrich, analytical pure, and aqueous solution (DI water) was used for all experiments. The electrochemical analysis in this section were carried out in 0.1 M PBS, pH=7.4, to best mimic human blood pH. Since the electrolyte was slightly basic, we further stabilized AuGNF drop-coated BDDEs with Ni^{2+}, following the same procedure mentioned in the previous section and chapter 5.

6.3.4.1 Effect of Loading and Synthesis Methods

Similar to the detection of As (III), we investigated the most optimal loading of AuGNF for glucose detection using CV, to see if the conclusion was still the same with Ni^{2+} modification in alkaline media. 5 µL, 10 µL, 20 µL, 30 µL and 40 µL of AuGNF were drop-coated on to individual electrodes using a volumetric pipette and were modified with Ni^{2+} afterwards. Electrodeposition of Au followed the same protocol in section 6.3.2.1 to make sure the amount of Au electrodeposited was similar to that of 20 µL colloidal AuGNF. In this section, the CV was scanned from -0.5 V to 0.8 V and recorded under a

scan rate of 100 mV/s, with supporting electrolyte 0.1 M PBS pH=7.4, and analyte glucose 0.1 mM.

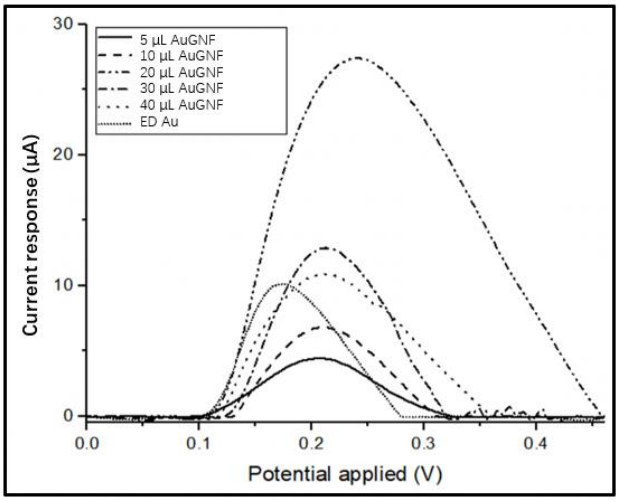

Figure 6.9 Effect of loading of AuGNF-Ni and synthesis method in detection of 50 mM glucose.

The detection of glucose was sucessful using CV and the oxidation peak of glucose appeared at around 0.23 V. Compared with As (III) detection, same conclusion was drawn. Amongst all samples, 20 µL of AuGNF-Ni drop-coated BDDE showed the highest current response and therefore is the most optimal loading. Electrodeposited Au, although having a similar amount of metal on the electrode, was not able to outperform 20 µL colloidal AuGNF-Ni, since the particles were larger in size and aggregation was heavy (proved in previous chapters). But notably the oxidation potential of glucose on electrodeposited Au was lower, that might originate from the extra stabilisation of Ni^{2+} for colloidal AuGNF. However, this could not be further investigated since AuGNF alone was very soluble in alkaline media, and the detection was therefore impossible to proceed sucessfully.

6.3.4.2 Limit of Detection

Using the same CV setting as before, the limit of glucose detection could be pushed down to 1 mM (at a signal to noise ratio of 3) with a sensitivity of 0.7 μM$(cm2)^{-1}$/mM, and a linear relationship within a range 5 mM to 25mM could be drawn between glucose concentration and current response (each data spot was averaged over 3 samples, with an error of ~±1.7 μA for linear area). (Figure 6.10).

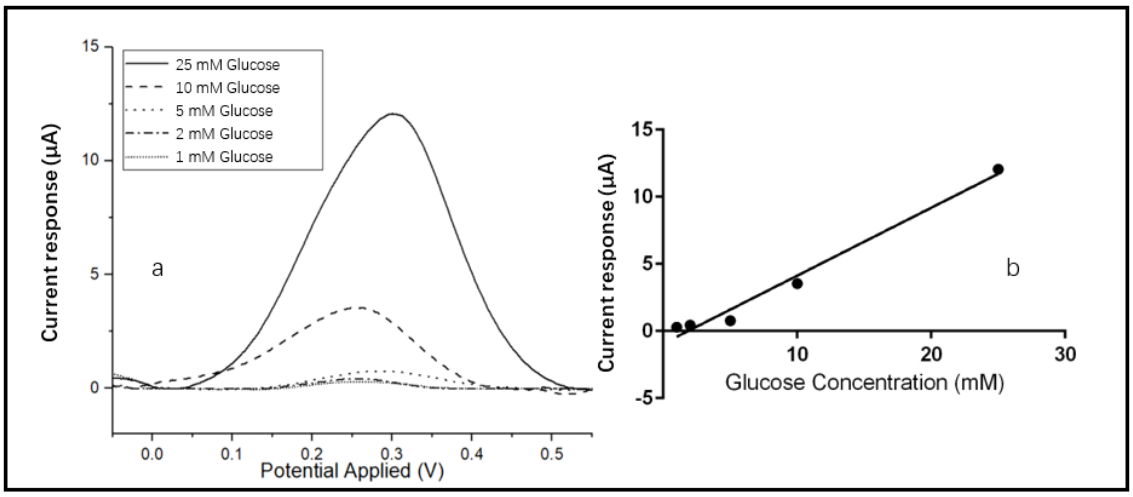

Figure 6.10 Detection of glucose at various concentrations using CV(a); and plot of current response against glucose concentration (b)

With LOD down to 1 mM, this detection is suitable for real-world physiological applications with almost all meaningful blood sugar levels covered:

1. 11 mM: blood sugar level for diabetics after food
2. 7 mM: blood sugar for diabetics without food
3. 5.5 mM: normal blood sugar level
4. 3 mM: low blood sugar level. [80]

Similar work has been done by Zhou *et al.*, using AuNPs integrated in a nanotube array on porous anodic alumina (PAA). Although they were able to reach a theoretical LOD of 10 μM (at a signal to noise ratio of 3), the limit of the linear range was also 1mM with a

higher sensitivity 1.13 μ M$(cm^2)^{-1}$/mM. [81]

In comparison, our LOD was the same as their limit of linear range, using a smaller amount of Au, and the advantage of our method was the simple synthesis, easy application and characterization, since the synthesizing scheme of AuNP integrated nanotube array proposed by Zhou et al. required more steps such as pretreatment, Sn^{2+} activation of PAA, and deposition of AgNPs as catalyst for Au reduction, which takes more than 8 hours to achieve.[81]

6.3.5 Electrochemical Detection of Hydroquinone

Hydroquinone (HQ) and catechol (CAT) was purchased from Sigma Aldrich (analytical pure), and aqueous solution (DI water) was used for detections. All electrochemical analysis were carried out under 0.1 M PBS buffer (pH=3.15) in this section. Since the supporting electrolyte was again acidic, colloidal AuGNF was drop-coated onto BDDEs using volumetric pipette without further modification.

6.3.5.1 Effect of cx-GNF Stabilization and Synthesis Method

20 μL of AuGNF and colloidal AuNP were drop-coated onto BDDEs using a volumetric pipette since this loading was able to produce the highest current intensity from the previous sections. Similar amounts of AuNPs were electrodeposited via the same procedure mentioned in previous sections for comparison. We recorded the CV of 0.5 mM HQ detection from 0 V to 0.65 V, at a scan rate of 100 mV/s.

Not surprisingly, the electrode modified with AuGNF showed the highest current response, followed by electrodeposited Au, colloidal Au at around 0.32 V. Bare BDDEs

were not suitable for HQ sensing since no signal at this potential range was recorded. The outstanding stability and performance in electrochemical sensing of AuGNF modified BDDE have been once again confirmed (Figure 6.11).

Notably, in previous work by Hu *et al.*, an AuNPs electrodeposited carbon ionic liquid electrode (CILE) was also used for HQ detection. In their work, graphene (GR) played a similar role to cx-GNF to further prevent AuNPs from aggregation through simultaneous electrodeposition. The intensity of the peak current of CV recorded by them in 0.5 mM HQ detection using an AuGR modified CILE was comparable to that of AuGNF modified BDDEs in our work. The performance of AuGNF modified BDDEs surpassed Au-CILE and GR-CILE in the literature. [82]

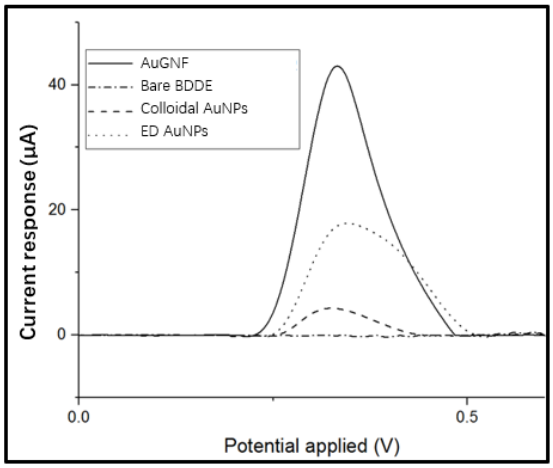

Figure 6.11 Effect of cx-GNF stabilization and method in HQ (0.5 mM) detection.

6.3.5.2 Limit of Detection

At higher concentrations of HQ (μ M level), CV was used as the primary detection method, with same setting in the previous section and LOD was 2 μM (at a signal to noise ratio of 3) with a sensitivity of 0.08 μA/μM, following a linear relationship in the range 2μM to 0.5mM, each data spot over 3 samples, with an error from ~±0.7 μA (for lower

concentration of HQ) to $\sim \pm 3.5$ μA (for higher concentration of HQ) (Figure 6.13a). The LOD and sensitivity in our experiments were comparable to a previous research done by Tashkhourian *et al.*, in which a gold nanoparticles mesoporous silica modified carbon paste electrode was used for HQ detection.[83]

As for the detection of HQ at lower concentration in nM scale, DPV was used as a more sensitive method. The parameters were tested, and the most optimal set was confirmed: amplitude=50 mV, pulse width=0.05 s, and pulse period=0.2 s, in 0.1 M PBS buffer (pH=3.15). The detection of HQ using DPV began at a concentration of 1 **μ**M and the LOD was 25 nM (at a signal to noise ratio of 3) with sensitivity of 7.75 **μ**A/uM, and the relationship between HQ concentration and current response was linear within the range from 25 nM to 0.5 **μ**M, each data spot was averaged over 3 samples, with error of $\pm \mathbf{0.3\ \mu A}$ (for lower concentration of HQ) to $\sim \pm \mathbf{0.8\ \mu A}$ (for higher concentration of HQ) (Figure 6.12b). Switching the detection method from CV to DPV increased the sensitivity about 100 times, meaning DPV is preferred at lower concentration level detection. In the previously mentioned work done by Hu et al., DPV was also chosen to

detect the presence of HQ with low concentration, and the LOD from their work was 18 nM, which is very close to ours.

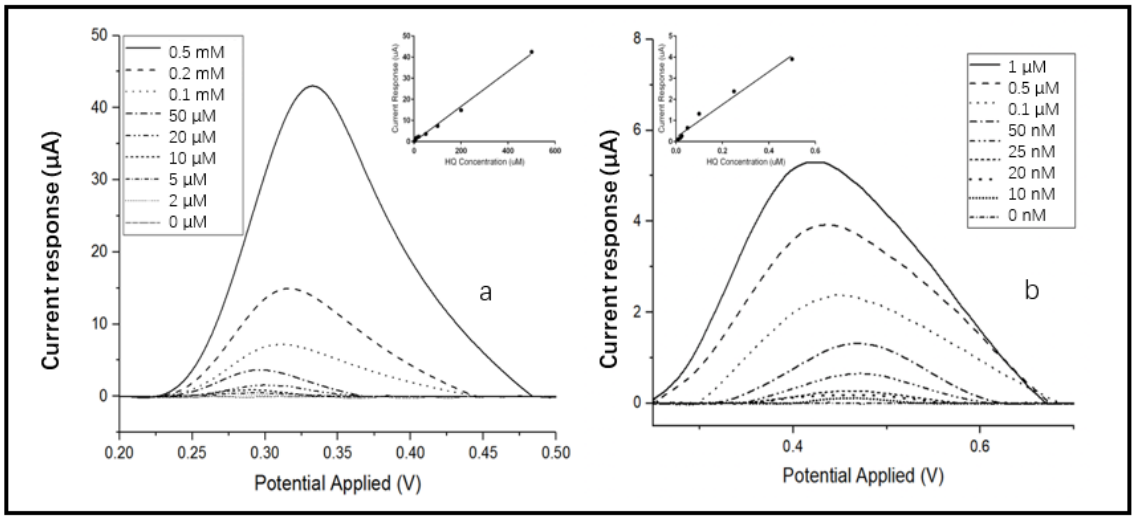

Figure 6.12 Detection of HQ at various concentrations using CV at higher concentrations (a, inset: plot of peak height against HQ concentration); and DPV at lower concentrations (b, insert: plot of peak height against HQ concentration).

6.3.5.3 Detection of HQ with CAT as an Interfering Molecule

First, 0.5 mM HQ and CAT was detected individually. Full cycle CV scans were recorded with AuGNF modified BDDEs, using the same parameters as in section 6.3.5.1. It turned out the sensitivity of HQ and CAT detection was roughly the same because the current responses of oxidation peaks were similar. However, the oxidation peak potential and peak to peak separation were quite different, HQ was oxidized at a lower potential at around 0.34 V, and CAT's oxidation peak appeared at 0.46 V. The different peak to peak separation suggested the important electrochemical parameters of the two (table 6.3), such as α and k_s, where α is the transfer coefficient which shows the sensitivity of the transitional state corresponding to the potential variation between the electrode and solution, and k_s corresponding to the speed and reversibility of the reaction. Both parameters and their important meanings in electrochemical reactions were

comprehensively discussed in chapter 2, therefore will not be repeated here.

Table 6.3 Important electrochemical data in CV of 0.5 mM HQ and CAT, repectively.

	Oxidation Peak Potential (V)	**Current response at Oxidation Peak (µA)**	**Peak separation (V)**
HQ	0.34	7.78	0.085
CAT	0.46	8.23	0.1196

Afterward, 0.5 mM HQ was mixed with different concentrations of CAT and the detections were performed by DPV using the parameters mentioned in section 6.3.5.2.

As a result, the simultaneous detection was successful and the two peaks could be distinguished clearly, since the concentration of HQ was constant, the intensity of peak at 0.34 V remained unchanged. A fairly linear relationship between CAT concentration (120 µM to 10 µM) and current response could be drawn (each data spot was averaged over 3 samples, with error of $\sim \pm$ 1.0 µA), LOD 10 µM CAT and the sensitivity of DPV detection was 0.28 µA/µM CAT (Figure 6.13).

In the work by Tashkhourian *et al.* simultaneous detection of HQ and CAT were done using SWV with a LOD of 30 **µ**M CAT in 0.3 mM HQ. That means they were able to detect CAT that is 10 times more dilute than HQ. In this sense, our work was able to

increase that limit by 5 times using DPV, meaning we were able to detect CAT that is 50 times more dilute than HQ.[83]

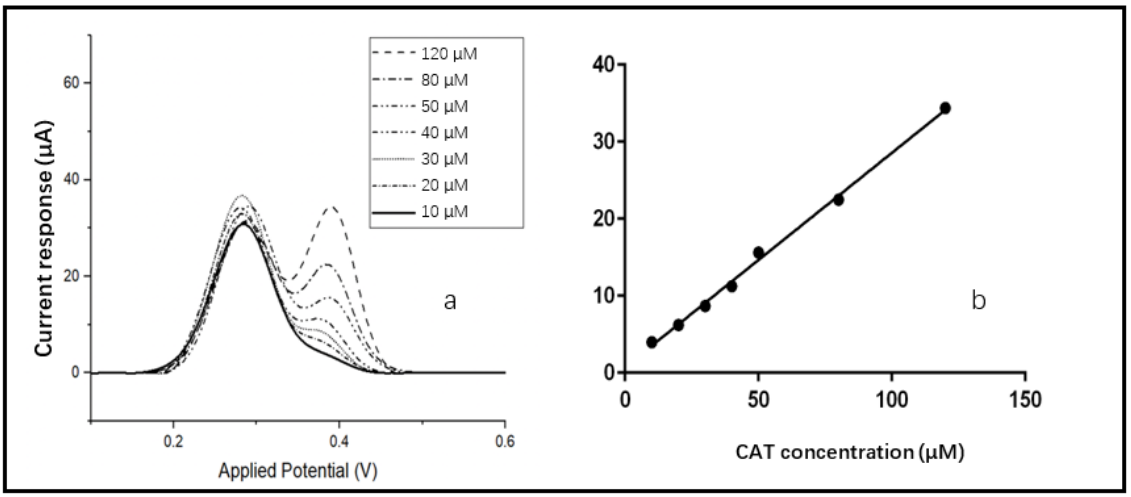

Figure 6.13 Simultaneous detection of HQ and CAT using DPV (a), the concentration of HQ was 0.5 mM; and plot of current response for CAT oxidation peak against its concentration (b).

6.4 Conclusion

We explored how carboxylated graphene nanoflakes (cx-GNF) colloidal metal nanoparticles can facilitate the electrochemical sensing and improve the performance in this chapter, following the success of applications in catalysis of hydrogen generation reactions.

There are many ways to detect small molecules and ions, but electrochemical sensing using metal nanoparticle modified electrodes has the advantage of fast, simple assembly, and high accuracy. As (III), 4-nonylphenol (4-NP), *d*-glucose (glucose), and hydroquinone (HQ) were chosen to be the analytes of electrochemical sensing. As (III) and 4-NP are common contaminants of environment, and they can be harmful for human beings and animals once consumed. The concentration of glucose in blood, or blood sugar level, is an important indicator for diagnosing and monitoring diabetics. HQ is a common

additive of cosmetics and can also be found in water as pollutant, however, in real-world detection, is often mixed with catechol (CAT), which is structurally similar to that of HQ. Therefore, the sensitive and quantitative detection with low limit of detection (LOF) of these four molecules are very meaningful.

AuGNF was synthesized through the 1 step in-situ reduction we proposed in chapter 5 and the resulting colloidal solutions were drop-coated onto BDD electrodes for experiments. We confirmed the formation of AuGNF nanoparticles through UV-Vis and observed a redshift in plasmonic peaks compared with unstabilized ones, which is consistent with what we have seen in chapter 5. This peak is a result of non-covalent electrostatic interaction between Au and the graphenic surface of cx-GNF. TEM was used directly to determine the size and distribution of AuGNF, since SEM was hard to view nanoparticles with size smaller than 10 nm clearly as an experience from chapter 5. As a result, nanoparticles with size of sub 5 nm were obtained with even size distributions.

XPS was used to determine the surface composition AuGNF, and a higher amount of surface Au compared to unstabilized AuNPs again confirmed that cx-GNF successfully prevented aggregation. The Au peak fitting of AuGNF illustrated a high purity of Au in AuGNF, meaning the reduction was complete. Moreover, the carbon 1s peak of AuGNF also exhibited a subtle peak indicating the formation of metal-πbond at the position between graphenic carbon and carboxylates carbon, which is coherent with our results in chapter 5.

We confirmed that cx-GNF can boost the sensing performance by comparing the sensing abilities of AuGNF, unstabilized AuNPs, and electrodeposited AuNPs, and enhanced

current responses were observed for detections of all molecules mentioned above. Moreover, the influence of pH in 4-NP detection was especially explored, and neutral pH is the optimal condition since the molecules were not ionized and the adsorption of 4-NP was favoured for electrodes. For neutral and basic electrolytes, AuGNF was further stabilized by forming an insoluble salt with Ni^{2+}, using the scheme in chapter 5. Throughout the experiments, CV was used as the primary detection method, and SWV and DPV were used for detection at lower analyte concentrations, if needed. The linear relationships between analytes concentrations and current responses were drawn, and the LOD and sensitivity of them were compared with previous work, confirming we were able to get similar or better results with minimum effort during synthesis and characterization. For As (III) detection, the LOD was 10 μM using CV, and 0.1 nM using SWV; for 4-NP, the LOD was 0.3 μM using CV; for glucose, the LOD was 0.3 mM, covering the meaningful range for physiological application; for HQ, the LOD was 2 μM using CV, and 0.5 nM using DPV; simultaneous detection of HQ and CAT was also successful, with LOD of CAT 50 times more dilute than HQ.

References

(1) Liu, L.; Fang, Z.; Zheng, X.; Xi, D. Nanopore-Based Strategy For Sensing Of Copper(II) Ion And Real-Time Monitoring Of A Click Reaction. *ACS Sensors* 2019, *4*, 1323-1328.

(2) Rana, S.; Kaur, A.; Bharti, A.; Singh, S.; Bhatnagar, A.; Prabhakar, N. Electrochemical Detection Of Hepcidin Based On Spiegelmer And Mos2nf-GNR@Aunps As Sensing Platform. *Analytica Chimica Acta* 2021, *1181*, 338863.

(3) Ozdemir, M. A Novel Chromogenic Molecular Sensing Platform For Highly Sensitive And Selective Detection Of Cu^{2+} Ions In Aqueous Environment. *Journal of Photochemistry and Photobiology A: Chemistry* 2019, *369*, 54-69.

(4) Lee, H.; Hong, Y.; Baik, S.; Hyeon, T.; Kim, D. Enzyme-Based Glucose Sensor: From Invasive To Wearable Device. *Advanced Healthcare Materials* 2018, *7*, 1701150.

(5) Rüdel, H.; Körner, W.; Letzel, T.; Neumann, M.; Nödler, K.; Reemtsma, T. Persistent, Mobile And Toxic Substances In The Environment: A Spotlight On Current Research And Regulatory Activities. *Environmental Sciences Europe* 2020, *32*.

(6) Rajabnejad, S.; Badibostan, H.; Verdian, A.; Karimi, G.; Fooladi, E.; Feizy, J. Aptasensors As Promising New Tools In Bisphenol A Detection - An Invisible Pollution In Food And Environment. *Microchemical Journal* 2020, *155*, 104722.

(7) Torrinha, Á.; Oliveira, T.; Ribeiro, F.; Correia, A.; Lima-Neto, P.; Morais, S. Application Of Nanostructured Carbon-Based Electrochemical (Bio)Sensors For Screening Of Emerging Pharmaceutical Pollutants In Waters And Aquatic Species: A Review. *Nanomaterials* 2020, *10*, 1268.

(8) Sarkar, A.; Kalita, D.; Baruah, S. Nanomaterials For Aquatic Contamination Sensing And Remediation. *Aquananotechnology* 2021, 67-89.

(9) Manjavacas, G.; Nieto, B. Hydrogen Sensors And Detectors. *Compendium of Hydrogen Energy* 2016, 215-23

(10) Antuña-Jiménez, D.; González-García, M.; Hernández-Santos, D.; Fanjul-Bolado, P. Screen-Printed Electrodes Modified With Metal Nanoparticles For Small Molecule Sensing. *Biosensors* 2020, 10, 9.

(11) Huang, A.; He, Y.; Zhou, Y.; Zhou, Y.; Yang, Y.; Zhang, J.; Luo, L.; Mao, Q.; Hou, D.; Yang, J. A Review Of Recent Applications Of Porous Metals And Metal Oxide In Energy Storage, Sensing And Catalysis. *Journal of Materials Science* 2018, *54*, 949-973.

(12) Song, Y.; Cho, D.; Venkateswarlu, S.; Yoon, M. Systematic Study On Preparation Of Copper Nanoparticle Embedded Porous Carbon By Carbonization Of Metal–Organic

Framework For Enzymatic Glucose Sensor. *RSC Advances* 2017, *7*, 10592-10600.

(13) Li, F.; Li, R.; Feng, Y.; Gong, T.; Zhang, M.; Wang, L.; Meng, T.; Jia, H.; Wang, H.; Zhang, Y. Facile Synthesis Of Au-Embedded Porous Carbon From Metal-Organic Frameworks And For Sensitive Detection Of Acetaminophen In Pharmaceutical Products. *Materials Science and Engineering: C* 2019, *95*, 78-85.

(14) Karaduman, I.; Er, E.; Çelikkan, H.; Erk, N.; Acar, S. Room-Temperature Ammonia Gas Sensor Based On Reduced Graphene Oxide Nanocomposites Decorated By Ag, Au And Pt Nanoparticles. *Journal of Alloys and Compounds* 2017, *722*, 569-578.

(15) Halkare, P.; Punjabi, N.; Wangchuk, J.; Nair, A.; Kondabagil, K.; Mukherji, S. Bacteria Functionalized Gold Nanoparticle Matrix Based Fiber-Optic Sensor For Monitoring Heavy Metal Pollution In Water. *Sensors and Actuators B: Chemical* 2019, *281*, 643-651.

(16) Saxena, M.; Jain, K.; Saxena, R. Green Synthesized Nanomaterial-Based Colorimetric Sensors For Detection Of Environmental Toxicants. *ChemNanoMat* 2021, *7*, 392-414.

(17) Vilela, P.; El-Sagheer, A.; Millar, T.; Brown, T.; Muskens, O.; Kanaras, A. Graphene Oxide-Upconversion Nanoparticle Based Optical Sensors For Targeted Detection Of Mrna Biomarkers Present In Alzheimer'S Disease And Prostate Cancer. *ACS Sensors* 2016, *2*, 52-56.

(18) Luo, X.; Morrin, A.; Killard, A.; Smyth, M. Application Of Nanoparticles In Electrochemical Sensors And Biosensors. *Electroanalysis* 2006, *18*, 319-326.

(19) Nasresfahani, S.; Zargarpour, Z.; Sheikhi, M.; Nami Ana, S. Improvement Of The Carbon Monoxide Gas Sensing Properties Of Polyaniline In The Presence Of Gold Nanoparticles At Room Temperature. *Synthetic Metals* 2020, *265*, 116404.

(20) Wallentine, S.; Bandaranayake, S.; Biswas, S.; Baker, L. Plasmon-Resonant Vibrational Sum Frequency Generation Of Electrochemical Interfaces: Direct Observation Of Carbon Dioxide Electroreduction On Gold. *The Journal of Physical Chemistry A* 2020, *124*, 8057-8064.

(21) De, A.; Kumari, A.; Jain, P.; Manna, A.; Bhattacharjee, G. Plasmonic Sensing Of Hg(II), Cr(III), And Pb(II) Ions From Aqueous Solution By Biogenic Silver And Gold Nanoparticles. *Inorganic and Nano-Metal Chemistry* 2020, 1-12.

(22) Vigneshvar, S.; Senthilkumaran, B. Current Technological Trends In Biosensors, Nanoparticle Devices And Biolabels: Hi-Tech Network Sensing Applications. *Medical Devices & Sensors* 2018, *1*, e10011.

(23) Cui, X.; Wei, T.; Hao, M.; Qi, Q.; Wang, H.; Dai, Z. Highly Sensitive And Selective Colorimetric Sensor For Thiocyanate Based On Electrochemical Oxidation-Assisted Complexation Reaction With Gold Nanostars Etching. *Journal of Hazardous Materials* 2020, *391*, 122217.

(24) Liu, Y.; Xie, R.; Yang, P.; Lu, L.; Shen, L.; Tao, J.; Liu, Z.; Zhao, P. An Excellent Electrochemical Sensor Based On Highly Porous Gold Film Modified Gold Electrode For Detecting Quercetin In Food And Medicine. *Journal of The Electrochemical Society* 2020, *167*, 047514.

(25) Lau, H.; Wu, H.; Wee, E.; Trau, M.; Wang, Y.; Botella, J. Specific And Sensitive Isothermal Electrochemical Biosensor For Plant Pathogen DNA Detection With Colloidal Gold Nanoparticles As Probes. *Scientific Reports* 2017, *7*.

(26) Fan, T.; Du, Y.; Yao, Y.; Wu, J.; Meng, S.; Luo, J.; Zhang, X.; Yang, D.; Wang, C.; Qian, Y. et al. Rolling Circle Amplification Triggered Poly Adenine-Gold Nanoparticles Production For Label-Free Electrochemical Detection Of Thrombin. *Sensors and Actuators B: Chemical* 2018, *266*, 9-18.

(27) Cui, H.; Xu, T.; Sun, Y.; Zhou, A.; Cui, Y.; Liu, W.; Luong, J. Hairpin DNA As A Biobarcode Modified On Gold Nanoparticles For Electrochemical DNA Detection. *Analytical Chemistry* 2015, *87*, 1358-1365.

(28) Saha, K.; Agasti, S.; Kim, C.; Li, X.; Rotello, V. Gold Nanoparticles In Chemical And Biological Sensing. *Chemical Reviews* 2012, *112*, 2739-2779.

(29) Tian, T.; Dong, J.; Xu, J. Direct Electrodeposition Of Highly Ordered Gold Nanotube Arrays For Use In Non-Enzymatic Amperometric Sensing Of Glucose. *Microchimica Acta* 2016, *183*, 1925-1932.

(30) Nriagu, J.; Bhattacharya, P.; Mukherjee, A.; Bundschuh, J.; Zevenhoven, R.; Loeppert, R. Arsenic In Soil And Groundwater: An Overview. *Trace Metals and other Contaminants in the Environment* 2007, 3-60.

(31) Hu, Y.; Xiao, T.; Zhang, A. Associations Between And Risks Of Trace Elements Related To Skin And Liver Damage Induced By Arsenic From Coal Burning. *Ecotoxicology and Environmental Safety* 2021, 208, 111719.

(32) Uppal, J.; Zheng, Q.; Le, X. Arsenic In Drinking Water—Recent Examples And Updates From Southeast Asia. *Current Opinion in Environmental Science & Health* 2019, *7*, 126-135.

(33) Mochizuki, H. Arsenic Neurotoxicity In Humans. *International Journal of Molecular Sciences* 2019, *20*, 3418.

(34) Mendez, W.; Eftim, S.; Cohen, J.; Warren, I.; Cowden, J.; Lee, J.; Sams, R. Relationships Between Arsenic Concentrations In Drinking Water And Lung And Bladder Cancer Incidence In U.S. Counties. *Journal of Exposure Science & Environmental Epidemiology* 2016, *27*, 235-243.

(35) Song, Y.; Swain, G. Development Of A Method For Total Inorganic Arsenic Analysis Using Anodic Stripping Voltammetry And A Au-Coated, Diamond Thin-Film Electrode. *Analytical Chemistry* 2007, *79*, 2412-2420.

(36) Xiao, L.; Wildgoose, G.; Compton, R. Sensitive Electrochemical Detection Of Arsenic (III) Using Gold Nanoparticle Modified Carbon Nanotubes Via Anodic Stripping Voltammetry. *Analytica Chimica Acta* 2008, *620*, 44-49.

(37) Yang, M.; Chen, X.; Jiang, T.; Guo, Z.; Liu, J.; Huang, X. Electrochemical Detection Of Trace Arsenic(III) By Nanocomposite Of Nanorod-Like A-MnO_2 Decorated With ~5 nm Au Nanoparticles: Considering The Change Of Arsenic Speciation. *Analytical Chemistry* 2016, *88*, 9720-9728.

(38) Li, S.; Zhou, W.; Jiang, M.; Guo, Z.; Liu, J.; Zhang, L.; Huang, X. Surface Fe(II)/Fe(III) Cycle Promoted Ultra-Highly Sensitive Electrochemical Sensing Of Arsenic(III) With Dumbbell-Like Au/Fe_3O_4 Nanoparticles. *Analytical Chemistry* 2018, *90*, 4569-4577.

(39) Shao, B.; Hu, J.; Yang, M.; An, W.; Tao, S. Nonylphenol And Nonylphenol Ethoxylates In River Water, Drinking Water,And Fish Tissues In The Area Of Chongqing, China. *Archives of Environmental Contamination and Toxicology* 2005, *48*, 467-473.

(40) Yadetie, F.; Arukwe, A.; Goksøyr, A.; Male, R. Induction Of Hepatic Estrogen Receptor In Juvenile Atlantic Salmon In Vivo By The Environmental Estrogen, 4-Nonylphenol. *Science of The Total Environment* 1999, *233*, 201-210.

(41) Srivastava, A.; Singh, S.; Allen, T.; Dhiman, A. Heavy Metal Toxicity Of Water Of The Delhi Segment Of River Yamuna To Fresh Water Fish Channa Punctatus. *Agricultural Research* 2015, *4*, 405-410.

(42) Tsuda, T.; Suga, K.; Kaneda, E.; Ohsuga, M. Determination Of 4-Nonylphenol, Nonylphenol Monoethoxylate, Nonylphenol Diethoxylate And Other Alkylphenols In Fish And Shellfish By High-Performance Liquid Chromatography With Fluorescence Detection. *Journal of Chromatography B: Biomedical Sciences and Applications* 2000, *746*, 305-309.

(43) Zhou, Q.; Lei, M.; Li, J.; Zhao, K.; Liu, Y. Sensitive Determination Of Bisphenol A, 4-Nonylphenol And 4-Octylphenol By Magnetic Solid Phase Extraction With Fe@Mgal-LDH Magnetic Nanoparticles From Environmental Water Samples. *Separation and Purification Technology* 2017, *182*, 78-86.

(44) Whicher, C.; O'Neill, S.; Holt, R. Diabetes In The UK: 2019. *Diabetic Medicine* 2020, *37*, 242-247.

(45) Gouda, M.; Kumar, M.; Thakur, M.; Karanth, N. Enhancement Of Operational Stability Of An Enzyme Biosensor For Glucose And Sucrose Using Protein Based Stabilizing Agents. *Biosensors and Bioelectronics* 2002, *17*, 503-507.

(46) Lee, H.; Hong, Y.; Baik, S.; Hyeon, T.; Kim, D. Enzyme-Based Glucose Sensor: From Invasive To Wearable Device. *Advanced Healthcare Materials* 2018, *7*, 1701150.

(47) Hassan, M.; Vyas, C.; Grieve, B.; Bartolo, P. Recent Advances In Enzymatic And Non-Enzymatic Electrochemical Glucose Sensing. *Sensors* 2021, *21*, 4672.

(48) Syshchyk, O.; Skryshevsky, V.; Soldatkin, O.; Soldatkin, A. Enzyme Biosensor Systems Based On Porous Silicon Photoluminescence For Detection Of Glucose, Urea And Heavy Metals. *Biosensors and Bioelectronics* 2015, *66*, 89-94.

(49) Gong, X.; Gu, Y.; Zhang, F.; Liu, Z.; Li, Y.; Chen, G.; Wang, B. High-Performance Non-Enzymatic Glucose Sensors Based On Conicu Alloy Nanotubes Arrays Prepared By Electrodeposition. *Frontiers in Materials* 2019, *6*.

(50) Wang, J.; Gao, H.; Sun, F.; Xu, C. Nanoporous Ptau Alloy As An Electrochemical Sensor For Glucose And Hydrogen Peroxide. *Sensors and Actuators B: Chemical* 2014, *191*, 612-618.

(51) Zhu, Z.; Garcia-Gancedo, L.; Flewitt, A.; Xie, H.; Moussy, F.; Milne, W. A Critical Review Of Glucose Biosensors Based On Carbon Nanomaterials: Carbon Nanotubes And Graphene. *Sensors* 2012, *12*, 5996-6022.

(52) Lai, J.; Yi, Y.; Zhu, P.; Shen, J.; Wu, K.; Zhang, L.; Liu, J. Polyaniline-Based Glucose Biosensor: A Review. *Journal of Electroanalytical Chemistry* 2016, *782*, 138-153.

(53) Zhou, Y.; Yang, S.; Qian, Q.; Xia, X. Gold Nanoparticles Integrated In A Nanotube Array For Electrochemical Detection Of Glucose. *Electrochemistry Communications* 2009, *11*, 216-219.

(54) Shen, N.; Xu, H.; Zhao, W.; Zhao, Y.; Zhang, X. Highly Responsive And Ultrasensitive Non-Enzymatic Electrochemical Glucose Sensor Based On Au Foam. *Sensors* 2019, *19*, 1203.

(55) Liu, W.; Wu, L.; Zhang, X.; Chen, J. Simultaneous Electrochemical Determination Of Hydroquinone, Catechol And Resorcinol At Nitrogen Doped Porous Carbon Nanopolyhedrons-Multiwall Carbon Nanotubes Hybrid Materials Modified Glassy Carbon Electrode. *Bulletin of the Korean Chemical Society* 2014, *35*, 204-210.

(56) Lin, Z.; Kuo, Y.; Chang, C.; Lin, Y.; Chiu, T.; Hu, C. Highly Sensitive Sensing Of Hydroquinone And Catechol Based On B-Cyclodextrin-Modified Carbon Dots. *RSC Advances* 2018, *8*, 19381-19388.

(57) Enguita, F.; Leitão, A. Hydroquinone: Environmental Pollution, Toxicity, And Microbial Answers. *BioMed Research International* 2013, *2013*, 1-14.

(58) Schweigert, N.; Zehnder, A.; Eggen, R. Chemical Properties Of Catechols And Their Molecular Modes Of Toxic Action In Cells, From Microorganisms To Mammals. Minireview. *Environmental Microbiology* 2001, *3*, 81-91.

(59) Zhao, L.; Lv, B.; Yuan, H.; Zhou, Z.; Xiao, D. A Sensitive Chemiluminescence Method For Determination Of Hydroquinone And Catechol. *Sensors* 2007, *7*, 578-588.

(60) Yuan, X.; Wang, B.; Yan, C.; Lv, W.; Ma, Q.; Zheng, B.; Du, J.; Xiao, D. A Rapid And Simple Strategy For Discrimination And Detection Of Catechol And Hydroquinone By Fluorescent Silicon Nanoparticles. *Microchemical Journal* 2020, *158*, 105263.

(61) Chen, J.; Gao, Y.; Hu, X.; Xu, Y.; Lu, X. Detection Of Hydroquinone With A Novel Fluorescence Probe Based On The Enzymatic Reaction Of Graphite Phase Carbon Nitride Quantum Dots. *Talanta* 2019, *194*, 493-500.

(62) Marrubini, G.; Calleri, E.; Coccini, T.; Castoldi, A.; Manzo, L. Direct Analysis Of Phenol, Catechol And Hydroquinone In Human Urine By Coupled-Column HPLC With Fluorimetric Detection. *Chromatographia* 2005, 62, 25-31.

(63) Zhao, L.; Lv, B.; Yuan, H.; Zhou, Z.; Xiao, D. A Sensitive Chemiluminescence Method For Determination Of Hydroquinone And Catechol. *Sensors* 2007, *7*, 578-588.

(64) Yuan, X.; Yuan, D.; Zeng, F.; Zou, W.; Tzorbatzoglou, F.; Tsiakaras, P.; Wang, Y. Preparation Of Graphitic Mesoporous Carbon For The Simultaneous Detection Of Hydroquinone And Catechol. *Applied Catalysis B: Environmental* 2013, 129, 367-374.

(65) Huang, R.; Chen, S.; Yu, J.; Jiang, X. Self-Assembled Ti3c2 /Mwcnts Nanocomposites Modified Glassy Carbon Electrode For Electrochemical Simultaneous Detection Of Hydroquinone And Catechol. *Ecotoxicology and Environmental Safety* 2019, 184, 109619.

(66) Wu, F.; Zhao, J.; Han, D.; Zhao, S.; Zhu, R.; Cui, G. A Three-Electrode Integrated Electrochemical Platform Based On Nanoporous Gold For The Simultaneous Determination Of Hydroquinone And Catechol With High Selectivity. *The Analyst* 2021, 146, 232-243.

(67) Haiss, W.; Thanh, N.; Aveyard, J.; Fernig, D. Determination Of Size And Concentration Of Gold Nanoparticles From UV−Vis Spectra. *Analytical Chemistry* 2007, *79*, 4215-4221.

(68) Umadevi, D.; Sastry, G. Molecular And Ionic Interaction With Graphene Nanoflakes: A Computational Investigation Of CO_2, H_2O, Li, Mg, Li^+, And Mg^{2+} Interaction With Polycyclic Aromatic Hydrocarbons. *The Journal of Physical Chemistry C* 2011, *115* (19), 9656-9667.

(69) Gold http://sites.cardiff.ac.uk/xpsaccess/reference/gold/ (accessed Feb 15, 2022).

(70) Song, J.; Xu, L.; Zhou, C.; Xing, R.; Dai, Q.; Liu, D.; Song, H. Synthesis Of Graphene Oxide Based Cuo Nanoparticles Composite Electrode For Highly Enhanced Nonenzymatic Glucose Detection. *ACS Applied Materials & Interfaces* 2013, *5*, 12928-12934.

(71) Dai, X.; Nekrassova, O.; Hyde, M.; Compton, R. Anodic Stripping Voltammetry Of

Arsenic(III) Using Gold Nanoparticle-Modified Electrodes. *Analytical Chemistry* 2004, *76*, 5924-5929.

(72) Xiao, L.; Wildgoose, G.; Compton, R. Sensitive Electrochemical Detection Of Arsenic (III) Using Gold Nanoparticle Modified Carbon Nanotubes Via Anodic Stripping Voltammetry. *Analytica Chimica Acta* 2008, *620*, 44-49.

(73) Cheng, T.; Nasir, M.; Ambrosi, A.; Pumera, M. 3D-Printed Metal Electrodes For Electrochemical Detection Of Phenols. *Applied Materials Today* 2017, *9*, 212-219.

(74) R. G. Compton and C. E. Banks, *Understanding Voltammetry*. London: Imperial College Press, 2nd ed., 2011.

(75) Su, D.; Zhang, Y.; Wang, Z.; Wan, Q.; Yang, N. Decoration Of Graphene Nano Platelets With Gold Nanoparticles For Voltammetry Of 4-Nonylphenol. *Carbon* 2017, *117*, 313-321.

(76) Zhao, L.; Dong, P.; Xie, J.; Li, J.; Wu, L.; Yang, S.; Luo, J. Porous Graphene Oxide–Chitosan Aerogel For Tetracycline Removal. *Materials Research Express* 2013, *1*, 015601.

(77) Zhou, Q.; Lei, M.; Li, J.; Zhao, K.; Liu, Y. Sensitive Determination Of Bisphenol A, 4-Nonylphenol And 4-Octylphenol By Magnetic Solid Phase Extraction With Fe@Mgal-LDH Magnetic Nanoparticles From Environmental Water Samples. *Separation and Purification Technology* 2017, *182*, 78-86.

(78) Javadi, E.; Baghdadi, M.; Taghavi, L.; Ahmad Panahi, H. Removal Of 4-Nonylphenol From Surface Water And Municipal Wastewater Effluent Using Three-Dimensional Graphene Oxide–Chitosan Aerogel Beads. *International Journal of Environmental Research* 2020, *14*, 513-526.

(79) Zhou, W.; Zhao, B.; Huang, X.; Yang, X. Electrochemical Determination Of 4-Nonylphenol On Graphene-Chitosan Modified Glassy Carbon Electrode. *Chinese Journal of Analytical Chemistry* 2013, *41*, 675-680.

(80) Normal blood sugar ranges and blood sugar ranges for adults and children with type 1 diabetes, type 2 diabetes and blood sugar ranges to determine people with diabetes. https://www.diabetes.co.uk/diabetes_care/blood-sugar-level-ranges.html (accessed Feb 15, 2022).

(81) Zhou, Y.; Yang, S.; Qian, Q.; Xia, X. Gold Nanoparticles Integrated In A Nanotube Array For Electrochemical Detection Of Glucose. *Electrochemistry Communications* 2009, *11*, 216-219.

(82) Hu, S.; Wang, Y.; Wang, X.; Xu, L.; Xiang, J.; Sun, W. Electrochemical Detection Of Hydroquinone With A Gold Nanoparticle And Graphene Modified Carbon Ionic Liquid Electrode. *Sensors and Actuators B: Chemical* 2012, *168*, 27-33.

(83) Tashkhourian, J.; Daneshi, M.; Nami-Ana, F.; Behbahani, M.; Bagheri, A.

Simultaneous Determination Of Hydroquinone And Catechol At Gold Nanoparticles Mesoporous Silica Modified Carbon Paste Electrode. *Journal of Hazardous Materials* 2016, *318*, 117-124.

Chapter 7 Synthesis of Pd-Containing Bi-metal and Tri-metal Nanoalloys, and Applications in Various Fuel Cell Reactions

7.1. Introduction

Palladium metal was firstly discovered by British chemist William Hyde Wollaston[1] and has been used in many different fields including capacitors[2], sensors[3], dentistry[4], photography[5], and biomedical applications such as bacterial growth prohibitor and cytotoxic treatments towards human cancer cells.[6-8] But until today, the majority of Pd was used in heterogeneous catalysis. Palladium complexes like Lindlar's Palladium speed up selective hydrogenation, dehydrogenation, carbon-carbon bonding reactions including Heck reaction, Suzuki coupling, and the Wacker process.[9-15]. To maximize the effect of using Pd in catalysis, structural modifications become extremely crucial and PdNPs with advanced structures are extensively studied in many recent research areas. In the Heck reaction, a single PdNP can leach out from a nanocluster and form a defective surface, inducing further reactions to happen at a higher reaction speed. [16-18]

Supported PdNPs are also found in use for various electrocatalysis reactions including dissociative electron transfer (DET), selective oxidation and reduction. In recent years, PdNP-based catalysts have been gaining interest in fuel cell reactions, due to their higher resistance towards CO toxicity compared to Pt-based catalysts, which is thought to be the most ideal fuel cell catalyst.[19] PdNP catalysts are often found also in various fuel cell reactions, including the hydrogen evolution reaction, oxygen reduction reaction and

formic acid oxidation, as substitutes for Pt and exhibit comparable catalytic reactivities.[20-25] However, to realize the wide applications of Pd-based nanocatalysts in fuel cell reactions, modifications of composition and structure are vital to optimize the catalytic reactivity, reduce the amount of Pd used, and stabilize the nanostructure.

By alloying with other noble metals such as Pt, Ru and Au[25-26], and cheaper 3d metals such as Ni, Fe, Co, Cr and Cu, the catalytic abilities are promoted by the synergetic effect which modifies the electronic properties compared to Pd monomers.[27-30] In addition to these bi-metal nanoalloys, many tri-metal alloy systems were studied, including PdAuCo, PdCoMo, Pd_2NiAg and PdAuCu nanoalloys.[31-34] However, in most of these studies, these stable nanoalloys are formed through reduction at high temperatures between 500-900℃. Therefore, it is still crucial to formulate a practical and simple method to synthesis stablised Pd-containing tri-metal alloys ready for fuel cell applications under milder conditions, which to the best of our knowledge, is still waiting to be addressed.

To stabilize the structure of Pd and Pd-containing nanospecies, polymer stabilizers such as polyvinylpyrrolidone (PVP) are often used. PVP stabilizes PdNPs as a weak reducing reagent and prohibits the aggregation to nearby nanoparticles via steric effects.[35-36] Structurally, its stabilizing effect is attributed to the way it attaches to nanoparticles, which is similar to another polymer that we have introduced in chapter 5, Nafion. Their molecular formula both have a hydrophilic part that can attach to the nanoparticle and a hydrophobic bulky tail that extends to solvents, causing repulsive forces and hindering the adhesion between nearby nanoparticles via steric effects.[36] A more significant contribution of PVP in nanoparticle synthesis is to effectively control the shape of

nanoparticles because it prefers specific facets when attached to nanoparticles due to non-covalent attraction and facilitates binding between oxygen atoms at its tip and nanoparticles.[36-38] This will allow the growth of nanoparticles only along certain directions and forms distinct shapes of nanostructures.[36,39] Moreover, the molar ratio of metal nanoparticles and molecular weights (chain lengths) of PVP can also be altered to obtain different nanostructures.[36,40-43] These stabilizing and shaping effects were found meaningful in synthesis and catalytic applications of Pd nanoparticles, and exhibited extraordinary reactivities compared to the unstablised nanoparticles.[44] However, the high coverage of non-conductive PVP at the surface reduces active spots of nanoparticles when some surface sensitive experiments were done.[45] Therefore carbon or carbon-containing structures such as graphene nanotubes with high conductivity might be the better choice.[7,37-38] In this chapter, we compared the effectiveness of stabilizing colloidal Pd nanoparticles between PVP and cx-GNF in a straightforward, one-step reduction in aqueous phase.

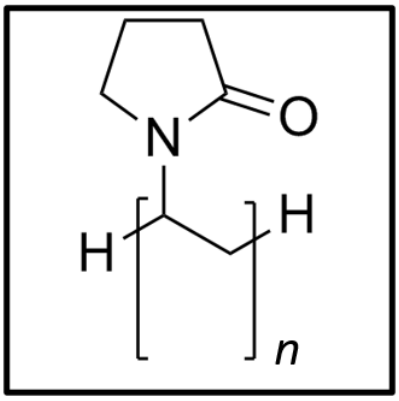

Figure 7.1 Structure of polyvinylpyrrolidone (PVP). The hydrophilic portion is the polar amide group within the pyrrolidone ring, and the non-polar hydrophobic group is the methine groups.

In the previous chapters, we examined the catalytic performance of various nanospecies

using the HER. As for this chapter, we would like to apply the Pd-containing nano-catalysts into two other important reactions: Oxygen Reduction Reaction (ORR) and Ethanol Oxidation Reaction (EOR). Both of them are relevant for real-world applications of fuel cells, such as fuel cell vehicles.

Oxygen is the most abundant element in the Earth crust, and ORR is one of the most crucial reactions in life including biological respiration. In fuel cells, ORR happens at cathodes, involves breaking of O=O bonds, and forms water (and H_2O_2 in one reaction pathway).[46] On the other hand, ethanol fuels are believed to have many advantages compared to hydrogen, including easier storage and transportation, high specific energy and wide availability and the Direct Ethanol Fuel Cell (DEFC) is one of the most promising electric power sources. The whole reaction involves breaking of the C-C bond, and ethanol being oxidized to produce CO_2.[47] Pt and Pd are common catalysts for EOR in ADEFC (alkaline direct ethanol fuel cell) and in basic media, the kinetics of both anodic oxidation reactions and catholic reduction reactions were more favoured.[48] To reduce cost and enhance reactivity, other transition metals such as Ru, Sn, Pb, Au, Ag, Cu, and Bi are used as alloys, deposits or ad-atoms.[47] Detailed mechanisms of these two reactions and highlights of Pd nanoparticle/Pd containing nanoalloys as catalysts will be discussed extensively in later sections.

7.2. Aim of this Chapter

In chapter 3, we noted that bulk Pd metal and Pd containing nanoalloys are widely used in the hydrogen production industry, and in this chapter, we investigate the different techniques for synthesizing Pd-containing nanospecies as heterogeneous catalysts

including both electrodeposition and a wet chemistry method. The galvanic replacement reaction between Cu and Pd is also introduced to minimize the usage of precious metal. We examine the stabilizing effect of cx-GNF versus PVP for colloidal Pd nanoparticles and form stable PdAuCu tri-metal colloidal nanoalloys. A comprehensive surface analysis of these species was done by XPS. As for the applications, since we have studied the HER system in Chapter 3, 4 and 5, we would like to study other important fuel cell reactions as well. Herein we chose ORR and EOR, together with the HER to examine the performance of Pd-containing nanoalloys. For each reaction system, the electrodeposited groups were compared with the colloidal group. Within each group, Pd-containing nanoalloys were compared with AuCu nanoalloy and Pd nanoparticles. The best candidate was determined, and the most economic option was also proposed.

7.3. Results and Discussion

7.3.1. Synthesis of Pd-containing Nanospecies

7.3.1.1. Electrodeposition and Galvanic Replacement Reaction

Au nanoparticles were electrodeposited on the surface of BDDEs via a two-step scheme that we introduced in chapter 3 and 4. Afterwards, Cu nanoparticles were plated via a single-step scheme. The source of Au and Cu used for electrodeposition was 1 mM $HAuCl_4$, and 2 mM $CuSO_4$, respectively. The supporting electrolyte for electrodeposition was 0.1 M H_2SO_4. Au nanoparticles were plated as core through a 2-step scheme: -0.7 V for 2 s; 0 V for 150 s; Cu nanoparticles were plated on top of Au nanoparticles by holding

the potential at -0.55 V for 150 s. Using a two-step scheme ensured the formation of Au nanoparticles with diameter 100~200 nm with high dispersity.

The Pd solution used for galvanic replacement reaction was 2 mM $PdCl_2$ in 0.1 M HCl. AuCu-BDDE was immersed directly into Pd solution at room temperature for 30 min, rinsed and dried for further analysis. The standard oxidation/reduction potential for these two metals are:

$$\mathrm{Pd}^{2+} + 2e^- = \mathrm{Pd} \qquad E^\circ = +0.987\mathrm{V}$$

$$\mathrm{Cu} = \mathrm{Cu}^{2+} + 2e^- \qquad E^\circ = +0.339\mathrm{V}$$

The reduction potential of the Pd ion is much higher than the oxidation potential of Cu, this difference became the driving force of the following reaction to happen easily at room temperature:[49]

$$\mathrm{Pd}^{2+} + \mathrm{Cu} = \mathrm{Cu}^{2+} + \mathrm{Pd}$$

When BDDE plated with AuCu nanoalloy is immersed into the solution of $PdCl_2$, the Galvanic Replacement Reaction (GRR) happened spontaneously, and occur particularly faster at sites with higher surface energy, namely, defects. [50] Therefore, the expected nanostructure of AuCu with high dispersity (similar to what we saw in chapter 4, the sAgAuNA case) can facilitate the GRR process. The oxidized Cu atoms dissolved into the solution, generating a small hole on the surface of the nanostructure. As predicted by Marcus Theory, electrons rapidly migrate to the surface of the nanoparticles and bond by surrounding Pd ions to generate Pd atoms. The Au core will not react with Pd in the solvent at room temperature since it has higher oxidation potential (1.69 V).[49]

As a result, the structure of the catalysts made through GRR is more porous and tend to

preserve higher catalytic activities. The size of Cu and Pd atoms are different, and the modified electronic structures varied when bonded with Cu. This size difference resulted in incompletes coverage of Pd on top of Au, making the structure more porous with many defect. [50-51]The condition of replacement can be viewed using XPS, by comparing the percentage of surface Cu and Pd, but we expect a full replacement of Pd because a Pd monomer shell is thermodynamically more stable than segregation of Pd and Cu.

7.3.1.2. Wet-chemistry Method

Colloidal nanospecies were synthesized via the same techniques as previous chapters: a single-step reduction by $NaBH_4$ in icebath. The metal solutions: 2 mM $PdCl_2$ (in 0.1 M HCl), 1 mM $HAuCl_4$, and 2 mM $CuSO_4$ were mixed with cx-GNF water solution (0.5 mg/mL) before being reduced. The volume ratio of metal solution: cx-GNF solution was 1:1, and the concentration of $NaBH_4$ was 5 mM. Metal + GNF solution was added dropwise into chilled $NaBH_4$ solution and wrapped with aluminum foil for storage. Unstabilised PdNPs were also made for control experiments swapping cx-GNF for same volume of pure water.

In chapter 5, we showed the advantage of using cx-GNF as a stabilizer for colloidal nanoparticles in electrocatalysis by comparing it with a widely used stabilizer sodium citrate. In this chapter, similar control studies were done, and we compared cx-GNF with PVP for their stabilizing abilities.

PVP of molar weight 55000 g/mol was used and the concentration was 100 mmol in methanol. PVP stabilized nanoparticles were synthesized in an ice bath, with stirring. $NaBH_4$ solution with same concentration was used, injected slowly into the mixture of

Pd^{2+} and PVP using a pipette. The molar ratio of Pd: PVP was 1:50. After the addition of reducing agent, the system was left with stirring in an ice bath for 1 hour.

We examined the stability of PdPVP and PdGNF with UV-Vis spectra. Pd^{2+} aqueous solutions are yellow, meaning they have a peak at wavelength about 400-420 nm. When homogeneous Pd nanoparticles are formed, that peak will disappear and the UV-Vis spectrum for Pd nanoparticles has no peak in range of visible light (300-800 nm), thus colloidal Pd nanoparticle solutions will appear black.[52] However, that was not the case for PdPVP. The solution turned brownish as reducing agent was slowly added, and the colour faded away with stirring and time. In the end, the solution was light yellow. The UV-Vis spectrum of PdPVP showed that not all Pd^{2+} ions were reduced. In fact, when we compared it with the spectrum of Pd^{2+} ions, we concluded that only 2/3 of the species were reduced (Figure 7.2a).

We attempted to make fully reduced PdPVP using two approaches:

1. We observed colour change from yellow to blackish as reducing agent was added and the colour faded away with vigorous stirring. Therefore, we synthesized PdPVP without stirring, only gently swirled the volumetric flask to mix the reagents.
2. Since the UV-Vis spectrum showed an incomplete reduction, we attempted to add more reducing agent: 3 times the concentration of $NaBH_4$ compared to the previous experiment.

The corresponding UV-Vis spectra showed that, when the reaction was performed without stirring, Pd nanoparticles were fully reduced (Figure 7.2a). This suggested,

surprisingly, that stirring dissolved oxygen from the air into the solution, and the solution became resistant to full reduction. There are studies that illustrated how stirring time and speed can affect the size, shape, morphology and composition of resulting nanoparticles during synthesis.[53-54]After repeating the experiments, we conclude that gentle swirling during a shorter synthesis time might be better for this particular reaction. Tripling the concentration of reducing reagent did not completely reduce Pd^{2+}, since there was still a small peak at around 420 nm indicating the presence of Pd^{2+} ions. Although we seemed to have optimized the approach for synthesizing PdPVP, the colloidal solutions were not stable enough. Visible aggregation happened after one day, and the solutions were no longer suitable for electrochemical analysis (Figure 7.2b).

On the other hand, when we looked at the UV-Vis spectra of cx-GNF stabilized Pd nanoparticles, we saw a convincing full reduction and excellent stability over 14 days since the peak around 400 nm completely disappeared (Figure 7.2a). In addition to the stability, milder synthesis conditions and mechanism, cx-GNF preserves high solubility in water and superior conductivity are some advantages that PVP does not have, and these are very important for the modification, electroanalysis, and cleaning of BDDEs. Therefore, for further study, we used PdGNF as the studied system and used cx-GNF to stabilize all other nanospecies.

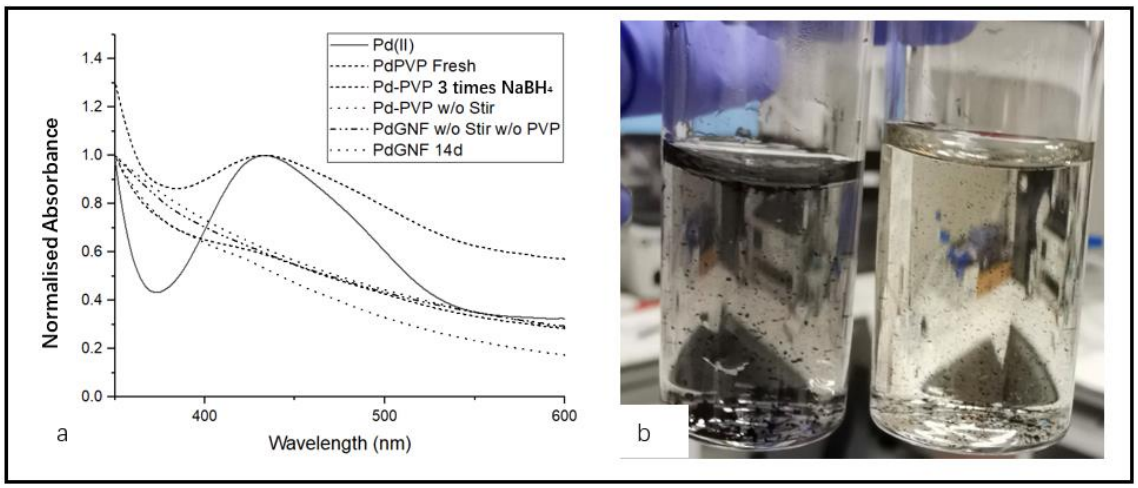

Figure 7.2 UV-Vis spectra of Pd-containing species (a); aggregated unstabilised Pd (b-left), and Pd-PVP (b-right) 1 day after synthesis.

7.3.2. Surface Analysis using SEM and XPS

7.3.2.1 SEM Analysis

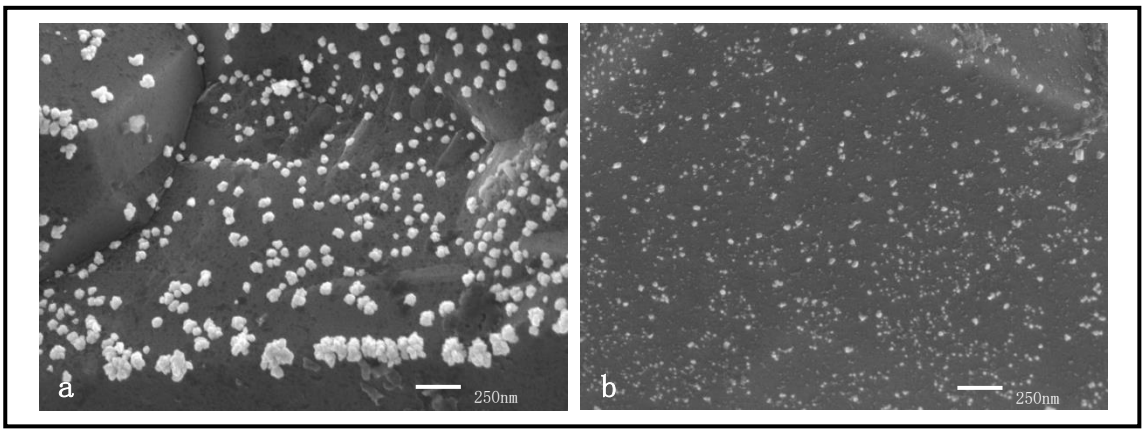

Figure 7.3 HR-SEM of PdAu (Cu) nanoalloy made by electrodeposition + GRR (a); HR-SEM of PdAuCu colloidal nanoalloy stabilized by GNF (b).

SEM was used to compare the relative particle size and dispersion that varied with synthesis method. From the high-resolution SEM, it was obvious that none of the samples showed heavy aggregation. The colloidal Pd-containing nanoalloys stabilized by GNF have smaller average size of sub 10 nm with more of a spherical shape, and the distribution was more even on the electrode. On the other hand, the Pd containing

nanoalloy synthesized through electrodeposition followed by GRR have an average size of 150nm with irregular polyhedral shapes and tend to grow on the defects of BDDEs. This observation is consistent with that obtained in chapter 5, colloidal GNF stabilized nanospecies are able to maintain the mono-dispersity and regular shapes.

7.3.2.2 XPS Analysis

Table 7.1 Summary of XPS data on survey spectra.

Sample #		**Cu%**	**Au%**	**Pd%**	**Method**
1	ED Cu	0.73	/	/	1-step electrodeposition
2	ED AuCu	0.70	0.46	/	Au core (2-step electrodeposition) + Cu shell (1-step electrodeposition);
3	ED AuCuPd	/	0.45	0.73	Sample 2 + GRR
4	CuGNF	0.94	/	/	1-step reduction using $NaBH_4$; cx-GNF stablized Drop-coated onto BDDEs
5	AuCuGNF	0.46	0.22	/	
6	AuCuPdGNF	0.28	0.43	2.75	
7	AuCuGNF-Pd	/	0.36	0.73	Sample 5 + GRR

XPS was the most important surface analysis in this study. From XPS data, we were able to understand our systems better from three aspects.

By comparing the absolute metal amount on electrodes, we can review the stabilizing ability of cx-GNF in preventing aggregation of nanospecies. When comparing sample 1

with sample 4, we saw a rise in Cu percentage, suggesting that the cx-GNF stabilised Cu nanoparticles with dispersity. Therefore, the percentage of surface Cu was higher in sample 4, even if the amount of metal loading was similar. The mechanism on cx-GNF stabilizing nanospecies was discussed comprehensively in chapter 5, and this experiment confirmed this.

As mentioned in previous sections, we can observe the completeness of GRR by comparing the surface percentage of Cu and Pd in sample 2 and 3. For both electrodeposited and colloidal samples, GRR went to completion and all Cu atoms on samples 2, 5 were substituted by Pd in sample 3, 7. Moreover, if we compare sample 3 and 7, the composition was very similar. This showed that GRR in this experiment was very reliable and was suitable for both electrodeposited and colloidal samples. The compositional similarity between sample 3 and 7 might indicate similar catalytical abilities, which will be discussed later in this chapter.

For the colloidal tri-metal alloy system, we can get a rough understanding about the alloying pattern and compare it with that of the bi-metal alloy system. To keep the amount of metal loading similar between the two methods, in colloidal samples, the ratio of Cu: Au was 2:1. In sample 5, Cu: Au was 0.46:0.22. This ratio is very close to 2:1, which suggested that unlike sample 2, which was likely to be a core-shell structure designated by rigid deposition order, when Cu and Au was reduced together through a 1-step scheme, it tended to form a cluster alloy. However, when three metals were reduced together, a more complex situation was presented and more factors need to be considered. As we have discussed in chapter 4, there are 3 factors that decide the inner elemental

arrangement of alloys: atomic size, surface energy and metal-metal bond length.

Cu and Au have about the same atomic radii, 135pm. Therefore, when we only had Cu and Au in our system, they will naturally tend to form a cluster alloy. However, Cu has larger surface energy E_{surf} (eV per site) of 0.46 eV than that of Au, which is 0.38 eV, making it more favorable to be the core. On the other hand, Cu-Cu bond length is 2.44 Å whereas Au-Au metal bond length is 2.48 Å, this also indicated that Cu is more likely to be the core, followed by Au, and Pd with a larger atomic radius (140 pm), surface energy, and longest metal-metal bond is going to be the surface element. This prediction is coherent with what we saw in sample 6.[55-58]

7.3.3. Hydrogen Evolution Reaction

The amount of charge transfer during electrodeposition of Au and Cu was calculated through chrono-voltammetry and 30 μL of colloidal species were drop-coated onto BDDEs were controlled to be roughly the same for the following analysis. The catalytic activities of nanospecies in the HER were monitored using LSV from 0 V to -2.0 V at 20 mV/s performed in 0.5 M sulfuric acid.

The basic principle of the hydrogen evolution reaction was thoroughly discussed in the previous chapters, therefore will not be repeated in this section. In this chapter, since we have two types of nanospecies (electrodeposited and colloidal), ranging from single nanoparticle, bi-metal nanoalloys, to tri-metal nanoalloys, the emphasis was to ensure a complete comparison amongst them.

Figure 7.4, together with table 2 and 3 gave a comprehensive summary about the current

density of each species at designated potentials, with Figure 7.4 left and Table 7.2 (each data spot was averaged over 3 samples, with error of $\sim \pm 0.5$ mA/cm^2)for colloidal species, and Figure 7.4b and Table 7.3 (each data spot was averaged over 3 samples, with error of $\sim \pm 0.5$ mA/cm^2) for electrodeposited species. In Figure 7.4 right and Table 7.3, the best two samples from the colloidal group, PdAuCuGNF and Pd-AuCuGNF GRR were also included for direct comparison.

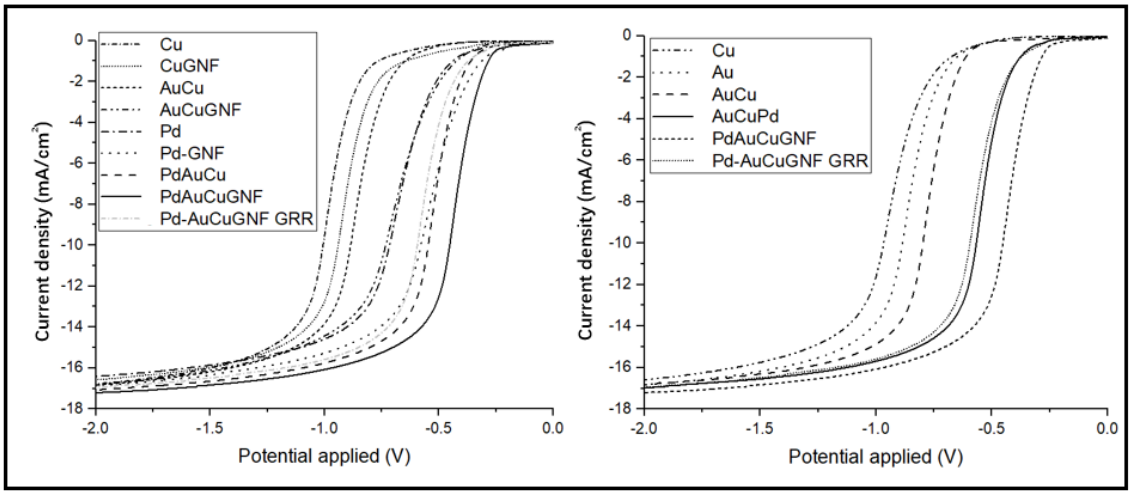

Figure 7.4 Summary of current densities in the HER for colloidal nanospecies (left). Summary of current densities in the HER for ED nanospecies and colloidal nanospecies with best performance. (right).

Table 7.2 Summary of Current densities in the HER for Colloidal Nanospcies

	***J* (mA/cm^2) at -0.8V**	***J* (mA/cm^2) at -1.0V**
Cu	1.3	9.6
CuGNF	2.7	12.8
AuCu	4.7	13.8
AuCuGNF	12.3	14.4
Pd	12.8	14.6
PdGNF	14.3	15.3
PdAuCu	15.0	15.8

PdAuCuGNF	15.5	16.1
Pd-AuCuGNF-GRR	14.7	15.6

Table 7.3 Summary of current densities in the HER for ED nanospecies and colloidal nanospecies with best performances..

	J **(mA/cm^2) at -0.8V**	***J*** **(mA/cm^2) at -1.0V**
Cu ED	2.8	12.0
Au ED	4.7	13.8
AuCu ED	10.4	14.9
Pd-AuCu ED GRR	14.9	15.7
Pd-AuCuGNF GRR	14.7	15.6
PdAuCuGNF	15.5	16.1

For the colloidal group (Figure 7.2a and Table 7. 2), several notable findings were made. First, cx-GNF stablised samples exhibited better catalytic reactivities than unstablised ones; all samples stablised with cx-GNF were better than a single metal. The stablising effect came from the metal-to-carbon atom charge transfer and was discussed in detail in chapter 5. In this chapter, we saw the same effect for Pd-containing bi-metal and tri-metal nanoalloys. The better dispersity of metal nanospecies on the surface of cx-GNF were proven by the XPS analysis. This made more active sites for reactions available.

Second, samples that containing Pd showed higher current responses under designated potentials. All Pd containing samples showed outstanding catalytic performance. In Figure 7.2a, there is a huge gap dividing Pd-containing and non-Pd containing samples. As shown in Figure 7.5, the volcano plot, Pd has a very similar adsorption energy compared to Pt. In acidic media, the first discharge step involves the coupling of a proton

with an electron at the catalyst's surface, forming an adsorbed hydrogen atom. Therefore, the low Gibb's free energy barrier and exchange current density of Pd made it a perfect catalyst for the HER.

Pd has an empty 5s orbital and readily accepts electrons from other donors, which explains its high affinity to adsorption of hydrogen atoms. After hydrogen atoms are adsorbed onto the surface of Pd, they occupy the octahedral voids within the Pd lattice, forming stable PdH_x compounds.

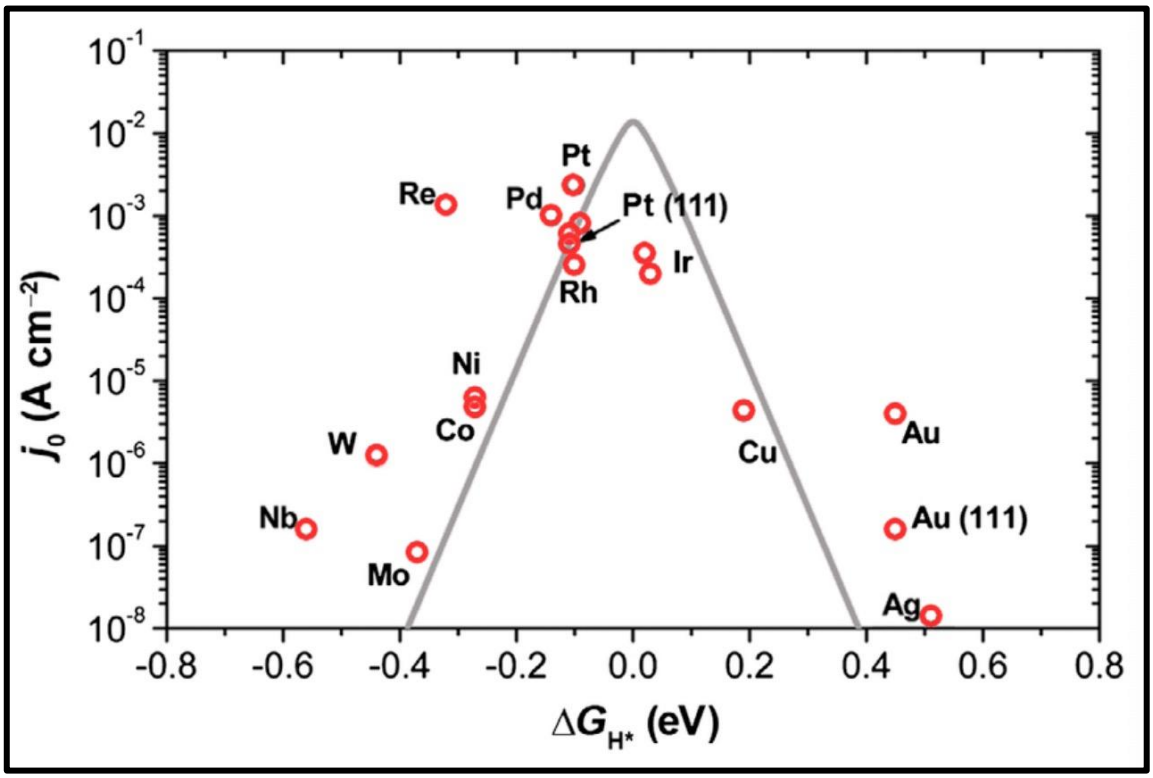

Figure 7.5 Volcano plot of exchange current density (j_0) as a function of the DFT-calculated Gibb's free energy (ΔG_{H^*}) of the adsorbed atomic hydrogen on a pure metal (adapted from[7]).

As expected, alloyed samples had better performance in the HER catalysis. When Pd is alloyed with Au, the synergistic effects made the catalytic performance enhanced, compared with Pd nanoparticles alone. Specifically, in this reaction, the key factor that changed when Pd is alloyed with Au is the solubility of H at the surface. Namba et al.

have done DFT calculations regarding the significant acceleration of hydrogen adsorption with addition of Au. They found that the enhancement is explained by the destabilization of the chemisorbed surface hydrogen attributed to the change of surface electronic states, therefore reducing the penetration barrier of hydrogen kinetically. [59]

In the trimetallic nanoalloy sample, the synergistic effects were magnified. The types of heterogenous interfaces were increased compared to bimetallic nanoalloys, therefore, more changes in surface electronic states and defects at interfaces were presented, and thus made the structure more porous and promoted the reactivity of active sites even more. In real applications, the ratio of metals and advanced architectures are also essential factors to consider when optimising the solution for a multi-metal nano-catalyst.

Overall, the performance of nanoalloys was consistent with predictions from XPS results. Two PdAu nanoalloy samples prepared via galvanic replacement had similar surface composition and showed quite similar reactivity in the HER catalysis. The PdAuCu tri-metal alloy sample, with the highest percentage of surface Pd, showed highest current responses at designated potentials.

7.3.4. Oxygen Reduction Reaction

The catalytic activities of nanospecies in ORR were monitored using LSV from 1.0 V to -0.2 V at 20 mV/s performed in 0.5 M sulfuric acid purged with oxygen for 2 hours before analysis.

In acidic aqueous solution, ORR reactions undergo two different processes, involving either a four-electron transfer, producing water, or a two-electron transfer, producing

H_2O_2. The unstable peroxide gets further reduced to water through a two-electron transfer scheme:

$$O_2 + 4H^+ + 4e^- \rightarrow 2H_2O;\ E° = +1.229V \quad (31)$$

$$O_2 + 2H^+ + 2e^- \rightarrow 2H_2O_2; E° = +0.670V \quad (32$$

$$H_2O_2 + 2H^+ + 2e^- \rightarrow 2H_2O; E° = +1.770V \quad (33)$$

The four-electron transfer scheme is preferred due to high efficiency.

Amongst common fuel cell reactions, ORR is probably the slowest reaction because ofthe high activation energy barrier due to the high bond energy of the oxygen molecule and the positive entropy change caused by dissociation of oxygen gas molecules. Hence, at room temperature, an electrocatalyst is used for this reaction, directly decrease the activation energy barrier by lowering the cathode potential.

The catalyzed four-electron pathway ORR on a catalytic surface takes place in following sequence:

$$O_2(g) \rightarrow {O_2}^* \quad (34)$$

$$\frac{1}{2}{O_2}^* \rightarrow O^* \quad (35)$$

$$O^* + H^+(aq) + e^- \rightarrow HO^* \quad (36)$$

$$HO^* + H^+(aq) + e^- \rightarrow H_2O^* \quad (37)$$

* means active spots on catalytic surface. Herein the four steps are oxygen adsorption, oxygen dissociation, OH formation and water formation, respectively. For the two-electron transfer scheme, after the oxygen molecule gets adsorbed onto catalytic sites, formation of OOH and H_2O_2 takes place as:

$${O_2}^* + H^+(aq) + e^- \rightarrow HOO^* \quad (38)$$

$$HOO^* + H^+(aq) + e^- \rightarrow H_2O_2 \qquad (39)$$

The unstable HOO^* can dissociate by itself as:

$$HOO^* \rightarrow O^* + HO^* \qquad (40)$$

When metal nanoparticles are used for catalysis, it is essential to determine which step above is the rate determining step. According to Nørskov *et.al.*, for most of the nanometal surfaces, the adsorbed oxygen molecule $O_2{}^*$ and hydroxyl intermediate HO^* are quite stable at the equilibrium potential. They found that the calculated rate constant for the activated proton/electron transfer to these two intermediates is quantitatively related for the observed kinetics, leaving the rate determining step to be either the splitting of oxygen molecule at the catalytic surface (35), or formation of water (37). In other words, the binding energies towards oxygen molecules and hydroxyl intermediates are crucial factors in oxygen reduction activities for metal nanoparticles.

Using theoretical DFT calculation, Nørskov *et-al* formed two volcanic diagrams on the oxygen reduction activity as a function of oxygen binding energy and hydroxyl binding energy, respectively (Figure 7.6). Similar to the case in the HER, Pt has the highest activity in catalyzing ORR, followed by Pd. [60]

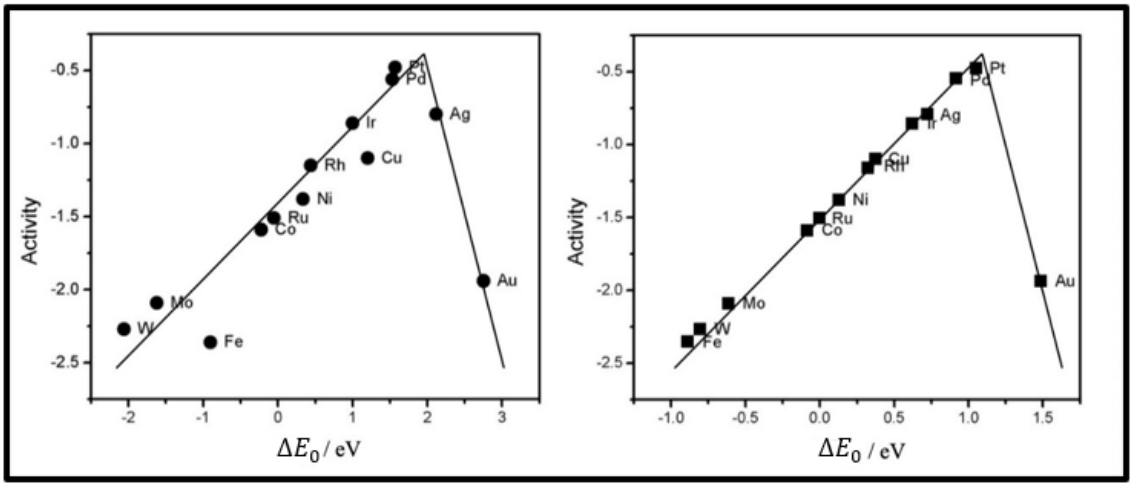

Figure 7.6 Trends in oxygen reduction activity plotted as a function of the oxygen binding energy and OH binding energy (adapted from [60])

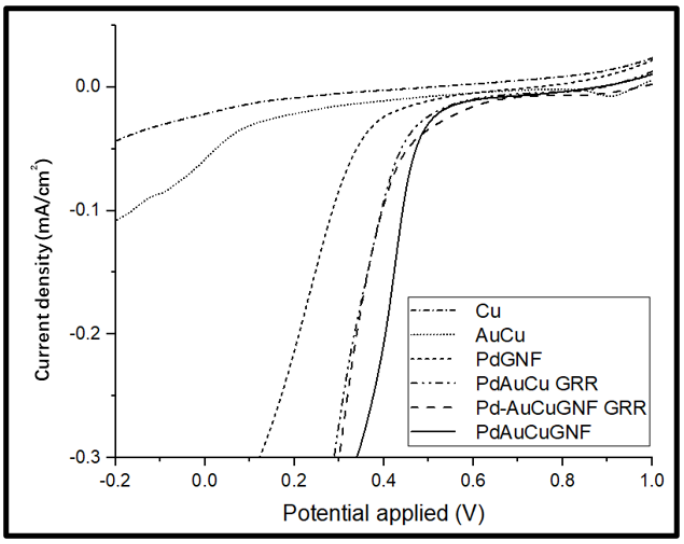

Figure 7.7 Summary of current densities in the HER for various nanospecies.

Back to our study, the catalytic effects of Cu and AuCu (electrodeposited ones) were not ideal, and the current density was quite low, therefore the comparisons with colloidal Cu/Au containing species were not repeated. This can be rationalized by the Sabatier Principle, the interactions between the catalyst and the substrate should not be too strong or too weak. When the interaction is too weak, the bonding is difficult to happen, but when the interaction is too strong, it will slow the desorption process of the intermediates from the catalytic surface, and the active spots will no longer be active anymore, hindering any further reaction. The volcano plot illustrates this principle very well. Cu has a negative binding energy, meaning the binding between Cu and O/OH intermediates are very strong, thus increasing the desorption barrier, such that the rate is limited by the desorption of intermediates. Au has a positive binding energy, meaning the interaction between Au and O/OH intermediates is weak, and the reaction is limited by the adsorption of the reactant. Therefore, neither Cu nor AuCu alloy showed outstanding catalytic

performance.

All Pd-containing alloys (colloidal and electrodeposited) showed enhanced current density compared to PdGNF monomer. The enhancement in ORR catalysis of PdAu nanoalloys has been studied by Xing et al, and they found that the observed ORR activities may be attributed to the surface strain and the shift of the d-band center. The interplay of both compressive and tensile lateral strain and radial contraction (compressive strain) can lead to the improvement of ORR catalysis. This explains our observations that PdAu nanoalloys prepared via GRR exhibited better catalytic performances.

The tri-metal nanoalloy had the best catalytic reactivity, because there was larger amount of metal on the electrode surface. However, another fact that need to be highlighted is that Pd was on top of the core-shell tri-metal nanoalloy structure. Stamenkovic et al have shown when a layer of Pt is deposited on top of other 3d metals or alloys, the activity in ORR reaction will increase. This can be used to explain the beneficial effect in catalysis of Pd at the top layer of our PdAuCuGNF nanoalloy.

7.3.5. Ethanol Oxidation Reaction

The catalytic activities of nanospecies in the EOR were monitored using cyclovotammetry from -1.0 V to 0.25 V at 50 mV/s performed in 1.0 M KOH + 1.0 M ethanol.

It is generally accepted that the EOR takes place via two parallel pathways in alkaline media. In the C2 pathway, the C-C bond in ethanol is not broken, but oxidized to

acetaldehyde, and then to acetate. According to Lai et al, in alkaline media, the deprotonated form of hydrated acetaldehyde (CH_3CHOHO^-) is the active species for the final of the whole reaction: acetaldehyde oxidation. In the C1 pathway, the C-C bond is broken, producing CO and CH_x as unstable intermediates, which are further oxidized to carbonate in alkaline media. Lai et al also stated that at lower temperature, the $CH_3CH_2O^-$ intermediate in C2 pathway can break down to acetate and carbonyl, changing the reaction towards the C1 pathway. The overall reaction scheme is shown below:

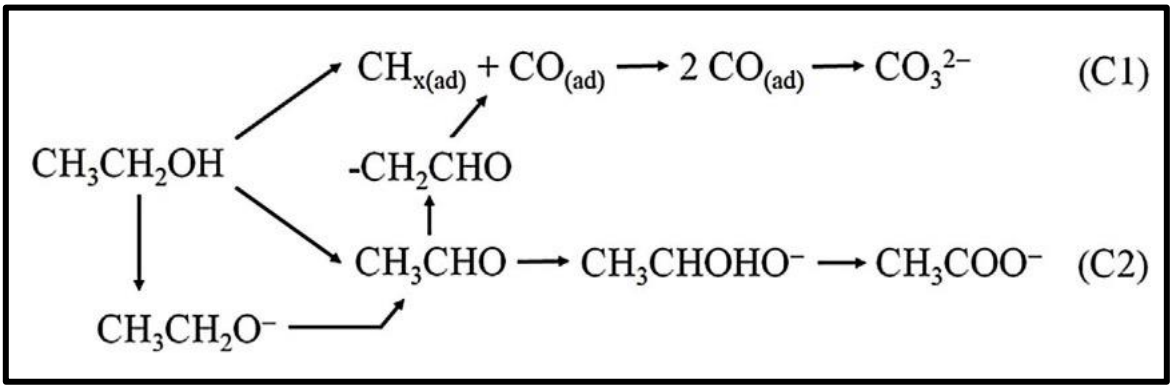

Scheme 7.1 EOR reaction scheme in alkaline media, reproduced from [47]

When EOR is catalyzed by Pd nanoparticle, particularly, Liang *et al.* concluded that a C2 pathway is followed:

$$\mathrm{Pd-(CH_3CO)_{ads}} + \mathrm{Pd-OH_{ads}} \xrightarrow{\text{r.d.s}} \mathrm{Pd-(CH_3COOH)_{ads}} + \mathrm{Pd}$$

$$\mathrm{Pd-(CH_3COOH)_{ads}} + \mathrm{OH^-} \xrightarrow{\text{fast}} \mathrm{Pd} + \mathrm{CH_3COO^-} + \mathrm{H_2O}$$

Since the first step is the rate determining step, the high affinity of Pd will increase the concentration of $\mathrm{Pd-OH_{ads}}$ absorbates on the catalytic surface and drive the reaction more towards the right. An insufficient coverage of hydroxy intermediate will lead to a decrease in the peak current, therefore Pd (and Pt) are the best candidates for metal nanoparticle catalysts.[47]

When Au (and Cu) are alloyed with Pd, more porous active sites are created, thus opening more channel for adsorption and desorption of the reactants, intermediates, and products, meaning the mass transfer is promoted. Also, Au (and Cu) can also form $Au(\text{or } Cu) - OH_{ads}$ intermediate, which can also react with other intermediate fragments of ethanol. On the other hand, Lv et al. pointed that PdAu (Cu) alloy showed the synergistic effect by modifying the electron energy states of Pd. This modification is especially meaningful in the EOR catalysis as it will weaken the adsorption interactions between carbonaceous intermediates and Pd atoms.[61]

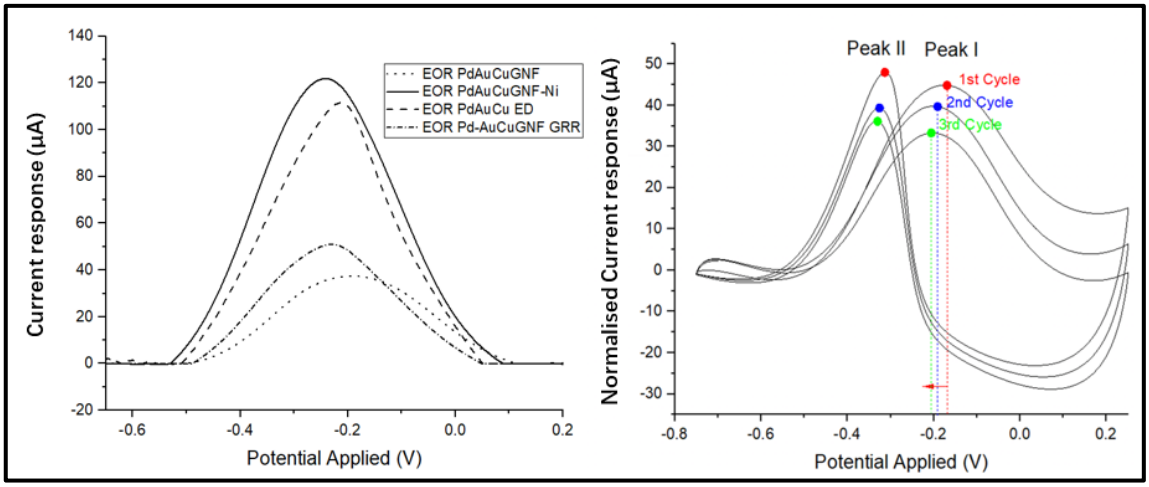

Figure 7.8 Forward oxidation peak of EOR for various nanospecies (left), and 3 cycles of entire CV of PdAuCuGNF catalyzed EOR (right).

We focused our study on the catalytic reactivities of Pd-containing nanoalloys: PdAuCuGNF tri-metal nanoalloy, PdAu nanoalloys synthesized through electrodeposition and GRR, and colloidal PdAuGNF synthesized via GRR. The supporting electrolyte used was 1 M KOH and the analyte was 1 M ethanol. Figure 7.8 left showed the forward scan of the whole CV across different species, which records the oxidation of ethanol. Ethanol oxidation for all catalysts began at about -0.5 V, while an

oxidation peak appeared around -0.2 V. at a larger potential, the ethanol oxidation current response rapidly dropped due to the formation of Pd oxide, making the catalytic surface no longer available for our target reaction. The fast adsorption of OH^- to the catalytic surface will facilitate the formation of a sharp and high current density peak, thus is expected for the most optimal catalyst. [62]

PdAuCuGNF should, in principle, exhibit the highest current response with lower onset potential, however, due to the solvation and instability of cx-GNF in alkaline solutions, it showed the highest onset potential, the highest peak potential, and lowest peak current response. All these indicated that PdAuCuGNF needed further stabilization to make it suitable for EOR under basic conditions. Ni^{2+} stabilization is a technique we discussed in chapter 5. It utilizes the strong affinity of the carboxylate ends of cx-GNF towards Ni^{2+} ions, resulting an insoluble precipitation. And since the metal nanoalloy is fully reduced on the graphene planes of cx-GNFs, this modification will not affect the nanoalloy catalyst. With Ni^{2+} modification, PdAuCuGNF-Ni exhibited the highest current response, plus the most negative onset potential and peak potential, making it the most optimal catalyst of them all, meaning better ethanol kinetics at lower potentials.

PdAu nanoalloy synthesized via electrodeposition + GRR showed comparably outstanding catalytic performances since the current response was not much smaller compared to PdAuCuGNF-Ni, but the onset potential and peak potential were shifted to the right by about 0.05 V. In our studies of the HER and ORR, the data for colloidal PdAuGNF-GRR nanoalloy were almost identical with those from the electrodeposition + GRR PdAu nanoalloy due to the similar surface composition. However, in this study, the

current response for PdAuGNF-GRR was only about half of the other GRR sample. The experiment was repeated many times, and this result was confirmed. To make the cx-GNF in this sample stable, Ni^{2+} modification was also used. The sequence was: AuCuGNF – Ni^{2+} modification – Pd GRR. We wondered if the sequence of the latter two would affect the result. We changed the order and figured out the sequence of Ni^{2+} modification and GRR was not the problem. There are two possible explanations: 1. The electrode was immersed into solutions twice, and some catalysts that were not immobilized from the first round of immersion got rinsed off during the second immersion (but in principle, once the species is drop-coated and dried, it should be immobilized). 2. The solvent for Pd^{2+} used was HCl, although cx-GNF has an affinity towards Ni^{2+}, there is chance that HCl competes with cx-GNF for Ni^{2+} and strips off the Ni^{2+} ions from cx-GNF, making it less stable as we predicted.

Table 7.4 Catalytic ability of Pd-containing nanoalloys concluded from forward scan of EOR

Nanoalloy	**On-set Potential (V)**	**Peak Potential (V)**	**Specific Activity at Peak (A/m^2)**
PdAuCuGNF	-0.49	-0.22	0.80
PdAuCuGNF-Ni	-0.53	-0.24	2.60
PdAu(Cu) (ED GRR)	-0.51	-0.21	2.37
PdAu(Cu) GNF (GRR)	-0.50	-0.19	1.06

The catalytic ability of Pd-containing nanoalloys were summaried in Table 7.4 (each data

spot was averaged over 3 samples, and specific activity at peak for samples has an error of ~$\pm$0.15A/m^2, except for PdAuCuGNF) and this observation leads to the conclusion of the most optimal electrocatalyst for EOR in our study. PdAuCuGNF was the most optimal catalyst, since it has the lowest onset potential, peak potential, and the highest specific activity at peak. But the amount of Pd used during its synthesis is the largest, and another round of stabilization with Ni^{2+} is essential. PdAuED-GRR has less Pd at the catalytic surface yet has high current response. More importantly it is not restricted by pH, so it does not need further stabilization, and thus any unpredicted fluctuations in results can be avoided.

Figure 7.8 right shows 3 cycles of entire CV during EOR for PdAuCuGNF tri-metal nanoalloy as an example of an alloys' full cycle pattern. There are two peaks, Peak I is the oxidation peak which we have discussed and compared with other systems, and Peak II is the reduction peak of PdO recycling to its active form and become ready to react with fresh ethanol. The peaks for three cycles were represented with red, blue, and green dots, respectively. The height of Peak I and Peak II are comparable, meaning the recycling of Pd-containing catalysts are nearly complete. Moreover, the heights have not decreased significantly across three cycles, meaning the catalysts have superior stability. On the other hand, however, the peak potential for three cycles shifted towards the negative side, meaning the reaction is more favoured and easier as Pd is recycled and re-activated.

7.3.6. Stability Tests

The stabilities of colloidal nanospecies under natural aggregation was examined by

leaving colloidal solutions for 10 days at room temperature and the being drop-coated onto electrodes before analysis. The stability of different Ag modified species was done by comparing the percentage of Ag species on the BDDE after 2-hour chrono voltammetry at a constant potential of 0.5 V. the HER was used as an example reaction to value the stabilities (Figure 7.9).

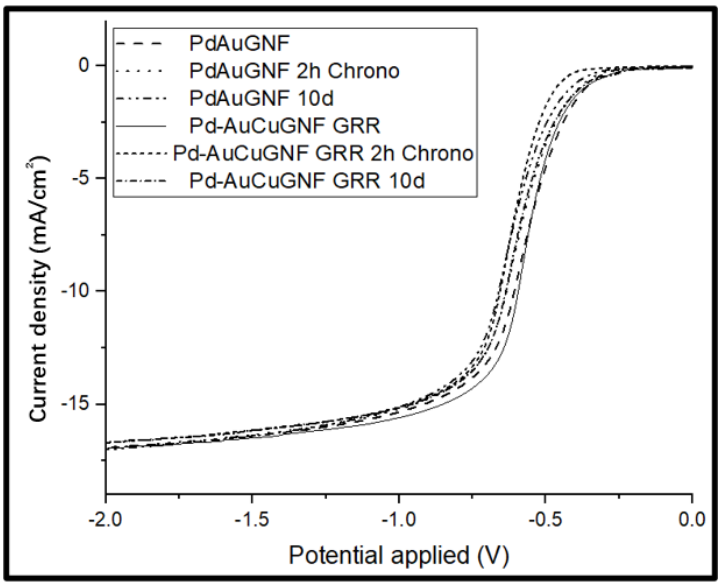

Figure 7.9 Stability of colloidal nanoparticles, examined via the HER and compared with the results of fresh-made ones.

Although the synthesis of cx-GNF stabilized nanoparticles seemed to be easier than electrodeposition, involving only a one-step reduction, its stability in real applications is much more important. Lack of stability means lack of reproductivity of the results, and if fresh colloidal nanoparticles have to be made for every trial, the waste of chemicals will be problematic. Herein, we report the stability of bi-metal colloidal nanoalloys, of PdAuGNF made from direct reduction and galvanic replacement reaction.

Compared with the freshly made samples, the natural aggregation over 10 days did not cause a significant reduction in current density. After the electrodes decorated with nanoparticles were kept at 0.5 V for 2-hour chrono test, the curves shifted more to the left

than in the natural aggregation case. The overall ranking of current densities at -0.75 V is:Pd-AuCuGNF(GRR) 2 h chrono < PdAuGNF 2 h chrono < Pd-AuCuGNF (GRR) 10d < PdAuGNF 10d < Pd-AuCuGNF (GRR) < PdAuGNF

However overall, we did not observe a significant loss in current density, and can thus conclude, that the colloidal nanoparticles stabilized with cx-GNF showed promising stability in electrocatalysis.

7.4 Conclusion

Previously we investigated economic alternatives to Pd and Pt metal as catalysts for the hydrogen production, and how different synthesis techniques can improve the efficiency. In this chapter we synthesized Pd nanoparticles and Pd-containing nanoalloys- PdAu and PdAuCu via electrodeposition followed by the galvanic replacement reaction (GRR) and single-step reduction in aqueous phase using $NaBH_4$ as reducing reagent. All of the modified BDDEs showed superior catalytic reactivities in various important fuel cell reactions.

For electrodeposition, Au(core)Cu(shell) nanoalloys were plated on BDDEs and Cu was then substituted by Pd through GRR, resulting a PdAu decorated electrode surface. On the other hand, colloidal Pd nanoparticles stabilized by cx-GNF were synthesized and a common polymer capping agent PVP was used as control experiment for observing stabilizing outcomes. Aqueous Pd (II) salt was yellow and showed a peak around 400 nm in an UV-Vis spectrum. However, that peak disappeared when Pd was reduced to Pd (0). Pd-PVP was not able to prevent the aggregation and drive full conversion of Pd

nanoparticles and the solution turned back to yellow after one day, with precipitation of bulk Pd metal. PdGNF on the other hand showed extraordinary stability. Afterwards, PdAuGNF and PdAuCuGNF were also synthesized. Colloidal Pd containing species exhibited excellent conductivity and stability against both natural aggregation and chrono-voltammetry.

SEM analysis was done to compare the size and dispersity of nanoparticles synthesized through different techniques. None of the particles synthesized showed aggregation, but the colloidal ones have better dispersion all over the electrode surface, while electrodeposited ones gathered at edges and defects. Electrodeposited Pd containing nanoalloy has an average diameter of 150 nm, which is 10 times of that of colloidal PdAuCu nanoalloy. The surface composition and alloying pattern was investigated further by XPS. For the sample prepared by electrodeposition + GRR, Complete replacement of Cu by Pd was confirmed. For colloidal nanoparticles, XPS showed the structure of the tri-metal alloy was appeared to be an overall core-shell model with Pd at the surface, Au lying in the middle layer and Cu being the core.

The reactivity and stability of those species were examined via the HER. Apart from the HER, which has been extensively investigated in previous chapters, the catalysis of other two fuel cell reactions: oxygen reduction reaction (ORR) and ethanol oxidation reaction (EOR) using Pd-containing nanospecies were also studied. Alkaline media was used particularly for EOR, and colloidal species were further modified with Ni^{2+} ions as mentioned in chapter 5.

Amongst these reactions, Pd-containing nanospecies showed better catalytic reactivity

than all other nanospecies in previous chapters since Pd preserves higher reaction activity in both hydrogen, oxygen and OH binding processes. Alloys exhibited higher current density and peak current response than Pd monomers due to the synergetic effect that modified the surface morphology and electronic structure of nanospecies. Colloidal PdAuCu tri-metal nanoalloy showed the most optimal result in every reaction, indicated by the highest current responses. On the other hand, PdAu nanoalloys synthesized through GRR showed competitive catalytic abilities. Considering the amount of Pd used in GRR process was a lot less than that of 1-step reduction, the compelling performance of these Pd nanoalloys suggested a more economic option.

References

(1) William Hyde Wollaston | British scientist. https://www.britannica.com/biography/William-Hyde-Wollaston (accessed Jan 27, 2021).

(2) Mroczkowski, R. Electronic connector handbook; *McGraw-Hill: New York*, 1998; p pp.3.

(3) Allen, T.; Root, W. An Improved Palladium Chloride Method For The Determination Of Carbon Monoxide In Blood. *Journal of Biological Chemistry* 1955, 216 (1), 319-323.

(4) Colon, P.; Pradelle-Plasse, N.; Galland, J. Evaluation Of The Long-Term Corrosion Behavior Of Dental Amalgams: Influence Of Palladium Addition And Particle Morphology. *Dental Materials* 2003, 19 (3), 232-239.

(5) McEwen, A.; Guttieri, M.; Maier, W.; Laine, R.; Shvo, Y. Metallic Palladium, The Actual Catalyst In Lindlar And Rosenmund Reductions? *The Journal of Organic Chemistry* 1983, 48 (23), 4436-4438.

(6) Adams, C.; Walker, K.; Obare, S.; Docherty, K. Size-Dependent Antimicrobial Effects Of Novel Palladium Nanoparticles. *PLoS ONE* 2014, 9 (1), e85981.

(7) Sachse, A.; Linares, N.; Barbaro, P.; Fajula, F.; Galarneau, A. Selective Hydrogenation Over Pd Nanoparticles Supported On A Pore-Flow-Through Silica Monolith Microreactor With Hierarchical Porosity. *Dalton Trans*. 2013, 42 (5), 1378-1384.

(8) Chaloupka, K.; Malam, Y.; Seifalian, A. Nanosilver As A New Generation Of Nanoproduct In Biomedical Applications. *Trends in Biotechnology* 2010, 28, 580-588.

(9) An introduction to Platinum/Palladium printing - by Scott Hays | Emulsive. https://emulsive.org/articles/an-introduction-to-platinum-palladium-printing-by-scott-hays (accessed Jan 27, 2021).

(10) Lindlar, H. Ein Neuer Katalysator Für Selektive Hydrierungen. *Helvetica Chimica Acta* 1952, 35 (2), 446-450.

(11) Pham-Huu, C.; Keller, N.; Ehret, G.; Charbonniere, L.; Ziessel, R.; Ledoux, M. Carbon Nanofiber Supported Palladium Catalyst For Liquid-Phase Reactions. *Journal of Molecular Catalysis A: Chemical* 2001, 170 (1-2), 155-163.

(12) Quicker, P.; Höllein, V.; Dittmeyer, R. Catalytic Dehydrogenation Of Hydrocarbons In Palladium Composite Membrane Reactors. *Catalysis Today* 2000, 56 (1-3), 21-34.

(13) Beletskaya, I.; Cheprakov, A. The Heck Reaction As A Sharpening Stone Of Palladium Catalysis. *Chemical Reviews* 2000, 100 (8), 3009-3066.

(14) Wolfe, J.; Singer, R.; Yang, B.; Buchwald, S. Highly Active Palladium Catalysts For Suzuki Coupling Reactions. *Journal of the American Chemical Society* 1999, 121 (41), 9550-9561.

(15) Mitsudo, K.; Kaide, T.; Nakamoto, E.; Yoshida, K.; Tanaka, H. Electrochemical Generation Of Cationic Pd Catalysts And Application To Pd/TEMPO Double-Mediatory Electrooxidative Wacker-Type Reactions. *Journal of the American Chemical Society* 2007, 129 (8), 2246-2247.

(16) J. Le Bars , U. Specht , J. S. Bradley and D. G. Blackmond , *Langmuir,* 1999, 15 , 7621

(17) A. Gniewek , A. M. Trzeciak , J. J. Ziólkowsky , L. Kepinski , J. Wrzyszcz and W. Tylus , *J. Catal.,* 2005, 229 , 332

(18) M. B. Thathagar , J. E. ten Elshof and G. Rothenberg , *Angew. Chem., Int. Ed.,* 2006, 45 , 2886

(19) Chatterjee, S.; Griego, C.; Hart, J.; Li, Y.; Taheri, M.; Keith, J.; Snyder, J. Free Standing Nanoporous Palladium Alloys As CO Poisoning Tolerant Electrocatalysts For The Electrochemical Reduction Of CO_2 To Formate. *ACS Catalysis* 2019, 9, 5290-5301.

(20) N. Pentland, J. O'M. Bockris and E. Sheldon, *J. Electrochem. Soc.* 1957, 104, 182

(21) Kelly, T.; Hunt, S.; Esposito, D.; Chen, J. Monolayer Palladium Supported On Molybdenum And Tungsten Carbide Substrates As Low-Cost Hydrogen Evolution Reaction (HER) Electrocatalysts. *International Journal of Hydrogen Energy* 2013, 38, 5638-5644.

(22) Yin, K.; Cheng, Y.; Jiang, B.; Liao, F.; Shao, M. Palladium – Silicon Nanocomposites As A Stable Electrocatalyst For Hydrogen Evolution Reaction. *Journal of Colloid and Interface Science* 2018, 522, 242-248.

(23) Shao, M.; Yu, T.; Odell, J.; Jin, M.; Xia, Y. Structural Dependence Of Oxygen Reduction Reaction On Palladium Nanocrystals. *Chemical Communications* 2011, 47, 6566.

(24) Shao, M.; Odell, J.; Humbert, M.; Yu, T.; Xia, Y. Electrocatalysis On Shape-Controlled Palladium Nanocrystals: Oxygen Reduction Reaction And Formic Acid Oxidation. *The Journal of Physical Chemistry* C 2013, 117, 4172-4180.

(25) Shao, M.; Huang, T.; Liu, P.; Zhang, J.; Sasaki, K.; Vukmirovic, M.; Adzic, R. Palladium Monolayer And Palladium Alloy Electrocatalysts For Oxygen Reduction. *Langmuir* 2006, 22, 10409-10415.

(26) Shao, M.; Liu, P.; Zhang, J.; Adzic, R. Origin Of Enhanced Activity In Palladium Alloy Electrocatalysts For Oxygen Reduction Reaction. *The Journal of Physical Chemistry B* 2007, 111, 6772-6775.

(27) Thi, M.; Tran, T.; Anh, P.; Nhac-Vu, H.; Bui, Q. An Innovative Catalyst Of Nickel-Palladium Alloy Nanocrystals Embedded Nitrogen-Doped Graphene For Efficient Oxygen Reduction Reaction. Journal of Alloys and Compounds 2019, 797, 314-324.

(28) Sha, Y.; Yu, T.; Merinov, B.; Goddard, W. DFT Prediction Of Oxygen Reduction Reaction On Palladium–Copper Alloy Surfaces. *ACS Catalysis* 2014, *4*, 1189-1197.

(29) Fouda-Onana, F.; Bah, S.; Savadogo, O. Palladium–Copper Alloys As Catalysts For The Oxygen Reduction Reaction In An Acidic Media I: Correlation Between The ORR Kinetic Parameters And Intrinsic Physical Properties Of The Alloys. *Journal of Electroanalytical Chemistry* 2009, *636*, 1-9.

(30) Savadogo, O.; Lee, K.; Oishi, K.; Mitsushima, S.; Kamiya, N.; Ota, K. New Palladium Alloys Catalyst For The Oxygen Reduction Reaction In An Acid Medium. *Electrochemistry Communications* 2004, *6*, 105-109.

(31) Ulas, B.; Caglar, A.; Kivrak, A.; Kivrak, H. Atomic Molar Ratio Optimization Of Carbon Nanotube Supported Pdauco Catalysts For Ethylene Glycol And Methanol Electrooxidation In Alkaline Media. *Chemical Papers* 2018, *73*, 425-434.

(32) Raghuveer, V.; Manthiram, A.; Bard, A. Pd−Co−Mo Electrocatalyst For The Oxygen Reduction Reaction In Proton Exchange Membrane Fuel Cells. *The Journal of Physical Chemistry B* 2005, *109*, 22909-22912.

(33) Liu, S.; Zhang, Q.; Li, Y.; Han, M.; Gu, L.; Nan, C.; Bao, J.; Dai, Z. Five-Fold Twinned Pd2niag Nanocrystals With Increased Surface Ni Site Availability To Improve Oxygen Reduction Activity. *Journal of the American Chemical Society* 2015, *137*, 2820-2823.

(34) Darmadi, I.; Nugroho, F.; Kadkhodazadeh, S.; Wagner, J.; Langhammer, C. Rationally Designed Pdaucu Ternary Alloy Nanoparticles For Intrinsically Deactivation-Resistant Ultrafast Plasmonic Hydrogen Sensing. *ACS Sensors* 2019, *4*, 1424-1432.

(35) Xiong, Y.; Cai, H.; Wiley, B.; Wang, J.; Kim, M.; Xia, Y. Synthesis And Mechanistic Study Of Palladium Nanobars And Nanorods. J*ournal of the American Chemical Society* 2007, 129, 3665-3675.

(36) Koczkur, K.; Mourdikoudis, S.; Polavarapu, L.; Skrabalak, S. Polyvinylpyrrolidone (PVP) In Nanoparticle Synthesis. *Dalton Transactions* 2015, 44, 17883-17905.

(37) Xia, Y.; Xiong, Y.; Lim, B.; Skrabalak, S. Shape-Controlled Synthesis Of Metal Nanocrystals: Simple Chemistry Meets Complex Physics?. *Angewandte Chemie International Edition* 2008, 48, 60-103.

(38) Saidi, W.; Feng, H.; Fichthorn, K. Binding Of Polyvinylpyrrolidone To Ag Surfaces: Insight Into A Structure-Directing Agent From Dispersion-Corrected Density Functional Theory. *The Journal of Physical Chemistry C* 2013, 117, 1163-1171.

(39) Sun, Y. Shape-Controlled Synthesis Of Gold And Silver Nanoparticles. *Science* 2002, 298, 2176-2179.

(40) Sun, Y.; Yin, Y.; Mayers, B.; Herricks, T.; Xia, Y. Uniform Silver Nanowires Synthesis By Reducing Agno3 With Ethylene Glycol In The Presence Of Seeds And Poly(Vinyl Pyrrolidone). *Chemistry of Materials* 2002, 14, 4736-4745.

(41) Tsuji, M.; Tang, X.; Matsunaga, M.; Maeda, Y.; Watanabe, M. Shape Evolution Of Flag Types Of Silver Nanostructures From Nanorod Seeds In PVP-Assisted DMF Solution. *Crystal Growth & Design* 2010, 10, 5238-5243.

(42) Wiley, B.; Sun, Y.; Xia, Y. Synthesis Of Silver Nanostructures With Controlled Shapes And Properties. *Accounts of Chemical Research* 2007, 40, 1067-1076.

(43) Wiley, B.; Wang, Z.; Wei, J.; Yin, Y.; Cobden, D.; Xia, Y. Synthesis And Electrical Characterization Of Silver Nanobeams. *Nano Letters* 2006, 6, 2273-2278.

(44) Li, Y.; Boone, E.; El-Sayed, M. Size Effects Of PVP−Pd Nanoparticles On The Catalytic Suzuki Reactions In Aqueous Solution. *Langmuir* 2002, 18, 4921-4925.

(45) Polavarapu, L.; Manga, K.; Cao, H.; Loh, K.; Xu, Q. Preparation Of Conductive Silver Films At Mild Temperatures For Printable Organic Electronics. *Chemistry of Materials* 2011, 23, 3273-3276.

(46) Si, F.; Zhang, Y.; Yan, L.; Zhu, J.; Xiao, M.; Liu, C.; Xing, W.; Zhang, J. Electrochemical Oxygen Reduction Reaction. *Rotating Electrode Methods and Oxygen Reduction Electrocatalysts* 2014, 133-170.

(47) Guo, J.; Chen, R.; Zhu, F.; Sun, S.; Villullas, H. New Understandings Of Ethanol Oxidation Reaction Mechanism On Pd/C And Pd_2Ru/C Catalysts In Alkaline Direct Ethanol Fuel Cells. *Applied Catalysis B: Environmental* 2018, 224, 602-611.

(48) Antolini, E.; Gonzalez, E. Alkaline Direct Alcohol Fuel Cells. *Journal of Power Sources* 2010, 195, 3431-3450.

(49) McCord, P. Standard Potential Redox Tables http://mccord.cm.utexas.edu/courses/spring2016/ch302/standard-pots-redox.php (accessed Aug 3, 2021).

(50) Wang, X.; Chen, S.; Reggiano, G.; Thota, S.; Wang, Y.; Kerns, P.; Suib, S.; Zhao, J. Au–Cu–M (M = Pt, Pd, Ag) Nanorods With Enhanced Catalytic Efficiency By Galvanic Replacement Reaction. *Chemical Communications* 2019, 55, 1249-1252.

(51) Jones, C.; Cappillino, P.; Stavila, V.; Robinson, D. Control Of Both Particle And Pore Size In Nanoporous Palladium Alloy Powders. *Powder Technology* 2014, 267, 95-102.

(52) Nemamcha, A.; Rehspringer, J.; Khatmi, D. Synthesis Of Palladium Nanoparticles By Sonochemical Reduction Of Palladium(II) Nitrate In Aqueous Solution. *The Journal of Physical Chemistry B* 2006, 110, 383-387.

(53) Li, D.; Kaner, R. Shape And Aggregation Control Of Nanoparticles: Not Shaken, Not Stirred. *Journal of the American Chemical Society* 2006, 128, 968-975.

(54) Valenzuela, R.; Fuentes, M.; Parra, C.; Baeza, J.; Duran, N.; Sharma, S.; Knobel, M.; Freer, J. Influence Of Stirring Velocity On The Synthesis Of Magnetite Nanoparticles (Fe3o4) By The Co-Precipitation Method. *Journal of Alloys and Compounds* 2009, 488, 227-231.

(55) Helmenstine, T. Periodic Table of Element Atom Sizes https://sciencenotes.org/periodic-table-chart-element-sizes/ (accessed Aug 3, 2021).

(56) Frey, K.; Schmidt, D.; Wolverton, C.; Schneider, W. Implications Of Coverage-Dependent O Adsorption For Catalytic NO Oxidation On The Late Transition Metals. *Catal. Sci. Technol.* 2014, 4, 4356-4365.

(57) Lavine, M. Materials Science: A Bit Of A Stretch. *Science* 2003, 299, 981b-981.

(58) Hope, H.; Power, P. X-Ray Crystal Structure Of A Late-Transition-Metal Dialkylamide, $[(CuNEt_2)_4]$. *Inorganic Chemistry* 1984, 23, 936-937.

(59) Namba, K.; Ogura, S.; Ohno, S.; Di, W.; Kato, K.; Wilde, M.; Pletikosić, I.; Pervan, P.; Milun, M.; Fukutani, K. Acceleration Of Hydrogen Absorption By Palladium Through Surface Alloying With Gold. *Proceedings of the National Academy of Sciences* 2018, 115, 7896-7900.

(60) Nørskov, J.; Rossmeisl, J.; Logadottir, A.; Lindqvist, L.; Kitchin, J.; Bligaard, T.; Jónsson, H. Origin Of The Overpotential For Oxygen Reduction At A Fuel-Cell Cathode. *The Journal of Physical Chemistry B* 2004, 108, 17886-17892.

(61) Lv, H.; Sun, L.; Lopes, A.; Xu, D.; Liu, B. Insights Into Compositional And Structural Effects Of Bimetallic Hollow Mesoporous Nanospheres Toward Ethanol Oxidation Electrocatalysis. *The Journal of Physical Chemistry Letters* 2019, 10, 5490-5498.

(62) Zhang, Z.; Xin, L.; Sun, K.; Li, W. Pd–Ni Electrocatalysts For Efficient Ethanol Oxidation Reaction In Alkaline Electrolyte. *International Journal of Hydrogen Energy* 2011, 36, 12686-12697.

Chapter 8 Conclusion and Future Prospects

8.1 Conclusion

The entire thesis examined how BDDE performance in electrochemical catalysis and sensing can be influenced by the morphology, surface composition, and additional stabilisation of metal nanoparticle modifiers. To achieve the best outcome for the systems of interest, we particularly concentrated on how the properties of modifiers can be fine-tuned by changing the synthesis technique and parameters.

The following is a list of significant discoveries and accomplishments from the experimental chapters.

Chapter 3:

- Successful **synthesis of three types of AgNPs** (pAgNPs, dAgNPs, and sAgNPs) via 1-step and 2-step electrodeposition. The morphologies were effectively controlled by method and overpotential.
- Variations in surface compositions and structures is directly related to the **catalytic performance and stabilities of different types of AgNPs** together, and sAgNPs modified BDDE is the best candidate for electrocatalysis (using the HER as an example).

Chapter 4:

- Successful **synthesis of two types of AgAuNAs** (dAgAuNAs, sAgAuNAs) via electrodeposition and the morphologies were effectively controlled by varying ED methods.
- Determination of **structural differences** between the two types of AgAuNAs using XPS and sequential ED of Au onto different substrates. **Enhanced performance of NAs** was seen in

HER catalysis, and a direct relationship between alloying structure and catalytic performance was concluded.

Chapter 5:

- Successful **synthesis of cx-GNF stabilised colloidal NPs and NAs** via chemical reduction method, with **outstanding stability against natural aggregation** for over 14 days.
- **Enhanced performance in HER catalysis** of cx-GNF stabilised nanospecies, compared to nanospecies made through ED, and other types of colloidal nanospecies.

Chapter 6:

- Successful **electrochemical sensing** of AuGNF towards detection of As (III), 4-NP, glucose, and hydroquinone with:
  - simple synthesis set-ups;
  - LOD and sensitivity comparable to previous works with higher Au loading and complex modifications;
  - simultaneous detection of structurally similar molecules with high sensitivity;
  - ability to withstand different pHs.

Chapter 7:

- **Successful synthesis of Pd containing nanoalloys** via ED, GRR, and chemical reduction methods.
- Variations in **surface compositions and structures** were determined and analysed, especially for the tri-metal PdAuCuNA.

- **Enhanced catalytical performances of Pd-containing NAs** were observed for various fuel cell reactions (HER, EOR, ORR), and the performances were directly related to the synthesis method, structure, and surface composition of individual species.

8.2 Future Prospects

There are several perspectives that can further improve the understanding of the works in the thesis:

- Synthesis and structures:
  - Determination of roles of E_1, E_2, t_1, t_2 individually in 2-step electrodeposition, on how each of them can determine what characteristic aspect of the NPs resulted using controlled electrodepositions and SEM.
  - Investigation on how the average size distributions and variations look like for different types of nanospecies by using image J for particle counts in TEM and explore how they can potentially affect the electrochemical performance.
  - Confirmation of differences in alloy structures of NA (core-shell, cluster, *etc.*) using AFM, EXAFS, and TEM, to compare and compensate with the present conclusions from XPS.
- Electrochemical applications:
  - Comparison of differences in catalytical performances between nanospecies that are modified onto different types of electrodes (*e.g.* BDDE vs. GCE), using the same synthesis methods, parameters, and the HER as an example.
  - Determination of the adsorption surfaces of different types of nanoalloys, using EXAFS, to get information on what the reaction interfaces looks like.

- Investigation of how surface termination of BDDEs (HBDDE and OBDDE) would affect the selectivity towards electrochemical detections of different molecules, using CV, SWV and DPV.
- Determination of how the NAs surface atoms would interact with the adsorbates in the atmosphere (*e.g.*, O_2, H_2) via ligand effect, and how it would modify the characteristics of NAs using EXAFS for structural information, and the HER for electrochemical information.